

Plasmon logic gates designed by modal engineering of 2-dimensional crystalline metal cavities

Upkar Kumar

▶ **To cite this version:**

Upkar Kumar. Plasmon logic gates designed by modal engineering of 2-dimensional crystalline metal cavities. Micro and nanotechnologies/Microelectronics. Université Paul Sabatier - Toulouse III, 2017. English. NNT : 2017TOU30170 . tel-01963241

HAL Id: tel-01963241

https://theses.hal.science/tel-01963241

Submitted on 21 Dec 2018

HAL is a multi-disciplinary open access archive for the deposit and dissemination of scientific research documents, whether they are published or not. The documents may come from teaching and research institutions in France or abroad, or from public or private research centers.

L'archive ouverte pluridisciplinaire **HAL**, est destinée au dépôt et à la diffusion de documents scientifiques de niveau recherche, publiés ou non, émanant des établissements d'enseignement et de recherche français ou étrangers, des laboratoires publics ou privés.

Université de Toulouse

THÈSE

En vue de l'obtention du

DOCTORAT DE L'UNIVERSITÉ DE TOULOUSE

Délivré par : *l'Université Toulouse 3 Paul Sabatier (UT3 Paul Sabatier)*

Présentée et soutenue le *08/11/2017* **par :**

Upkar KUMAR

Plasmon logic gates designed by modal engineering of 2-dimensional crystalline metal cavities

---

JURY

David GUÉRY-ODELIN	Professeur d'Université	Président du Jury
Celine FIORINI-DEBUISSCHERT	Chercheur	Rapporteur
Antoine MOREAU	Assistant Professeur	Rapporteur
Cyriaque GENET	Directeur de Recherche	Examinateur
Alexandre BOUHELIER	Directeur de Recherche	Membre du Jury
Christian GIRARD	Directeur de Recherche	Membre du Jury
Erik DUJARDIN	Directeur de Recherche	Co-directeur de thèse
Aurélien CUCHE	Chargé de Recherche	Co-directeur de thèse

École doctorale et spécialité :
SDM : Nano-physique, nano-composants, nano-mesures - COP 00

Unité de Recherche :
Centre d'Élaboration de Matériaux et d'Études Structurales (UPR 8011)

Directeur(s) de Thèse :
Erik DUJARDIN et *Aurélien CUCHE*

Rapporteurs :
Celine FIORINI-DEBUISSCHERT et *Antoine MOREAU*

ACKNOWLEDGEMENTS

It is my pleasure to express my deep sense of thanks to several individuals who were instrumental in completion of my PhD.

First and foremost, I would like to express my sincere gratitude to my mentors and supervisors Dr. Erik Dujardin and Dr. Aurélien Cuche for all their valuable suggestions, guidance and unconditional support over the period of my PhD through both good times and bad times. I truly enjoyed working in an environment which stimulates original thinking and initiative which they created. Their guidance, innovative ideas and stoic patience are greatly appreciated.

I would like to acknowledge the valuable inputs from Dr. Christian Girard who was always happy to discuss, assist and resolve most difficult modelling issues. His timely advices have immensely helped in shaping my research. I would also like to pass on my sincere vote of thanks to Dr. Alexandre Bouhelier for hosting me several times at Dijon and providing me chance to work on his state of art of lab at ICB, Dijon. Special thanks to Dr. Sviatlana Viarbitskaya for her help during the experimental missions at Dijon.

These acknowledgements would not be complete without mentioning my lab and office colleagues: Bulent Baris, Janak Prasad, Marie Herve, Mohanad Alchar, Laureen Moreaud, Marc Nunez, Victor Freire, Delphine Sordes and Benoit Eydoux. It was great working with them and I really appreciate their ideas, help and good humour.

Aside from the main physics crowd, I would also like to thank those who were and still are there for me outside my lab. Thanks to Prerna Bagri, Raghuveer Kasaraneni, Vandita Banka, Hari Prasath, Aishwarya Balaji, Alok Singh, Neeti Singh and Anvika Singh for making my stay at Toulouse pleasant and a memorable one.

Lastly and most importantly, I would like to thank my parents and other family members who are eagerly waiting for my return, for their patience, continuous support and encouragement. It is of no surprise that I dedicate this work to them. With regards to the numerous questions about my future endeavours from family and friends, I shall answer in the words of Sir Winston Churchill: “Now this is not the end, it is not even the beginning of the end. But, it is perhaps the end of the beginning”.

Table of Contents

I Motivations 9

II Introduction 15

2.1 Introduction to plasmonics 15

2.1.1 Surface plasmon polaritons 16

2.1.2 Localized Surface Plasmons 21

2.1.3 Micrometre sized metallic structures 23

2.2 Local density of states 24

2.2.1 Photonics LDOS 25

2.2.2 Surface plasmon local density of states (SPLDOS) 27

2.2.3 Non-linear photon luminescence and SPLDOS 28

2.3 Single crystalline colloidal system 30

2.3.1 Top down and bottom up approaches 30

2.3.2 Crystalline colloidal systems for reconfigurable plasmonic devices 32

III Materials and methods 39

3.1 Experimental fabrication and characterization techniques 39

3.1.1 Wet Chemical synthesis 39

3.1.2 Focussed Ion Beam 40

3.1.3 Dark field scattering microscopy 42

3.1.4 Non-linear photon luminescence microscopy 45

3.1.5 Leakage radiation microscopy 48

3.2 Simulation techniques 50

3.2.1 Green Dyadic Method 50

3.2.2 Transmission Maps 53

3.2.3 SPLDOS and TPL Maps 56

IV Spectral engineering of two – dimensional plasmonic nanoprisms 63

4.1 Introduction 63

4.2 Au nanoprisms on ITO substrate 64

4.2.1 Spectral response of Au nanoprisms and Lorentzian decomposition 64
4.2.2 Variation of spectral features with size of the cavity 67
4.3 Spectral control of SP resonances in a MIM configuration 71
4.3.1 Spectral response of Au nanoprisms on 30nm thin Au film 71
4.3.2 Tuning of spectral responses of Au prism with different metallic substrates ... 75
4.4 Spectral response of Au nanoprism in presence of hole 76
4.5 Conclusions 79

V Multimodal bowtie antennas for efficient far-field to near-field conversion 84
5.1 Introduction 84
5.2 TPL response of the multimodal bowtie antenna 85
5.3 Local field enhancement and multiscale nature of the antennas 91
5.4 Conclusions 94

VI Designing transmission eigenstates for tailoring SPP propagation in 2D plasmonic device 99
6.1 Introduction 99
6.2 Computation of the transmission maps 101
6.2.1 Excitation of the diabolo structure by a dipole 101
6.2.2 Excitation of the diabolo structure by a Gaussian shaped plane wave 102
6.2.3 Excitation of the diabolo structure by real Gaussian function 103
6.3 Designing of diabolo 104
6.4 Transmittance of plasmonic signal in a 2D diabolo cavity 106
6.4.1 Tuning of transmittance with incident polarization and excitation position ... 108
6.4.2 Tuning of transmittance with incident wavelength 117
6.4.3 Spectral detuning in asymmetrical diabolo 117
6.5 Conclusion 120

VII Reconfigurable modal plasmonic logic gates 124
7.1 Introduction 124
7.2 Gedanken Experiment 126
7.3 Choice of the structure for the modal logic gates device 130

7.4 Realization of modal logic gates on double hexagon structures 133
7.4.1 Numerical proof of the principle 133
7.4.2 Experimental implementation 135
7.5 Reconfiguration of the modal plasmonic logic gates 138
7.5.1 Reconfiguration of logic gates with different threshold 138
7.5.2 Reconfiguration based on different set of input locations 140
7.5.3 Reconfiguration based on different set of polarizations 141
7.6 Conclusion 143

VIII Conclusions and future perspectives 147

Résumé en français de la thèse 153

Chapter I

Motivations

In 1959, when Richard Feynman said "*There is plenty of room at the bottom*" [1], his statement was not received so enthusiastically by the scientific community. But in a little more than a decade, the interest for the nano-world had increased rapidly leading to the emergence of a new field called nanotechnology [2]. Besides electronics, one of the fields of nanotechnology that has undergone a remarkable expansion and progress is plasmonics, the technology based on the interaction between free electrons in noble metals and impinging electromagnetic fields [3], [4]. The plasmon resonances can be categorized in two types – surface plasmon polaritons (SPP), which are collective electronic waves propagating along a metal-dielectric interface and localized surface plasmon, (LSP) which are confined oscillations of surface electrons on a metal nanoparticle. Research on plasmons has essentially investigated the properties of either macroscopic metallic structures that facilitate propagation, wave guiding and routing of SPP or nanometre-scale metallic particles that produce intense resonances and a strong field confinement. Beyond a wealth of fascinating physics, this field has generated innovative applications ranging from superfast computer [5], [6] to treatment of cancer [7], [8] , highly sensitive molecular detectors [9], data storage devices [10], [11], optical information processing [12], [13] , quantum optics [14], [15] etc.

Surprisingly, much less attention has been paid to an intermediate regime of micrometer-sized structures in which both localized LSP resonances and propagating SPP co-exist and contribute equivalently to the optical properties of the structure. This doctoral work is dedicated to a comprehensive study of individual metallic structures in this intermediate size regime and will explores new possible applications in plasmon-based information processing.

So far, the most advanced plasmonic devices and interconnects are produced by a standard top-down microfabrication approach [16]. In the micrometer-size range, the performances of such devices are limited are by scattering-related energy dissipation which essentially originates in the amorphous or polycrystalline nature of the original metallic film [17]. More than a decade ago, it was shown that chemically produced crystalline nanowire suffered comparatively less energy dissipation than top-down fabricated plasmonic waveguide

of identical geometry [18]. This was generalized to flat two-dimensional plasmonic antennas carved out inside thin crystalline gold plates [19]. Information processing circuits and prototypes exploiting the properties of crystalline nanowires of flakes have been demonstrated. However, generally, the working principle involves the encoding of both the input information and the transfer function of the device in the form of polarization or wavelength of the incident beam(s). For example, a full family of logic gates was recently realized using polarization and phase dependent interferences between plasmon signals propagating along silver nanowires [20]. While complex logic gate functions have been reported by cascading elementary logic gates [20], [21], the performances of such interferential devices are limited by the precision of the relative positioning of the active building blocks with respect to each other and of the excitation spot.

In this thesis, we propose to revert this paradigm, i.e. to design plasmonic devices in two dimensions and in a size regime that confers them with characteristic confined resonances or modes independently from the excitation configuration. We will seek to tailor and control the spectral and spatial behaviour of the mesoscale structures, to exploit them for capturing photons to excite plasmons, routing plasmonic signal from one point to another and to explore new ideas for the realization of complex plasmonic modal logic gates.

Chapter II of this thesis provides a brief introduction to the field of plasmonics. Plasmon phenomena are exposed along with the basic models describing them. Next we detail the concept of local density of plasmonic states which conveniently describes the properties of objects bearing a large but finite number of modes. The chapter concludes by a description of the specific crystalline plasmonic nanoparticles used in this work. These are ultrathin triangular or hexagonal platelets with lateral dimensions comprised between 0.5 and 5.0 μm.

The third chapter collects the technical details regarding all the experimental fabrication procedures and characterization techniques used throughout the thesis. A detailed section is dedicated to the description of simulation tools based on Green Dyadic Method developed by Christian Girard (CEMES). All the simulations presented in this work were performed using these codes.

In chapter IV, we present, a systematic study of the spectral properties of sharp triangular gold nanoprisms as their size is increased from 400nm to 900nm. These objects host a collection of resonances the characteristics of which will be experimentally examined and compared to simulations. Next we wondered if the spectral response of the gold nanoprisms

supported on glass could be altered by the presence of a nearby thin metal film or by the introduction of a hollow defect in the gold nanoprism.

Chapter V will focus on one first information processing function: far-field to near-field conversion antennas. A bowtie antenna configuration will be constructed by the coupling between two of these crystalline mesoscale prisms. The effect of the relative size of the prism cavities will be studied. In particular, we will investigate, whether, the incident polarization and relative position of one cavity with the other have an effect on the properties of the antenna.

In chapter VI, we will focus on the ways to transmit information from one incident point to another emitting point by exciting delocalized modes with well-defined spatial distribution. For this we will consider introducing a rectangular channel connecting two individual triangular cavities in a diabolo-like geometry. A comprehensive experimental and numerical study of the plasmon transmittance will be conducted by examining the effects of changing the incident polarization, the excitation position, the relative size of the two prisms or the excitation wavelength. This study will indicate how a tailored two dimensional metallic cavity can be relevant to the design of more complex modal plasmonics devices

Chapter VII presents the most advanced proposal of this work as it described the design and implementation of a modal plasmonic architecture realizing the function of Boolean logic gates. Gedanken experiments proposed earlier in our group will be experimentally implemented for the first time. In particular, we will demonstrate how to create 2-input, 1-output logic gates based on the modal features of the 2D metallic structures. In the final part of this chapter, we will investigate the concept of reconfigurable logic gates that demonstrates the high potential of our non-conventional approach for creating even more complex information processing devices.

References

[1] R. P. Feynman, “There’s plenty of room at the bottom: An invitation to enter a new field of physics,” *Eng. Sci.*, vol. 23, pp. 22–35, 1960.

[2] E. K. Drexler, “Molecular Machinery and Manufacturing With Applications to Computation,” *Engineering*, no. 1977, pp. 1–487, 1977.

[3] L. Novotny and B. Hecht, "Principles of Nano-Optics", *Cambridge University Press*, 2nd Ed., no. 1. 2012.

[4] S. A. Maier, “Plasmonics: Fundamentals and Applications,” *Springer*, 2007.

[5] H. A. Atwater, “The promise of plasmonics,” *ACM SIGDA Newsl.*, vol. 37, no. 9, pp. 1–1, 2007.

[6] J. R. Kerrn, “Perspective on plasmonics,” *Nat. Photonics*, vol. 6, no. 11, pp. 714–715, 2012.

[7] C. Yang, L. Ma, X. Zou, G. Xiang, and W. Chen, “Surface plasmon-enhanced Ag/CuS nanocomposites for cancer treatment,” *Cancer Nanotechnol.*, vol. 4, no. 4–5, pp. 81–89, 2013.

[8] S. B. Lakshmanan, X. Zou, M. Hossu, L. Ma, C. Yang, and W. Chen, “Local field enhanced Au/CuS nanocomposites as efficient photothermal transducer agents for cancer treatment,” *J. Biomed. Nanotechnol.*, vol. 8, no. 6, pp. 883–890, 2012.

[9] J. N. Anker, W. P. Hall, O. Lyandres, N. C. Shah, J. Zhao, and R. P. Van Duyne, “Biosensing with plasmonic nanosensors,” *Nat. Mater.*, vol. 7, no. 6, pp. 442–453, 2008.

[10] D. O’Connor and A. V. Zayats, “Data storage: The third plasmonic revolution,” *Nat. Nanotechnol.*, vol. 5, no. 7, pp. 482–483, 2010.

[11] P. Zijlstra, J. W. M. Chon, and M. Gu, “Five-dimensional optical recording mediated by surface plasmons in gold nanorods,” *Nature*, vol. 459, no. 7245, pp. 410–413, 2009.

[12] B. Lamprecht, J. R. Krenn, G. Schider, H. Ditlbacher, M. Salerno, N. Felidj, A. Leitner, and F. R. Aussenegg, “Surface plasmon propagation in microscale metal stripes,” *Appl. Phys. Lett.*, vol. 79, no. 1, pp. 51–53, 2001.

[13] J. Liu, G. Fang, H. Zhao, Y. Zhang, and S. Liu, “Plasmon flow control at gap waveguide junctions using square ring resonators,” *J. Phys. D. Appl. Phys.*, vol. 43, no. 5, p. 55103, 2010.

[14] D. E. Chang, A. S. Sorensen, P. R. Hemmer, and M. D. Lukin, “Quantum optics with surface plasmons,” *Phys. Rev. Lett.*, vol. 97, no. 5, 2006.

[15] A. V. Akimov, A. Mukherjee, C. L. Yu, D. E. Chang, A. S. Zibrov, P. R. Hemmer, H. Park and M. D. Lukin, “Generation of single optical plasmons in metallic nanowires coupled to quantum dots,” *Nature*, vol. 450, no. 7168, pp. 402–406, 2007.

[16] W. Pfaff, A. Vos, and R. Hanson, “Top-down fabrication of plasmonic nanostructures for deterministic coupling to single quantum emitters,” *J. Appl. Phys.*, vol. 113, no. 2, 2013.

[17] A. Trügler, J.-C. Tinguely, J. R. Krenn, A. Hohenau, and U. Hohenester, “Influence of surface roughness on the optical properties of plasmonic nanoparticles,” *Phys. Rev. B*, vol. 83, no. 8, p. 81412, 2011.

[18] H. Ditlbacher, A. Hohenau, D. Wagner, U. Kreibig, M. Rogers, F. Hofer, F. R. Aussenegg, and J. R. Krenn, “Silver Nanowires as Surface Plasmon Resonators,” *Phys. Rev. Lett.*, vol. 95, no. 25, p. 257403, 2005.

[19] J.-S. Huang, V. Callegari, P. Geisler, C. Brüning, J. Kern, J. C. Prangsma, X. Wu, T. Feichtner, J. Ziegler, P. Weinmann, M. Kamp, A. Forchel, P. Biagioni, U. Sennhauser and B. Hecht “Atomically flat single-

crystalline gold nanostructures for plasmonic nanocircuitry," *Nat. Commun.*, vol. 1, no. 9, p. 150, 2010.

[20] H. Wei, Z. Wang, X. Tian, M. Käll, and H. Xu, "Cascaded logic gates in nanophotonic plasmon networks," *Nat. Commun.*, vol. 2, p. 387, 2011.

[21] H. Wei and H. Xu, "Nanowire-based plasmonic waveguides and devices for integrated nanophotonic circuits," *Nanophotonics*, vol. 1, no. 2, pp. 155–169, 2012.

Chapter II

Introduction

2.1 Introduction to Plasmonics

The invention of laser in 1960 brought a revolution in the field of optics and photonics which has since then grown into an important technology with widespread applications including optical information processing. The development in silicon photonics have resulted in the realization of small on-chip devices which enable routing and modulation of optical signals [1]. Few examples of photonics based devices which have been demonstrated on small chips are optical switches, optical modulators, optical sensors, photonic interconnects, photonic waveguides, etc. [2]–[5]. These photonic devices, however, are diffraction limited which means that, it is not possible to confine light into the regions that are smaller than its wavelength [6]. This diffraction limit can be overcome by using photons to excite surface plasmons, which provide us a way to manipulate and guide light at a sub-wavelength scale via strong electromagnetic field confinement [7], [8].

The scientific investigation of plasmonic effects began as early as 1902 by Robert Wood when he observed a dark band in spectrum of light diffracted from a metallic grating which is now called Wood's anomalies [9]. It was followed by the physical interpretation of the phenomenon by Lord Rayleigh [10] in 1907 who suggested that the anomaly in the spectrum of diffracted light takes place at a wavelength for which the scattered wave emerges tangentially to the surface. It took a couple of decades before Ugo Fano predicted the existence of polarized quasi stationary waves resonating along metal surface associated with these anomalies [11]. In 1957, R. H. Ritchie recorded loss of energy of an electron beam when diffracted at thin metallic foils [12]. He predicted that this energy loss is due to the coherent excitations of electrons inside the metal which were later on termed as surface plasmons. However, it was not before 1968 that the systematic study of the surface plasmon could start, when Erich Kretschmann [13] and Andreas Otto [14], almost simultaneously came up with techniques to optically excite surface plasmons. In last five decades, with the breakthroughs in various nanofabrication and characterization techniques and development of electromagnetic modelling, plasmonics has evolved from a physical phenomenon to an optical technology which has kept researchers across the spectrum interested.

2.1.1 Surface plasmon polaritons

Surface plasmon polaritons (SPP) are two dimensional electromagnetic wave travelling along an interface between materials with dielectric constants of opposite sign (i.e. a conductor and a dielectric) and evanescent in the direction perpendicular to the interface. The schematic of a SPP propagating along a metal-dielectric interface is shown in figure 2.1.

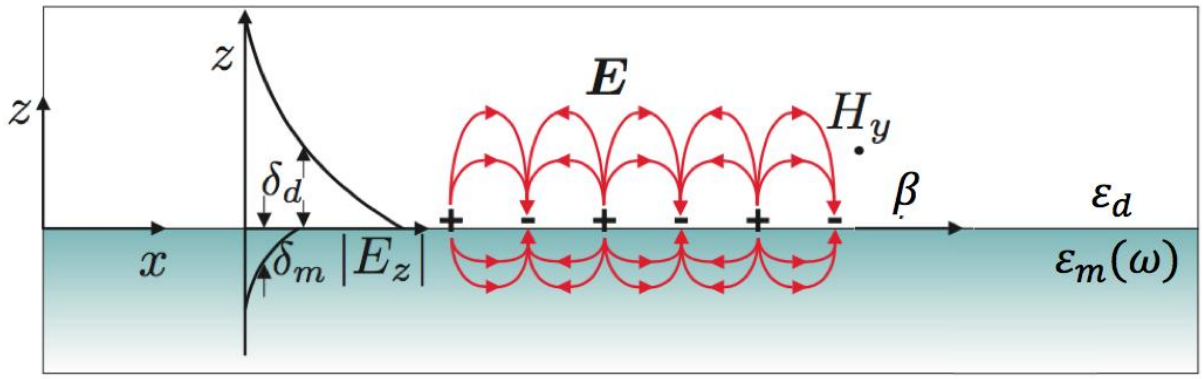


Figure 2.1 Schematic of SPP propagation at an interface of metal and dielectric with dielctric constants $\varepsilon_m(\omega)$ and ε_d respectively.

The SPP waves are propagating along the x axes and the field has no spatial dependence along the y-direction. The x-y plane overlaps with the interface between a metal with a dielectric constant $\varepsilon_m(\omega)$ and a dielectric medium (z > 0) with the positive dielectric constant ε_d. These evanescent waves confined to the interface exists only for transverse magnetic (TM) polarization where field components E_x, E_z and H_y are non zero. For TE modes, field components H_x, H_z and E_y are non zero and are given by –

$$E_y(z) = A_2\, e^{i\beta x} e^{-k_d z} \tag{2.1a}$$

$$H_x(z) = -iA_2 \frac{1}{\omega\mu_0} k_2\, e^{i\beta x} e^{-k_d z} \tag{2.1b}$$

$$H_z(z) = -iA_1 \frac{1}{\omega\mu_0}\, e^{i\beta x} e^{-k_d z} \tag{2.1c}$$

for z > 0 and

$$E_y(z) = A_1\, e^{i\beta x} e^{-k_m z} \tag{2.1d}$$

$$H_x(z) = -iA_1 \frac{1}{\omega\mu_0}\, k_1 e^{i\beta x} e^{-k_m z} \tag{2.1e}$$

$$H_z(z) = -iA_1 \frac{1}{\omega\mu_0}\, e^{i\beta x} e^{-k_m z} \tag{2.1f}$$

for z < 0. Here, H_x and E_y will be continuous at the interface only when

$$A_1(k_d + k_m) = 0 \tag{2.2}$$

Since k_d and k_m are both of same sign, the condition can be fulfilled only when A_1 and A_2 both are zero.

Thus, SPP modes is only possible with the TM polarization where the electric field, *E* is parallel to the plane of incidence and thus we have component of electric field along x and z directions. To better understand this, let us first consider the solutions of the propagating wave confined to the interface for TM polarization [15] –

$$H_y(z) = A_2\, e^{i\beta x} e^{-k_d z} \tag{2.3a}$$

$$E_x(z) = -iA_2 \frac{1}{\omega \varepsilon_0 \varepsilon_2} k_2\, e^{i\beta x} e^{-k_d z} \tag{2.3b}$$

$$E_z(z) = -iA_1 \frac{1}{\omega \varepsilon_0 \varepsilon_2}\, e^{i\beta x} e^{-k_d z} \tag{2.3c}$$

for z > 0 and

$$H_y(z) = A_1\, e^{i\beta x} e^{-k_m z} \tag{2.3d}$$

$$E_x(z) = -iA_1 \frac{1}{\omega \varepsilon_0 \varepsilon_1} k_1 e^{i\beta x} e^{-k_m z} \tag{2.3e}$$

$$E_z(z) = -iA_1 \frac{1}{\omega \varepsilon_0 \varepsilon_1}\, e^{i\beta x} e^{-k_m z} \tag{2.3f}$$

for z < 0. For continuity of E_x, E_z and H_y at the interface, A_1 and A_2 must be equal we must fulfil following conditions -

$$\frac{k_d}{k_m} = -\frac{\varepsilon_d}{\varepsilon_m} \tag{2.4a}$$

$$k_m{}^2 = \beta^2 - k_0{}^2 \varepsilon_m \tag{2.4b}$$

$$k_d{}^2 = \beta^2 - k_0{}^2 \varepsilon_d \tag{2.4c}$$

Combining above three relations results in the dispersion relation for SPP propagating along the interface which is given by -

$$\beta = k_0\sqrt{\frac{\varepsilon_m(\omega)\varepsilon_d}{\varepsilon_m(\omega)+\varepsilon_d}} \tag{2.5}$$

where β is the SPP propagation constant. The SPPs exponentially decay in the dielectric and the metallic mediums as shown in the figure 2.1. The penetration depths δ_d and δ_m respectively in the two mediums are given by –

$$\delta_i = \frac{\lambda}{2\pi}\sqrt{\frac{Re|\varepsilon_m|+\varepsilon_d}{(\varepsilon_i)^2}} \tag{2.6}$$

where '*i*' denotes the medium in which SPP is penetrating. The corresponding SPP dispersion curve is shown in figure 2.2 along with the dispersion curve for a free space photon. The figure shows that the SPP dispersion relation curve is always placed to the right of the light line. A momentum projection of photons falling on the interface at an angle 'θ' to the normal surface, $k_x = k_0 sin\theta$ will always be smaller than β. This condition makes it impossible to excite the SPP with a standard propagating electromagnetic wave. Before discussing the possible techniques to excite SPP, it is worth understanding damping and losses mechanism in SPPs. The dielectric constant of metal, $\varepsilon_m(\omega)$ in the dispersion relation consists of both real and imaginary components. The imaginary part of the dielectric constant describes the energy dissipation due to electron oscillations in the metal which is also called as Ohmic damping. This imaginary part of the dielectric constant also appears in the solution for the SPPs in form of an exponentially decaying damping term which leads to an SPP propagation length given by

$$\delta_{SP} = \frac{1}{2Im(\beta)} \tag{2.7}$$

The momentum of light and SPP can be matched using different coupling configurations based on uses of prisms [13], [14], grating [16]–[18], optical fibre tip [19], and high numerical aperture objective lens [20]. There are basically two different prism based SPP excitation techniques. Both techniques are based on the coupling of the SPPs to the evanescent electromagnetic field that is formed upon total internal reflection of a light beam at the surface of a thin metal film. The first configuration is called the Kretschmann configuration [13] where, the metal film is evaporated on top of a glass prism and is then illuminated through the dielectric prism at an angle of incidence greater than the critical angle. Now, the light reflected at the interface between the prism and the metal film has an in-plane momentum of $k_x = k_0\sqrt{\epsilon_{prism}}\ sin\theta$. Under these conditions, the resonant light tunnel through the thin metal layer and couples to the SPP.

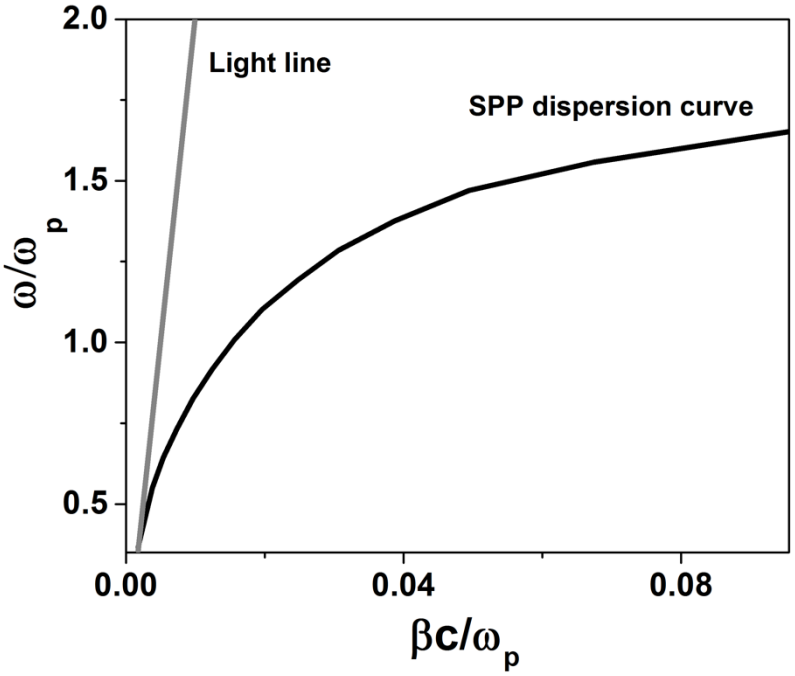


Figure 2.2 The dispersion curve for a SPP propagating at a gold – dielectric interface. The grey line to the right of SPP dispersion curve is the light line. The value of dielectric constant has been taken from Johnson and Christy 1972. Frequency, ω is normalized by plasma frequency, ω_p.

The principle of the Kretschmann configuration is shown in figure 2.3(a). However, with the increase in the thickness of the metal film, the tunnelling distance also increases which result in decrease in the efficiency of the SPP excitation. For the thicker metal film, Otto's configuration is used to excite the SPP (figure 2.3(b)). Here the prism is place close to the metal surface with a gap of air in between and thus the tunnelling occurs through the air gap between the prism and metal. The resonant conditions are similar to those in the Kretschmann configuration. This excitation configuration is also useful when the direct contact of the metal film and the prism needs to be avoided. The other coupling technique used to avoid the mismatch in the SPP and the impinging photon wave vectors is a grating coupling technique. The phase matching for a one dimensional grating of grooves with lattice constant 'a' as shown in figure 2.3(c) will occur at the following condition -

$$\beta = k_0 \sin\theta \pm nG \tag{2.8}$$

where $G = \frac{2\pi}{a}$ is the reciprocal vector of the grating and n is an integer. Similar to the prism coupling, excitation of the SPPs can be detected by a minimum in the reflected light. One of

the most widely used technique to excite SPP in thin films is by using a high numerical aperture oil microscope objective. The numerical aperture of an objective lens is given by

$$NA = n \sin\theta \tag{2.9}$$

where 'n' is the refractive index of the medium in which the lens is working and 'θ' is the maximum half angle of the cone of light that can enter through or leave the objective lens.

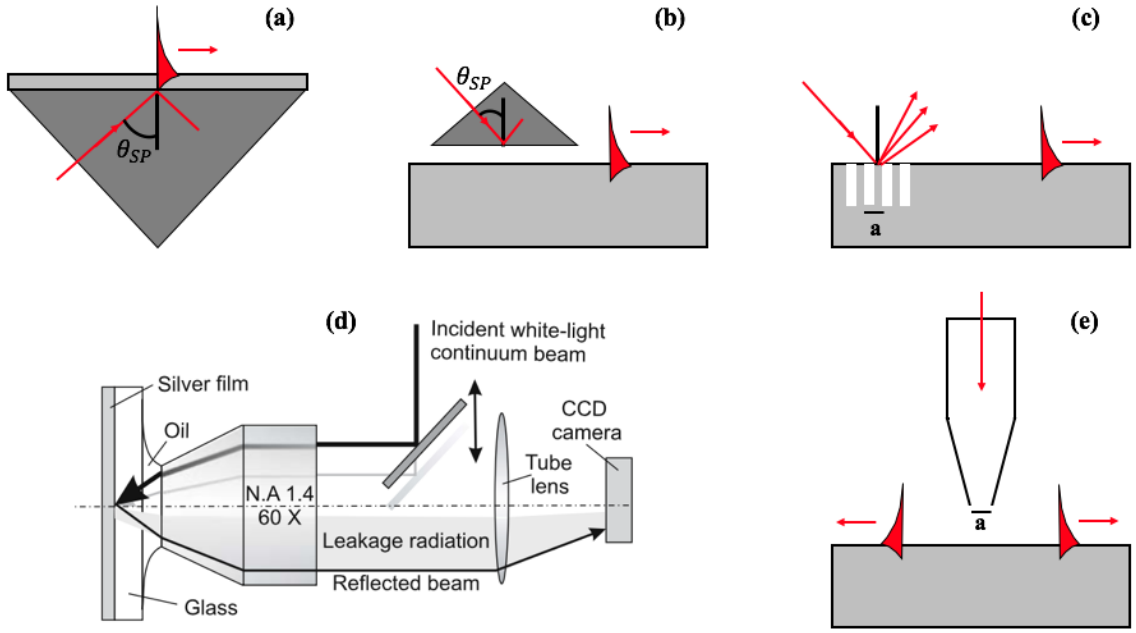


Figure 2.3 SPP excitation by means of (a, b) prism coupling in Kretschmann configuration and Otto configuration respectively, (c) grating coupling, (d) high aperture oil immersion objective lens coupling [Reprinted with permission from reference [20]] and (e) optical fibre based coupling in scanning near field microscope (SNOM).

When the *NA* of the objective lens is high, a large angular spread of the focused excitation beam is obtained. This also includes angles θ greater than θ_c, the critical angle for total internal reflection, thus allowing the phase matched excitation of SPPs at the metal-air interface at an angle $\theta_{SPP} = \sin^{-1}\frac{\beta}{nk_0}$. The excited SPPs leak back into the glass substrate through an index matching liquid where an oil immersion objective is used to collect the signal (See figure 2.3(d)).

The excitation mechanism discussed above excite the SPPs over a macroscopic area defined by size of the incident beam. In contrast, scanning near field optical microscopy (SNOM) technique excite the SPPs locally over an area much less than the wavelength of the incident beam, λ_0. The SNOM is equipped with a small fibre probe tip of aperture $a \leq \lambda_{SPP} \leq$

λ_0 which illuminates the metallic film in the near field (See figure 2.3 (e)). The smaller aperture of the tip ensure that the light from the tip consists of wave vector components $k \geq \beta \geq k_0$ which fulfils the condition for phase-matching to SPPs at the metal/air interface. SPPs propagating from the illumination spot can be collected in form of leakage radiation into the substrate as explained, in the previous case, for thin films.

Thus, various excitation configurations can be used to overcome the phase matching limitation in case of SPPs and thus excite them. This last excitation scheme has been used throughout this thesis. On the other hand, the non-propagating counterparts of SPPs, which are termed as localized surface plasmon (LSP) can be excited by direct coupling with a spatially profiled beam of light with no special condition. We will discuss the LSP in detail in the next section.

2.1.2 Localized Surface Plasmons

Localized surface plasmons (LSP) are another fundamental plasmonic excitation which results from the confinement of electron gas in a nanoparticle of size comparable to or smaller than the wavelength of light used to excite the plasmon. For such small isolated metal nanoparticles with sizes in the range of the penetration depth of an electromagnetic field, an external field can easily penetrate into the volume and drives coherently, the conduction electrons with respect to the ion lattice. This oscillations of the conduction electrons with respect of the positive ion lattice depends on the charge density, effective electron mass and size and shape of the nanoparticles. The simplest design in which LSP modes can exists is a metallic sphere. We will describe here the case of the dipolar plasmon resonance in a metal sphere with a radius 'a' much smaller than the wavelength of the incident field ($a < \lambda$). This gives us the freedom to treat this case in the quasi-static approximation, in which the Helmhotz equation reduces to Laplace equation which is given by [21]–

$$\nabla^2 \varphi = 0 \tag{2.10}$$

where 'φ' is the scalar potential. The above equation gives us the electric field, '*E*' as

$$\boldsymbol{E} = -\nabla\varphi \tag{2.11}$$

The boundary conditions at the interface between the metallic sphere and the surroundings medium can be satisfied when both the tangential component of the electric field and the

normal component of the displacement field vector are continuous. The obtained solution for the electric field has a component of the applied field E_0 and an electric dipole with a dipole moment given by (CGS units) -

$$p = \alpha E_0 \tag{2.12}$$

where α is the polarizability of the metallic nanospheres and is given by

$$\alpha = a^3 \frac{\epsilon_m - \epsilon_s}{\epsilon_m + 2\epsilon_s} \tag{2.13}$$

In equation (2.12), $\epsilon_m$and ϵ_s are the permittivity of the metal and the surrounding medium respectively. The relation (2.2) suggest that a resonant condition can be achieved when denominator of $Re\{(\epsilon_m + 2\epsilon_s)\} = 0$. This requirement, called the Frohlic condition, can be satisfied in the case of noble metals for which the real part of the permittivity is negative at optical frequencies.

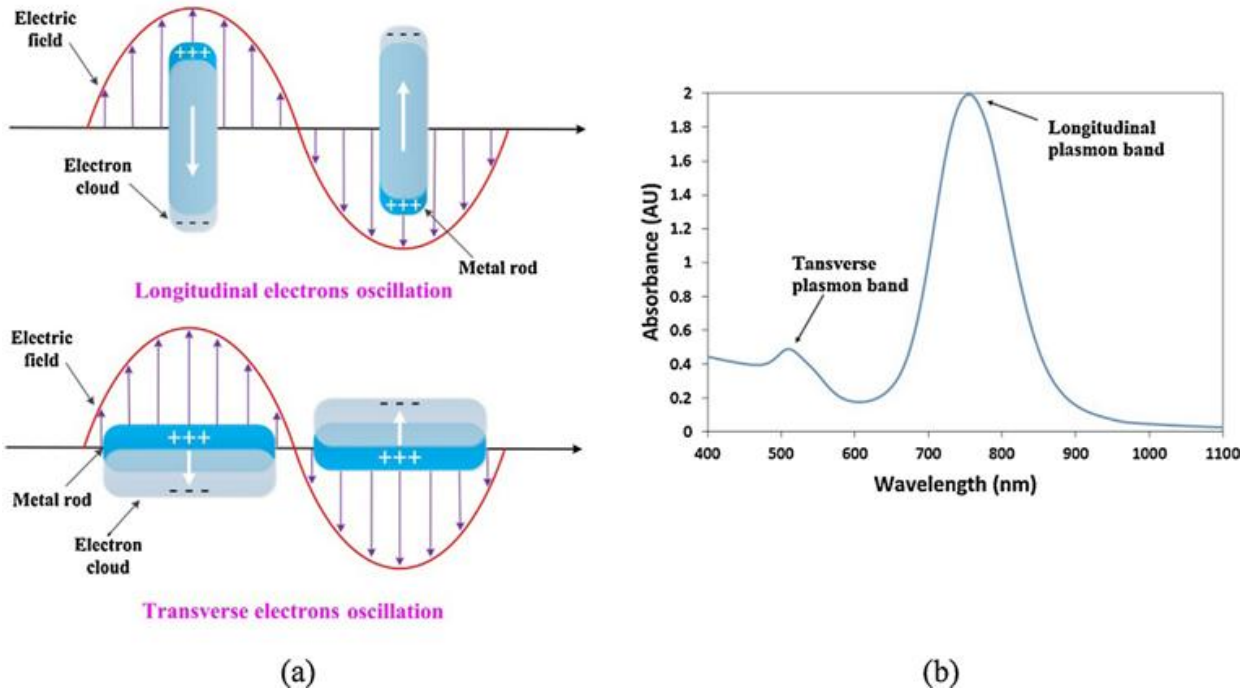


Figure 2.4 An illustration of LSPR excitation for a nanorod. The discrepant oscillation of electrons at longitudinal and transverse plasmon bands results in different plasmonic spectra [Reprinted with permission from reference [22]]

The equation (2.12) defines the parameters which can be used to tune the LSP resonance such as size of the metallic sphere (a), dielectric permittivity of the metal and the surrounding

medium. However, for a slightly asymmetric nanostructure like a nanorod, two polarization states of the electromagnetic waves with respect to the two orthogonal axes of the nanoparticle are possible. Figure 2.4 (a) shows the LSP excitation mechanism for a metallic nanorod geometry. In the absorption spectra shown in figure 2.4 (b), there are two peaks present, one corresponds to the higher energy transverse plasmon mode and the other to the lower energy longitudinal plasmon mode.

For larger and more complex nanoparticles, the quasi-static limit is not valid any more. For example, in larger micrometre sized structures, higher order modes (quadrupole, octopole, etc.) are also present. The energy dissipation associated with the movement of electrons in the metal is described by the imaginary part of the dielectric function of the metal. In case of gold, in the visible to near-UV regions, the interband transitions also contribute to the imaginary part of the dielectric function which results in smaller line width and thus sharper peaks. As the size of the nanoparticle increase, the energy loss due to coupling of LSP oscillation with the radiation field becomes significant [23]. This effect is known as radiation damping. As a result for a particular mode, with the increase in the size of the nanoparticles, the line width increases.

2.1.3 Micrometre sized metallic structures

The macroscopic metallic structures support propagation [24], [25] and waveguiding and [26] of the SPP signal, while nanometer scale metallic structures supports LSP resonances whic produce evanescent field, strong confinement [27]. In this thesis, we have used metallic nanostructures which falls in the size range between nanometer scale systems and macroscopic scale system and thus are called micrometer sized metallic structures. The micrometer-sized system combines the characteristics of both SPP and LSP and thus has proven to be a useful candidate for designing plasmonic based optical devices. The micrometric plasmonic structures sustain higher order plasmon modes that have been used in this study to implement different functionalities such as (a) plasmonic transmittance between two selected locations in the system and routing of the plasmonic signal from one location to another, and (b) Boolean logic gate devices. These systems contain higher order plasmonic modes in the visible and near infra red and a new approach is required to describe the modal behaviour of these systems because modes are no more discrete and well separated as in the case of smaller nanoparticles. This can be better understood with the help of figure 2.5 where electron energy loss spectroscopy (EELS) intensity maps recorded over metallic rods of sizes (a) 630nm, (b) 1250nm and (c)

3230nm respectively has been displayed. The corresponding SEM images are shown above the EELS maps with scale bars of 200nm each.

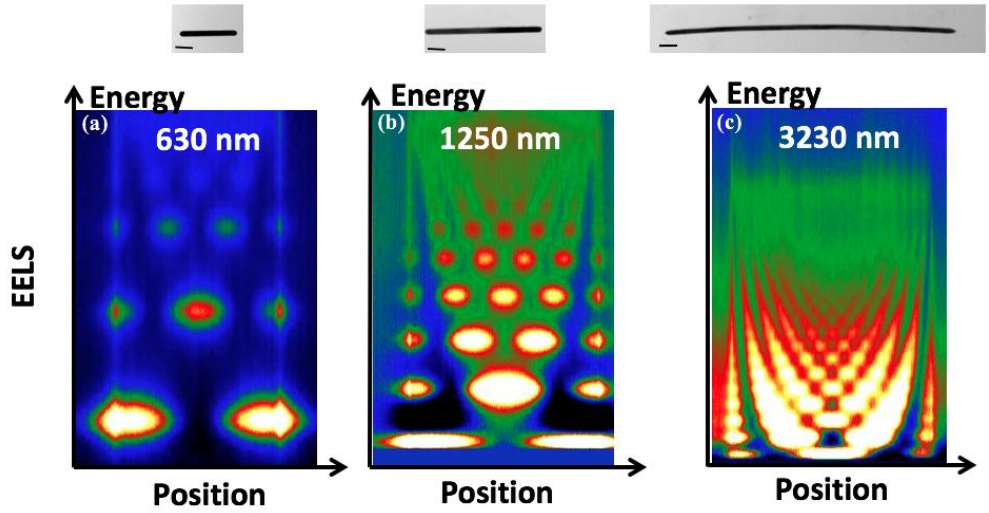


Figure 2.5 EELS intensity map measured over metallic nanorods of three different sizes (a) 630nm, (b) 1250nm and (c) 3230nm respectively. The SEM images of the metallic rods are shown above the EELS maps. The scale bars in white are 200nm. [This unpublished work was done previously in collaboration between E. Dujardin and M. Bosman in IMRE Singapore].

In figure 2.5 (a), when the size of the metallic rod is small, the modes are energetically well separated. In this case, the modal behaviour of the metallic rod can be reasonably accounted for by considering dipolar mode and neglecting the two next modes. For the rod of larger dimension in figure 2.5 (b), the modes start appearing closer to each other and for rod of even larger size figure 2.5(c), the modes appear so close to each other that the individual modes are difficult to single out and any optical response will result from contribution of many modes. The modal behaviour of such a system can be better understood in terms of plasmon local density of states (SPLDOS) which provides the modal information inside a given ensemble of nanostructures irrespective of the illumination mode and by taking into account all contributing modes. We discuss in detail about the plasmonic local density of states in the next section.

2.2 Local density of states

Density of states (DOS) is a scalar function, when multiplied with the energy in a given interval gives us the total number of available states in that energy range. For a non-homogenous system, the spatial variation can be taken into account by considering local properties and thus we calculate the local density of states (LDOS) instead. The notion of LDOS thus become very important in case of nanometre scale systems. It is well established

fact that the LDOS of both electrons [28] and photons [29] is modified by the presence of a surface. M. F. Crommie in 1993 used a scanning tunnelling microscope (STM) to show that the electronic LDOS inside an iron corral built on a copper (111) surface gives eigenmodes expected for an electron trapped in a 2D round object [30]. This experiment was followed by theoretical explanations [31], [32] including one based on Green function formalism by Crampin and Bryant [31] in which a fully 3D scattering calculation of the electronic standing wave around the iron corral was explained by the authors. The optical analogy of these electronic quantum corrals was proposed by G. Colas des Francs and C. Girard [33]. The authors performed full scattering calculations of the change in electromagnetic LDOS in the near field when moving from a disordered arbitrary geometry to a perfect circular corral. The change of optical LDOS was found to increase significantly above each pad of the corral. The experimental realization was performed on gold nanoparticle arranged in a corral shape on a dielectric surface [34]–[36]. A scanning near-field optical microscope (SNOM) was used to image the projected LDOS which revealed the electric field confinement around the gold corrals for two orthogonal polarizations of the source dipole. This LDOS corresponding to the optical system is termed as photonic LDOS.

In this chapter, we first recall the definition of photonic LDOS. This is followed by the extension of the concept of photonic LDOS to the plasmonic states inside the metallic nanostructure called surface plasmon local density of states (SPLDOS). We then demonstrate how the intensity of the non linear photoluminescence (NPL) signal depends on the plasmonic modes supported by the metallic nanostructures.

2.2.1 Photonics LDOS

The probability of finding the intensity of the electric field associated with photons of energy $'\hbar\omega'$ in an infinitesimal small volume '$d\mathbf{r}$' at a given point '$\mathbf{r}$' is $\rho(\boldsymbol{r},\omega)$. The term $\rho(\boldsymbol{r},\omega)$ is the photonic LDOS and is the given by -

$$\rho(\boldsymbol{r},\omega) = \sum_n |\boldsymbol{E_n}(\boldsymbol{r},\omega_n)|^2 \delta(\omega - \omega_n) \tag{2.14}$$

where $|\boldsymbol{E_n}(\boldsymbol{r},\omega_n)|$ is the amplitude of the normalized electromagnetic field associated with the nth electromagnetic mode and is given by –

$$\int |\boldsymbol{E_n}(\boldsymbol{r},\omega_n)|^2 \delta\boldsymbol{r} = 1 \tag{2.15}$$

Photonic LDOS can be computed by GDM based formulism based on calculation of the electric field susceptibility $\boldsymbol{S}(\boldsymbol{r},\boldsymbol{r}',\omega)$. All these electromagnetic modes obey the Helmholtz equation derived from Maxwell's equation [36] –

$$-\nabla \times \nabla \times \boldsymbol{E_n}(\boldsymbol{r}, \omega_n) + k_n^2 \boldsymbol{E_n}(\boldsymbol{r}, \omega_n) = 0 \tag{2.16}$$

and a closure formula –

$$\sum_n \boldsymbol{E_n}(\boldsymbol{r}, \omega_n)\boldsymbol{E_n^*}(\boldsymbol{r}, \omega_n) = \boldsymbol{I}\delta(\boldsymbol{r} - \boldsymbol{r'}) \tag{2.17}$$

where $\boldsymbol{I}$ is the unit dyadic and $\delta(\boldsymbol{r} - \boldsymbol{r'})$ is the Dirac delta function which can be represented by

$$\delta(x) = -\frac{1}{\pi}\lim_{y\to 0} Im(\frac{1}{x+iy}) \tag{2.18}$$

Using equation (2.18), we can rewrite equation (2.3) as

$$\rho(\boldsymbol{r}, \omega) = -\frac{1}{\pi}\lim_{y\to 0} Im(\frac{|\boldsymbol{E_n}(\boldsymbol{r},\omega_n)|^2}{k_0^2 - k_n^2 + iy}) \tag{2.19}$$

Next, we define the electric field susceptibility of the system, $\boldsymbol{S}(\boldsymbol{r}, \boldsymbol{r'}, \omega)$ similar to equation (2.16)

$$-\nabla \times \nabla \times \boldsymbol{S}(\boldsymbol{r}, \boldsymbol{r'}, \omega) + k_0^2 \boldsymbol{S}(\boldsymbol{r}, \boldsymbol{r'}, \omega) = -4\pi k_0^2 \boldsymbol{I}\delta(\boldsymbol{r} - \boldsymbol{r'}) \tag{2.20}$$

The closure formula (2.17) can be used here to deduce the spectral representation of the propagator of the system as a function of the $|\boldsymbol{E_n}(\boldsymbol{r}, \omega_n)|$ -

$$\boldsymbol{S}(\boldsymbol{r}, \boldsymbol{r'}, \omega) = -4\pi k_n^2 \sum_n \frac{\boldsymbol{E_n}(\boldsymbol{r},\omega_n)\boldsymbol{E_n^*}(\boldsymbol{r},\omega_n)}{k_0^2 - k_n^2} \tag{2.21}$$

From equations (2.19) and (2.21), we arrive at following equation –

$$\rho(\boldsymbol{r}, \omega) = \frac{1}{4\pi k_0^2} Im[Tr\{\boldsymbol{S}(\boldsymbol{r}, \boldsymbol{r'}, \omega)\}] \tag{2.22a}$$

The equation (2.22a) gives the relationship between photonic LDOS and the propagator associated with a metal structure, which is a dyadic tensor containing the whole electromagnetic response of the object. This equation can also be expressed in terms frequency unit, ω as –

$$\rho(\boldsymbol{r}, \omega) = \frac{1}{2\pi\omega^2} Im[Tr\{\boldsymbol{S}(\boldsymbol{r}, \boldsymbol{r'}, \omega)\}] \tag{2.22b}$$

Using this equation (2.22), we can calculate the photonic LDOS as a function of frequency at a given point of space around the metal structure. This equation also concludes that the photonic LDOS gives us the spectral distribution of different electromagnetic modes irrespective of the characteristics of the illumination field. Figure 2.6(a) presents an example where this technique has been used by C. Girard et. al. [36] to calculate the photonics LDOS maps in a plane parallel to the surface of nanometer sized gold arranged in form of a hexagonal corral at a constant distance of z = 120nm above the structure. The signal modulation inside the hexagonal corral reveals the confined electromagnetic states sustained by the corral. A nice symmetrical image of the hexagonal corral was obtained by using a circularly polarized light. This numerical simulation quantitatively reproduced the experimental map measured by SNOM in the near vicinity of the system (displayed in figure 2.6 (b)).

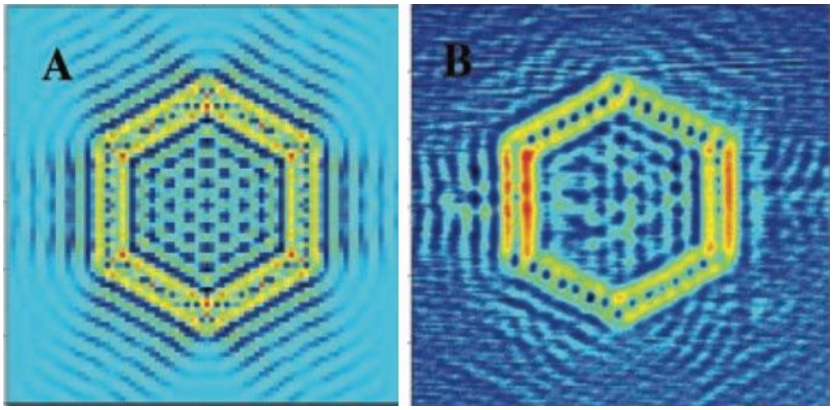


Figure 2.6 SNOM images computed (A) and measured (B) in the vicinity of nanometer- sized gold arranged like a hexagonal corral (image size: 6 μm × 6 μm). The imaging wavelength is λ_0 =543nm. [Reference [36]]

2.2.2 Surface plasmon local density of states (SPLDOS)

To understand the concept of surface plasmon local density of states, let us consider an example of triangular gold nanoprism. Figure 2.7 (a), (b) and (c) shows the photonic LDOS maps calculated at a plane parallel to the gold nanoprism at Z =100nm, 50nm and 25nm respectively above the prism. For the first map, when Z =100nm, the photonic LDOS consists of non-evanescent complex intensity pattern mostly outside the gold nanoprism. When we decrease the height of the observation plane to Z=50nm, the photonic LDOS pattern starts shrinking. At Z=25nm, it further shrinks and the photonic LDOS which was previously mostly present outside the metallic nanoprism now appears mostly along the outer perimeter and some contrast emerges directly above the nanoprism This implies that as we move closer and closer to the nanostructure there is a significant increase in evanescent states near to the edges of the nanoprism. In figure 2.7 (d), when we go to Z=0nm, the LDOS present in the system is now related to the plasmonic modes inside the metallic nanostructure. At this stage, we would like to introduce an equivalent but distinct concept called surface plasmon local density of states or SPLDOS which are the local density of the states occupied by collective electron oscillations inside a metallic nanostructure. These states govern various properties of metallic nanoparticles like local heat generation, energy loss of a passing by electron, etc. Figure 2.7 (c) in which LDOS has been calculated in near vicinity of the nanoprism appears related to the LDOS map in figure 2.7 (d) but the two maps describe completely different quantities which are photonic LDOS and SPLDOS respectively. Indeed in figure 2.7d, SPLDOS is strictly null out of the structure. SPLDOS can be probed by experimental techniques such as electron energy loss spectroscopy (EELS) and cathodoluminescence [37],. In this work, we have used another very widely used experimental technique called nonlinear photon luminescence microscopy (NPL)

to probe SPLDOS inside a metallic nanostructure. NPL is preferred over PL because, as a consequence of nonlinear excitation in NPL, the emission intensity is proportional to nth power of the excitation intensity where n is the number of photons used in multi-photon excitation. This higher luminescence intensity compared to PL, results in better image contrast . In the next section we will establish the relationship between the plasmonic modes supported by the gold nanostructures and nonlinear photon luminescence (NPL).

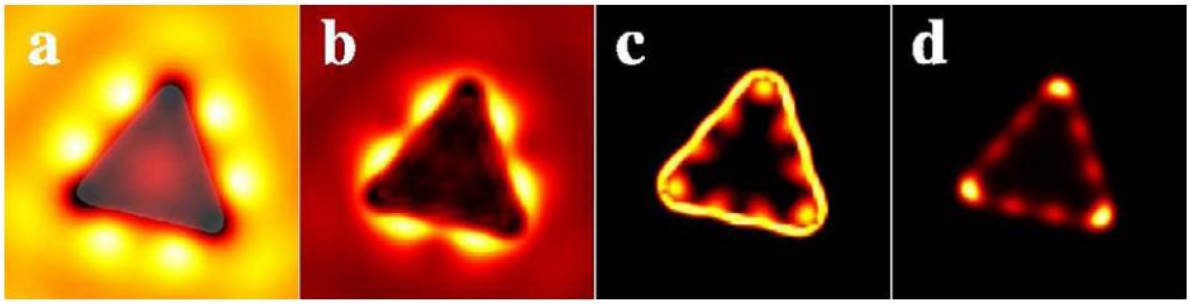


Figure 2.7 (a), (b) and (c) photonic LDOS maps calculated in three planes (Z=constant) located at Z=100 nm, Z=50 nm, and Z=25 nm above a triangular gold nanoprism. (d) SP–LDOS of the same structure given for comparison. [Reference [38]]

2.2.3 NPL and SPLDOS

To derive a relation between NPL and SPLDOS, we start with considering the standard relation for quantity of energy radiated in a linear process, by an elementary cell of volume '$\delta\boldsymbol{r}$' positioned at '$\boldsymbol{r}$' in the nanostructure supported by a transparent substrate and subjected to an illumination field, $\boldsymbol{E_o}(\boldsymbol{r_0}, \boldsymbol{r}, \omega)$ position in '$\boldsymbol{r_0}$' –

$$I(\boldsymbol{r}) = A\chi^2(\omega_0)\,|\boldsymbol{E}\,(\boldsymbol{r_0}, \boldsymbol{r}, \omega_0)|^2\delta\boldsymbol{r}^2 \tag{2.23}$$

where 'A' is a real constant and $\boldsymbol{E}\,(\boldsymbol{r_0}, \boldsymbol{r}, \omega_0)$ is the local field induced by the illumination field $\boldsymbol{E}\,(\boldsymbol{r_0}, \boldsymbol{r}, \omega_0)$ and $\chi\,(\omega_0)$ is the linear susceptibility of the nanostructure in vacuum. The dipole induced in the nanostructure by the illumination field is given by –

$$\boldsymbol{P_0}(\boldsymbol{r}, t) = \chi\,(\omega_0)\,\boldsymbol{E_0}\,(\boldsymbol{r_0}, \boldsymbol{r}, \omega_0)\delta\boldsymbol{r} \tag{2.24}$$

By applying Gauss' theorem to the oscillating dipole, we can rewrite the equation for radiated energy as [33] -

$$I(\boldsymbol{r}) = -\langle \int_V d\boldsymbol{r}\,\boldsymbol{J}(\boldsymbol{r}, t)\,\boldsymbol{E}(\boldsymbol{r}, t)\rangle \tag{2.25}$$

where $\langle\,\rangle$ defines the time average over a period of oscillation, $\boldsymbol{E}(\boldsymbol{r}, t)$ denotes the local electric field and $\boldsymbol{J}(\boldsymbol{r}, t)$ describe the current density due to the oscillating dipole. Performing Fourier transform on induced current density and local electric field, equation (2.25) can be rewritten as –

$$I(\boldsymbol{r}) = -\langle \int_V d\boldsymbol{r} \int_{-\infty}^{\infty} d\omega \int_{\infty}^{\infty} d\omega' \ \boldsymbol{J}(\boldsymbol{r},\omega).\boldsymbol{E}(\boldsymbol{r},\omega') \exp[-i(\omega+\omega')t]\rangle \quad (2.26)$$

Now, since the dipole $\boldsymbol{P_0}(\boldsymbol{r},t)$ is induced by the monochromatic illumination field and circularly polarized in XOY plane, it can be written as –

$$\boldsymbol{P_0}(\boldsymbol{r},t) = (\boldsymbol{P_0}\, cos(\omega_0 t), \boldsymbol{P_0}\, sin(\omega_0 t), 0) \quad (2.27)$$

and the current density associated with the oscillating dipole can written as –

$$\boldsymbol{J}(\boldsymbol{r},\omega) = -i\omega \boldsymbol{P_0}(\boldsymbol{r},\omega)\delta(\boldsymbol{r}'-\boldsymbol{r}) \quad (2.28)$$

where $\boldsymbol{P_0}(\boldsymbol{r},\omega)$ is the Fourier transform of $\boldsymbol{P_0}(\boldsymbol{r},t)$. Now introducing the propagator $\boldsymbol{S}(\boldsymbol{r},\boldsymbol{r_0},\omega)$ corresponding to the system which connects the local field to the dipole, we have –

$$\boldsymbol{E}(\boldsymbol{r},\omega) = \boldsymbol{S}(\boldsymbol{r},\boldsymbol{r_0},\omega).\boldsymbol{P_0}(\boldsymbol{r},\omega) \quad (2.29)$$

Then from equation (2.22), (2.24) and (2.25) we have

$$I(\boldsymbol{r}) = -\langle \int_{-\infty}^{\infty} d\omega \int_{-\infty}^{\infty} d\omega' \omega \times \boldsymbol{P_{0\alpha}}(\boldsymbol{r},\omega)\, \boldsymbol{P_{0\beta}}(\boldsymbol{r},\omega')\, \boldsymbol{S_{\alpha\beta}}(\boldsymbol{r},\boldsymbol{r},\omega) \exp[-i(\omega+\omega')t]\rangle \quad (2.30)$$

where $(\alpha,\beta) =$ x or y and

$$P_{0x}(\omega) = \frac{P_0}{2}[\delta(\omega-\omega_0) \pm \delta(\omega+\omega_0)]$$

and $$P_{0y}(\omega) = \frac{P_0}{2i}[\delta(\omega-\omega_0) \pm \delta(\omega+\omega_0)] \quad (2.31)$$

After time averaging equation (2.26), we finally obtain –

$$I(\boldsymbol{r}) = \frac{\omega_0 {P_0}^2}{2} Im\{S_{x,x}(\boldsymbol{r},\boldsymbol{r},\omega_0) + S_{y,y}(\boldsymbol{r},\boldsymbol{r},\omega_0)\} \quad (2.32)$$

Now since the SP-LDOS is given by –

$$\rho_{||}(\boldsymbol{r},\omega_0) = \frac{1}{2\pi^2\omega_0} Im\{S_{x,x}(\boldsymbol{r},\boldsymbol{r},\omega_0) + S_{y,y}(\boldsymbol{r},\boldsymbol{r},\omega_0)\} \quad (2.33)$$

we can rewrite equation (2.32) as –

$$I(\boldsymbol{r}) = {P_0}^2 \pi^2 {\omega_0}^2 \rho_{||}(\boldsymbol{r},\omega_0) \quad (2.34)$$

Now correlating equation (2.23) for energy radiated at position '$\mathbf{r}$' to equation (2.24) and (2.34), we arrive at the equation –

$$|\boldsymbol{E}(\boldsymbol{r_0},\boldsymbol{r},\omega)|^2 = |\boldsymbol{E_0}(\boldsymbol{r_0},\boldsymbol{r},\omega)|^2 \pi^2 {\omega_0}^2 A^{-1} \rho_{||}(\boldsymbol{r},\omega_0) \quad (2.35)$$

Equation (2.35) tells us that the local field distribution at a given position '$\boldsymbol{r}$' is directly proportional to the SPLDOS present at '$\boldsymbol{r}$'. Now the non linear photon luminescence intensity coming out of the metallic nanostructure depends upon the non-linear co-efficient, $\eta(\omega_0)$ associated to the metal. In our case, the non-linearity is mostly close to second order [39]. So we will from now onwards in this work, term the non-linear photoluminescence as two photon luminescence (TPL). The TPL intensity coming out of an elementary cell of volume 'v' is thus given by –

$$I_{TPL}(\boldsymbol{r_0}, \boldsymbol{r}, \omega) = [\,\eta(\omega_0).|\boldsymbol{E}(\boldsymbol{r_0}, \boldsymbol{r}, \omega)|^2]^2 \nu \quad (2.36)$$

Replacing value of $|\boldsymbol{E}(\boldsymbol{r_0}, \boldsymbol{r}, \omega)|^2$ from equation (2.35) in to equation (2.36), we get –

$$I_{TPL}(\boldsymbol{r_0}, \boldsymbol{r}, \omega) = \eta^2(\omega_0)\pi^4{\omega_0}^4 A^{-2} \int_V |\boldsymbol{E_0}(\boldsymbol{r_0}, \boldsymbol{r}, \omega)|^4 \, {\rho^2}_{||}(\boldsymbol{r}, \omega_0) d\boldsymbol{r} \quad (2.37)$$

Equation (2.36) shows us the relationship between TPL signal generated at a point 'r' and the existing SPLDOS at the same point '$\boldsymbol{r}$'. It tells us that TPL intensity results from the convolution of squared SPLDOS with the Gaussian beam profile at a given point '$\boldsymbol{r}$'. When the beam waist tends to zero, the TPL maps converge towards the squared-SPLDOS maps. Figure 2.8 shown below has four TPL maps calculated with decreasing beam waist diameter (a) 300nm, (b) 200nm, (c) 100nm and (d) 50 nm respectively. The TPL maps clearly shows that the TPL features depends on the beam waist diameter and as we decrease the beam waist diameter it converges towards SPLDOS map (of figure 2.7fd).

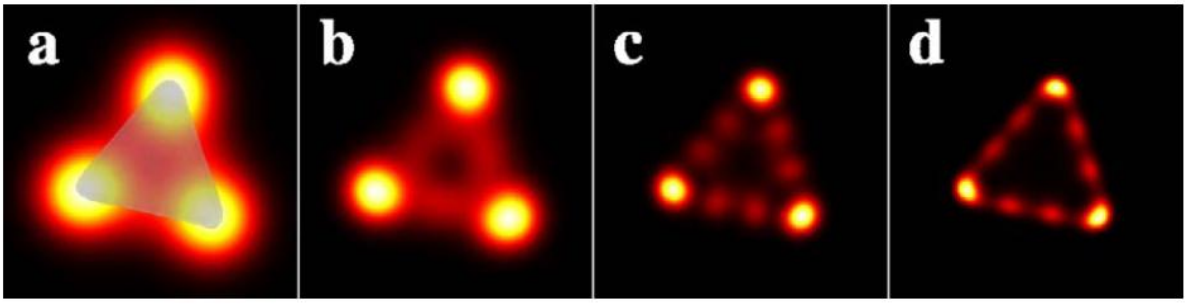


Figure 2.8 TPL maps computed on a gold triangular nanoprism illuminated with a circularly polarized light of beam waist diameter of 300 nm, 200 nm, 100 nm, and 50 nm for (a), (b), (c), (d)) respectively. A SEM image of the object is superimposed to the computed map in (a). [38]

2.3 Single crystalline colloidal system

The exploration of optical characteristics of metallic structures has led to the development of different nanofabrication tools and techniques. All these nanofabrication techniques can be categorized into two parts – top down fabrication approach and bottom up fabrication approach. In this section we briefly discuss the two different nanofabrication approaches, their advantages and shortcomings. We then discuss why the single crystalline colloidal systems are a suitable candidate for the use in plasmonic based devices.

2.3.1 Top down and bottom up approaches

Top-down fabrication is a subtractive process in which material is removed to synthesize nanostructures of desired shapes and sizes. The most common example of the top

down fabrication approach is lithography. Lithography consists of a series of fabrication which help in transferring an image from a mask to a substrate. A typical lithographic process has following three steps: (i) coating a substrate with a sensitive precursor material called resist, (ii) exposing the resist to light, electrons or ion beams, (iii) and finally developing the resist image with a suitable chemical, which reveals an image on the substrate. For example, in the case of an electron beam lithography system, nanometer sized focused beam of electrons is used to form a latent image in a layer of resist. This exposure is performed in order to render the resist either more soluble (called a positive tone resist) or less soluble (negative tone resist) in an appropriate developer solution. A desired material is then deposited by physical approach like sputtering or electron beam physical vapour deposition. The left out resist is then etched out of the substrate. Another top down approach, that is widely used for fabrication of nanostructures is focussed ion beam(FIB) milling. In this technique, a focussed ion beam is used to directly mill out a particular structure out of a metallic film. Figure 2.9 (a) shows a silver nanoprism milled out of a silver film by FIB at CEMES. The advantage of the top down approach is the amazing control on the positioning, size and geometry of the fabricated nanostructure. However, the nanostructures fabricated by top down approaches are amorphous in nature, contains granular boundaries and are potentially contaminated by the sputtering atoms or adsorbed resist. These boundaries can be easily seen in the figure 2.9(a). Due to the granular boundaries present on the surface, propagating SPPs scatters in the surface or radiates out of the surface in form of light [17], [40]. This is in addition to the ohmic losses encountered by the conduction electron. Thus scattering through these granular boundaries results in significant SP damping and reduced propagation lengths which leads to limited performance of the plasmonic devices based on the above mentioned fabrication techniques.

The bottom up fabrication on the other hand is an additive process in which atoms are controlled to synthesize different nanostructures like nanowires, nanorods, nanoprisms, etc. Bottom up methods can be divided into gas-phase and liquid-phase methods. In both cases, the nanomaterial is fabricated through a controlled fabrication route that starts from the single atom or molecules. Gas-phase methods include plasma arcing [42] and chemical vapour deposition while sol-gel synthesis [43], [44], colloidal chemistry [45] and molecular self-assembly [46] are the example of the liquid phase methods. The nanostructures synthesized from bottom up approaches are highly crystalline in nature. Crystalline surface suffers comparatively less scattering related losses and the losses in the nanostructures are limited by the ohmic losses. Figure 2.9(b) shows the SEM images of nanostructures fabricated by colloidal chemistry. We can clearly observe the difference in the crystallinity of the nanostructures fabricated by the

two different approaches discussed above. The reduced losses in these highly crystalline nanostructures make them suitable candidates for designing plasmonic based devices.

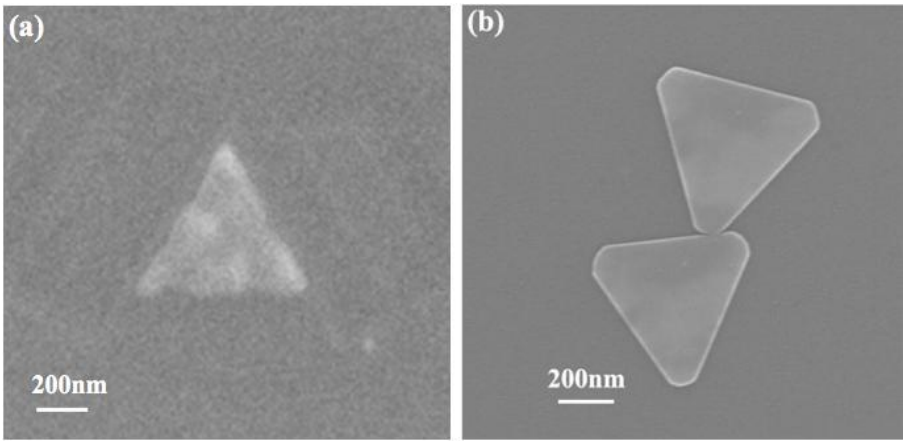


Figure 2.9 (a)SEM image of silver nanoprism obtained by focussed ion beam milling [41] of 30nm thin Ag film deposited by electron beam physical vapour deposition technique, (b) SEM image of gold nanoprism fabricated by colloidal chemistry

In this work, we have taken advantages of control of geometry from top down approach and high crystallinity from bottom up approach and when necessary, combined the two fabrication approaches to design our nanostructures. In chapter VI and VII, the desired plasmonic devices have been milled out of the highly crystalline gold micro-platelets of size of several of microns by focussed ion beam. This mixed approach has been developed as a tool to design highly efficient plasmonic devices for information transfer and processing related applications.

2.3.2 Crystalline colloidal systems for reconfigurable plasmonic devices

In recent years, there has been abundant scientific literature on interesting plasmonic based devices and information processing prototypes [47]–[50]. The performance of these devices and prototypes however are limited by the scattering losses by the lattice defects and granular boundaries of the system [51]. The increase in imaginary component of the dielectric permittivity of the system results in the damping of SPP signal which further reduce the SPP propagation length and enhancement of the electric field intensity [52], [53]. These limitations in the presently available plasmonic based devices can be overcome by using bottom up strategies. The effort to control shape and size of the nanostructures have led to development of many different chemical synthesis routes for nanorods [54], [55], triangular prisms [56]–[58], nanocubes [59], [60] and many more. These synthesis protocols have gone through continuous improvement over past few decades by gaining a better control over various

reaction parameters, homogeneity and the production yield. High crystallinity of the nanostructure produced by the chemical synthesis has led to it use for designing of nanoscale optical interconnects. For example, in a recently reported work by group of M. Kall and N. Hallas, a complete set of basic logic gate operations have been realized using highly crystalline silver nanowires interconnects [61]. The polarization and phase dependent interference between plasmon beams propagating through the wire interconnects were used to realized the logic gate operations. The authors further have proposed more complex logic gates operations and photonic circuits designed by cascading the basic gates. However, the challenge with such kind of interferential devices is the control over positioning of each building block. In addition, cascading of building blocks for realising complex logic gate operations is very difficult because of dissipation in the metallic nanostructures.

These limitations can be overcome by designing plasmonic based devices which can support all complex logic gates operations on single structure. To realize such plasmonic based device, Viarbitskaya et. al. [62] in their work, proposed the use of large 2D Au crystalline nanoprisms which sustain delocalized plasmon modes extending up to micrometre range. The authors have emphasized on the use of SPLDOS as a tool in plasmonic information technology which can be effectively engineered by the control of shape, size and geometry of the gold cavities. This proposal serves as the basis of the designing of the plasmonic based devices in this thesis.

In this work we have used two different gold nanostructures for our studies. The first one is the triangular and hexagonal nanoprisms of size ranging from 300nm to 2μm and with a thickness of 20±2 nm. Spatial properties of these gold cavities and different techniques to tailor and control these properties have been extensively probed by Viarbitskaya et. al. [62], [63] and Cuche et. al. [64]. In this work, these gold cavities will be further probed for understanding of their spectral characteristics in chapter IV. This will be followed by the probing of these gold cavities in a bowtie antenna configuration in chapter V.

Another type of gold nanostructures used in this work has been produced by one pot method (discussed next chapter). These gold nanoparticles are comparatively larger than the previous gold cavities with size ranging from 1 to 20 microns and thickness of 30±2 nm. These cavities have been used for designing plasmonic cavities of particular shape, size and geometry by focussed ion beam(FIB) milling. These specifically designed resonators with multiple inputs and outputs have been used in this work to realize plasmonic based information processing (chapter VI) and reconfigurable logic gate devices (chapter VII).

References:

[1] M. Asghari and A. V. Krishnamoorthy, "Silicon photonics: Energy-efficient communication," *Nat. Photonics*, vol. 5, no. 5, pp. 268–270, 2011.

[2] J. Leuthold, C. Koos, and W. Freude, "Nonlinear silicon photonics," *Nat. Photonics*, vol. 4, pp. 534–544, 2010.

[3] A. Politi, M. J. Cryan, J. G. Rarity, S. Yu, and J. L. O'Brien, "Silica-on-silicon waveguide quantum circuits.," *Science*, vol. 320, no. 5876, pp. 646–9, 2008.

[4] M. Kohnen, M. Succo, P. G. Petrov, R. A. Nyman, M. Trupke, and E. A. Hinds, "An array of integrated atom–photon junctions," *Nat. Photonics*, vol. 5, no. 1, pp. 35–38, 2011.

[5] G. Lepert, M. Trupke, M. J. Hartmann, M. B. Plenio, and E. A. Hinds, "Arrays of waveguide-coupled optical cavities that interact strongly with atoms," *New J. Phys.*, vol. 13, no. 113002, pp. 1–22, 2011.

[6] C. Girard, A. Dereux, O. J. F. Martin, and M. Devel, "Importance of confined fields in near-field optical imaging of subwavelength objects," *Phys. Rev. B*, vol. 50, no. 19, pp. 14467–14473, 1994.

[7] W. L. Barnes, A. Dereux, and T. W. Ebbesen, "Surface plasmon subwavelength optics," *Nature*, vol. 424, no. 6950, pp. 824–30, 2003.

[8] D. K. Gramotnev and S. I. Bozhevolnyi, "Plasmonics beyond the diffraction limit," *Nat. Photonics*, vol. 4, no. 2, pp. 83–91, 2010.

[9] R. W. Wood, "On a Remarkable Case of Uneven Distribution of Light in a Diffraction Grating Spectrum," *Proc. Phys. Soc. London*, vol. 18, no. 1, pp. 269–275, 1902.

[10] L. Rayleigh, "On the Dynamical Theory of Gratings," *R. Soc. London*, vol. 79, no. 532, pp. 399–416, 1907.

[11] U. Fano, "The Theory of Anomalous Diffraction Gratings and of Quasi-Stationary Waves on Metallic Surfaces (Sommerfeld's Waves)," *J. Opt. Soc. Am.*, vol. 31, no. 3, p. 213, 1941.

[12] R. H. Ritchie, "Plasma Losses by Fast Electrons in Thin Films," *Phys. Rev.*, vol. 106, no. 5, pp. 874–881, 1957.

[13] E. Kretschmann and H. Raether, "Radiative Decay of Non Radiative Surface Plasmons Excited by Light," *Zeitschrift fur Naturforschung - Section A Journal of Physical Sciences*, vol. 23, no. 12. pp. 2135–2136, 1968.

[14] A. Otto, "Excitation of nonradiative surface plasma waves in silver by the method of frustrated total reflection," *Zeitschrift f??r Phys.*, vol. 216, no. 4, pp. 398–410, 1968.

[15] S. a Maier, *Plasmonics : Fundamentals and Applications*, vol. 677, no. 1. 2004.

[16] A. Kocabas, A. Dåna, and A. Aydinli, "Excitation of a surface plasmon with an elastomeric grating," *Appl. Phys. Lett.*, vol. 89, no. 4, pp. 1–4, 2006.

[17] H. Raether, "Surface Plasmons on Smooth and Rough Surfaces and on Gratings," *Springer Tracts in Modern Physics*, vol. 111. p. 136, 1988.

[18] S. Park, G. Lee, S. H. Song, C. H. Oh, and P. S. Kim, "Resonant coupling of surface plasmons to radiation modes by use of dielectric gratings," *Opt. Lett.*, vol. 28, no. 20, p. 1870, 2003.

[19] B. Hecht, H. Bielefeldt, L. Novotny, Y. Inouye, and D. Pohl, "Local Excitation, Scattering, and Interference of Surface Plasmons," *Phys. Rev. Lett.*, vol. 77, no. 9, pp. 1889–1892, 1996.

[20] a Bouhelier and G. P. Wiederrecht, "Surface plasmon rainbow jets.," *Opt. Lett.*, vol. 30, no. 8, pp. 884–

886, 2005.

[21] K. Milton and Ernest M. Loebl, *The Scattering of Light and Other Electromagnetic Radiation*, 1969th ed. Academic Press, 1969.

[22] J. Cao, T. Sun, and K. T. V Grattan, "Gold nanorod-based localized surface plasmon resonance biosensors: A review," *Sensors Actuators, B Chem.*, vol. 195, pp. 332–351, 2014.

[23] A. Wokaun, J. P. Gordon, and P. F. Liao, "Radiation damping in surface-enhanced Raman scattering," *Phys. Rev. Lett.*, vol. 48, no. 14, pp. 957–960, 1982.

[24] R. M. Dickson and L. A. Lyon, "Unidirectional plasmon propagation in metallic nanowires," *J. Phys. Chem. B*, vol. 104, no. 26, pp. 6095–6098, 2000.

[25] B. Lamprecht *et al.*, "Surface plasmon propagation in microscale metal stripes," *Appl. Phys. Lett.*, vol. 79, no. 1, pp. 51–53, 2001.

[26] S. Kumar, N. I. Kristiansen, A. Huck, and U. L. Andersen, "Generation and controlled routing of single plasmons on a chip," *Nano Lett.*, vol. 14, no. 2, pp. 663–669, 2014.

[27] P. Fan *et al.*, "An electrically-driven GaAs nanowire surface plasmon source," *Nano Lett.*, vol. 12, no. 9, pp. 4943–4947, 2012.

[28] J. Tersoff and D. R. Hamann, "Theory of the scanning tunneling microscope," *Phys. Rev. B*, vol. 31, no. 2, pp. 805–813, 1985.

[29] G. S. Agarwal, "Quantum electrodynamics in the presence of dielectrics and conductors. I. Electromagnetic-field response functions and black-body fluctuations in finite geometries," *Phys. Rev. A*, vol. 11, no. 1, pp. 230–242, 1975.

[30] M. F. Crommie, C. P. Lutz, and D. M. Eigler, "Confinement of Electrons to Quantum Corrals on a Metal Surface," *Science (80-.).*, vol. 262, no. 5131, pp. 218–220, 1993.

[31] S. Crampin, M. H. Boon, and J. E. Inglesfield, "Influence of bulk states on laterally confined surface state electrons," *Phys. Rev. Lett.*, vol. 73, no. 7, pp. 1015–1018, 1994.

[32] S. Crampin and O. Bryant, "Fully three-dimensional scattering calculations of standing electron waves in quantum nanostructures: The importance of quasiparticle interactions," *Phys. Rev. B*, vol. 54, no. 24, pp. R17367–R17370, 1996.

[33] G. Colas des Francs *et al.*, "Optical Analogy to Electronic Quantum Corrals," *Phys. Rev. Lett.*, vol. 86, no. 21, pp. 4950–4953, 2001.

[34] C. Chicanne *et al.*, "Imaging the Local Density of States of Optical Corrals," *Phys. Rev. Lett.*, vol. 88, no. 9, p. 97402, 2002.

[35] A. Dereux *et al.*, "Subwavelength mapping of surface photonic states," *Nanotechnology*, vol. 14, no. 8, pp. 935–938, 2003.

[36] C. Girard *et al.*, "Imaging surface photonic states with a circularly polarized tip," *Europhys. Lett.*, vol. 68, no. 6, pp. 797–803, 2004.

[37] A. Losquin and M. Kociak, "Link between Cathodoluminescence and Electron Energy Loss Spectroscopy and the Radiative and Full Electromagnetic Local Density of States," *ACS Photonics*, vol. 2, no. 11, pp. 1619–1627, 2015.

[38] S. Viarbitskaya *et al.*, "Tailoring and imaging the plasmonic local density of states in crystalline nanoprisms," *Nat. Mater.*, vol. 12, no. 5, pp. 426–432, 2013.

[39] T. Haug, P. Klemm, S. Bange, and J. M. Lupton, “Hot-Electron Intraband Luminescence from Single Hot Spots in Noble-Metal Nanoparticle Films,” *Phys. Rev. Lett.*, vol. 115, no. 6, 2015.

[40] D. L. Mills and A. A. Maradudin, “Surface roughness and the optical properties of a semi-infinite material; The effect of a dielectric overlayer,” *Phys. Rev. B*, vol. 12, no. 8, pp. 2943–2958, 1975.

[41] A. Cuche *et al.*, “Near-field hyperspectral quantum probing of multimodal plasmonic resonators,” *Phys. Rev. B*, vol. 95, no. 12, 2017.

[42] D. P. Macwan, C. Balasubramanian, P. N. Dave, and S. Chaturvedi, “Thermal plasma synthesis of nanotitania and its characterization,” *J. Saudi Chem. Soc.*, vol. 18, no. 3, pp. 234–244, 2014.

[43] M. Epifani, C. Giannini, L. Tapfer, and L. Vasanelli, “Sol – Gel Synthesis and Characterization of Ag and Au Nanoparticles in,” *J. Am. Ceram. Soc*, vol. 83, no. 10, pp. 2385–2393, 2000.

[44] Y. Kobayashi, M. a Correa-duarte, and L. M. Liz-marzan, “Sol - Gel Processing of Silica-Coated Gold Nanoparticles,” *Langmuir*, vol. 17, no. 13, pp. 6375–6379, 2001.

[45] Y. Chen, X. Gu, C.-G. Nie, Z.-Y. Jiang, Z.-X. Xie, and C.-J. Lin, “Shape controlled growth of gold nanoparticles by a solution synthesis.,” *Chem. Commun. (Camb).*, vol. 1, no. 33, pp. 4181–3, 2005.

[46] S. Weigelt *et al.*, “Molecular self assembly from building blocks synthesized on a surface in ultrahigh vacuum: Kinetic control and topo-chemical reactions,” *ACS Nano*, vol. 2, no. 4, pp. 651–660, 2008.

[47] H. Choo *et al.*, “Nanofocusing in a metal–insulator–metal gap plasmon waveguide with a three-dimensional linear taper,” *Nat. Photonics*, vol. 6, no. 12, pp. 838–844, 2012.

[48] D. F. P. Pile *et al.*, “Two-dimensionally localized modes of a nanoscale gap plasmon waveguide,” *Appl. Phys. Lett.*, vol. 87, no. 26, pp. 1–3, 2005.

[49] S. Yokogawa, S. P. Burgos, and H. A. Atwater, “Plasmonic color filters for CMOS image sensor applications,” *Nano Lett.*, vol. 12, no. 8, pp. 4349–4354, 2012.

[50] K. Yamaguchi, M. Fujii, T. Okamoto, and M. Haraguchi, “Electrically driven plasmon chip: Active plasmon filter,” *Appl. Phys. Express*, vol. 7, no. 1, 2014.

[51] P. R. West, S. Ishii, G. V. Naik, N. K. Emani, V. M. Shalaev, and A. Boltasseva, “Searching for better plasmonic materials,” *Laser and Photonics Reviews*, vol. 4, no. 6. pp. 795–808, 2010.

[52] J. H. Park *et al.*, “Single-crystalline silver films for plasmonics,” *Adv. Mater.*, vol. 24, no. 29, pp. 3988–3992, 2012.

[53] H. Ditlbacher *et al.*, “Silver Nanowires as Surface Plasmon Resonators,” *Phys. Rev. Lett.*, vol. 95, no. 25, p. 257403, 2005.

[54] B. Nikoobakht and M. A. El-Sayed, “Preparation and growth mechanism of gold nanorods (NRs) using seed-mediated growth method,” *Chem. Mater.*, vol. 15, no. 10, pp. 1957–1962, 2003.

[55] N. R. Jana, L. Gearheart, and C. J. Murphy, “Seed-mediated growth approach for shape-controlled synthesis of spheroidal and rod-like gold nanoparticles using a surfactant template,” *Adv. Mater.*, vol. 13, no. 18, pp. 1389–1393, 2001.

[56] J. E. Millstone, S. Park, K. L. Shuford, L. Qin, G. C. Schatz, and C. A. Mirkin, “Observation of a quadrupole plasmon mode for a colloidal solution of gold nanoprisms,” *J. Am. Chem. Soc.*, vol. 127, no. 15, pp. 5312–5313, 2005.

[57] G. S. Métraux and C. A. Mirkin, “Rapid thermal synthesis of silver nanoprisms with chemically tailorable thickness,” *Adv. Mater.*, vol. 17, no. 4, pp. 412–415, 2005.

[58] R. Jin, Y. Charles Cao, E. Hao, G. S. Métraux, G. C. Schatz, and C. A. Mirkin, “Controlling anisotropic nanoparticle growth through plasmon excitation,” *Nature*, vol. 425, no. 6957, pp. 487–490, 2003.

[59] Y. Sun and Y. Xia, “Shape-controlled synthesis of gold and silver nanoparticles.,” *Science*, vol. 298, no. 5601, pp. 2176–9, 2002.

[60] D. Yu and V. W. W. Yam, “Controlled synthesis of monodisperse silver nanocubes in water,” *J. Am. Chem. Soc.*, vol. 126, no. 41, pp. 13200–13201, 2004.

[61] H. Wei, Z. Wang, X. Tian, M. Käll, and H. Xu, “Cascaded logic gates in nanophotonic plasmon networks.,” *Nat. Commun.*, vol. 2, p. 387, 2011.

[62] S. Viarbitskaya *et al.*, “Tailoring and imaging the plasmonic local density of states in crystalline nanoprisms,” *Nat. Mater.*, vol. 12, no. 5, pp. 426–432, 2013.

[63] S. Viarbitskaya *et al.*, “Morphology-induced redistribution of surface plasmon modes in two-dimensional crystalline gold platelets,” *Appl. Phys. Lett.*, vol. 103, p. 131112, 2013.

[64] A. Cuche, S. Viarbitskaya, J. Sharma, A. Arbouet, C. Girard, and E. Dujardin, “Modal engineering of Surface Plasmons in apertured Au Nanoprisms,” *Sci. Rep.*, vol. 5, no. Umr 6303, p. 16635, 2015.

Chapter III

Materials and methods

3.1 Experimental fabrication and characterization techniques

3.1.1 Wet Chemical synthesis

Two different samples produced by colloidal chemistry have been used during this work. From the perspective of this work, they exclusively differ by their lateral sizes which is 0.3 to 2μm for the first one and 1 to 30μm for the second one. The crystalline gold nanoprism used in this work has been synthesized by a new one-pot method developed by J. Sharma [1]. The method is based on the direct reduction of Au precursors by polyvinylpyrrolidone (PVP) in alkaline conditions at room temperature. An aqueous solution of 0.143mM NaNO3, 0.143mM KI, 0.477mM HAuCl4 and 19.1mM PVP (a total of 209.6ml) was mixed with 0.2ml of 1M NaOH solution. The solution was diluted with deionized water and kept for 18hrs. The supernatant liquid was then decanted and the Au colloids were redispersed in the deionized water. The size of Au nanoprisms thus prepared ranges from 300nm to 2μm and are 20±2nm thick. Figure 3.1 (a) shows the SEM image of one such gold nanoprisms deposited on ITO coated glass substrate. The Au nanoprisms come with various degree of truncation resulting in different geometries like sharp triangular prism, truncated prism and hexagons.

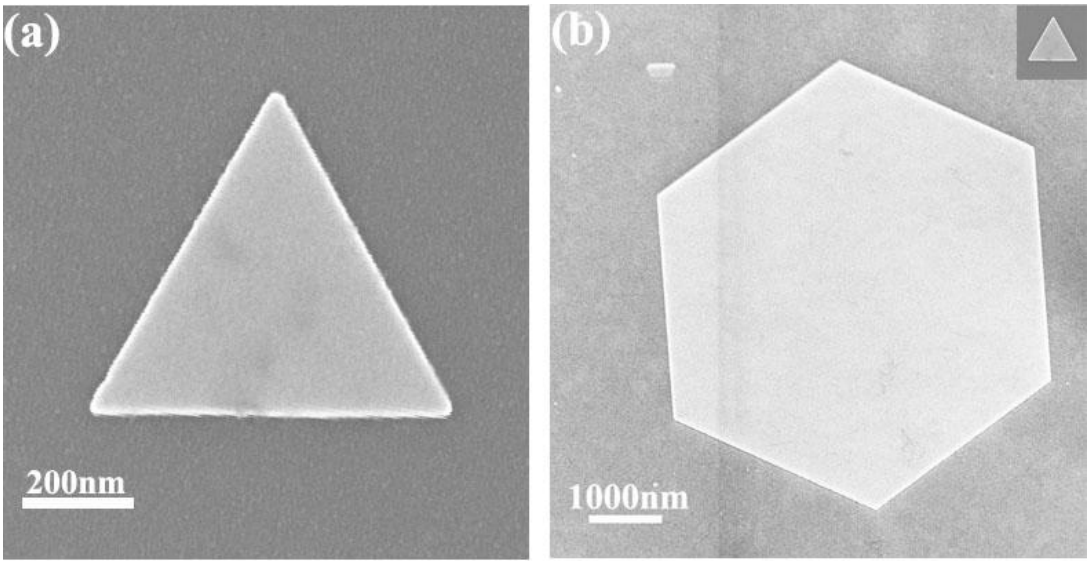


Figure 3.1 SEM image of highly crystalline (a) smaller gold nanoprism. (b) micrometer sized gold platelets, inset shows smaller gold nanoprism (from figure (a)) with same scale as shown in figure (b).

The other Au nanoprisms used in this work are 30nm-40nm thick and the size ranges from 1m to 30m. These Au micro-platelets have been synthesized and provided by Raffaele Mezzenga and co-workers [2]. The micro platelets result from reducing an aqueous solution of chloroauric acid by β-lactoglobulin amyloid protein fibrils. SEM image of one such Au micro-platelet is shown in the Figure 3.1 (b). In the inset of figure 3.1(b), small nanoprism from 3.1(a) has been shown with the same scale just to understand the size difference between the two particles.

3.1.2 Focussed Ion Beam

Focussed ion beam (FIB) systems are very versatile tools which can be used for imaging, and structuring of any kind of material[3]–[6]. The working principle of FIB systems is similar to that of scanning electron microscopes (SEM) except for the fact that the FIB use a finely focussed ion beam when operated at low beam currents, it allows to perform imaging High beam currents are used for site specific sputtering or milling.

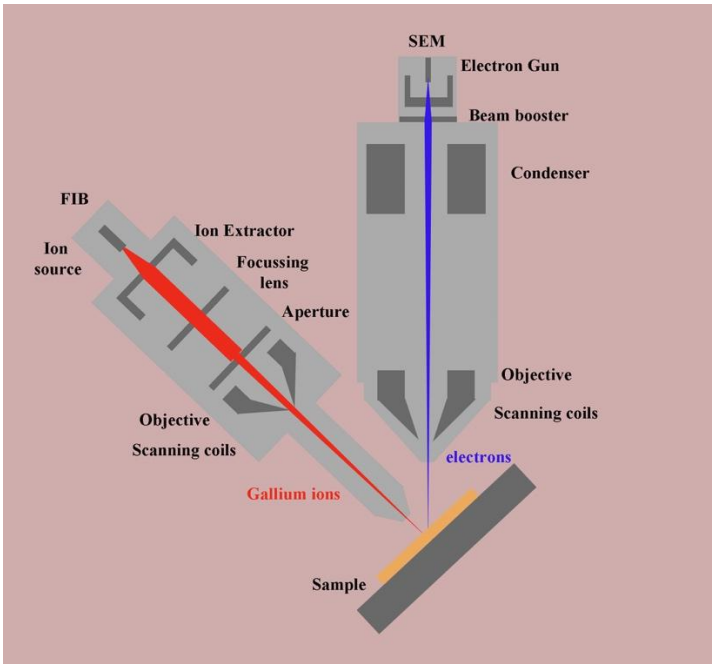


Figure 3.2 Scheme of the FIB-SEM column used for the experiments. The angle between FIB column and SEM column is 54°. The system can be used for in-situ imaging of the sample while milling is being performed.

Typically, a copper wire with a tip covered with liquid gallium is used as ion source. Ga atoms from the ion source are extracted and ionized with high tensions. Ga+ ions are then accelerated and focused on the sample with electromagnetic lenses. Apertures are chosen to allow a desired

current range which results in controlled beam diameter and milling rate. In the end, scanning coils are used to scan systematically across the sample. The primary beam interacts with the material resulting in secondary ions, secondary electrons and neutral ions. The amount of material removed by sputtering is proportional to the primary current and milling time. The smallest features are typically 10-20nm. The FIB system (Orsay Physics) used in this work is equipped with an SEM (Zeiss crossbeam) which is extremely useful since it allows in situ SEM imaging of the sample while milling and restructuring is being performed by FIB. The ion and the electron columns are aligned at angle of 54° with respect to each other which allow for a tilted SEM imaging during FIB processing (Figure 3.2). In this thesis, the FIB system has been used to mill out specific structures out of single crystalline gold nanoplatelets.

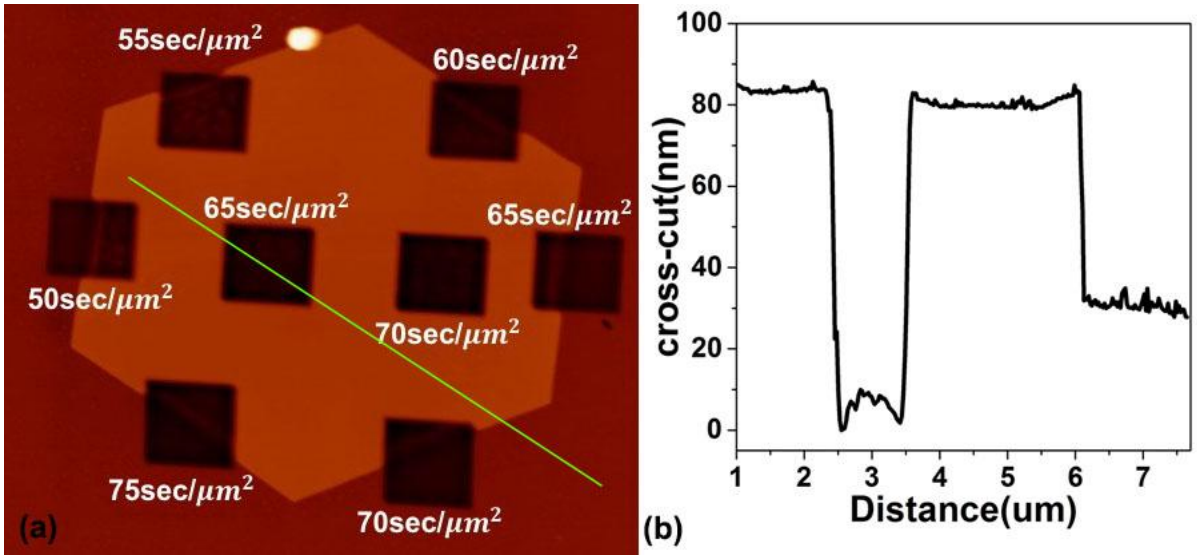


Figure 3.3 (a)AFM image of squares milled on a hexagonal gold nanoprism with milling time of 50, 55, 60, 65, 70 and 75 sec/μm^2. The green line represents the cross-cut done on the milled hexagonal nanoprism, (b) The cross-cut profile corresponding to the green line in (a).

The important FIB milling parameters that has been used to control the milling process are ion current and dose. Dose is given by the product of ion current and milling time per unit area. The ion current used for milling in this work for different sample is between 0.6-1.0 pA. We have performed a calibration of the dose by milling 1μm^2 square boxes with a current of 0.6pA and different milling time. The etched depth was then characterized under atomic force microscopy (AFM) to decide the right dose. Figure 3.3 (a) shows an AFM image of square boxes milled on a hexagonal gold prism with a milling time of 50sec/μm^2 to 75sec/μm^2 with a step size of 5sec/μm^2. The boxes with milling time of 50sec/μm^2 and 55 sec/μm^2 have some gold left on the surface. The milling time of 60sec/μm^2 appears to remove all the gold from the

surface. So, we chose a milling time of 65sec/μm^2 with an ion current of 0.6 pA (i.e. a dose of around 39 pC/μm^2) to make sure that all the material is removed from a desired area. This si confirmed from figure 3.3b, which shows the depth profile plotted from the cross-cut in green (figure 3.3a). It suggests that with a dose of 39 pC/μm^2, an extra milling of around 20-30nm inside the substrate is performed. A repetition test was also done by milling another box with same parameter in order to test the robustness of the procedure. The minimum diameter of a circular hole milled with the FIB system is around 60nm (with a depth of around 50-60nm). The imaging was performed by SEM after milling.

3.1.3 Dark field scattering microscopy

Dark field scattering microscopy is a simple yet powerful optical technique that can be used for studying the spectral behaviour of the nanostructures with minimal background. In this microscopy technique, the direct light from the lamp does not fall on the sample. The dark field condenser produces a ring of light at an extremely oblique angle to the surface of the sample, which is focussed on it. It then diverges so strongly that only the light scattered by the specimen enters the objective. An essential requirement for realizing the dark field microscopy setup is that the numerical aperture of the condenser must be larger than that of the objective lens. This is in order to prevent direct light from entering the objective lens [7].

The first use of dark field microscopy dates back to 1922, when Zsigmondy and co-workers used it to observe and count single metal particles in a liquid, and estimate their size [8]. The simplicity of the technique and its ease of use has since led to its wide use for characterization of different samples over the years. In past few decades, the technique has been revived to characterise the optical properties of the noble metals [9]. The dependence of the LSPR peaks on size and shape of the particle and surrounding conditions has been extensively studied using dark field spectroscopy technique[10]–[12]. The coupling between two nanoparticles or coupling of a nanoparticle with thin films have also been reported using dark field spectroscopy[13], [14].

In our case, we have used this tool to perform single particle dark field scattering spectroscopy measurements where scattered signal from only a single nanoparticle is collected. The single particle dark field scattering spectroscopy was performed using a custom-built set up shown in the figure (3.4). A Nikon inverted optical microscope forms the base of the measurement setup. The setup is equipped with light sources for illumination of the sample in both reflection (episcopic) and transmission (diascopic) geometries.

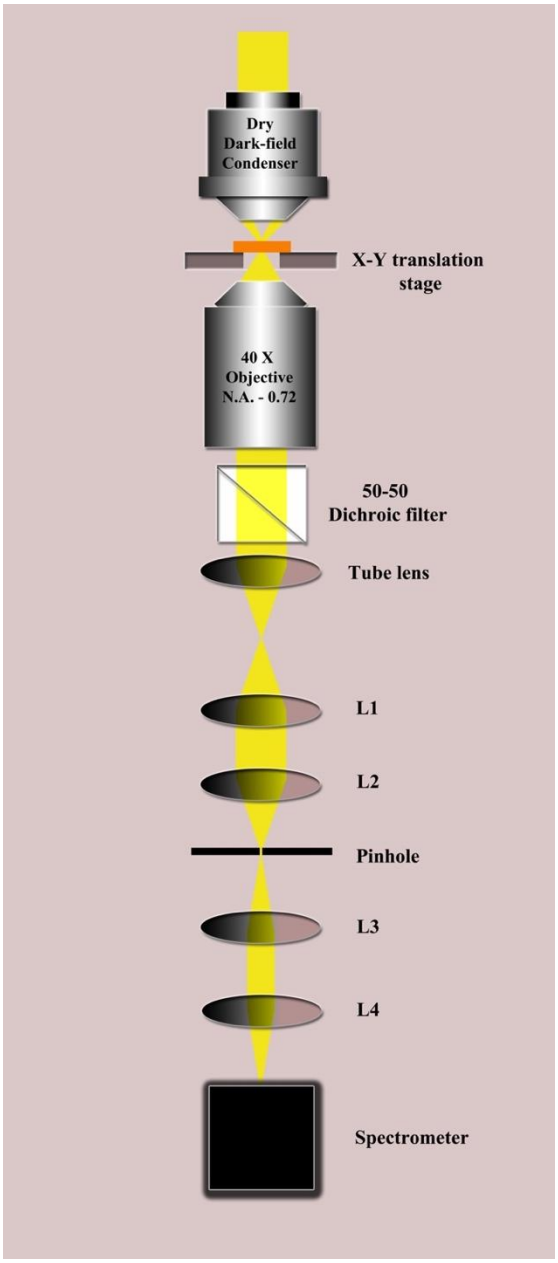


Figure 3.4 Scheme of the dark field scattering microscopy set up used during this work. The light is focussed onto the sample from top using dark-field condenser and the scattered light is collected by a 40X objective (NA = 0.72). The DF scattered signal is then passed through a pinhole placed at the conjugate image plane and the unwanted scattered signal is cut off by the pinhole. The rest of the signal is then focussed onto a spectrometer by means of convex lenses.

A 100W halogen lamp has been used for transmission measurements in this work. The halogen lamp was left to stabilise for atleast 30 minutes before starting the experiments. The incident light was focused using a Nikon dry dark field condenser (NA = 0.95-0.80) onto the sample (figure 3.4). The dark field condenser used in the experiments should be kept at a distance of 4.5mm from the specimen in order to obtain a good focus. The scattered light was

collected in the transmission configuration using a 40X Nikon objective with NA 0.72. The light is then focused on to the conjugated image plane using series of convex lens of focal lengths 10cm (L_1) and 6 cm (L_2) respectively. A pinhole of diameter 50µm is inserted to select scattering from a single Au NP (collection from an area with a diameter of 750nm) and remove unwanted scattering from nearby adjacent nanoparticles.

The scattered signal is then focussed on to the spectrometer using another set of convex lens of focal lengths 6cm(L_3) and 10cm(L_4) respectively. The broadband spectral background was removed from the recorded raw spectrum by subtracting the scattered light from a region of the substrate near the nanoprism. The final spectrum was corrected for the spectral efficiency of the entire spectrometer by normalization with the scattering spectrum of the halogen lamp. The dark field scattering spectra recorded on a given nanoparticle cavity was found to be highly sensitive to the focusing condition of the objective lens.

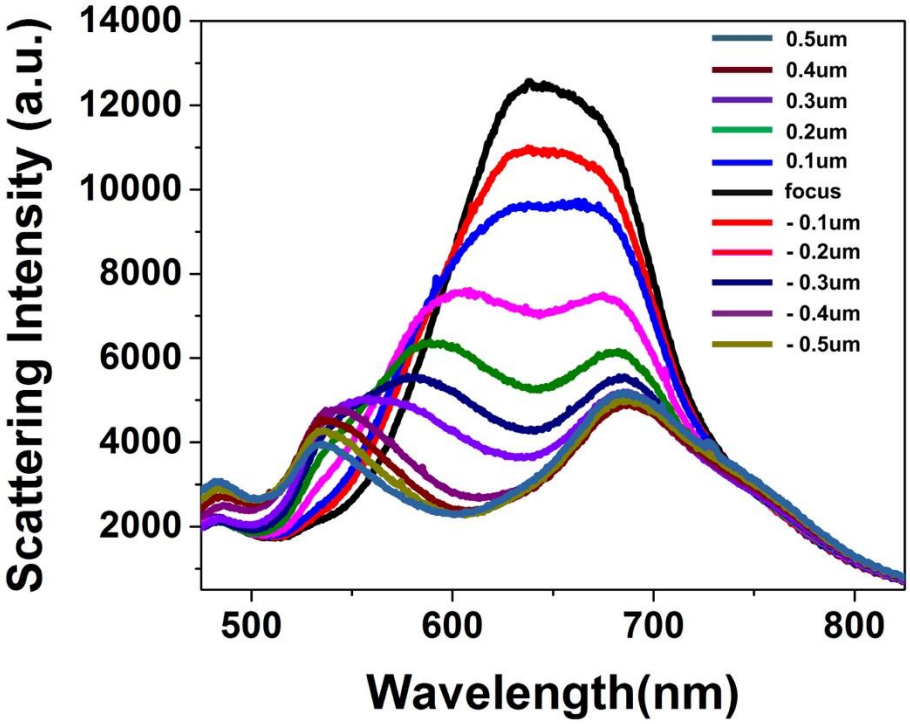


Figure 3.5 Dark field spectra of the gold nanocavity with varying focus of the objective lens have been shown in different colors. The curve in black is considered to be best focused because of the maximum scattering intensity.

A slight variation in the focus resulted in completely different DF scattering spectra. To make sure that we are collecting the scattered signal at right focus, the objective lens was first focussed manually while looking at the eyepiece. Once the manual focussing is done, we went 5 steps (0.1µm each) upward and then 10 steps backward and collected the intensities on 10

different positions (5 above the manually focused position and 5 below it). Figure 3.5 shows the variation of intensity and scattering spectra profile with change in focus. The scattering intensity curve in black is a broad curve centred around 645nm. But as we defocussed step by step, the curve not only had a change in intensity but also a change in the profile of the curve. The scattering intensity profile (shown in dark cyan) has two broader peaks centred around 534nm and 685nm respectively. This variation of intensity and profile of the scattering curve with focusing and defocussing of the objective lens led us to decide the position with maximum scattering intensity to be considered at the best focus. This procedure was followed to obtain best focus before recording each the dark field spectra in this work.

3.1.4 Non-linear photon luminescence microscopy

When a metal is subjected to a low - intensity electric field $\boldsymbol{E}(\mathbf{r}, t)$, the electromagnetic response of the system, which is represented by it's dipole moment per unit volume $\mathbf{p}(\mathbf{r},t)$ is considered linear. However, for sufficiently stronger electric field, the response also depends on higher power of the field and is given by -

$$\mathbf{p}(\mathbf{r}, t) = \mathbf{p}^{(1)}(\mathbf{r}, t) + \mathbf{p}^{(2)}(\mathbf{r}, t) + \mathbf{p}^{(3)}(\mathbf{r}, t) + \ldots \quad (3.1)$$

where $\boldsymbol{p}^{(1)}(\boldsymbol{r},t) = \int_{-\infty}^{t} \chi^{(1)}\,(t-t').\boldsymbol{E}(\boldsymbol{r},t').dt'$

$$\boldsymbol{p}^{(2)}(\boldsymbol{r},t) = \int_{-\infty}^{t}\int_{-\infty}^{t} \chi^{(2)}\,(t-t', t-t''):\boldsymbol{E}(\boldsymbol{r},t').\boldsymbol{E}(\boldsymbol{r},t'')dt'dt''$$

where $\chi^{(n)}$ represents nth order non-linear susceptibility of the medium. For linear process, only the first term is valid. For non-linear processes, the higher order susceptibilities become significant. The most commonly used non-linear optical microscopy processes is non-linear photon luminescence microscopy (NPL).

Maria Goppert-Mayer in 1931, in her doctoral dissertation for the first time predicted that an atom or a molecule could absorb more than one photons simultaneously in the same quantum process by in her doctoral dissertation [15]. However, it took another three decades before her claim could be verified when laser was invented in 1960. Since then NPL has been exploited as an optical characterization tool for various applications such as imaging higher order modes of gold nanorods [16], [17], studying spectral properties of nanoantennas [18], observing delocalization of nonlinear radiation in plasmonic nanoantennas [19] and many more. The principle of multi-photon excitation is based on the idea that two or more photons, of comparably lower photon energy than needed for one photon excitation, can also excite a molecule. For example, in the case of the two photon luminescence(TPL) microscopy, each

photon carries approximately half the energy necessary for transition. An excitation results in the subsequent emission of a photon, typically at a higher energy than either of the two excitation photons.

Figure 3.6 shows two photon absorption mechanism for a gold film. A first near-IR photon assists an intraband transition inside the sp conduction band. The second photon excites an interband transition between the d and the sp bands. Following the absorption through interband transitions, the generated electron−hole pairs recombine and emit a photon.

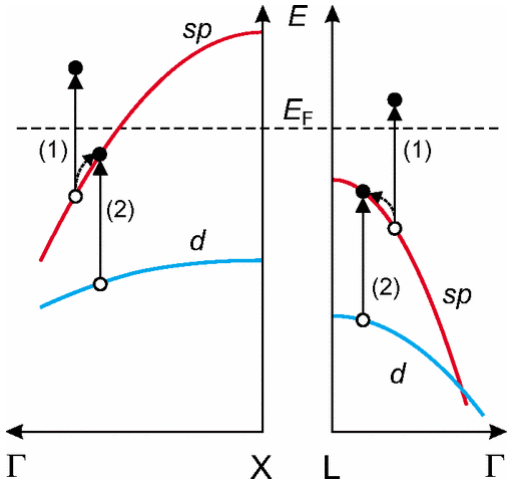


Figure 3.6 Two-photon-induced excitation in gold. The first photon allows an indirect sp intraband transition. The absorption of the second photon creates a hole in the d band by exciting an electron to recombine with the previously created sp hole. [Reprinted with permission from [17]]

The probability of the near-simultaneous absorption of multiple photons is extremely low and a high flux of excitation photons, typically 10^{20} to 10^{30} photons per cm^2 sec is required. The two photons arrived nearly-simultaneously within a time window of 10^{-18} seconds. Hence under normal illumination conditions (such as arc lamp or continuous laser), the probability of multiple photons excitation is virtually zero [20]. Pulsed laser is thus required to generate this high flux. We have used a Ti-Saphhire laser for our experiments. In addition, a high numerical aperture (1.49) oil immersion objective is used to focus the laser beam to a diffraction-limited volume. Thus, the probability of multi- photon absorption is greatly enhanced by concentrating photons both temporally and spatially. In case of NPL, to obtain a higher resolution image we restrict the excitation volume. The other approach is used in confocal microscopy where we restrict the emission volume by placing a pinhole at the conjugate image plane and cutting off

the unfocussed signal. As mentioned in chapter II, in our case, the non-linearity is closer to second order, so we will be using TPL term throughout this thesis.

All the TPL maps in this work has been recorded with S. Viarbitskaya on TPL bench set up by Alexandre Bouhelier at Laboratoire Interdisciplinaire Carnot de Bourgogne(ICB) CNRS-UMR 6303, Université de Bourgogne, Dijon as described in figure 3.7. The linearly polarized beam from a Ti: sapphire femtosecond laser with 180 fs near-infrared pulses tuned between 750nm and 850nm was tightly focused onto the sample placed on a XY piezo translation stage by a high-numerical-aperture oil-immersion microscope. The average laser power used in the experiment is 5mW at the entrance of the microscope. The polarization of the incident light was controlled by a λ/2 plate, positioned at the output of the polarized laser system. TPL signal generated from the gold structure was collected in an epi-collection geometry by the same objective lens and then the excitation beam is separated from the TPL signal by a dichroic mirror (375-700 nm) and an additional low pass filter. The XY piezo translation stage is used to raster scan the sample with a typical step size of 25nm to 50 nm. The size of the step is chosen such that it is less than the size of the beam and we don't miss any area while scanning the sample. The beam spot diameter is estimated by using the formula, FWHM spot diameter $= \frac{0.515\lambda}{NA}$ which is 280nm for 810nm excitation and 260nm for 750nm excitation [1].

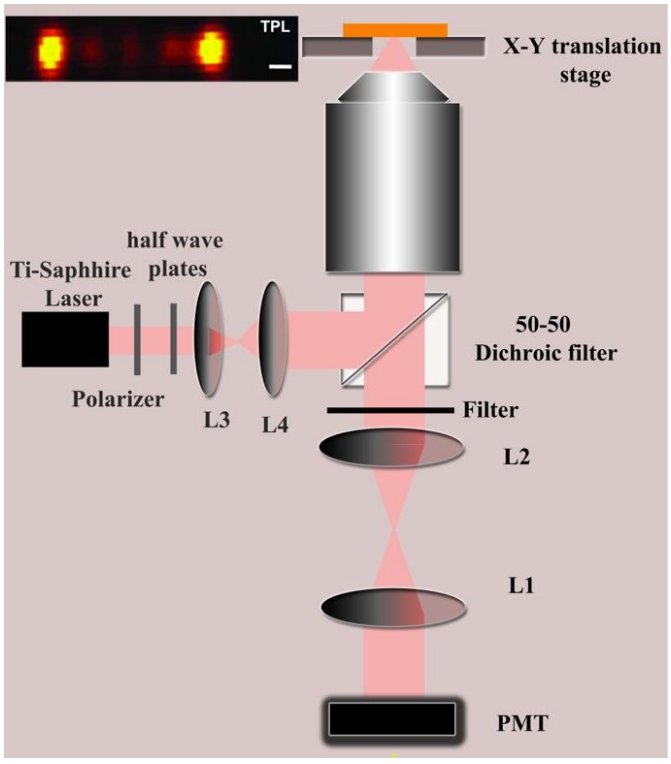


Figure 3.7 Schematic of the TPL setup used for the experimentation. Inset – Confocal TPL map of a 1500nm long nanowire. (Scale bar =200nm)

3.1.5 Leakage radiation microscopy

The development of 2D SPP devices like passive nanostructures such as mirrors or beam splitters coupled with active elements like molecules or quantum dots requires experimental investigation techniques capable of imaging the propagation of SPPs in the 2D systems. Near field optical imaging and characterization technique is one such method which is capable of collecting evanescent electromagnetic field associated with SPPs. However, in the case of thin metallic 2D optical nanostructures, another possibility for imaging propagating SPPs is to use the evanescent tunnelling of SPPs through the supporting metal film into the dielectric substrate and their decoupling into propagating light due to momentum conservation [21]–[24]. This simple, yet efficient, far-field optical detection technique is termed as leakage radiation microscopy (LRM) and allows a quantitative imaging of SPP propagation on thin 2D metallic nanostructures.

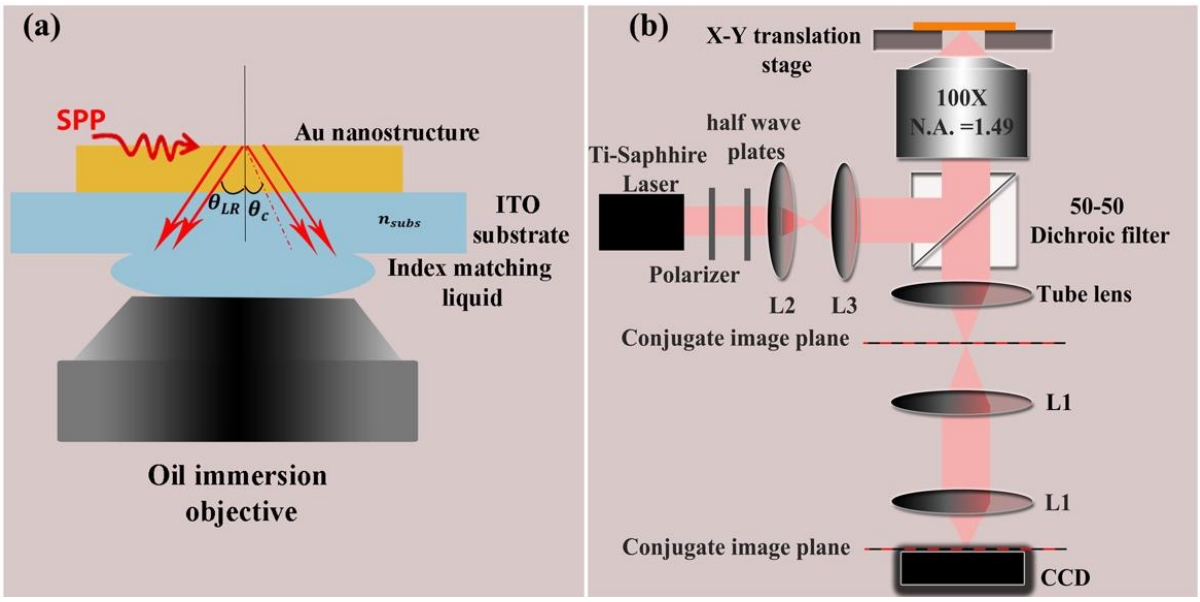


Figure 3.8(a) Schematic showing the principle of LRM. The SPPs leak through the thin gold film in to the glass substrate due to boundary conditions and conservation of the in-plane wave-vector along the different interfaces. The use of index matching liquid further felicitate the leakage of the SPP signal from the substrate to the immersion objective lens. (b) Scheme of Leakage radiation microscopy set up used for the experiments. The linearly polarised laser beam from a Titanium – Sapphire pulsed laser is focussed on the gold sample by oil immersion objective. The leaked SPP signal is then collected back by the same objective and passed through a dichroic beam splitter and tube lens which focus it on conjugate image plane. Two convex lenses L1(f=100mm) focus the signal at the conjugate image plane where a CCD device is used to record the signal.

This tool has been used in most part of the thesis for understanding and investigating 2D plasmonic devices. An index matching liquid is used in this technique to allow the leakage

of SPP signal from substrate to the immersion objective. The first reported use of immersion objective for the leakage radiation experiment is by B. Hecht for imaging freely propagating plasmons in 1996 [25]. The technique was further developed quantitatively by Ditlbacher and co-workers in 2003 [26]. Since then, due to the ease of handiness and simplicity, it has been widely applied to the imaging of SPPs in plasmonic waveguides [27]–[30] and in dielectric loaded plasmonic components [31], [32]. The schematic explaining the principle of leakage radiation of SPPs is shown in figure 3.8(a). The use of immersion objective and index matching liquid is important in this experiment. In their absence, the leakage signal goes through total internal reflection at the substrate-air interface as the leakage radiation angle, θ_{LR} for gold film is greater than the critical angle (above which the signal gets internally reflected) at the substrate – air interface. The leakage radiation angle, θ_{LR} is given by

$$\theta_{LR} = \sin^{-1}\left(\frac{Re(\beta)}{n_{subs}k_0}\right) \tag{3.2}$$

where β is the SPP propagation constant and n_{subs} is the refractive index of the substrate. The formula for critical angle for total internal reflection is given by –

$$\theta_c = \sin^{-1}\left(\frac{n_{air}}{n_{subs}}\right) \tag{3.3}$$

For λ = 700nm, $\varepsilon_{gold}(\omega)$ = -16.48 + 1.04i (Data from Johnson and Christy 1972) and n_{subs} = 1.51. The SPP propagation constant can be calculated from equation (2.2). This gives a leakage radiation angle, θ_{LR} = 43.4° and critical angle, θ_c = 41.8°. As, $\theta_{LR} > \theta_c$, the leakage radiation will go through total internal reflection which can be avoided by the used of index matching liquid. Figure 3.8(b) shows the schematic of optical setup used in our experiments. It relies on an inverted optical microscope equipped with a high numerical aperture oil immersion objective (NA =1.49) which is used to focus excitation beam from the 180fs Ti-Saphhire femtosecond laser source on the sample in episcopic excitation configuration. The laser beam is passed through a series of optical components including polarizer, half wave-plate, beam expander and beam splitter. The polarizer and half wave-plate are used to control the polarization of the incident beam. Two convex lenses, L2 and L3 are used for expanding the beam. The leakage radiation signal is collected from the same objective lens and is passed through 50-50 dichroic beam splitter (350nm -700nm). The signal is then focussed to a conjugate image plane with a series of tube lens and convex lens, L1 (focal length =100mm), where the signal is recorded by charge couple device (CCD) camera.

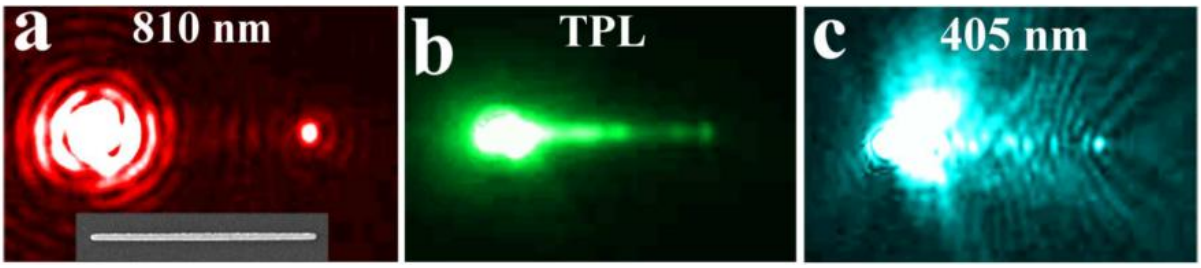


Figure 3.9 (a), (b) and (c) are colorized direct image plane micrographs emphasizing the excitation of propagating SP mode in a 1950 nm-long gold rod nanoantenna. Images are spectrally filtered to record emission at the fundamental, the TPL, and SHG wavelengths, respectively [19].

An example of image recorded with LRM experimental setup at ICB Dijon is shown in figure 3.9 [19]. The laser with excitation wavelength of 810nm is focussed on the left extremity of a 1950nm long gold nanorods nanoantenna. The images are filtered to record (a) fundamental wavelength(810nm) (b) TPL emission and (c) SHG wavelengths (405nm).

3.2 Simulation techniques

3.2.1 Green Dyadic Method

Recent advancements in the fabrication and characterization techniques have required concomittant efforts on theoretical fronts in understanding the optical properties of mesoscopic and nanometric scale systems. The most used theoretical tools for studying far-field and near field optical phenomena are coupled dipole approximation (CDA)[33], perturbation diffraction theory [34], finite difference time domain (FDTD)[35]. However, for realistic mesoscopic systems, it is difficult to control and match the electromagnetic boundary condition at the interface due to low symmetry and complexity of the system. In out group, these difficulties have been overcome by the implementation of an exclusive numerical tool based on Green Dyadic method by C. Girard. This approach is used to simulate realistic experimental structures. The entire response to a given incident field inside any arbitrary nanostructure can be derived from a unique generalized field propagator. To describe this method, we consider an arbitrary shaped nanostructure of volume V embedded in a dielectric medium of permittivity $\varepsilon_d(\omega)$. We first recall the Maxwell's equations in frequency domain (CGS units have been used throughout this chapter) -

$$\nabla \times \boldsymbol{E}(\boldsymbol{r},\omega) = ik_0 \boldsymbol{B}(\boldsymbol{r},\omega) \tag{3.4}$$

$$\nabla . \boldsymbol{B}(\boldsymbol{r},\omega) = 0 \tag{3.5}$$

$$\varepsilon(\omega)\nabla . \boldsymbol{E}(\boldsymbol{r},\omega) = 4\pi\rho(\boldsymbol{r},\omega) \tag{3.6}$$

$$\nabla \times \boldsymbol{B}(\boldsymbol{r},\omega) = -ik_0\,\varepsilon(\omega)\boldsymbol{E}(\boldsymbol{r},\omega) + \frac{4\pi}{c}\,\boldsymbol{j}(\boldsymbol{r},\omega) \tag{3.7}$$

where $\rho(\boldsymbol{r},\omega)$ and $\boldsymbol{j}(r,\omega)$ are charge density and current density related to the nanostructure. The wave equation corresponding to the electric field $\boldsymbol{E}(\boldsymbol{r},\omega)$ in presence of the nanostructure can then be obtained by solving the equations (3.4) and (3.7) and replacing the charge and current densities term with the polarization density, $P(\boldsymbol{r},\omega)$

$$\Delta\boldsymbol{E}(\boldsymbol{r},\omega) + {k_0}^2\varepsilon(\omega)\,\boldsymbol{E}(\boldsymbol{r},\omega) = -4\pi\left[\boldsymbol{I}k_0^2 + \frac{1}{\varepsilon(\omega)}\nabla\nabla\right].\boldsymbol{P}(\boldsymbol{r},\omega) \tag{3.8}$$

The above equation can be rewritten in form of differential operators '$\mathcal{O}$' and 'Q' as –

$$\mathcal{O}\boldsymbol{E}(\boldsymbol{r},\omega) = -4\pi Q(\boldsymbol{r},\omega).\boldsymbol{P}(\boldsymbol{r},\omega), \tag{3.9}$$

where $$\mathcal{O} = \Delta + {k_0}^2\varepsilon \quad \text{and} \tag{3.10a}$$

$$\boldsymbol{Q} = k_0^2\boldsymbol{I} + \frac{1}{\varepsilon(\omega)}\Delta\Delta \tag{3.10b}$$

These two operators can be used to define the field susceptibility tensor, S_0 , associated with the wave equation as-

$$\boldsymbol{S_0}(\boldsymbol{r},\boldsymbol{r}',\omega) = -4\pi\mathcal{O}^{-1}\boldsymbol{Q}\delta(\boldsymbol{r}-\boldsymbol{r}') \tag{3.11}$$

The solution of equation (3.8) then can be obtained using equation (3.11) as –

$$\boldsymbol{E}(\boldsymbol{r},\omega) = \boldsymbol{E_0}(\boldsymbol{r},\omega) + \int \boldsymbol{S_0}(\boldsymbol{r},\boldsymbol{r}',\omega).\boldsymbol{P}(\boldsymbol{r}',\omega)\,d\boldsymbol{r}' \tag{3.12}$$

where $\boldsymbol{E_0}(\boldsymbol{r},\omega)$ is the electric field in the absence of the nanostructure. The polarization density can be expressed in the term of electric field $\boldsymbol{E}(\boldsymbol{r}',\omega)$ and susceptibility, $\chi_o(\boldsymbol{r}',\omega)$ of the nanostructure as

$$\boldsymbol{P}(\boldsymbol{r}',\omega) = \chi_o(\boldsymbol{r}',\omega).\boldsymbol{E}(\boldsymbol{r}',\omega) \tag{3.13}$$

where $$\chi_o(\boldsymbol{r}',\omega) = \frac{\varepsilon_m - \varepsilon_{env}}{4\pi} \quad \text{inside} \tag{3.14a}$$

$$= 0 \quad \text{outside} \tag{3.14b}$$

Equation (3.12), can thus be rewritten into

$$\boldsymbol{E}(\boldsymbol{r},\omega) = \boldsymbol{E_0}(\boldsymbol{r},\omega) + \int \boldsymbol{S_0}(\boldsymbol{r},\boldsymbol{r}',\omega).\chi_o(\boldsymbol{r}',\omega).\boldsymbol{E}(\boldsymbol{r}',\omega)\;\; d\boldsymbol{r}' \tag{3.15}$$

This self-consistent equation is also called Lippmann-Schwinger equation for the optical electric field. The notion of Dyadic tensor $\boldsymbol{S_0}(\boldsymbol{r},\boldsymbol{r}',\omega)$ can be stated more clearly by introducing the scalar Green tensor $\mathcal{G}_0(\boldsymbol{r},\boldsymbol{r}',\omega)$ corresponding to equation (3.8) as –

$$\mathcal{G}_0(\boldsymbol{r},\boldsymbol{r}',\omega) = -4\pi\mathcal{O}^{-1}\boldsymbol{Q}\delta(\boldsymbol{r}-\boldsymbol{r}') \tag{3.16}$$

By multiplying both sides of the above equation by $\mathcal{O}\,\boldsymbol{Q}$ and using the commutation property of the two operators, we arrive at following relation between a scalar function and the Green tensor

$$\boldsymbol{S_0}(\boldsymbol{r},\boldsymbol{r'},\omega) = \boldsymbol{Q}\mathcal{G}_0(\boldsymbol{r},\boldsymbol{r'},\omega) \tag{3.17}$$

where the scalar function is given by [36]

$$\mathcal{G}_0(\boldsymbol{r},\boldsymbol{r'},\omega) = \frac{e^{ik|\boldsymbol{r}-\boldsymbol{r'}|}}{|\boldsymbol{r}-\boldsymbol{r'}|} \tag{3.18}$$

Putting the value of the scalar function in equation (3.17) from the equation (3.18) and applying the operator Q over it results in the following relation –

$$\boldsymbol{S_0}(\boldsymbol{r},\boldsymbol{r'},\omega) = [-k^2 T_1(\boldsymbol{R}) - ikT_2(\boldsymbol{R}) + T_3(\boldsymbol{R})]\frac{e^{ik|\boldsymbol{R}|}}{\varepsilon(\omega)} \tag{3.19}$$

where $k = {k_0}^2\varepsilon$ whereas T_1, T_2 and T_3 are three dyadic tensors which relate the far field and near field and are given by

$$T_1(\boldsymbol{R}) = \frac{\boldsymbol{RR}-\boldsymbol{I}R^2}{R^3} \quad , \tag{3.20a}$$

$$T_2(\boldsymbol{R}) = \frac{3\boldsymbol{RR}-\boldsymbol{I}R^2}{R^4} \quad , \tag{3.20b}$$

$$T_3(\boldsymbol{R}) = \frac{3\boldsymbol{RR}-\boldsymbol{I}R^2}{R^5} \quad , \tag{3.20c}$$

and $$\boldsymbol{R} = (\boldsymbol{r}-\boldsymbol{r'}) \tag{3.20d}$$

In case of the nanostructure supported by a planar substrate, the equation (3.15) becomes

$$\boldsymbol{E}(\boldsymbol{r},\omega) = \boldsymbol{E_0}(\boldsymbol{r},\omega) + \int_V \boldsymbol{S}(\boldsymbol{r},\boldsymbol{r'},\omega).\chi_o(\boldsymbol{r'},\omega).\boldsymbol{E}(\boldsymbol{r'},\omega)d\boldsymbol{r'} \tag{3.21}$$

where $$\boldsymbol{S}(\boldsymbol{r},\boldsymbol{r'},\omega) = \boldsymbol{S}_0(\boldsymbol{r},\boldsymbol{r'},\omega) + \boldsymbol{S_{subs}}(\boldsymbol{r},\boldsymbol{r'},\omega) \tag{3.22}$$

$\boldsymbol{S_{subs}}(\boldsymbol{r},\boldsymbol{r'},\omega)$ depends on the optical properties of the planar substrate supporting the nanostructure. Equation (3.21) can be rewritten in form of generalized field propagator as [37], [38] –

$$\boldsymbol{E}(\boldsymbol{r},\omega) = \int d\boldsymbol{r'}\boldsymbol{K}(\boldsymbol{r},\boldsymbol{r'},\omega)\boldsymbol{E_0}(\boldsymbol{r'},\omega) \tag{3.23}$$

where $$\boldsymbol{K}(\boldsymbol{r},\boldsymbol{r'},\omega) = \delta(\boldsymbol{r}-\boldsymbol{r'})\boldsymbol{I} + \chi_0(\boldsymbol{r'},\omega)\boldsymbol{S}(\boldsymbol{r},\boldsymbol{r'},\omega) \tag{3.24}$$

Here, **I** is the identity tensor. The generalized field propagator depends only on the geometry of the nanostructure and not on the incident illumination field $\boldsymbol{E_o}(\boldsymbol{r'},\omega)$. This generalized field propagator contains response of entire nanostructure at any frequency ω and can be used in equation (3.23) to obtain the optical field distribution for any arbitrary illumination field $\boldsymbol{E_o}(\boldsymbol{r'},\omega)$. The generalized field propagator can be computed by discretizing the whole nanostructure into N cells of volume 'v' each and calculate optical field distribution for every beam waist location 'r_0' using equation (3.21) which now takes the following form -

$$E(\boldsymbol{r_i},\boldsymbol{r_0},\omega) = \sum_{j=1}^{N}\boldsymbol{K}(\boldsymbol{r_i},\boldsymbol{r_j},\omega).\boldsymbol{E_o}(\boldsymbol{r_j},\boldsymbol{r_0},\omega) \tag{3.25}$$

and the equation for generalized field propagator then is given by -

$$\boldsymbol{K}(\boldsymbol{r_i}, \boldsymbol{r_j}, \omega) = v\boldsymbol{I}\delta_{ij} + \boldsymbol{S}(\boldsymbol{r_i}, \boldsymbol{r_j}, \omega).\, v\boldsymbol{\chi}(\boldsymbol{r_j}, \omega) \tag{3.26}$$

The field susceptibility tensor in above equation can be calculated by iterative computation scheme by the Dyson sequence algorithm proposed by Olivier J.F. Martin et al. [39] –

$$\boldsymbol{S}(\boldsymbol{r_i}, \boldsymbol{r_i}, \omega) = \boldsymbol{S_0}(\boldsymbol{r_i}, \boldsymbol{r_i}, \omega) + \sum_{k=1}^{N} \boldsymbol{\chi_k}(\boldsymbol{R_k}, \omega)\, \boldsymbol{S}(\boldsymbol{r_i}, \boldsymbol{R_k}, \omega)\boldsymbol{S}(\boldsymbol{R_k}, \boldsymbol{r_i}, \omega) \tag{3.27}$$

where $\boldsymbol{S_0}(\boldsymbol{r_i}, \boldsymbol{r_i}, \omega)$ is the field-susceptibility in the absence of nanostructures. Here, the nanostructure has been divided into 'N' cells centred at $\boldsymbol{R_k}$ and $\boldsymbol{r_i}$ is any point in the observation plane. The term '$\boldsymbol{\chi_k}$' in the equation (3.27) is defined by the size of each discretized cell, V_k and the dielectric function of the metal structure, $\boldsymbol{\epsilon}(\boldsymbol{R_k}, \omega)$ and is given by –

$$\boldsymbol{\chi}_k(\boldsymbol{R_k}, \omega) = (\, \epsilon(\boldsymbol{R_k}, \omega) - 1)\, \frac{V_k}{4\pi} \tag{3.28}$$

3.2.2 Transmission Maps

In order to calculate the local field at any given point, we first need to define the illumination field, E_o.We have used Gaussian illumination beam for performing all the simulations in this thesis which can be described by using the model developed by Török et al in 1995 [40]. The model explains in detail the characteristics of the electric field given by a plane wave when it is focussed at an interface of two materials with different refractive indices [41]. This modelling of the illumination field as a Gaussian spot is based on plane wave expansion in the wave vector domain and is given by –

$$\boldsymbol{E_0}(\boldsymbol{r'}, \boldsymbol{r_0}, \omega) = \int_{-\sqrt{\varepsilon_{sub}}k_0}^{\sqrt{\varepsilon_{sub}}k_0} d\alpha \int_{-\sqrt{\varepsilon_{sub}k_0^2-\alpha^2}}^{\sqrt{\varepsilon_{sub}k_0^2-\alpha^2}} d\beta\, \boldsymbol{\zeta} exp\left[-\frac{w_0^2(\alpha^2+\beta^2)}{4}\right] exp[i\alpha(x'-x_0) + i\beta(x'-y_0) + ik_z(x'-z_0)], \tag{3.26}$$

where $k_0 = \frac{\omega}{c}$ is the vacuum wave vector of the incident beam and $\boldsymbol{r_0} = (x_0, y_0, z_0)$ gives the positions of the excitation Gaussian beam spot. The beam waist w_0 is the lateral size of this incident Gaussian beam. The results of simulation performed for calculation of normalized intensity at the Gaussian illumination spot is presented in figure 3.10. The normalized intensity if calculated for polarization along the double headed arrow is shown in figure 3.10 (a) while figure 3.10 (b, c, d) gives the normalized intensity distribution along x, y, and z direction of the illumination field respectively.

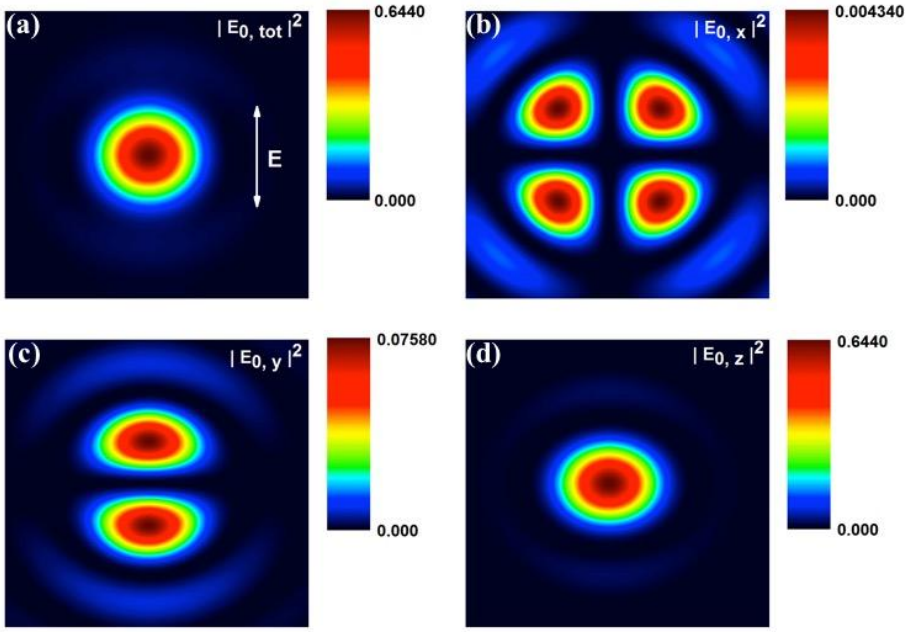


Figure 3.10 2x2 µm² simulated images showing the position and the normalized intensity distribution of the incident Gaussian illumination spot positioned at the center. (a) Total normalized intensity for a polarization along the double headed arrow shown in white. Normalized intensity of the x, y and z components of the field are respectively displayed in (b), (c) and (d).

The integration is performed in the 2D reciprocal space defined by the vector $\boldsymbol{k_{/\!/}} = (\alpha, \beta)$. The tangential components of the field vector ζ are given by -

$$\begin{pmatrix} \zeta_x \\ \zeta_y \end{pmatrix} = \mathrm{T} \begin{pmatrix} E_{0,x'} \\ E_{0,y}{}' \end{pmatrix}, \tag{3.27}$$

with T the transmission matrix:

$$\mathrm{T} = \begin{pmatrix} (\tau_{\parallel} - \tau_{\perp}) \cos^2 \delta + \tau_{\perp} & (\tau_{\parallel} - \tau_{\perp}) \cos \delta \sin \delta \\ (\tau_{\parallel} - \tau_{\perp}) \cos \delta \sin \delta & (\tau_{\parallel} - \tau_{\perp}) \sin^2 \delta + \tau_{\perp} \end{pmatrix}, \tag{3.28}$$

Here, $\tau_{\parallel}$ and $\tau_{\perp}$ are the Fresnel coefficients associated to the interface and δ is an angle in the xy plane between the x-axis in Cartesian coordinates and the direction of the wave vector $\boldsymbol{k_{/\!/}}$. The normal component ζ_z of $\boldsymbol{\zeta}$ in equation (3.26) is obtained using the following expression-

$$\zeta_z = -\frac{(\alpha \zeta_{inc,x'} + \beta \zeta_{inc,y'})}{(\varepsilon_{sub} k_0^2 - \alpha^2 - \beta^2)^{1/2}} \tag{3.29}$$

Now, we can use equation (3.26) to calculate the local electric field, at a given point 'r ' due to excitation by a focused illumination E_0 of angular frequency ω positioned at r_0 as shown in figure 3.11 -

$$E(\boldsymbol{r}, \boldsymbol{r_0}, \omega) = \int_V K(\boldsymbol{r}, \boldsymbol{r'}, \omega).\, E_0(\boldsymbol{r'}, \boldsymbol{r_0}, \omega)\, d\boldsymbol{r'} \tag{3.30}$$

where
$$K(\boldsymbol{r}, \boldsymbol{r'}, \omega) = \chi_0(\boldsymbol{r'}, \omega) S(\boldsymbol{r}, \boldsymbol{r'}, \omega) \tag{3.31}$$

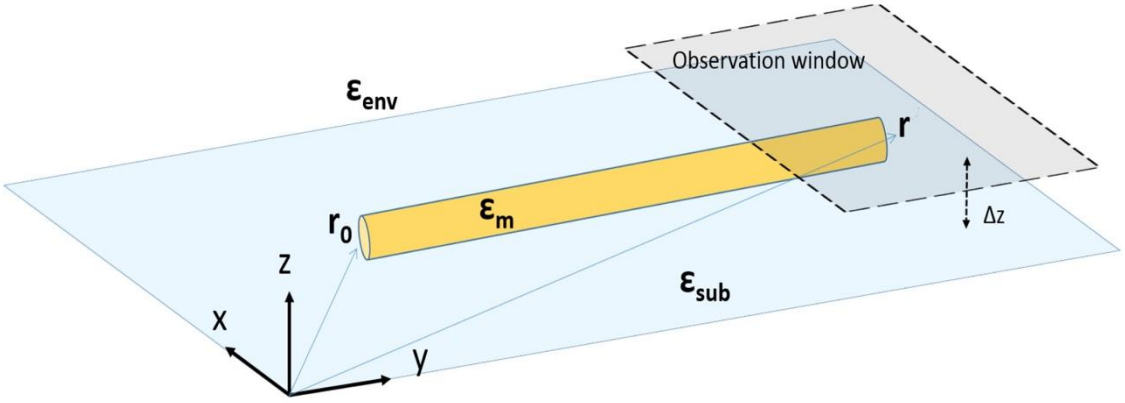


Figure 3.11 Schematic geometry of a plasmonic 1D channel, supported by a transparent dielectric substrate, and the associated observation window above the structure used for simulations. The size of this window can be adjusted to the dimensions of the structure.

In equation, (3.31) we have not used the Dirac delta distribution for defining the generalized propagator as we only calculate the plasmon-mediated field transfer in the metallic structures and not direct contribution of the incident illumination at the output location 'r'.

The intensity generated at the given point then takes the form -

$$I(\boldsymbol{r}, \boldsymbol{r_0}, \omega) = |E(\boldsymbol{r}, \boldsymbol{r_0}, \omega)|^2 \tag{3.32}$$

Figure 3.12(b)-(c) present the simulated transfer maps showing the plasmon- mediated field transfer in the 1.5 μm gold nanowire for illumination along two orthogonal polarization directions, when excited at one of the extremities of the nanowire as denoted by red dot in figure 3.12 (a). The white dashed line shows the outline of the nanowire. The simulated maps suggest the transfer of the signal for when the illumination field is polarized along the channel, while for the orthogonal polarization, the field transfer ceases.

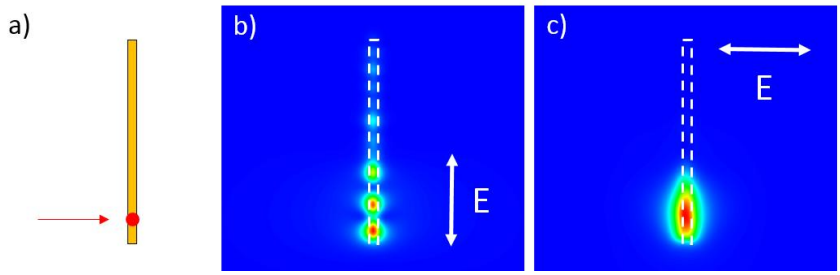


Figure 3.12 a) Schematic view of the Gaussian excitation spot position (red dot) with respect to the 1.5 µm long gold wire. (b,c) Corresponding 2x2 µm² simulated images showing the intensity distribution of the total field propagating in the wire once illuminated by the Gaussian spot. The incident polarization is indicated by the white arrows. The four maps are computed at a distance of 30 nm above the metallic wire.

3.2.3 SPLDOS and TPL Maps

To calculate SPLDOS and TPL maps, the direct distribution of incident illumination field has to be taken into account unlike in the calculation of the transmission maps. The electromagnetic response of a given nanostructure to an arbitrary illumination field is obtained by computing the optical field distribution inside a given nanostructure at each beam waist position, '$\boldsymbol{r_0}$'. Now, as discussed in chapter 2, the local field distribution at a given position '$\boldsymbol{r}$' is directly proportional to the SPLDOS present at '$\boldsymbol{r}$' and is governed by the equation –

$$|\boldsymbol{E}(\boldsymbol{r},\boldsymbol{r_0},\omega)|^2 = |\boldsymbol{E_0}(\boldsymbol{r},\boldsymbol{r_0},\omega)|^2 \pi^2 {\omega_0}^2 A^{-1} \rho_{||}(\boldsymbol{r},\omega_0) \tag{3.33}$$

Also, since the TPL signal from gold involves second order nonlinear optical processes we can describe it by introducing an effective ω–dependent nonlinear coefficient η (ω_0) associated with the metal [42]. Thus, the TPL intensity coming out of an elementary cell of volume 'v' if thus given by –

$$I_{TPL}(\boldsymbol{r},\boldsymbol{r_0},\omega) = [\,\eta(\omega_0).|\boldsymbol{E}(\boldsymbol{r},\boldsymbol{r_0},\omega)|^2]^2 v \tag{3.34}$$

In the next step we integrate the TPL intensity over the entire volume 'V' of the given nanostructure. Thus replacing the value of $|E(\boldsymbol{r},\boldsymbol{r_0},\omega)|^2$ from equation (3.33) into equation (3.34), and adding up the TPL intensity of over entire volume, we get –

$$I_{TPL}(\boldsymbol{r},\boldsymbol{r_0},\omega) = \eta^2(\omega_0)\pi^4 {\omega_0}^2 A^{-2} \int_V |\boldsymbol{E}_0(\boldsymbol{r},\boldsymbol{r_0},\omega)|^4 \, {\rho^2}_{||}(\boldsymbol{r},\omega_0) \tag{3.35}$$

The above equation shows that TPL intensity results from the convolution of the squared in-plane SPLDOS with the Gaussian beam profile at a given point 'r'. Interestingly, when the Gaussian beam waist tends to zero, the TPL maps converge to squared-SPLDOS maps. Figure 3.13(b, c) shows the TPL maps for a triangular gold nanoprism of lateral size 600nm(shown in figure 3.13(a)) simulated at λ = 810nm for two orthogonal in-plane polarization of the incident beam as denoted by the double headed arrow. The beam waist diameter of the incident beam used here is 250nm. Corresponding squared SPLDOS map with beam waist diameter of 50nm is shown in figure 3.13(d, e).

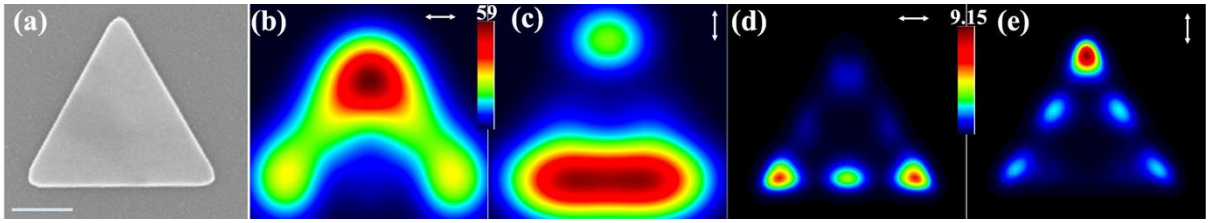


Figure 3.13 (a) SEM image of 600nm lateral size Au nanoprism. (b, c) Simulated TPL map obtained by integrating TPL intensity over the entire structure for two different polarizations (beam waist = 250nm). The scale bar in white is 200nm and the double headed arrow on the top shows the direction of in plane polarization of the incident beam. (d, e) Corresponding squared SPLDOS maps for two orthogonal polarizations with 50nm beam waist of the incident beam. Excitation wavelength for all four simulated maps is 810nm. The color scale for two TPL maps in figures (b) and (c) is same. Similarly color scale for squared SPLDOS maps in figures (d) and (e) is same.

The formalism explained in section 3.2.2 and 3.2.3 can also be used to compute transmission spectra and SPLDOS spectra respectively at a given point inside the structures. To obtain the spectra, we define a *n* x *m* matrix where *'nm'* is the total number of points on the structure on which the spectra has to be calculated. Next, we define the spectral window in which the spectra need to be computed. The resolution of the spectra depends on the number of wavelengths on which the spectra has been computed. In our calculation we have kept a maximum gap of 15nm between two consecutive wavelengths. For all the 2D nanostructures used in this study, we have designed the mesh by using hexagonal lattice of size 10nm. All the simulations have been carried out on the massive parallel computing centre, Calcul en Midi-Pyrénée (CALMIP). This system can be accessed from any PC in remote locations. The computation code is compiled by using Intel Fortran compiler (ifort) for linux. The maximum number of lattice points that is allowed on this system is around 20000. We have used 3 layered mesh for most of the part of the thesis except in the case of double hexagon structure where

the huge size of the structure does not allow use of 3 layered mesh. Thus for double hexagon, we have used single layered mesh for computation which keeps the number of lattice points well below the calculation limits. The mesh used for gold nanoprism in figure 3.13(a), for example, is 3 layered mesh with lattice size of 10nm and is composed of 5541 points. The maximum time allotted for the computation is 16 days. The SPLDOS or TPL maps take less time compared to corresponding spectra as the maps are calculated for only on wavelength while spectra need to be calculated for several wavelengths. For example, for the mesh in figure 3.13(a), it takes around 156 minutes to calculate an SPLDOS map. However, as the number of points is not directly proportional to the calculation time and increases with a power of 3.

Reference

[1] S. Viarbitskaya. A. Teulle, R. Marty, J. Sharma, C. Girard, A. Arbouet, and E. Dujardin,, "Tailoring and imaging the plasmonic local density of states in crystalline nanoprisms," *Nat. Mater.*, vol. 12, no. 5, pp. 426–432, 2013.

[2] S. Bolisetty, J. J. Vallooran, J. Adamcik, S. Handschin, F. Gramm, and R. Mezzenga, "Amyloid-mediated synthesis of giant, fluorescent, gold single crystals and their hybrid sandwiched composites driven by liquid crystalline interactions," *J. Colloid Interface Sci.*, vol. 361, no. 1, pp. 90–96, 2011.

[3] J.-S. Huang, V. Callegari, P. Geisler, C. Brüning, J. Kern, J. C. Prangsma, X. Wu, T. Feichtner, J. Ziegler, P. Weinmann, M. Kamp, A. Forchel, P. Biagioni, U. Sennhauser and B. Hecht "Atomically flat single-crystalline gold nanostructures for plasmonic nanocircuitry," *Nat. Commun.*, vol. 1, no. 9, p. 150, 2010.

[4] K. Narayan and S. Subramaniam, "Focused ion beams in biology," *Nat. Methods*, vol. 12, no. 11, pp. 1021–1031, 2015.

[5] P. Prewett, "Focused ion beams-microfabrication methods and applications (invited)," *Vacuum*, vol. 44, no. 3–4, pp. 345–351, 1993.

[6] M. J. Vasile, R. Nassar, J. Xie, and H. Guo, "Microfabrication techniques using focused ion beams and emergent applications.," *Micron*, vol. 30, no. 3, pp. 235–44, 1999.

[7] M. Hu, C. Novo, A. Funston, H. Wang, H. Staleva, S. Zou, P. Mulvaney, Y. Xia, and G. V. Hartland, "Dark-field microscopy studies of single metal nanoparticles: understanding the factors that influence the linewidth of the localized surface plasmon resonance," *J. Mater. Chem.*, vol. 18, no. 17, pp. 1949–1960, 2008.

[8] R. Zsigmondy, "Richard Zsigmondy - Nobel Lecture: Properties of Colloids," *Nobelprize.org. Nobel Media AB 2014*, vol. 1, p. Nobelprize.org. Nobel Media AB 2014, 1926.

[9] S. Schultz, D. R. Smith, J. J. Mock, and D. a Schultz, "Single-target molecule detection with nonbleaching multicolor optical immunolabels.," *Proc. Natl. Acad. Sci. U. S. A.*, vol. 97, no. 3, pp. 996–1001, 2000.

[10] J. J. Mock, M. Barbic, D. R. Smith, D. A. Schultz, and S. Schultz, "Shape effects in plasmon resonance of individual colloidal silver nanoparticles," *J. Chem. Phys.*, vol. 116, no. 15, pp. 6755–6759, 2002.

[11] W. Cao, T. Huang, X.-H. N. Xu, and H. E. Elsayed-Ali, "Localized surface plasmon resonance of single silver nanoparticles studied by dark-field optical microscopy and spectroscopy.," *J. Appl. Phys.*, vol. 109, no. 3, p. 34310, 2011.

[12] C. Sonnichsen, Franzl ,T. Wilk , G. V. Plessen ,J. Feldmann , O. Wilson, and P. Mulvaney, "Drastic reduction of plasmon damping in gold nanorods," *Phys. Rev. Lett.*, vol. 88, no. 7, pp. 774021–774024, 2002.

[13] J. J. Mock, R. T. Hill, A. Degiron, S. Zauscher, A. Chilkoti, and D. R. Smith, "Distance-dependent plasmon resonant coupling between a gold nanoparticle and gold film," *Nano Lett.*, vol. 8, no. 8, pp. 2245–2252, 2008.

[14] J. B. Lassiter, J. Aizpurua, L. I. Hernandez, D. W. Brandl, I. Romero, S. Lal, J. H. Hafner, P. Nordlander, and N. J. Halas "Close encounters between two nanoshells," *Nano Lett.*, vol. 8, no. 4, pp. 1212–1218, 2008.

[15] M. Göppert-Mayer, "Uber Elementarakte mit zwei Quantensprüngen," *Ann. Phys.*, vol. 401, no. 3, pp. 273–294, 1931.

[16] N. Verellen, D. Denkova, B. D. Clercq, A. V. Silhanek, M. Ameloot, Po. V. Dorpe, and V. V.

Moshchalkov, “Two-photon luminescence of gold nanorods mediated by higher order plasmon modes,” *ACS Photonics*, vol. 2, no. 3, pp. 410–416, 2015.

[17] K. Imura, T. Nagahara, and H. Okamoto, “Near-Field Two-Photon-Induced Photoluminescence from Single Gold Nanorods and Imaging of Plasmon Modes,” *J. Phys. Chem. B*, vol. 109, no. 27, pp. 13214–13220, 2005.

[18] M. D. Wissert, K. S. Ilin, M. Siegel, U. Lemmer, and H. J. Eisler, “Coupled nanoantenna plasmon resonance spectra from two-photon laser excitation,” *Nano Lett.*, vol. 10, no. 10, pp. 4161–4165, 2010.

[19] S. Viarbitskaya, O. Demichel, B. Cluzel, and A. Bouhelier, “Delocalization of Nonlinear Optical Responses in Plasmonic Nanoantennas,” 2015.

[20] W. Kaiser and C. Garrett, “Two-Photon Excitation in CaF^2: Eu^{2+},” *Phys. Rev. Lett.*, vol. 7, no. 6, pp. 229–231, 1961.

[21] A. Drezet, A. Hohenau, D. Koller, A. Stepanov, H. Ditlbacher, B. Steinberger, F.R. Aussenegg, A. Leitner, and J.R. Krenn. “Leakage radiation microscopy of surface plasmon polaritons,” *Mater. Sci. Eng. B Solid-State Mater. Adv. Technol.*, vol. 149, no. 3, pp. 220–229, 2008.

[22] S. P. Frisbie, C. F. Chesnutt, M. E. Holtz, A. Krishnan, L. G. De Peralta, and A. A. Bernussi, “Image formation in wide-field microscopes based on leakage of surface plasmon-coupled fluorescence,” *IEEE Photonics J.*, vol. 1, no. 2, pp. 153–162, 2009.

[23] A. Hohenau, J. R. Krenn, A. Drezet, O. Mollet, S. Huant, C. Genet, B. Stein, T.W. Ebbesen “Surface plasmon leakage radiation microscopy at the diffraction limit,” *Opt. Exp.*, vol. 81, no. 25, pp. 1762–1764, 2002.

[24] A. Drezet, A. Hohenau, A. L. Stepanov, H. Ditlbacher, B. Steinberger, N. Galler, F. R. Aussenegg, A.Leitner, and J. R. Krenn “How to erase surface plasmon fringes,” *Appl. Phys. Lett.*, vol. 89, no. 9, 2006.

[25] B. Hecht, H. Bielefeldt, L. Novotny, Y. Inouye, and D. Pohl, “Local Excitation, Scattering, and Interference of Surface Plasmons,” *Phys. Rev. Lett.*, vol. 77, no. 9, pp. 1889–1892, 1996.

[26] H. Ditlbacher, J. R. Krenn, a. Hohenau, a. Leitner, and F. R. Aussenegg, “Efficiency of local light-plasmon coupling,” *Appl. Phys. Lett.*, vol. 83, no. 18, pp. 3665–3667, 20. N. Chichkov, and M. Skorobogatiy “Photonic bandgap plasmonic waveguides,” *Opt. Lett.*, vol. 36, no. 13, p. 2468, 2011.

[28] C. Reinhardt, A. B. Evlyukhin, W. Cheng, T. Birr, A. Markov, B. Ung, M.Skorobogatiy, and B. N. Chichkov “Bandgap-confined large-mode waveguides for surface plasmon-polaritons,” *J. Opt. Soc. Am. B*, vol. 30, no. 11, p. 2898, 2013.

[29] J. Grandidier, S. Massenot, G. Colas des Francs, A. Bouhelier, J.-C. Weeber, L. Markey, A. Dereux, J. Renger, M. U. González, and R. Quidant, “Dielectric-loaded surface plasmon polariton waveguides: Figures of merit and mode characterization by image and Fourier plane leakage microscopy,” *Phys. Rev. B - Condens. Matter Mater. Phys.*, vol. 78, no. 24, 2008.

[30] S. Massenot, J. Grandidier, A. Bouhelier, G. Colas des Francs, L. Markey, J.-C. Weeber, and A. Dereux “Polymer-metal waveguides characterization by Fourier plane leakage radiation microscopy,” *Appl. Phys. Lett.*, vol. 91, no. 24, 2007.

[31] C. Reinhardt, S. Passinger, B. N. Chichkov, C. Marquart, I. P. Radko, and S. I. Bozhevolnyi, “Laser-fabricated dielectric optical components for surface plasmon polaritons.,” *Opt. Lett.*, vol. 31, no. 9, pp. 1307–1309, 2006.

[32] C. Reinhardt, R. Kiyan, S. Passinger, A. L. Stepanov, A. Ostendorf, and B. N. Chichkov, "Rapid laser prototyping of plasmonic components," *Appl. Phys. A Mater. Sci. Process.*, vol. 89, no. 2, pp. 321–325, 2007.

[33] E. M. Purcell and C. R. Pennypacker, "Scattering and Absorption of Light by Nonspherical Dielectric Grains," *Astrophys. J.*, vol. 186, p. 705, 1973.

[34] M. Testorf, "Perturbation theory as a unified approach to describe diffractive optical elements," *J. Opt. Soc. Am. A*, vol. 16, no. 5, pp. 1115–1123, 1999.

[35] J. Seidel, F. I. Baida, L. Bischoff, B. Guizal, S. Grafström, D. V. Labeke, and L. M. Eng, "Coupling between surface plasmon modes on metal films," *Phys. Rev. B*, vol. 69, no. 12, p. 121405, 2004.

[36] E. N. Economou, *Green's Functions in Quantum Physics*, vol. 7. 2006.

[37] O. J. F. Martin, C. Girard, and A. Dereux, "Generalized field propagator for electromagnetic scattering and light confinement," *Phys. Rev. Lett.*, vol. 74, no. 4, pp. 526–529, 1995.

[38] D. Barchiesi, C. Girard, O. J. F. Martin, Daniel Van Labeke, and D. Courjon, "Computing the optical near-field distributions around complex subwavelength surface structures: A comparative study of different methods," *Phys. Rev. E*, vol. 54, no. 4, pp. 4285–4292, 1996.

[39] O. J. F. Martin, A. Dereux, and C. Girard, "Iterative scheme for computing exactly the total field propagating in dielectric structures of arbitrary shape," *J. Opt. Soc. Am. A*, vol. 11, no. 3, p. 1073, 1994.

[40] P. Török, P. Varga, Z. Laczik, and G. R. Booker, "Electromagnetic diffraction of light focused through a planar interface between materials of mismatched refractive indices: an integral representation," *J. Opt. Soc. Am. A*, vol. 12, no. 2, p. 325, 1995.

[41] J.-C. Weeber, A. Dereux, C. Girard, J. R. Krenn, and J.-P. Goudonnet, "Plasmon polaritons of metallic nanowires for controlling submicron propagation of light," *Phys. Rev. B*, vol. 60, no. 12, pp. 9061–9068, 1999.

[42] A. Arbouet, A. Mlayah, C. Girard, and G. C. Des Francs, "Electron energy losses and cathodoluminescence from complex plasmonic nanostructures: Spectra, maps and radiation patterns from a generalized field propagator," *New J. Phys.*, vol. 16, 2014.

Chapter IV

Spectral engineering of two – dimensional plasmonic nanoprisms

4.1 Introduction

Two dimensional (2D) plasmonic nanoparticles of micrometric size hold great potential for the plasmonic device and information processing applications. These highly crystalline cavities sustain higher order longitudinal plasmonic modes and a transverse mode in the visible and near infra-red region [1]. These planar resonances arise from multiple interferences between degenerated high-order SP modes and yield optical near-fields that are strongly localized at specific hot spots along the apex, edges and at the centre of the structures. As a consequence, the high order resonances observed in these 2D systems combine the advantages of localized and delocalized resonances, namely field localization and 2D propagation. These higher order resonances, which depend upon the constituting material and the boundary conditions, can be modified and engineered for different device related applications. The design of device based on these multimodal plasmonic cavities as elementary building blocks requires efficient strategies to understand, control and manipulate the spatial and spectral features of SP modes. The spatial distributions of these modes sustained by 2D plasmonic cavities have been experimentally mapped in a great detail by Viarbitskaya et. al using confocal TPL to access the convoluted in plane SPLDOS [1] supported by the simulated SPLDOS map from our simulation tool based on Green Dyadic method. This work reports in detail about the evolution of TPL maps as the morphology of the gold nanostructure is varied from triangular to hexagonal. Furthermore, this study also reveals the dependence of the TPL maps on the size of the gold nanocavities. This study was followed by report of strategies to tailor the SP modal distribution in the individual gold nanoprisms by spatial coupling of the nanoprisms [2]. The modal engineering in these gold nanoprisms was then explored by Cuche et. al. by introducing a resonant defect in the nanoprism in form of a hole (it will be discussed later in this chapter) [3]. In this work, the effect of size and position of hole on the experimental TPL intensity maps with respect to the pristine prism has been reported. The author used GDM based simulation tool to understand spectral features of the SPLDOS in the pristine nanoprism and the also revealed the effect of the hole on the SPLDOS spectra. The theoretical study of spectral modal

engineering of the nanoprism has been carried forward experimentally and forms the core of this chapter. All the experimental studies in this chapter has been carried out on dark field microscopy and spectroscopy setup explained in chapter III. In first section, we describe in detail the spectral features of gold nanoprism on ITO coated silica substrate. This will be followed by study of spectral characteristics of gold nanoprism deposited on of 30nm thin gold film. This section will also demonstrate the effect of using different metallic substrates on the spectral response of the gold cavity. The last section deals with the demonstration of tuning of spectral response of gold nanoprisms by milling a nanometric sized hole following the aforementioned work of reference [3].

4.2 Au nanoprisms on ITO substrate

4.2.1 Spectral response of Au nanoprisms and Lorentzian decomposition

In this section, we have performed a comprehensive study of dark-field scattering spectra of individual crystalline triangular Au nanoprisms (Au NPs) of different sizes ranging from 400nm to 900nm placed on ITO coated silica substrates. These substrates are crossed-marked every 200μm using photolithography technique. A colloidal suspension of crystalline Au NPs is drop casted and dried onto glass substrate coated with 10nm ITO. These Au NPs are then subjected to 5min oxygen plasma to remove a 3nm thick PVP coating from the surfaces [4]. The sample is then taken inside SEM and sharp triangular prisms of different sizes, well separated from each other are identified and located. These labelled cross-markings with SEM make it easy to locate the prisms later on the substrate under the dark-field microscope. These nanoprisms are usually 20nm ± 3 in thickness and with lateral dimensions ranging from 300nm to 1.5μm. The single particle dark-field scattering spectroscopy was performed using our DF spectroscopy set up explained in "Materials and methods" chapter. The robustness of the experimental technique was assessed by repeating DF spectroscopy measurement over two gold cavities of similar sizes. Figure 4.1 display normalized DF spectra recorded over three gold cavities of same lateral size of 774nm. The SEM images of the three gold cavities are shown in the inset denoted by numbers from 1-3. The spectra corresponding to cavities 1 and 2 (in blue and red respectively) coincide almost perfectly over the entire wavelength range. The nice agreement between the spectral response of the two sharp cavities ensures that the repeatability of dark-field spectroscopy protocol. The scattering spectra of the third cavity (in black) has different spectral response in the higher wavelength region. This can be ascribed to the blunter apices of the cavity. This change in spectral response of the cavity with slight

truncations at the edges leads us to choose only sharp triangular cavities for the experimentation.

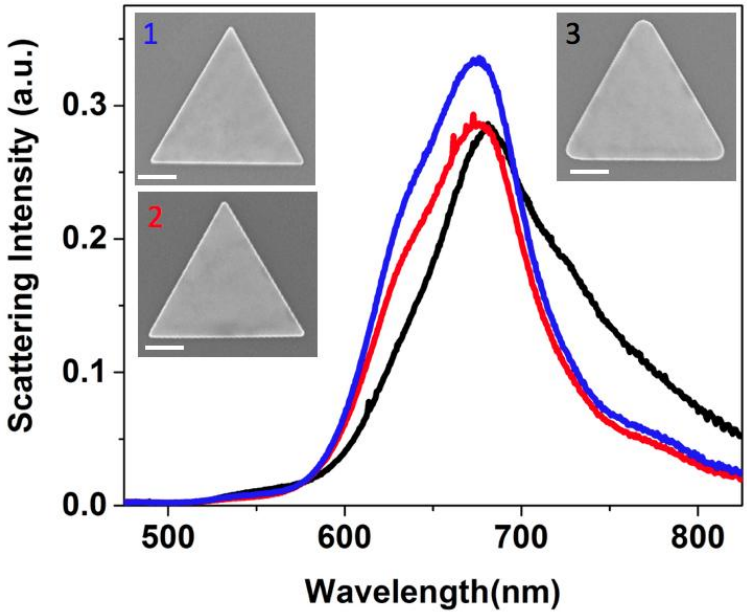


Figure 4.1 Normalized DF scattering spectra recorded over three different triangular gold prism of size 774nm. In the inset are the SEM images of the gold cavities on which the DF spectra have been recorded. The scale bar is 200nm for each case.

The normalized DF spectra for a triangular gold prism of lateral size 456nm deposited on ITO coated silica substrate is shown in figure 4.2. The corresponding SEM image is shown in the inset. The DF spectra reveals presence of at least two peaks. This indicates that the spectral response cannot be assimilated to a single resonance peak as is the case of small dipolar spherical particles at similar energies. Since SP resonances can be described as damped harmonic oscillators, Lorentzian function based fitting can be used to fit the experimental DF scattering spectra with multiple peaks associated to high order SP resonances in the gold cavity [5], [6]. The Lorentzian decomposition is done by an iterative fitting scheme where the fitting sequence is repeated till a minimal residual is obtained. The parameters involved in fitting are the peak position, number of peaks, the peak width and area. This vast parameter space can lead to multiple fitting solutions for a given experimental spectrum. These multiple fitting solutions are avoided by making certain assumptions on few parameters. The full width at half maximum (FWHM) for a resonance peak depends upon the damping of the SP oscillation, which, in turn, is determined by the internal and radiative losses of the system. Assuming that the radiative losses for all the higher order resonance peaks are equal, only the internal losses which is determined by the imaginary part, Im(ε) of the dielectric function ‘ε’ is left.

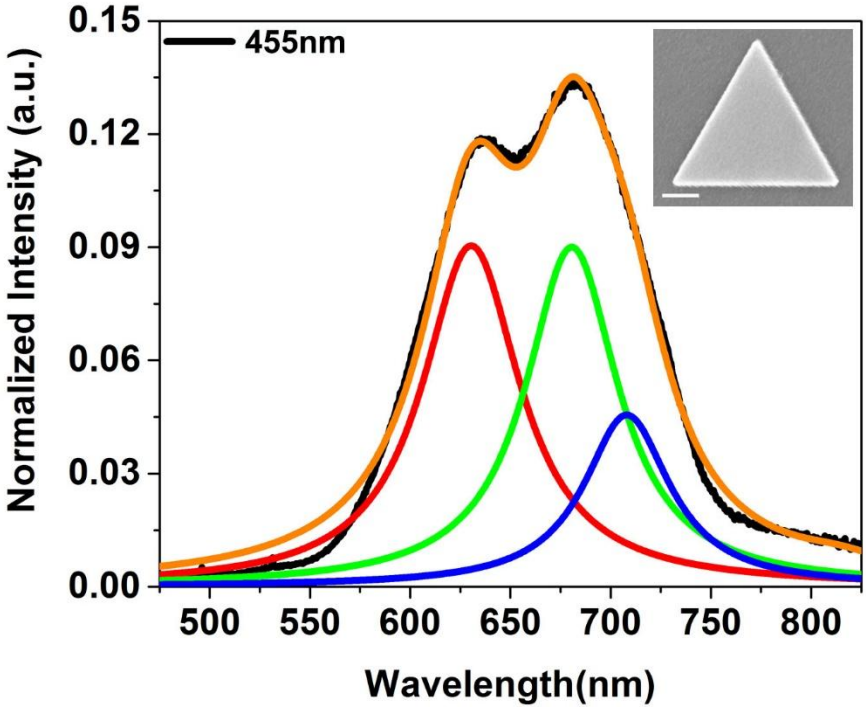


Figure 4.2 Dark field scattering spectrum of a 455nm sized triangular gold nanoprism (curve). The curves in red, green, and blue colours correspond to the Lorentzian decomposition. The orange curve is cumulative of the all the Lorentzian fitted peaks. Inset: SEM image of the sharp triangular gold nanoprism deposited on ITO coated glass substrate (thickness ~20nm). The scale bar in white is 100nm.

The imaginary part of the dielectric function describes all the parameters affecting the dephasing processes in metal nanoparticles like electron scattering into empty levels of conduction bands and electron - phonon coupling. In the near IR region, the dielectric function has mainly contribution from free electrons but at higher energy, the interband transitions should also be considered. In the case of gold, the interband transitions mainly takes place below 600nm. The variation of Im(ε) imposes that the FWHM (respectively the quality factor $Q=\lambda/\Delta\lambda$) of each peak of the fit decreases (increases) as the wavelength increases. Another constraint imposed on the fitting is the number of fitting Lorentzian curves *N*. We found out that the experimental spectra can be fitted with typically 3 to 5 Lorentzian peaks by increasing or decreasing the FWHM of each peaks respectively. To decide the number of Lorentzian peaks to be used for the fitting, we systematically compared the experimental scattering spectra with the simulated planar SPLDOS spectra computed with Green Dyadic method based numerical tool developed at CEMES by C. Girard (explained in Materials and methods). The planar SPLDOS gives us all the available planar states in the cavity at a given position and energy, independently of the incident illumination. The SPLDOS spectra were calculated at apex and centre of the edge of the triangular nanoprism in the same spectral window of 475nm to 825nm

at 24 different wavelengths. The number of peaks in the simulated SPLDOS spectra helps us to choose the parameter *N* for the fitting. Once the value of *N* is fixed, we start the fitting by selecting *N* numbers of peak positions λ_N on the experimental curve. The initial selection of λ_N is done by noticing peaks and shoulders on the spectra. The fit is then allowed to evolve freely without any constraint. The lower offset in fitted curves are then fixed to zero. We then run the iterative fitting scheme by imposing constraints to area of different curves till the minimal residual is achieved. Once the minimal residual is achieved, the area parameter is also set free before final fitting of the Lorentzian is done. An example of the Lorentzian fitted curves on the experimental scattering spectra recorded on 455nm triangular gold prism have been shown in the figure 4.2 in three colours (red, green and blue). The orange curve shows the cumulated sum of these three fitted peaks. The nice agreement between the experimental scattering spectrum and the cumulated sum of the Lorentzian peaks shows that our Lorentzian fitting approach based on different constraints discussed above is satisfactory. The multiple resonance peaks supported by these plasmonic cavities can be tuned and engineered by various techniques. One of the simplest way is to vary with the size of the gold cavity which we will study in the next subsection.

4.2.2 Variation of spectral features with size of the cavity

To study the effect of the cavity size on the spectral response, we recorded DF spectra on 16 gold Au NPs of sizes ranging from 400nm to 900nm. Figures 4.3(a, b, e, f) present the DF spectra of four such Au NPs of different sizes – 430nm, 565nm, 650nm and 710 nm respectively, with their corresponding Lorentzian fitted peaks. The selection of four spectra out of sixteen have been done in such a way that we can maintain a noticeable difference between the size of the cavities (~50 to 100nm). At first sight, the experimental scattering response of these four gold cavities appears to be similar and falling roughly in the same spectral window, with only slight modulations of the broad curves as a function of the wavelength. However, the deconvolution of the scattering spectra suggests a different picture in which the peaks resulting from Lorentzian decomposition for different gold cavities have different peak wavelength, area and FWHM. Also, a weak contribution of the transverse mode is observed in the experimental DF spectra. The transverse mode contribution is shown in the inset of figure 4.3(a) by magnifying it 20 times. The simulated near-field spectra corresponding to experimental spectra in the figure 4.3(a, b, e, f) are shown in figure 4.3(c, d, g, h) respectively. For each gold structure, the mesh for the simulation is designed to match the experimental geometry as

closely as possible. The point of computation has been chosen in accordance with knowledge of existence of nodes and antinodes at the apex and along the edges of the cavities because of presence of higher order resonances [1], [2]. The planar SPLDOS spectra are calculated at one apex and at the centre of the edge of the triangular cavity. The triangular structure in the figure 4.3 (c) denotes the positions of calculation of the SPLDOS spectra. The calculation of the in-plane SPLDOS provides the complete in-plane spectral plasmonic landscape of the gold cavities without leaving behind contribution due to any particular resonances. The global shape of the SP-LDOS spectra matches the broad DF experimental spectra in this spectral window. The simulated near field SP-LDOS spectra, however, shows several peaks.

In addition, like in the case of the experimental scattering spectra, the global SPLDOS spectra also stays more or less in the same spectral window. Furthermore, for a given size of the gold NP, the fitting reveals that the position of each Lorentzian peaks stays consistent with respect to the plasmonic resonances peaks obtained from simulation. To show this, black dashed lines have been drawn and aligned with the SPLDOS peaks. We can see overall a very nice agreement between experimental scattering fitted peaks and simulated SPLDOS peaks. However, a quantitative comparison of the SPLDOS spectra obtained from simulation with the experimental DF scattering spectra would not be fair, since the former provides a local and near-field information in the metal, without accounting for the far-field coupling and propagation, while the latter is a global measurement of the scattered signal in the far-field. But nevertheless, the qualitative comparison suggest that several planar high order SP resonances are contributing to the forward scattered light by these gold cavities.

To get further insight, we computed the spatial distribution maps corresponding to each peak in the simulated SPLDOS spectra. The calculated maps reveal the order of each resonance. This helped us in the comparison between deconvoluted peaks and the SPLDOS spectra beyond a simple assignment based on maximal wavelength. The inset of Figure 4.3(c, d, g, h) shows us that, each single peak in the spectra originates from a different resonance order with singular SPLDOS spatial distribution characterized by an increasing number of antinodes and/or an increasing number of maxima at the centre as the energy increases. With the help of these SPLDOS spatial distribution maps, we can follow the resonances from cavity of one size to another. For example, the modes denoted by number ‘1-3’ in figure 4.3(c) redshift but stay in figure 4.3(d) (see mode number 2-4). While the mode number ‘4’ in figure 4.3(c) red shift out of the spectral window in figure 4.3(d). At the same time a new mode appears in figure 4.3(d) denoted by number ‘1’. The same trend can be seen in the next set of SPLDOS spectra in figure 4.3 (g, h) as the size increases.

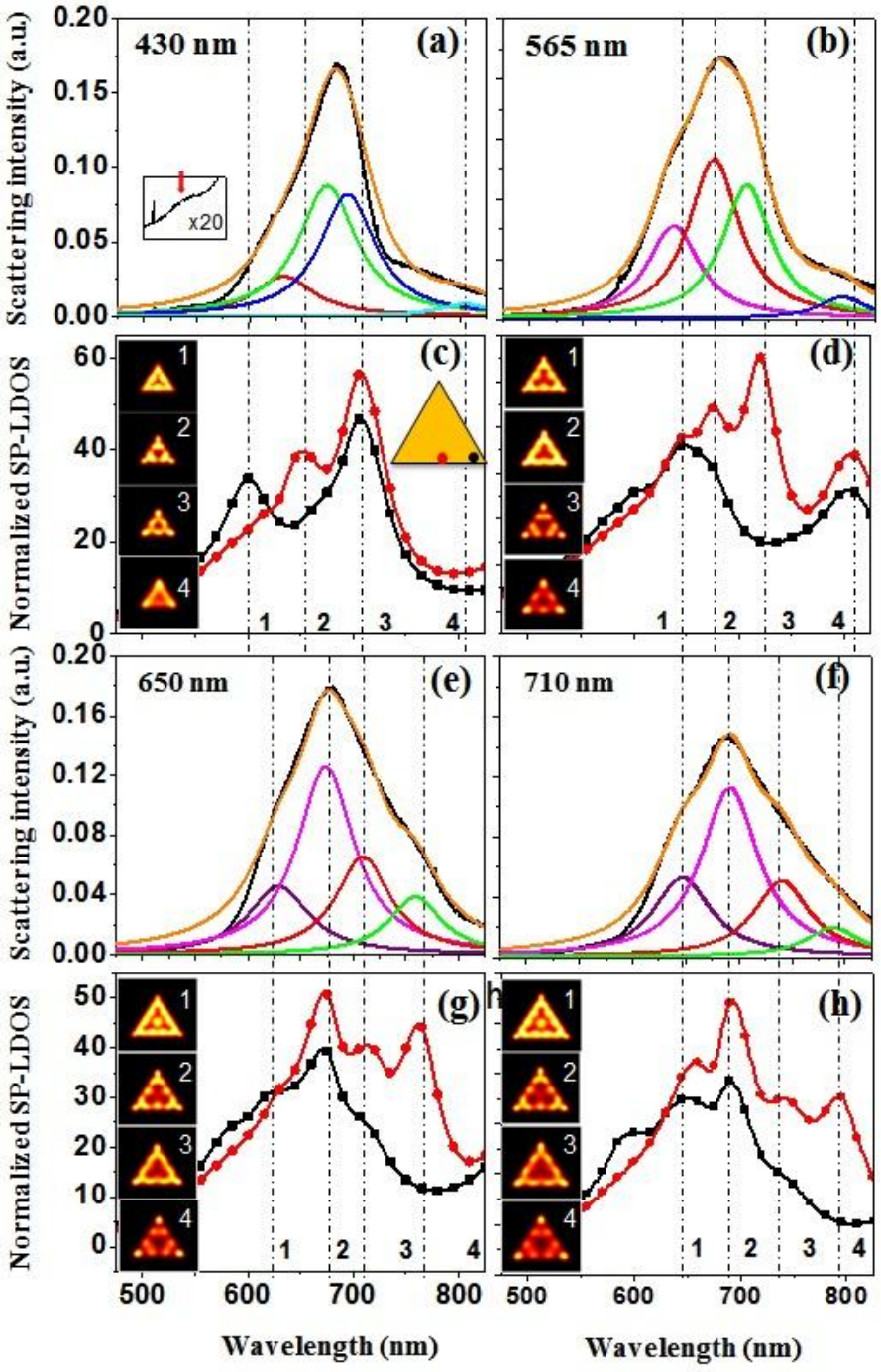


Figure 4.3: (a, b, e, f) Experimental dark-field scattering spectra (black curves) from crystalline gold triangular cavities of size (a) 430 nm (the contribution of the transverse mode is shown in inset), (b) 565 nm, (e) 650 nm and (f) 710 nm respectively. The spectra are fitted with Lorentzian peaks (coloured peaks). The orange curves are the sum of the individual Lorentzian peaks. Corresponding near-field SPLDOS spectra calculated at one apex (in black) and middle of the edge (in red) of the nanoprisms are shown in (c, d, g, h). These positions are illustrated by two red and black dots on the schematic cavity in the inset in (c).

From this trend, we can easily draw a clear redshift of these high order planar SP resonances as the cavity size increases. Also, we can notice that for a given energy, roughly for

each 100nm increase in the edge length there is a new SP resonance appearing in the cavity. This consistent matching between fitted and simulated peaks leads us to link Lorentzian peaks of cavity of one size to those present in another, and a color code is used to denote different orders of the resonances. If we follow this color code in figure 4.3, we can easily see that all the experimental resonance peaks are red shifting as the cavity size increases.

Also, new resonances emerge in the high energy part of the spectrum as the size of the cavity increases, for, roughly 100nm. For example, in figure 4.3(a), there are four Lorentzian peaks shown in red, green, blue and cyan. As the size difference between cavity in figure 4.3(a) and 4.3(b) is more than 100nm, the Lorentzian peak in cyan shifted out of the spectral window while there is a new Lorentzian peak emerging in pink. Similarly, when we move to next cavity in figure 4.3(e) where the size difference is around 100nm and the blue peak is red shifted out of the spectral window and we have emergence of new peak in violet. But when we move to the next cavity in figure 4.3(f), the size difference is around 60nm. Thus the same set of four resonances are observed with a significant red shift.

Applying the same colour assignment to the full set of fitted curves of 16 cavities, we draw a high order SP resonance dispersion curves (figure 4.4a). The red shift in the SP resonance peaks with increase in cavity size for all the 16 cavities can be reasserted from the dispersion curve. Similarly, for the simulated SPLDOS, we have prepared a dispersion based on the the SP mode peaks for different cavities (figure 4.4b). We observe that the SP resonances follow a similar trend for both the fitted and computed spectra. This is partially due to our initial fitting assumption in which the number of peaks for each cavity was set based on the SPDLOS spectra. But the position peak was allowed to evolve freely during the decomposition process. The spatial distribution of all the modes supported by these gold cavities in the spectral range of 475nm to 825nm is displayed in figure 4.4(c). The spatial distribution calculated here are in excellent agreement with the modes commonly described as edge and breathing eigenmodes in similar metallic geometries [7]. The edge modes are the modes confined at the periphery of flat 2D flat nanoparticles while breathing modes are confined inside the 2D nanoparticles. The colours in the circle relates the spatial distribution maps with different SP modes in figure 4.4 (a, b). The quality factor of these SP resonance is plotted in form of figure of merit in figure 4.4 (d). The quality factor for SP resonance curves falls between 7 to 15. This range of values is consistent with the values reported in literatures for plasmonic systems [5]. The QF versus peak position curves for different cavities intersect each other. This suggests that out far-field analysis does not reveal a global trend between QF and size of the cavity for such a complex system. The higher order planar resonances seem to have an almost equal

radiative damping as the QF is more or less the same. This Lorentzian decomposition of the experimental scattering spectra with the help of the simulated SPLDOS maps make possible a thorough description of the SP resonances along with their radiative nature in these thin gold cavities with prismatic boundary conditions.

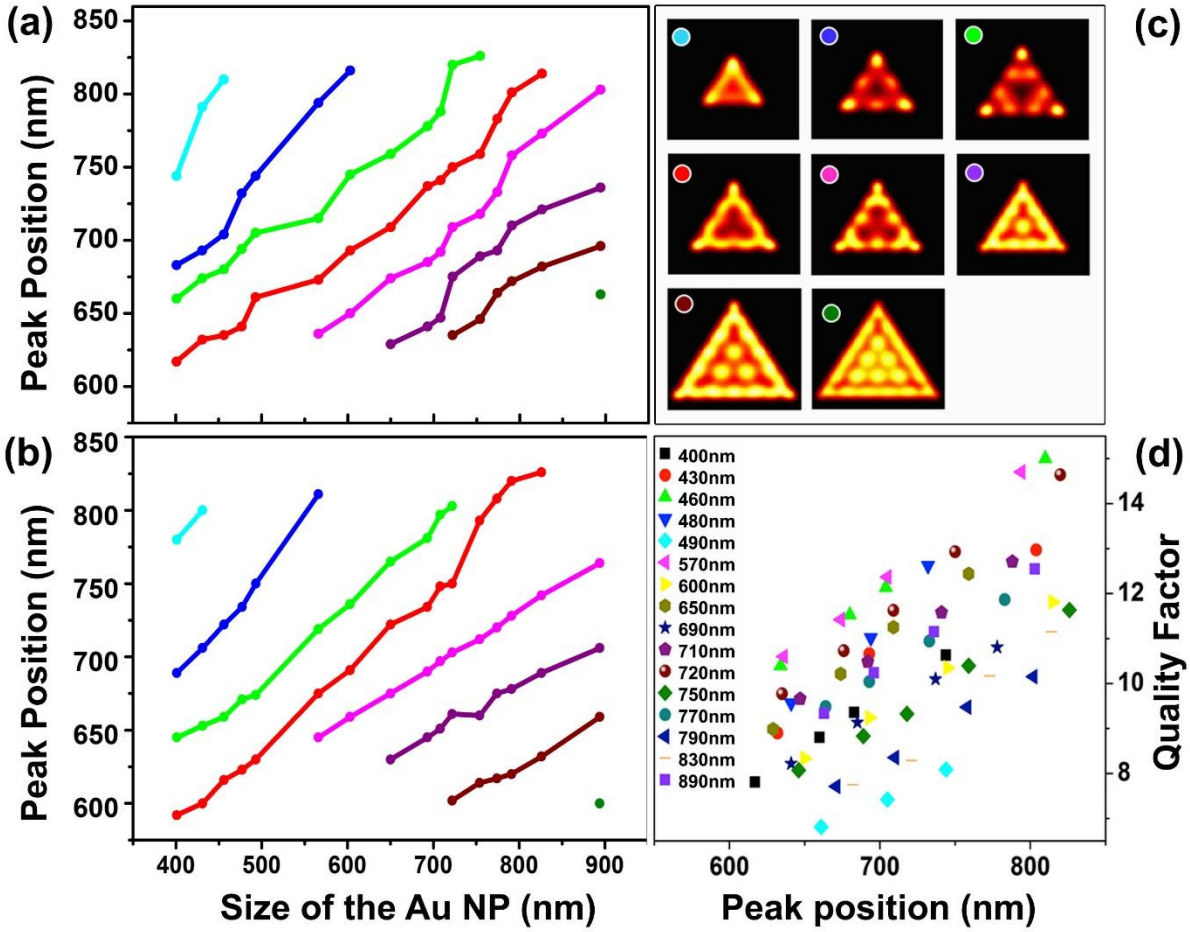


Figure 4.4 (a, b) High order SP resonance dispersion curves. The spectral position of the (a) fitted and (b) computed resonances are plotted as a function of the cavity edge size. A similar colour code has been used in figure 4.2 and 4.3. (c) SPLDOS maps corresponding to the resonances with same colour code in the circles. (d) Figure of merit - quality factors of different SP resonances for cavities of different sizes plotted against peak position of the resonances.

4.3 Spectral control of SP resonances in a MIM configuration

4.3.1 Spectral response of Au nanoprisms on 30nm thin Au film

The spectral response of these gold triangular prisms can be tuned by various techniques. One particularly common technique which has been used in numerous occasions in past is the introduction of a metallic thin film below the metallic cavities mainly in a metal-

insulator-metal (MIM) geometry [8]–[12]. This MIM system results into new longitudinal and transverse plasmonic modes. Numerous studies in past years have been centred around tuning the SP resonance wavelength of a simple dipolar structure by means of varying coupling strength of the MIM geometry. This is done by changing the distance between the metallic cavity and the metal thin film [11], [13]–[15]. In our case, the MIM geometry offers, therefore, a new degree of freedom to tailor the modal plasmonic characteristics and therefore the scattering properties of the system. To realize this geometry in our case, we deposited a 30nm thick gold film on ITO coated silica substrate by electron beam physical vapour deposition method. The thickness of the thin gold film is set in such a way that we can have some transmittance through to film in order to work in diascopic illumination configuration. The 30nm thickness allows around 8% signal to transmit through the film. The same gold NPs discussed in the previous section are then dropcasted onto the 30nm thick gold film. The cavities and the thin film are separated by thin spacing layer of 3nm which is formed by the native PVP polymer found on the AuNP basal facet. This residue could not be removed from the underneath surface in contact with the substrate during the plasma cleaning process [4].

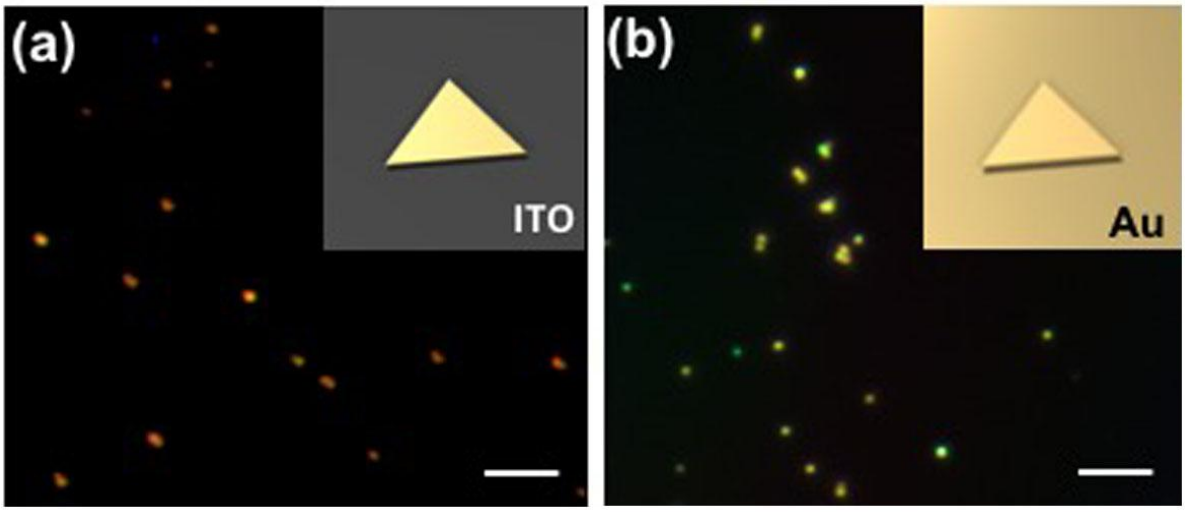


Figure 4.5: (a) and (b) show dark field images of Au cavities on ITO-covered glass and Au thin film respectively. The colored dark field images have been acquired with XPLORA multifunction spectrometer in reflection configuration. Artistic views of the two systems are shown in insets. Scale bars are 5 µm.

Figure 4.5 shows two dark field images of such cavities of different sizes deposited on ITO coated silica substrate and 30nm gold thin film respectively. The DF image on the ITO-covered glass substrate (figure 4(a)) exhibits a scattering of the gold cavities mostly in the orange-red part of the visible region while in the case of gold cavities on the Au thin film, the

scattering signal seems to be shifted in the yellow and green parts of the spectrum. This suggests a clear blue shift in the scattering signal collected from cavities on thin film with respect to ones on ITO substrate. To quantify this shift, we recorded DF spectra of prismatic cavities deposition on the thin film.

Figures 4.6 (a-c) show DF spectra recorded on gold cavities of three different sizes 455nm, 650nm and 720nm respectively deposited on ITO substrates and figure 4.6 (d-f) show DF spectra of gold cavities of similar sizes deposited on gold thin film. Interestingly, the variation of DF scattering intensity as a function of the size of the cavity is similar for cavities on gold to that on ITO substrate. The overall spectrum for a cavity of given size undergoes blue shift of about 50nm - 75nm in all three cases. This reveals the strong effect of the presence of metallic thin film on the optical response of the cavity and also the potential of the MIM system for the control of spectral response of the system.

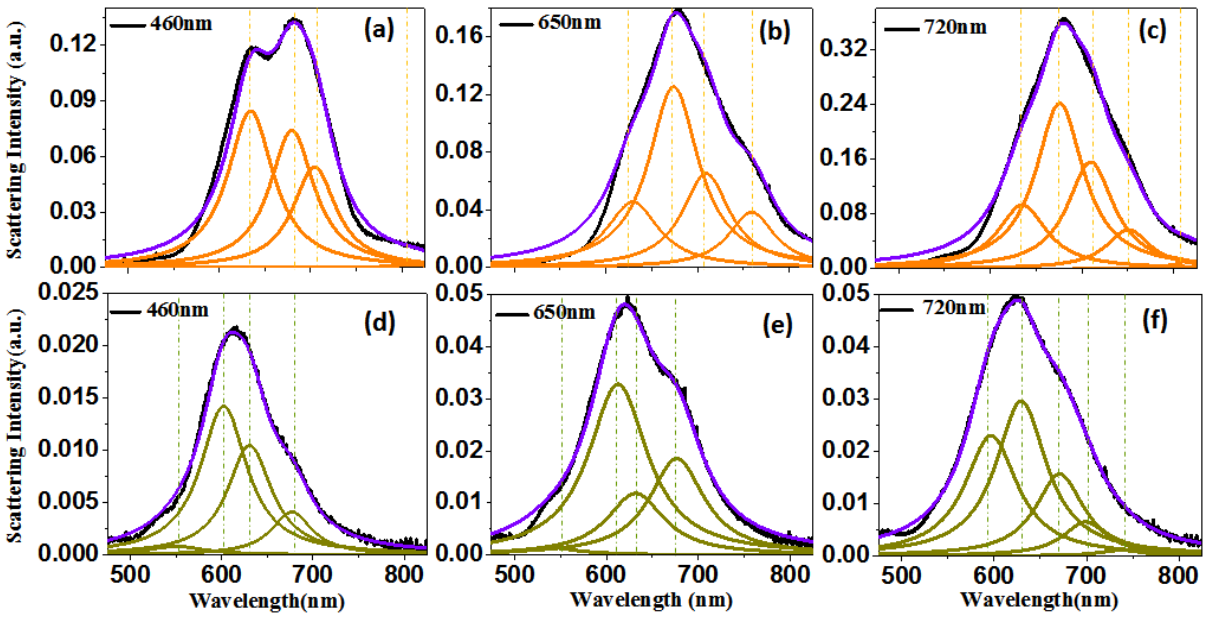


Figure 4.6 DF spectra (black curves) of Au cavities on an ITO-covered glass substrate with lateral sizes of (a) 460nm, (b) 650nm and (c) 720nm fitted by Lorentzian peaks (orange curves). The total fit (sum of the Lorentzian peaks) is displayed as a purple curve. (d)-(f) Similar as (b)-(c) for Au cavities on a 30 nm thick Au film.

For better understanding of the blue shift and the broadening or narrowing of the SP resonance peaks, the decomposition of the broad DF spectrum is performed. We have followed our previous Lorentzian fitting procedures for DF spectra of MIM systems without setting the initial peak position λ_N. A qualitative comparison of the fitted spectra is shown in Figure 4.6(d-f). The number of fitted resonances for a given size of the Au NP for both glass supported and Au supported NP was assumed to be same (4 in (a,d), 4 in (b,e), and 5 in (c, f)). This indicates

that the same set of resonance occurs for the spectra provided we consider a global blue shift of the entire scattering spectra.

The origin of the blue shift can be associated with several mechanisms. One of them is based on the static injection of charges in the resonant system (figure 4.7a). In that case, the shift is proportional to the carrier density in the metal as depicted in reference [17]. A possibility of charging of the cavity owing to the slight different between the work function of the crystalline gold cavity and the amorphous gold of the film is also possible. However, in our case, the distance between the cavity and the film is at least 3nm owing to the PVP coating, which reduce the chances of the charge transfer by tunnelling. Thus this behaviour is not compatible with the static charge injection picture.

We believe that the blue shift originates from an electromagnetic coupling between the film and the cavity. Plasmon hybridization model has also been invoked to understand the optical response of nanoparticles near metallic surfaces [18] (figure 4.7b). The plasmon hybridization mechanism is based on the hybridization between SP modes of the particle and delocalized SPP resonance of the substrate. The effect of hybridization is red or blue shift depending upon the relative energies of the SP modes of the particle and SPP resonance of the thin film [18]. In our case, indeed there is coupling but the interaction is probably not so strong.

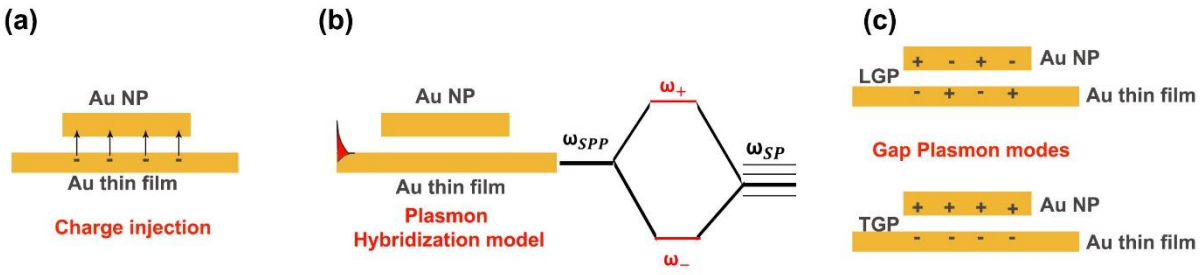


Figure 4.7 Schemes showing (a) charge injection from Au thin film to Au NP, (b) plasmon hybridization in metal-insulator-metal configuration and (c) presence of longitudinal gap mode (upper panel) and transverse gap mode (lower panel)

Apart from the longitudinal and transverse plasmon modes corresponding to the cavity there is also a possibility of presence of transverse gap modes (TGP) and longitudinal gap modes (LGP) along the film surface which is confined by the impedance mismatching at the boundaries of the cavity (figure 4.7c). The TGP modes for the flat surfaces are strongly coupled within the gap and very weakly radiative for a small sphere – thin film system [19]. The TGPs are essentially dark modes and thus have negligible effect on the far-field optical response of the small sphere – thin film system. The LGP modes, however, can be strongly radiative and

contribute to the optical response of the nanoparticles in far field . It depends upon gap size and the dimensions of the nanoparticle. These modes have not been taken into consideration for understanding the physical origin of the fitted peaks. We, at the moment, have no clue on the presence and eventually on the radiative nature of these transverse and longitudinal gap modes.

4.3.2 Tuning of spectral responses of Au prism with different metallic substrates

From figure 4.6 we can easily witness the potential of the MIM configuration to shift the higher order resonances supported by these gold cavities. Many studies have been mainly focused on varying the distance between nanoparticles and conductive film to tune the coupling strength of the electromagnetic field surrounding the nanoparticles and the conductive film which in turn tune the SP resonance wavelength [13]–[15]. In our case, we have kept the distance between gold cavity and the thin film constant. Instead, we have placed the resonators in the vicinity of films of different metals. In particular, we explored the influence of the dielectric constant of the metal on the cavity spectra. We prepared two substrates by coating 30nm aluminum and 30nm platinum film by electron beam vapour deposition method. Similar gold cavities were then dropcasted on these two substrates. Figure 4.8 (a-c) show the comparison between DF spectra of gold cavities of three different lateral sizes 460nm, 600nm and 725nm respectively on three different substrates – Al (blue), Au (black) and Pt (red). Here, all the metals have different transmittance (~4%, 8% and 2.5% for Al, Au and Pt respectively) which led us to use different acquisition time and lamp powers during the acquisition resulting in scattering curve with different intensities. In order to compare the spectra from gold cavities on three different metallic substrates, the scattering curves have been normalized with respective lamp spectrum and then normalized by their maximum value. The plots show as the metal film goes from platinum to gold to aluminum a consistent blue shift of the global scattering response of the MIM system for gold cavities. A similar blue shift has also been reported by Lassiter et. al. from simulated scattering spectrum computed on silver nanocubes when going from gold to silver thin film substrate [20]. The reason behind choosing aluminum and platinum for the experiment is the fact that plasmon frequency is directly proportional to the real part of the dielectric function of the metal. The real part of dielectric function of gold falls between that of the two given metals ($i.e.\ Re(\varepsilon_{Al}) > Re(\varepsilon_{Au}) > R(\varepsilon_{Pt})$ in the 1.5 eV to 3 eV energy range). Therefore, the global scattering spectra, which results from the film-particle coupling, follows the trend of the real part of the dielectric functions (aluminum - gold - platinum) of the metallic film independently of cavity size in the spectral window ranging from

450nm to 850nm. It therefore makes possible an on-demand spectral tuning of the high order planar resonance at work in these cavities.

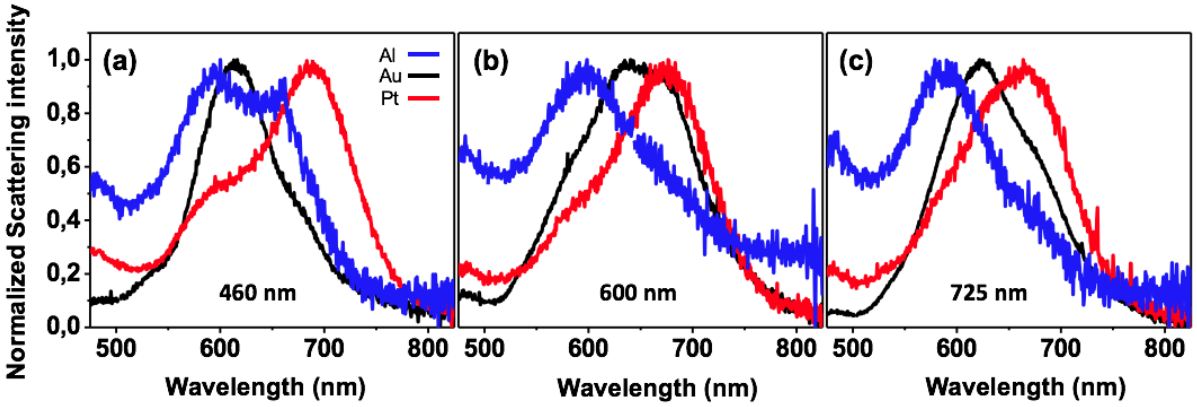


Figure 4.8: Normalized DF scattering spectra of gold nanoprism of sizes (a) 460 nm, (b) 600 nm and (c) 720 nm on three different thin metallic substrates – aluminium (blue), gold (black) and platinum (red). The thickness of each of the film is 30nm. The dark field spectra have been normalized by maximum value to make them comparable.

4.4 Spectral response of Au nanoprism in presence of hole

Another way to engineer the spectral response of the gold cavities is by introducing defect in the system in form of a hole. We have used FIB to mill hole of desired size and at desired position inside the gold cavity. The two important degrees of freedom to tune the spectral response by introducing hole defect in the gold cavities are size of the hole and position of the hole. Cuche et. al. observed that if the position of the hole is near apex or on the edge of the cavity there is more change in the spatial SPLDOS distribution compared to the hole in the centre of the cavity [3]. This was spectrally confirmed by simulation based on GDM. Figure 4.9 shows the results obtained from simulation. Figure 4.9(a) shows the SPLDOS spectra of a pristine prism calculated at one of the apex (indicated by black dot). There are 4 modes present in a spectral window ranging from 600nm to 1000nm. The SPLDOS spectra computed on triangular gold cavity of similar size with a hole in the centre of the cavity also contains four modes in the defined spectral window (figure 4.9b). The change in SPLDOS is shown in form of green bar. However, when the hole is moved to the edge, one three modes are present (figure 4.9c). One mode at 750nm is completely supressed. DF spectra are thus recorded on milled structures to investigate the tuning of the optical response of the triangular gold cavity by introduction of a hole.

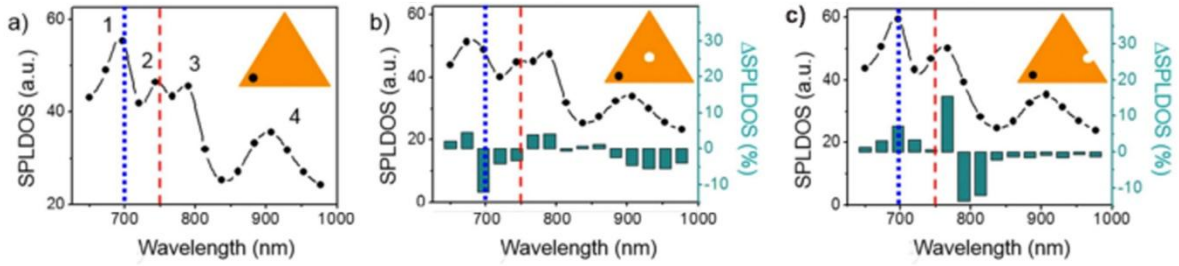


Figure 4.9 (a) Total SP-LDOS spectrum simulated for a 700 nm long reference gold prism without defect. (b,c) Total SP-LDOS spectrum simulated in the location indicated by the black dot in inset for the same reference gold prism with a defect. Spectral Δ SP-LDOS with respect to reference in (a) are plotted as histograms. Geometries and hole positions are displayed in insets (Reprinted with permission from [3]).

Figure 4.10(a) shows the experimental scattering spectra recorded over a pristine gold cavity of lateral size 600nm. The global spectral response of the pristine gold cavity is centred around 700nm with a broad curve extended till the end of the spectral window. On comparing it with the spectral response from gold cavity of same size in figure 4.10(b) which is milled at one of the edge (as shown in inset of the figure), we observe strong modification in the spectral response. The diameter of the hole milled is 110nm. The scattering spectra which was previously centred around 700nm is now at 660nm with a much narrower global response. The intensity of the scattering spectra has also gone down significantly. The corresponding SPLDOS spectra has been shown in figure 4.10 (d) and (e) for pristine and milled cavities respectively. The point of computation of the spectra has been shown in the inset of the figure 4.10 (a). The SPLDOS spectra for pristine prism support atleast three higher order SP mode in the spectral window ranging from 600nm to 750nm. This has been reduced to only two SP modes in the case of the milled structures which suggests that we have not only induced modification in two SP modes but also cut off one SP mode. Also, the overall envelope is blue shifted. It is important to note here that the SPLDOS intensity for apertured prism has increased. The DF of single holes of different diameters milled on gold thin film is shown in figure 4.10(g) [21]. It is clear from the spectra that resonance of the holes broadens and red shifts on increasing the size of the hole. Next, we increased the size of the hole to 150nm while keeping the position of the hole on the edge. The scattering spectra recorded over this gold cavity has been displayed in figure 4.10 (c). A shift of the global response towards blue part of the spectrum has been observed.

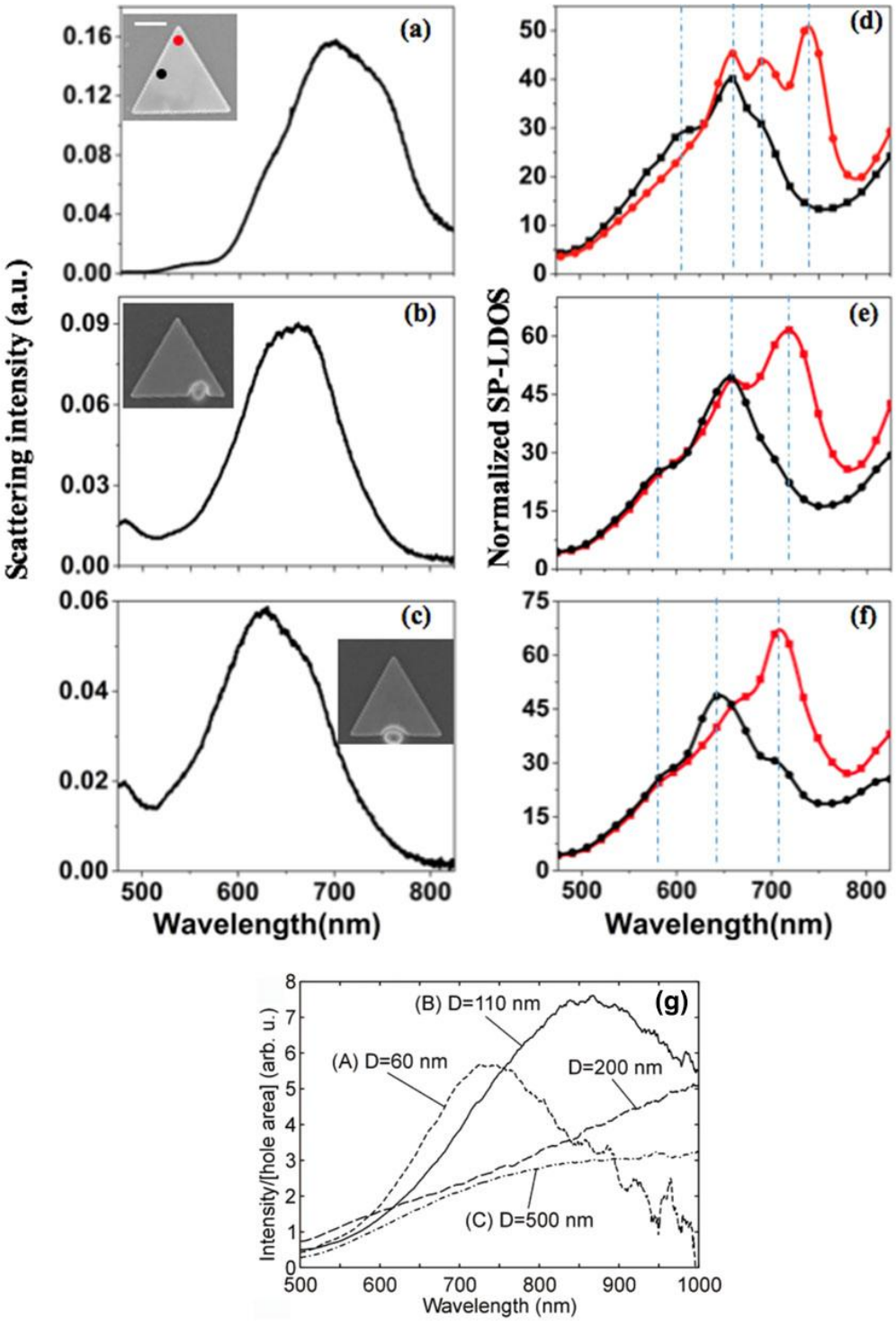


Figure 4.10 Experimental DF spectra of (a) pristine gold prism of size 600nm, (b) gold prism of same lateral dimension milled (diameter 110nm) on the edge, (c) gold nanoprism of same lateral dimension milled (diameter 150nm) on the edge. In the inset of figure (a), (b) and (c), we have corresponding SEM images with same scale bar of 200nm. Simulated SPLDOS spectra calculated at apex and edge corresponding to gold prism in (a,b,c) have been shown in (d),(e) and (f) respectively. The positions of computation of SPLDOS spectra have been denoted by red and black points in the inset of the (a). (g) DF spectra of single holes of different sizes (Reprinted with permission from [21])

This shift can also be noticed in the corresponding SPLDOS spectra shown in figure 4.10(f). This shift has been marked by blue dashed line in the SPLDOS spectra. There is also a noticeable further dip in the intensity of the experimental spectra in figure 4.11 (d) with respect to the previous spectra whereas the SPLDOS spectra intensity continues to rise. However, it will not be wise to quantitatively compare the near field SPLDOS spectra with the far – field scattering spectra of the gold cavity. We can fairly conclude that the experimental scattering spectra and simulated DF spectra show qualitatively the same trend upon engineering the gold cavity with a defect in the form of hole. Although, we lack a proper understanding of the mechanism propelling the modification of spectral response of the cavity, the study presents a strong basis for further continuation of a systematic study of these milled gold cavities for controlling spectral behaviour of such 2D cavities.

4.5 Conclusions

In conclusion, the spectral of crystalline gold cavities of sizes ranging from 400 to 900 nm have been investigated by dark field scattering spectroscopy. The global dark-field spectra were decomposed by multiple peaks Lorentzian fitting and compared to near-field SPLDOS spectra computed by GDM based numerical tool. These simulations along with the experimental results revealed that each planar mode obtained from the simulation can be associated to one Lorentzian fitted peak in the experimental spectra. The SP resonance peaks for each planar mode in these complex cavities have been found to be red shifted as we increase the size of the cavity. This have been found to be true for gold substrate too, defining the full plasmonic landscape for planar resonances in this system in the visible. Furthermore, the position of the Lorentzian fitted SP resonance peaks have been found to be highly dependent on the dielectric function of the substrate. Thus, by changing the nature of the metallic film in a MIM geometry, we demonstrated that a red- or blue-shift of the global resonance can be obtained. This strategy, based on a MIM geometry, allows for an efficient modal engineering in these cavities. Another strategy to tune the spectral response of the system based on introduction of a local defect in form of sub-wavelength hole has been studied. We noted that the position of the hole plays a significant role in the coupling efficiency, deciding the spectral response of the system. The hole milled at the edge of smaller triangular cavity (600nm) produced significant modification in the scattering spectra. Similarly, for larger triangular cavity of size 790nm a hole at centre produce a significant modification in spectral response of the gold cavity. A better understanding of the underlying mechanism of the spectral response recorded on the milled

cavities is required, which involve a more systematic investigation of this hole-cavity system. With a better control of this strategy in future, it can become an efficient tool for modal engineering in these 2D planar cavities. This study, thus, demonstrates in details techniques to engineer spectral response of a 2D gold cavities paving way for its use the realization of complex integrated components.

Reference

[1] S. Viarbitskaya, A. Teulle, A. Cuche, J. Sharma, C. Girard, E. Dujardin, A. Arbouet, "Morphology-induced redistribution of surface plasmon modes in two-dimensional crystalline gold platelets," *Appl. Phys. Lett.*, vol. 103, p. 131112, 2013.

[2] S. Viarbitskaya., A. Teulle, R. Marty, J. Sharma, C. Girard, A. Arbouet, E. Dujardin, "Tailoring and imaging the plasmonic local density of states in crystalline nanoprisms," *Nat. Mater.*, vol. 12, no. 5, pp. 426–432, 2013.

[3] A. Cuche, S. Viarbitskaya, J. Sharma, A. Arbouet, C. Girard, and E. Dujardin, "Modal engineering of Surface Plasmons in apertured Au Nanoprisms," *Sci. Rep.*, vol. 5, no. Umr 6303, p. 16635, 2015.

[4] J. Fedou, S. Viarbitskaya, R. Marty, J. Sharma, V. Paillard, E. Dujardin and A. Arbouet, "From patterned optical near-fields to high symmetry acoustic vibrations in gold crystalline platelets.," *Phys. Chem. Chem. Phys.*, vol. 15, no. 12, pp. 4205–13, 2013.

[5] M. Bosman, E. Ye, S. F. Tan, C. A. Nijhuis, J. K. W. Yang, R. Marty, A. Mlayah, A. Arbouet, C. Girard, and M. –Y. Han, "Surface Plasmon Damping Quantified with an Electron Nanoprobe," *Sci. Rep.*, vol. 3, pp. 1–7, 2013.

[6] M. Hu, C. Novo, A. Funston, H. Wang, H. Staleva, S. Zou, P. Mulvaney, Y. Xia, and G. V. Hartland, "Dark-field microscopy studies of single metal nanoparticles: understanding the factors that influence the linewidth of the localized surface plasmon resonance," *J. Mater. Chem.*, vol. 18, no. 17, pp. 1949–1960, 2008.

[7] A. Campos, A. Arbouet, J. Martin , D. Gérard, J. Proust, J.Plain, and M. Kociak, "Plasmonic Breathing and Edge Modes in Aluminum Nanotriangles," *ACS Photonics*, vol. 4, no. 5, pp. 1257–1263, 2017.

[8] G. Lévêque and O. J. F. Martin, "Tunable composite nanoparticle for plasmonics.," *Opt. Lett.*, vol. 31, no. 18, pp. 2750–2752, 2006.

[9] F. Le, N. Z. Lwin, J. M. Steele, and M. Ka, "Plasmons in the Metallic Nanoparticle − Film System as a Tunable Impurity Problem," 2013.

[10] S. Eah, H. M. Jaeger, N. F. Scherer, G. P. Wiederrecht, and X. Lin, "Scattered Light Interference from a Single Metal Nanoparticle and Its Mirror Image," pp. 11858–11861, 2005.

[11] J. J. Mock, R. T. Hill, A. Degiron, S. Zauscher, A. Chilkoti, and D. R. Smith, "Distance-dependent plasmon resonant coupling between a gold nanoparticle and gold film," *Nano Lett.*, vol. 8, no. 8, pp. 2245–2252, 2008.

[12] N. Nedyalkov, T. Sakai, T. Miyanishi, and M. Obara, "Near field distribution in two dimensionally arrayed gold nanoparticles on platinum substrate Near field distribution in two dimensionally arrayed gold nanoparticles," vol. 123106, no. 2007, pp. 1–4, 2010.

[13] L. He, E. A. Smith, M. J. Natan, and C. D. Keating, "The Distance-Dependence of Colloidal Au-Amplified Surface Plasmon Resonance," pp. 10973–10980, 2004.

[14] C. Ciraci, R. T. Hill, J. J. Mock, Y. Urzhumov, I. Fernandez-Dominguez, S. Maier, J. B. Pendry, J. B.; A. Chilkoti, and D. R. Smith, "Probing the Ultimate Limits of Plasmonic Enhancement," *Science (80-.).*, vol. 337, no. 6098, pp. 1072–1074, 2012.

[15] J. J. Mock, R. T. Hill, Y. J. Tsai, A. Chilkoti, and D. R. Smith, "Probing dynamically tunable localized surface plasmon resonances of film-coupled nanoparticles by evanescent wave excitation," *Nano Lett.*,

vol. 12, no. 4, pp. 1757–1764, 2012.

[16] X. Chen, Y. Yang, Y. H. Chen, M. Qiu, R. J. Blaikie, and B. Ding, "Probing Plasmonic Gap Resonances between Gold Nanorods and a Metallic Surface," *J. Phys. Chem. C*, vol. 119, no. 32, pp. 18627–18634, 2015.

[17] P. Mulvaney, J. Pérez-Juste, M. Giersig, L. M. Liz-Marzán, and C. Pecharromán, "Drastic surface plasmon mode shifts in gold nanorods due to electron charging," *Plasmonics*, vol. 1, no. 1, pp. 61–66, 2006.

[18] P. Nordlander and E. Prodan, "Plasmon hybridization in nanoparticles near metallic surfaces," *Nano Lett.*, vol. 4, no. 11, pp. 2209–2213, 2004.

[19] R. Esteban, G. Aguirregabiria, A. G. Borisov, Y. M. Wang, P. Nordlander, G. W. Bryant, and J. Aizpurua, "The morphology of narrow gaps modifies the plasmonic response," *ACS Photonics*, vol. 2, no. 2, pp. 295–305, 2015.

[20] J. B. Lassiter, F. McGuire, J. J. Mock, C. Cirac, R. T. Hill, B. J. Wiley, A. Chilkoti, and D. R. Smith, "Plasmonic waveguide modes of film-coupled metallic nanocubes," *Nano Lett.*, vol. 13, no. 12, pp. 5866–5872, 2013.

[21] J. Prikulis, P. Hanarp, L. Olofsson, D. Sutherland, and M. Käll, "Optical spectroscopy of nanometric holes in thin gold films," *Nano Lett.*, vol. 4, no. 6, pp. 1003–1007, 2004.

Chapter V

Multimodal bowtie antennas for efficient far-field to near-field conversion

5.1 Introduction

The need to optically control the molecular emitters at the nanoscale has been recently emphasized [1], [2]. The recent developments in experimental methods for optical imaging of single nanoparticles and molecules has offered exciting possibilities for controlling the optical interaction between molecules and nanoparticles [3]–[6]. These optical interactions are, however, limited by the mismatch between the absorption cross-section of the molecular emitters and the effective wavelength of an incident electromagnetic wave. This limitation can be overcame by using plasmonic antennas which connects the far-field photonic modes with highly confined and enhanced electric field hotspots [7]–[9]. SPP resonances in structured metallic films have shown immense possibilities for antennas application [10], [11] while localized surface plasmon resonances (LSP) rules the energy conversion and field enhancement in the standard sub-wavelength antenna geometry like dipolar bowtie antennas[12]–[15]. While an electronic antenna concentrates the electromagnetic signal in a confined geometry, at the same time it also connects the incoming signal to circuits and electronic components. This concept of electronic antennas can be transferred to their plasmonic counterparts by considering micrometer sized gold nanoparticles for antenna applications where both localized and delocalizes resonances can be simultaneously addressed. As discussed in the chapter III, these micrometric gold platelets sustain higher order SP modes in visible and near infrared [16], [17] They, therefore, can be suitable candidates for realizing the concept of plasmonic antennas integrated with optical information processing plasmonic devices.

In this work, we show that a bowtie antennas comprising two micrometer sized plasmonic cavities provides a richer optical response than the standard dipolar antennas. These bowtie antennas are probed by TPL microscopy to study the spatial distribution of the higher order modes borne by the plasmonic cavities. Experimental TPL maps are supported by corresponding simulated maps based on GDM formalism. A detailed numerical study of the normalized decay rate of a molecular system in the vicinity of the gap between the cavities as a function of the wavelength is also carried out. This work also highlights the usefulness of the

multimodal bowtie antennas as a good candidate for input-output gateway from an open space into nanoscale optical volumes.

5.2 TPL response of the multimodal bowtie antenna

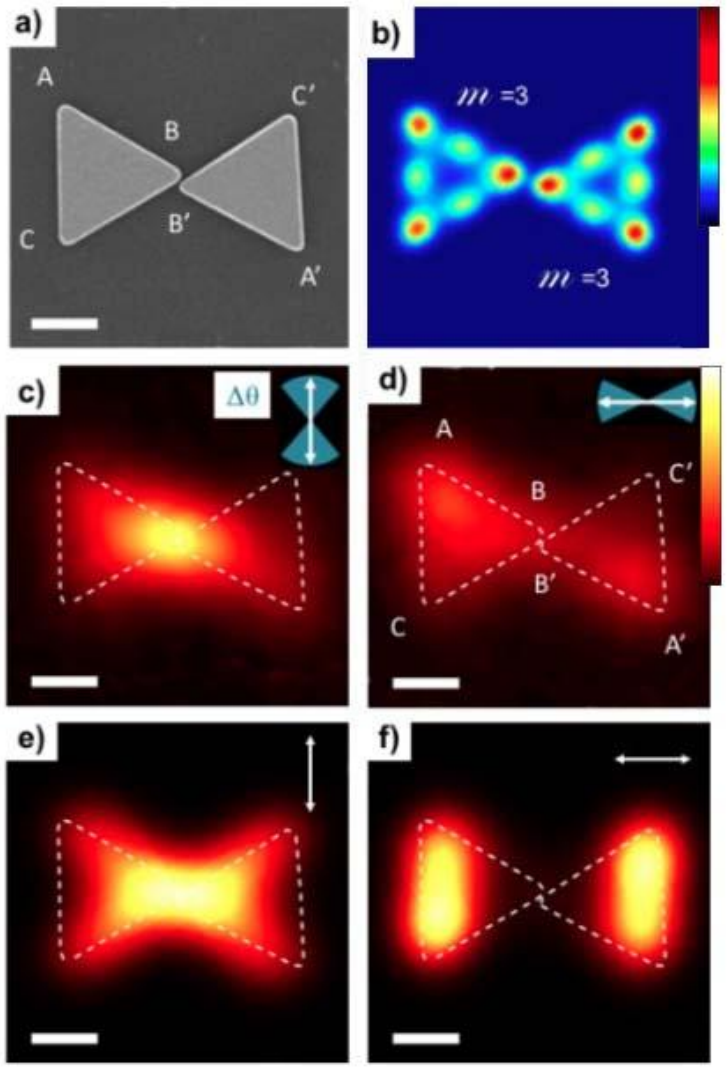


Figure 5.1 (a) SEM image of a symmetric bowtie antenna. (b) Simulated SPLDOS map corresponding to the antenna in (a). Experimental TPL maps of the coupled system for a incident polarization orthogonal (c) and parallel (d) to the main axis of the antenna, and corresponding simulated ones (e) and (f). The white arrow indicates the polarization orientation. The blue area represents the angular sector for which a central and two remotes hotspots are respectively observed. The white dashed lines represent the bowtie antenna contour. Scale bars are 200 nm

Figure 5.1(a) shows the SEM image of two symmetric multimodal antennas of lateral size 450nm separated by a gap of 10nm. The corresponding SPLDOS map is displayed in figure

5.1(b). Both antennas borne m=3 modes and is depicted by nodes and anti-nodes at the edges of the antennas. These higher order modes are generally found to be robust on undergoing through moderate modification in the structure of the metallic structure [19]. However, these modes can be significantly or moderately modified by introducing a defect in form of hole as discussed in previous chapter [20]. The spatial distribution of these high order SP modes can also be modified by electromagnetic coupling of two cavities [18]. This weak modification is also evident in the SPLDOS map shown in figure 5.1(b). The presence of the two structures close to each other has slightly impacted the two m=3 modes distribution. The experimental TPL maps of the individual cavities are shown in figure 5.1(c, d) for 90° and 0° incident polarizations respectively. The interaction between the two cavities has changed the TPL response of the two prism dramatically. The TPL response of the coupled triangular cavities appears to be different from the non-coupled isolated cavities of same dimensions. TPL response of individual triangular cavity has been discussed by Viarbitskaya et. al. and it shows a sequential appearing of hotspots at the apices of the triangular cavity as we change the linear polarization of the incident field [16]. The superimposition of the TPL maps of two orthogonal polarizations results in three hotspots at each of the three apices of the cavity matching the symmetry of the triangular cavity. However, in this case, this symmetry is not preserved in figure 5.1 (c) and (d). On superposition of the TPL responses of the coupled cavities, the intensities at B-B′ and A-A′ are not similar anymore. In addition, the hotspots at C and C′ are missing. These observations were also reported in a previous work in our group [18]. Now, if we consider the TPL response of the coupled antennas separately for two orthogonal polarizations, a strong response is observed at the central gap for a 90° polarization (figure 5.1c). For 0° polarization (figure 5.1d) two TPL hotspots are observed on the remote and symmetric location denoted by A and A′. These hotspots are less brighter than the one at central gap and are separated by a distance of around 900nm which is more than the effective SP wavelength on a flat gold film (λ = 679 nm). It is interesting to note here that this behavior of the multimodal bowtie antennas is in complete contrast to the standard sub-wavelength bowtie antennas, where the strong hot spot at the center is observed for a polarization of 0° while a 90° polarization results in shutting down of the TPL signal [21], [22]. The TPL maps were faithfully reproduced by simulation tool based on GDM. The simulation results for the two orthogonal polarizations are shown in figure 5.1(e,f). There is an excellent match between experimental and simulated results of the hotspot at the central gap for perpendicular polarization (figure 5.1c, e) while for parallel polarization, the TPL hotspot is symmetrical and more spread along the remote edges of the cavities (figure 5.1f). The TPL results, thus, indicate

that the multimodal cavities not only concentrate the electric field in the gap but also form a coupled system. This coupling, although a weak one, is sufficient enough to modify the SPLDOS distribution of the individual prisms. The coupling is further amplified in the TPL map.

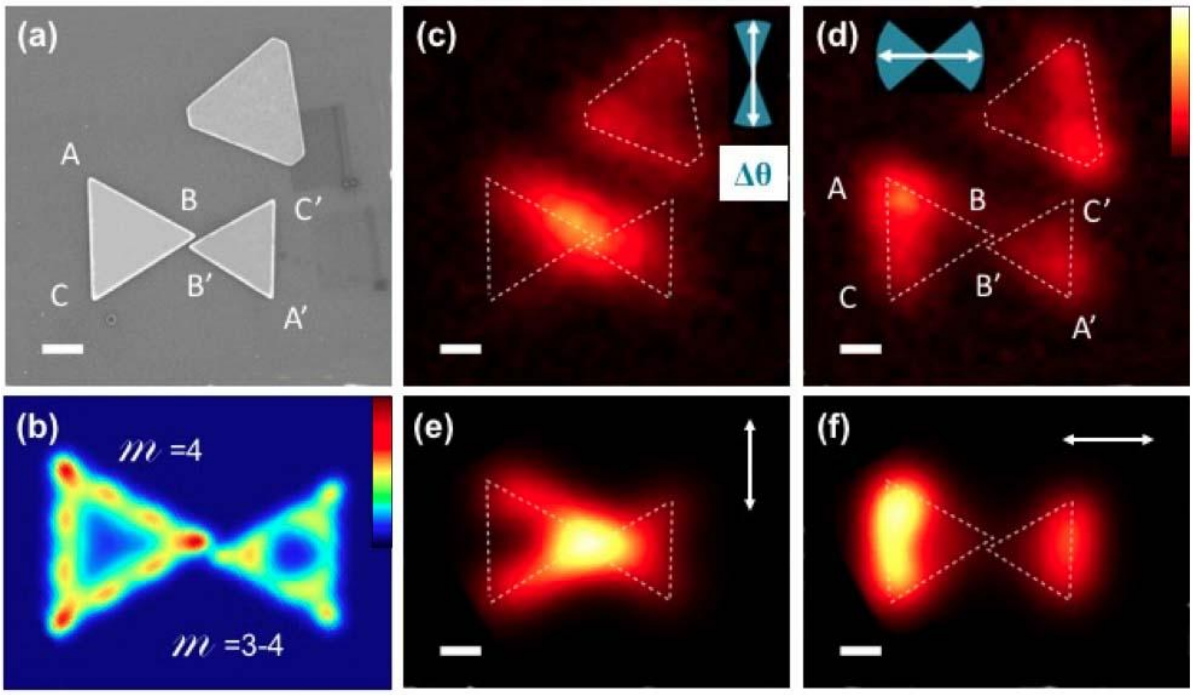


Figure 5.2 (a) SEM image of an asymmetric bowtie antenna. (b) Simulated SPLDOS map corresponding to the structure in (a). Experimental TPL maps of the coupled system for an incident polarization orthogonal (c) and parallel (d) to the main axis of the antenna, and corresponding simulated ones (e) and (f). The white arrow indicates the polarization orientation. The blue areas represent the angular sector for which a central and two remote hotspots are respectively observed. The white dashed lines represent the bowtie antenna contour. Scale bars are 200nm.

Unlike dipolar bowtie antennas, the order of resonance occurring in each arm of the multimodal antennas can be tuned. For instance, in figure 5.2 (a), two triangular gold cavities of edge lengths 600nm and 480 separated by a gap of 17nm are shown. A different higher order modal signature is observed on changing the size of the cavities [16]. The new bowtie exhibits a m=4 plasmonic mode for larger cavity and a m=3-4 (transition between 3 and 4) plasmonic mode for the smaller cavity for an excitation at λ =700nm (figure 5.2b). A well separated triangular cavity is also present near to the bowtie antennas which can be used for reference. If we compare the TPL response of the coupled cavities with that of the separated one we clearly see a modification of hot spot at the apices in the coupled structure as the apices C and C′ are dark irrespective of the incident polarization (figure 5.2c,d). The experimental TPL map for

polarization perpendicular to the main x- axis shows as high intensity spot as in the case of the symmetrical bowtie configuration (figure 5.2c). However, for the polarization parallel to the main axis, a break in symmetry is observed. A hot spot is observed on the distant apices A and A′ of the two cavities, but the intensity of the signal measured on the larger cavity is twice stronger than that on the smaller cavity. This difference in the TPL intensity is consistent with the difference in the SPLDOS distribution of the two cavities. A nice match is again obtained between the experimental and simulated TPL maps (figure 5.2e,f) for the asymmetrical bowtie antennas. Little discrepancies can be attributed to the fact that exact geometry of the antennas is difficult to design.

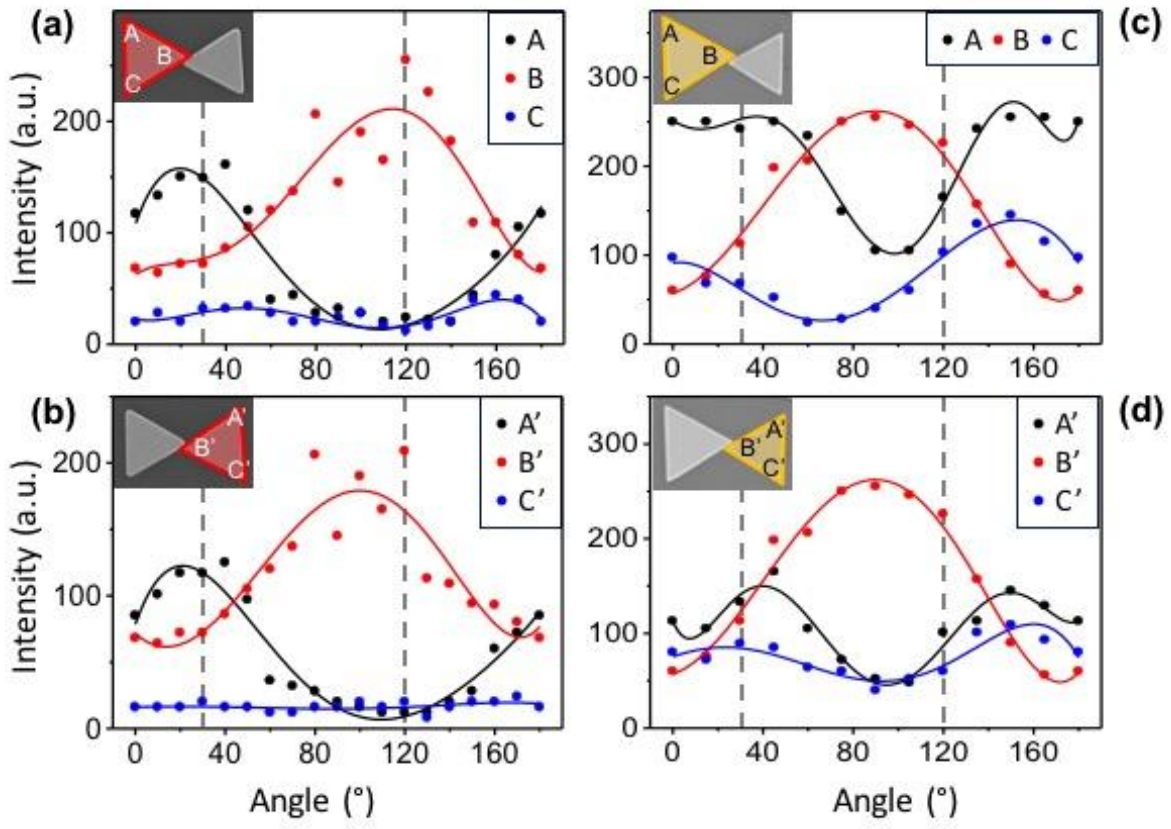


Figure 5.3 Study of the local variation of the TPL signal with the incident light polarization for the symmetric configuration when the light beam center is located at the A, B, C (a) and A′,B′, C′ (b) locations. Idem for the asymmetric situation at the positions A, B, C (c) and A′,B′,C′ (d)

The local amplitude of the SPLDOS can be quantified in the form of the evolution of the field enhancement at a certain point as we tune the polarization. This evolution of the field enhancement with respect to the polarization has been plotted for positions A, , B and C of the symmetrical cavity in figure 5.3 (a). Corresponding plots for position A′, B′ and C′ is displayed

in figure 5.3(b). The angular window in which either a bright spot at B-B′ or two hot spots at A and A′ are observed, can be easily predicted from the two plots.

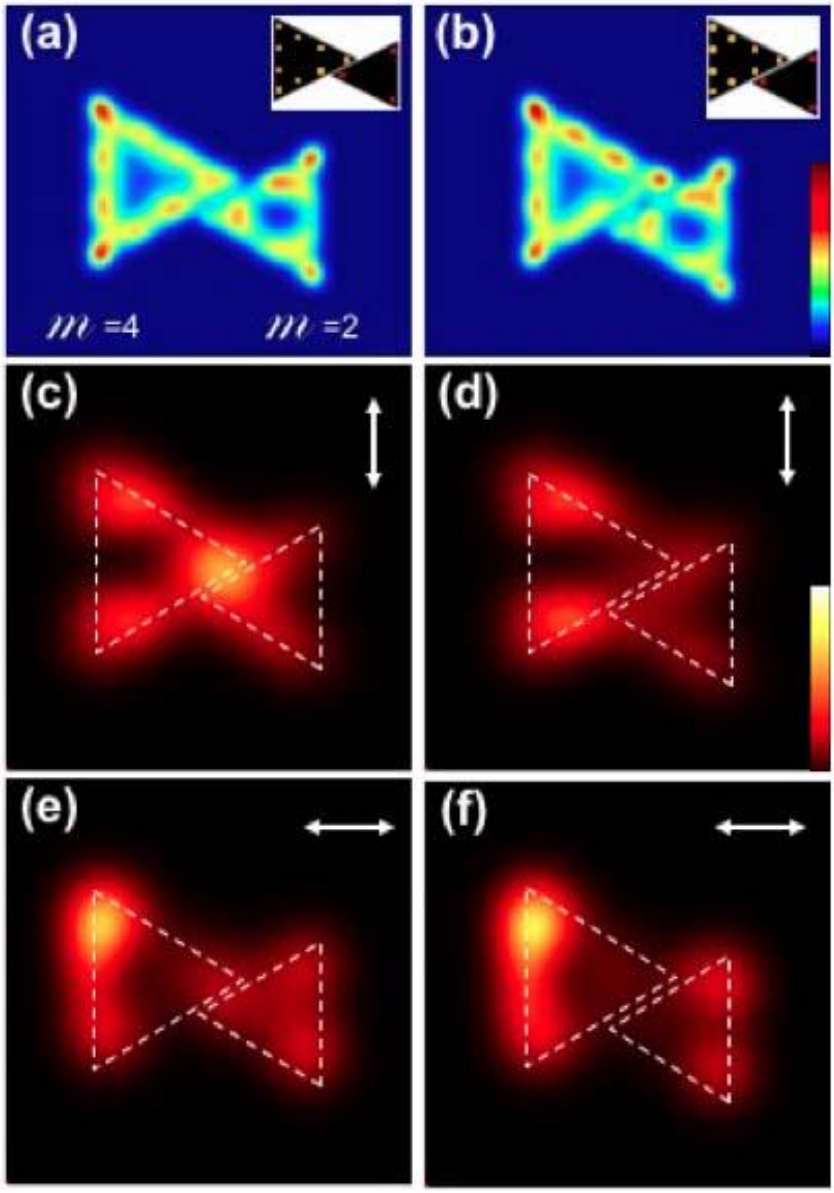


Figure 5.4 SPLDOS maps for asymmetric bowtie antenna for two different central overlaps corresponding to a spatial (a) antinode mismatch and (b) antinode match. Positions of the SPLDOS maxima are shown in inset. (c-d) Simulated TPL maps for a 90° incident polarization. (e-f) Simulated TPL maps for a 0° incident polarization.

A sequential lighting of A and A′ positions within an angular window of Δ =±25° around 20° (of the x –axis) is observed. On the other hand, for the hotspot ta B- B′, the sequential lighting is observed within an angular window of Δ = ± 40° around 105° (of the y axis). The asymmetrical bowtie antennas shows a different behaviour (figure 5.3c, d). The angular range for which the B-B′ central spot shows strong TPL response is narrowed down to Δ =±20° while

the two hotspots at A and A′ stays "on" for an angular range of 40° and 20° respectively. These results, thus, suggest that a fine tuning of the response of the antennas can be achieved by the choice of the arm size and consequently the SP mode order.

In comparison to dipolar bowtie antennas which are limited to an "on-off" polarization dependent response at the gap, the multimodal bowtie antennas make possible tuning of the field enhancement in different region of the antennas with the incident polarization. The spectral matching of the SP modes is governed by the size and shape of the cavity but their spatial matching is defined by the relative positioning of one cavity with another. The TPL response in the figure 5.2 shows a preferential axis at the antenna scale. We assume that the small overlap in the gap determines the local symmetry breaking. Sliding of one cavity with respect to another along this edge can result in alignment or misalignment of nodes of one cavity with the antinodes of the other cavity and vice versa. While the SPLDOS maps display a clear spatial distribution of the nodes and antinodes borne by the cavities, it is difficult to predict the TPL response of these antennas as TPL at a given position results from the convolution of the squared in-plane SPLDOS with the Gaussian profile of the excitation light beam integrated over the volume of the particle [18]. Thus, the relative positioning does not modify the native SP modes of the cavities but dramatically changes the global TPL response of the dimer. More importantly, it also has a huge impact on the local field enhancement. This has been demonstrated in the figures 5.4(a), (c) and (e),where the gold cavities are placed such that the first antinode of the small prism faces the first node of the large prism. A TPL hotspot is observed in B-B′ for a polarization perpendicular to the x-axis and mainly in A at for parallel polarization. This is similar to our observation in the tip-facing dimer (figure 5.2). However, unlike the TPL response in figure 5.2, a strong signal is observed in figure 5.4(c,d) at A and C for perpendicular polarization. Similarly, for the polarization parallel to the x-axis, the response from B-B′ is not "off". On increasing the overlap of the two prism, the TPL response changes even more drastically. In Figs. 5(b), (d) and (f), the gold cavities are placed such that the first antinode of the small cavity faces the second antinode node of the large cavity. This results in a strong reduction of TPL hotspot at B-B′ and a sharp increase in the TPL response from A and C for the vertical polarization whereas for the horizontal polarization the TPL pattern is similar to that observed in the tip-facing dimer. The multimodal bowtie antennas, thus, provide more degrees of freedom to tune the TPL response of the system compared to the dipolar antennas. The shape, size and interparticle distance along with the relative position of the cavities determines the spatial and the spectral behaviour of the dimer and thus governs the overall optical properties. These complementary parameters provide a way to control the localized and

delocalized plasmonic response of these antennas, setting a platform for an effective input-output components for 2D plasmonic information processing device. The gap region in this system can be effectively used to enhanced the absorption or emission of single emitters whereas the two cavities can be used as initial or terminal propagative structures. This perspective is discussed in the next section, where the relation between the dipole orientation of given single emitter and the local geometry of the gap in a multimodal bowtie antennas is investigated (figure 5.5).

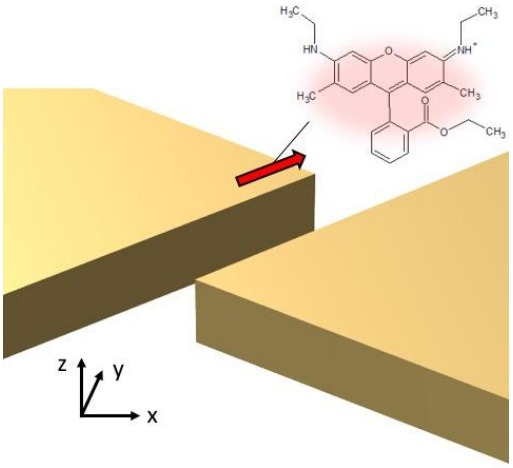


Figure 5.5 Illustration of a single dipole/molecule placed 15 nm above the central gap of the multimodal bowtie antenna

5.3 Local field enhancement and multiscale nature of the antennas

The photonics LDOS in the vicinity of a metallic nanoparticle is modified by the presence of evanescent plasmonic modes[23], [24]. The dynamics and the emission rate of a dipole corresponding to this weak coupling with antnennas can be quantified in form of normalized total decay rate, $\frac{\Gamma_{tot}}{\Gamma_0}$ (where Γ_0 is the decay rate in the vacuum) of the molecule positioned in the near vicinity gap of the bowtie antenna and computed as a function of the dipole orientation, **u**. The total decay rate as a function of position of the dipole, **R** is given by

$$\Gamma_{tot}(\boldsymbol{R}) = \Gamma_0 + \frac{2|m_{eg}|^2}{\hbar} Im\{\mathbf{S}(\mathbf{R},\mathbf{R},\omega):\mathbf{uu}\} \quad (5.1)$$

where m_{eg} is the moment associated to a transition between the excited state(e) and the ground state (g) of an ideal two level system. $\mathbf{S}(\mathbf{r},\mathbf{r}',\omega)$ is the generalized field propagator which takes into account the presence of the metallic system in the direct vicinity of the dipole located 15 nm above the gap. 'ħ' is the Planck's constant divided by 2π. The normalized total and radiative decay rate of the dipole in the vicinity of the bowtie antennas is shown in figure

5.6(a,b) and 5.6(c,d) for symmetric and asymmetric configurations respectively. The radiative decay rate is obtained by subtracting the dissipative decay rate from the total decay rate. The dissipative decay rate is given by –

$$\Gamma_{dis}(\boldsymbol{R}) = \frac{Q(\boldsymbol{R})}{\hbar\omega} = \frac{m_{eg}^2}{8\pi\hbar}\int_V \epsilon_m''|\boldsymbol{S_0}(\mathbf{r},\mathbf{R},\omega):\mathbf{uu}|^2\, d\boldsymbol{r} \qquad (5.2)$$

where, ϵ_m'' is the imaginary part of the dielectric function of the gold and $\boldsymbol{S_0}$ the vacuum field propagator and Q(**R**) is the power dissipated in the metal corresponding to the absorption of a photon emitted by the molecular system. The non-radiative processes contributes to the dissipative decay rate.

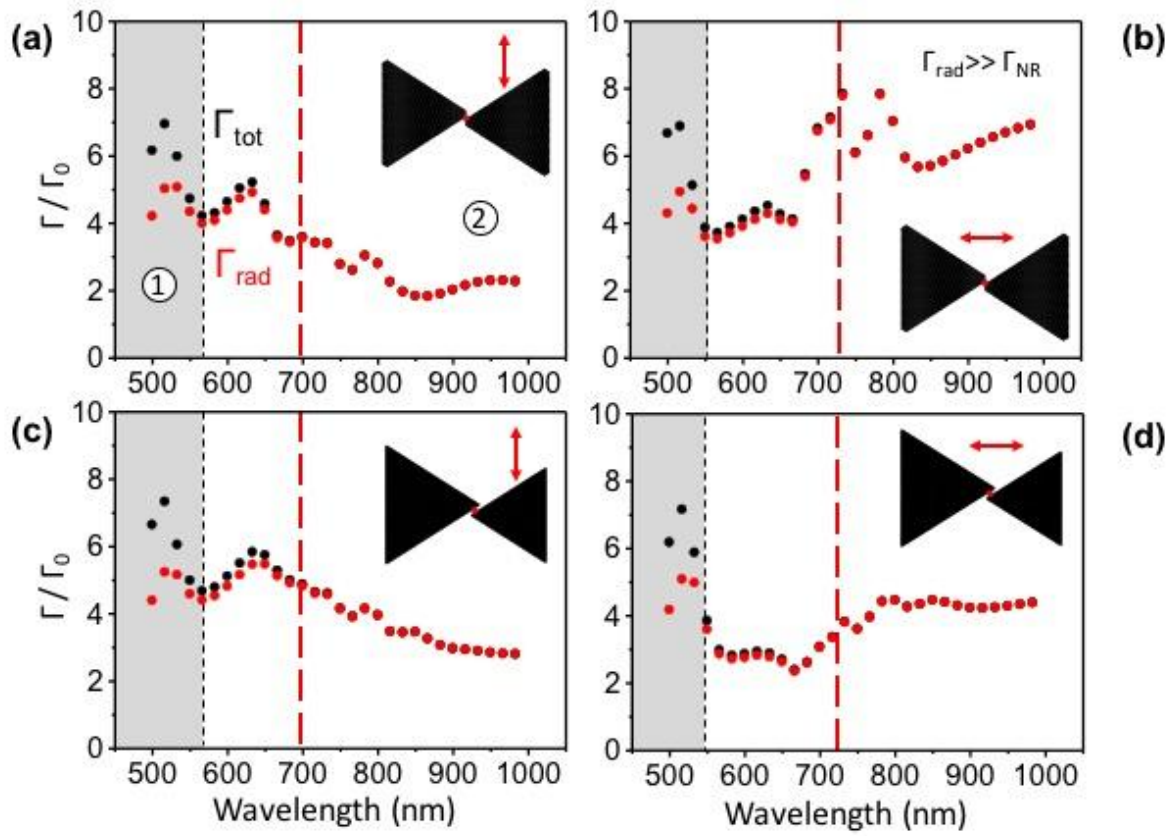


Figure 5.6 Normalized total (black dots) and radiative (red dots) decay rates for a dipole 15 nm above the symmetric antenna and oriented perpendicularly (a) or parallel(b) to the main axis. Idem for the asymmetric antenna for perpendicular (c) or parallel(d) dipole orientation. The region 2 corresponds to $\Gamma_{rad} \gg \Gamma_{dis}$ while the grey part (region 1) corresponds to the regime where $\Gamma_{rad} \sim \Gamma_{dis}$. The red dashed line depicts the experimental wavelength at 700 nm.

Figures 5.6(a–d) show that the multimodal bowtie antennas exhibit a polarization and wavelength dependent enhancement of dipole normalized emission rate in the near infrared range. The dissipative decay rate is very high for the wavelengths below 600nm. In gold, for energy greater than 2eV, the interband transitions results in non-radiative dissipation resulting

in a lower radiative decay rate [25]. For both symmetric and asymmetric configurations, a general increase of the normalized total decay rate is observed irrespective of wavelength for polarization perpendicular to the main axis. In spite of that, the emission rate also shows increase for dipole at 0°. The enhancement in the decay rate ranges from 2 fold to 8 fold. At 700nm wavelength, which is the wavelength used for recording the TPL maps, a 4 fold enhancement of the dipole decay rate is observed. The total decay rate is either equal or more for a dipole oriented perpendicular to the main x-axis in comparison to the one which is oriented along the x-axis.

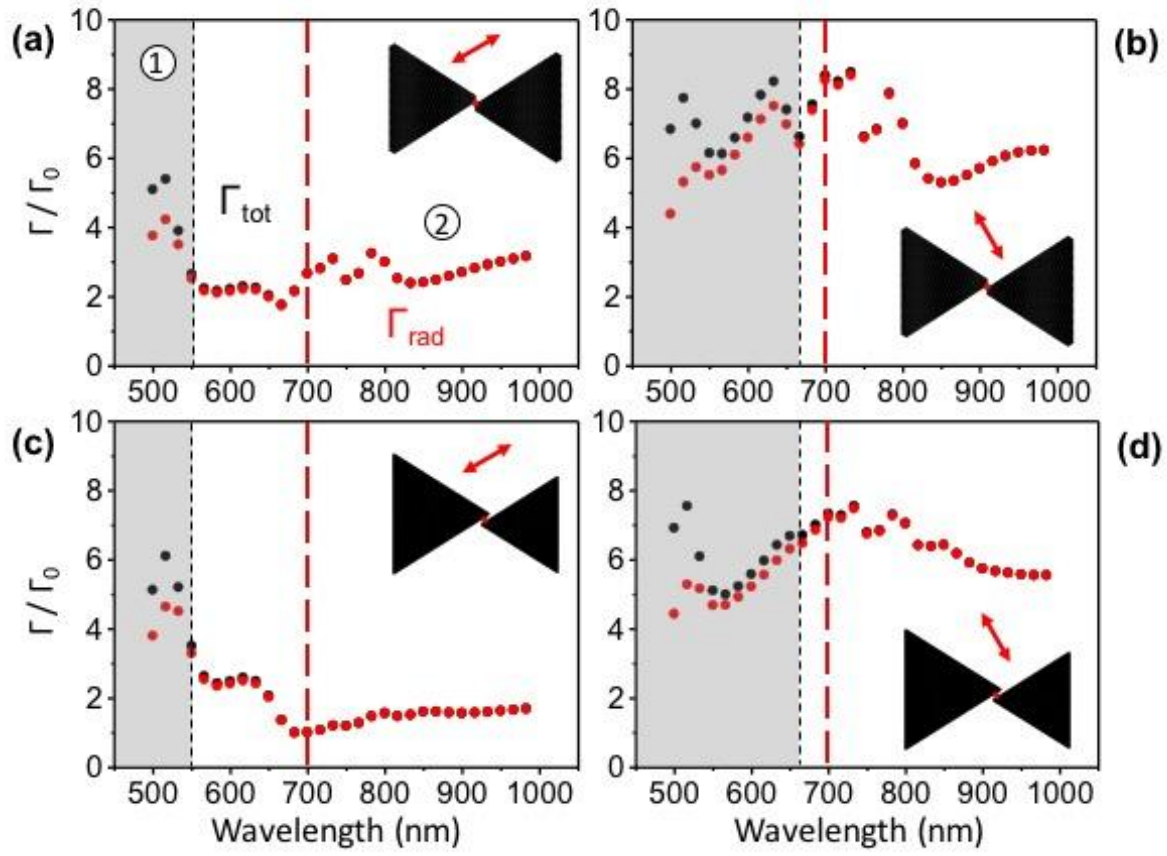


Figure 5.7 Normalized total (black dots) and radiative (red dots) decay rates for a dipole perpendicular (a) or parallel (b) to the gap of the symmetric antenna. Normalized total and radiative decay rates for the asymmetric antenna for perpendicular (c) and parallel (d) dipole orientation.

However, TPL response and thus the field enhancement at the gap for a 0° polarization is mute. This behaviour of the dipole in the vicinity of the bowtie structure contradicts the general intuition which suggest that the increase of the total emission rate and the enhancement of the local electric field displayed in the TPL maps are directly correlated. The same behavior of the

normalized decay rate is observed for both the bowtie configurations and for all the wavelengths

Research have shown that the emission dynamics of the dipole is governed by the local environment around the dipole and its orientation with respect to the surface in the vicinity of the dipole [26]. In the present case, the surfaces near to the dipole are the facets facing each other the orientation of which is different from the global symmetry of the entire antenna [27]. The edges overlapping the two apices of the cavities corresponds to preferential axis oriented parallel and perpendicular to the gap edges respectively. This corresponds to orientation of dipoles at 30° and 120° respectively. Figure 5.7 shows the normalized decay rate computed along these two orthogonal orientation of the dipole for both symmetric and asymmetric bowtie configurations. For a given dipole orientation, the wavelength dependency of the total and radiative decay rates is now similar for both antenna configurations. For dipole oriented along the 120° to the main x-axis, there is a significant contribution of dissipative decay rate. This is in contrast to the situation when the dipole oriented along the y axis. The onset of the negligible non-radiative loss is now shifted to around 650nm from 550nm (in figure 5.6). The total decay rate is now enhanced up to an 8-fold for a dipole perpendicular to the gap edges while for dipole orientation parallel to the gap edges leads to an enhancement of 3-fold. These results are consistent with the field enhancement observed in TPL, i.e. there is 8-fold enhancement of the decay rate for at 120° for which there is strong hot spot at the gap too. Fig. 5.3 shows that the TPL hotspot at 120° is almost as bright as it is for the 90° polarization. Thus we have a nice agreement with the rise of the decay rate observed in figure 5.7 (a) and (c). On the other hand, an incident polarization of 30° leads to hotspot at the apices A and A′ for both antennas which means a low field enhancement in the central gap which is in good agreement with the 3 fold enhancement of the total decay rate for dipole orientation along the same direction. This study emphasizes the importance of the local geometry of the gap.

5.4 Conclusions

To conclude, we have demonstrated that two multimodal prismatic plasmonic cavities coupled in a symmetric and asymmetric bowtie configuration exhibit a polarization-dependent field enhancement and a nanoscale field confinement at specific locations. The SP mode order in this new class of bowtie antenna dictates the spectral matching condition while the spatial matching in the gap is decided by the the relative positioning of the cavities with respect to each other. The multimodal nature of these antennas allow effective control of their response

by changing polarization while their mesoscopic dimensions allow the transfer of optical information through a plasmonic channel beyond the SP effective wavelength which is not possible with the standard sub-wavelength dipolar bowtie antennas (this will be discussed in more detail in the following chapter). This new family of plasmonic antennas offers excellent possibility of designing input-output plasmonic components aiming at the integration of far-field and coplanar plasmonic architectures.

References

[1] H. X. Xu, E. J. Bjerneld, M. Käll, and L. Börjesson, "Spectroscopy of single hemoglobin molecules by surface enhanced Raman scattering," *Phys. Rev. Lett.*, vol. 83, pp. 4357–4360, 1999.

[2] P. Andrew and W. L. Barnes, "Energy transfer across a metal film mediated by surface plasmon polaritons.," *Science*, vol. 306, no. 2004, pp. 1002–1005, 2004.

[3] S. W. Hell and J. Wichmann, "Breaking the diffraction resolution limit by stimulated emission: stimulated-emission-depletion fluorescence microscopy," *Opt. Lett.*, vol. 19, no. 11, p. 780, 1994.

[4] E. Betzig and R. J. Chichester, "Single molecules observed by near-field scanning optical microscopy," *Science*, vol. 262, no. 5138, pp. 1422–1425, 1993.

[5] M. Orrit and J. Bernard, "Single pentacene molecules detected by fluorescence excitation in a p-terphenyl crystal," *Phys. Rev. Lett.*, vol. 65, no. 21, pp. 2716–2719, 1990.

[6] W. E. Moerner and L. Kador, "Optical detection and spectroscopy of single molecules in a solid," *Phys. Rev. Lett.*, vol. 62, no. 21, pp. 2535–2538, 1989.

[7] L. Novotny and N. van Hulst, "Antennas for light," *Nat. Photonics*, vol. 5, no. 2, pp. 83–90, 2011.

[8] J. A. Schuller, E. S. Barnard, W. Cai, Y. C. Jun, J. S. White, and M. L. Brongersma, "Plasmonics for extreme light concentration and manipulation," *Nat. Mater.*, vol. 9, no. 3, pp. 193–204, 2010.

[9] P. Biagioni, J. Huang, and B. Hecht, "Nanoantennas for visible and infrared radiation," *Reports Prog. Phys.*, vol. 24402, p. 76, 2012.

[10] J. M. Yi, A. Cuche, E. Devaux, C. Genet, and T. W. Ebbesen, "Beaming Visible Light with a Plasmonic Aperture Antenna," *ACS Photonics*, vol. 1, no. 4, pp. 365–370, 2014.

[11] H. Aouani *et al.*, "Bright unidirectional fluorescence emission of molecules in a nanoaperture with plasmonic corrugations," *Nano Lett.*, vol. 11, no. 2, pp. 637–644, 2011.

[12] P. J. Schuck, D. P. Fromm, A. Sundaramurthy, G. S. Kino, and W. E. Moerner, "Improving the mismatch between light and nanoscale objects with gold bowtie nanoantennas," *Phys. Rev. Lett.*, vol. 94, no. 1, 2005.

[13] D. P. Fromm, A. Sundaramurthy, P. James Schuck, G. Kino, and W. E. Moerner, "Gap-dependent optical coupling of single 'bowtie' nanoantennas resonant in the visible," *Nano Lett.*, vol. 4, no. 5, pp. 957–961, 2004.

[14] H. Duan, A. Fernandez, M. Bosman, S. a Maier, and J. K. W. Yang, "Nanoplasmonics : Classical down to the Nanometer Scale Nanoplasmonics : Classical down to the Nanometer Scale," *Nano Lett.*, 2012.

[15] H. Kollmann *et al.*, "Toward plasmonics with nanometer precision: Nonlinear optics of helium-ion milled gold nanoantennas," *Nano Lett.*, vol. 14, no. 8, pp. 4778–4784, 2014.

[16] S. Viarbitskaya *et al.*, "Morphology-induced redistribution of surface plasmon modes in two-dimensional crystalline gold platelets," *Appl. Phys. Lett.*, vol. 103, p. 131112, 2013.

[17] S. Viarbitskaya *et al.*, "Plasmonic Hot Printing in Gold Nanoprisms," *ACS Photonics*, vol. 2, no. 6, pp. 744–751, 2015.

[18] S. Viarbitskaya *et al.*, "Tailoring and imaging the plasmonic local density of states in crystalline nanoprisms," *Nat. Mater.*, vol. 12, no. 5, pp. 426–432, 2013.

[19] D. Rossouw and G. A. Botton, "Plasmonic response of bent silver nanowires for nanophotonic subwavelength waveguiding," *Phys. Rev. Lett.*, vol. 110, no. 6, pp. 1–5, 2013.

[20] A. Cuche, S. Viarbitskaya, J. Sharma, A. Arbouet, C. Girard, and E. Dujardin, “Modal engineering of Surface Plasmons in apertured Au Nanoprisms,” *Sci. Rep.*, vol. 5, no. Umr 6303, p. 16635, 2015.

[21] J.-S. Huang *et al.*, “Atomically flat single-crystalline gold nanostructures for plasmonic nanocircuitry,” *Nat. Commun.*, vol. 1, no. 9, p. 150, 2010.

[22] N. Verellen *et al.*, “Two-photon luminescence of gold nanorods mediated by higher order plasmon modes,” *ACS Photonics*, vol. 2, no. 3, pp. 410–416, 2015.

[23] G. Colas des Francs *et al.*, “Plasmonic Purcell factor and coupling efficiency to surface plasmons. Implications for addressing and controlling optical nanosources,” *J. Opt.*, vol. 18, no. 9, p. 94005, 2016.

[24] Ǵ. Colas Des Francs, C. Girard, T. Laroche, G. Ĺevèque, and O. J. F. Martin, “Theory of molecular excitation and relaxation near a plasmonic device,” *J. Chem. Phys.*, vol. 127, no. 3, 2007.

[25] P. B. Johnson and R. W. Christy, “Optical constants of the noble metals,” *Physical Review B*, vol. 6, no. 12. pp. 4370–4379, 1972.

[26] K. H. Drexhage, “IV Interaction of Light with Monomolecular Dye Layers,” *Prog. Opt.*, vol. 12, no. C, pp. 163–232, 1974.

[27] R. Esteban *et al.*, “The morphology of narrow gaps modifies the plasmonic response,” *ACS Photonics*, vol. 2, no. 2, pp. 295–305, 2015.

Chapter VI

Designing transmission eigenstates for tailoring SPP propagation in 2D plasmonic device

6.1 Introduction

Rapid signal transfer and processing over a large distance, with minimum losses are some of the most desirable parameters in an information processing device. Most of these parameters can be easily met by presently available optical data communication devices such as optical fibers and dielectric waveguides. However, these technologies do not address the challenge of spatial confinement in sub-wavelength regime. This question has led to an ongoing effort to design plasmonic components and integrate them into efficient plasmonic circuits. However, there are several issues that need to be resolved before a fully working plasmonic based circuit becomes reality. One of the main challenges is modulate and control the SPP propagation. This has been addressed by changing the optical properties of the surrounding medium, for example by using quantum dots [1], [2], or by electro-optic modulation[3], [4]. Another reported approach consists of using photochromic molecules which can be switched between transparent and absorbing states using a free space optical pump [5]. However, the most of the aforementioned approaches exhibit a limited SPP modulation efficiency. More recently, Rudé et. al. suggested an active control over SPP propagation by using phase changing material [6]. Optical switches and modulators graphene have also been reported [7][8]. In this work, we propose an alternative way of controlling SPP propagation by specifically designing transmission eigenstates inside a multimodal 2D geometry. The characteristics of the plasmonic modes supported by individual and coupled gold cavities discussed in chapter IV and V hold the key to designing these transmission eigenstates.

The optical behavior of two coupled cavities is modified by the electromagnetic interaction between them. This coupling, however, is too weak to exploit these bowtie nanoantennas for designing plasmonic modal information transfer and logic gate devices as proposed by Viarbitskya et.al. [9]. Figure 6.1(a) displays the model of the bowtie antennas with red and blue circles denoting an input and output position. The transmittance image computed on this bowtie antenna with triangular cavities of lateral size 925nm each has been shown in figure 6.1 (b, c) for 0° and 90° incident polarizations respectively. The cavities are separated

by a distance of 50nm. The left triangular cavity is excited on the upper most apex, I (indicated by the red circle). The transmission images are computed based on GDM methodology as detailed in the section 3.2.2. The simulated images show transmission from one cavity to another for in-plane polarization of 0° while for 90° incident polarization there is no transmission. A low transmission in the coupled bowtie structure leads us to design a slightly modified structure called diabolo which comprised of two bowtie nanoantennas connected by rectangular metallic channel in order to facilitate the coupling between the two multimodal triangular prisms (figure 6.1d). The spatial distribution of the in-plane plasmon modes is designed in such a way that we can fully integrated the in-, out-coupling and directional transmission functions in a 2D metallic structure. This will lead the way for more sophisticated input/output plasmonic devices such as optical logic gates in chapter VII.

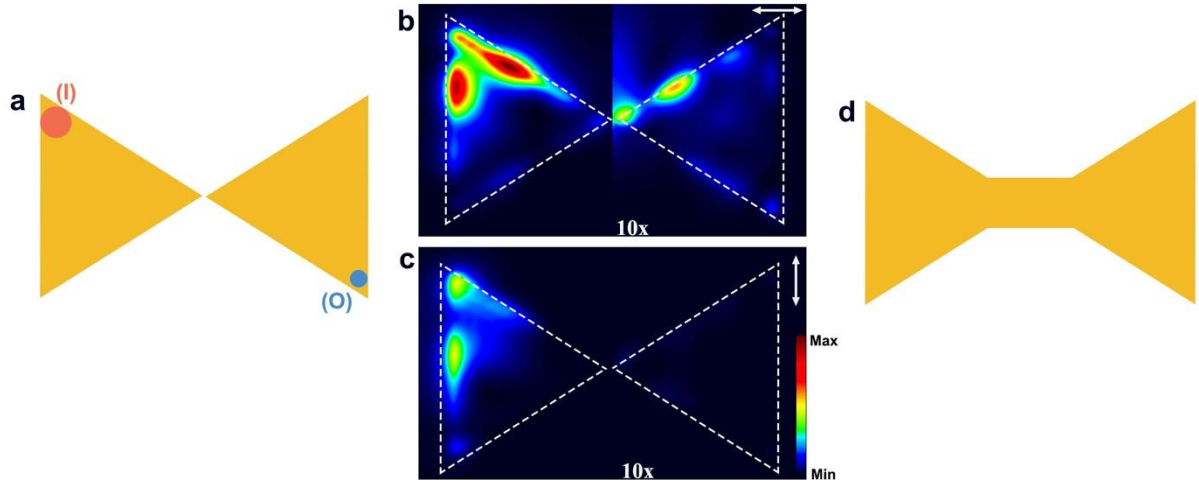


Figure 6.1 (a) Design of multimodal bowtie antennas, (b,c) Transmission image computed on a bowtie antenna with triangular prism of lateral size 925nm each for 0° and 90° in-plane polarizations respectively, (d) model of the proposed diabolo structure. The red circle on the upper left corner in (a) denotes the position of excitation and blue circle on the lower right corner denotes the output.

The first section details the modelling of the illumination source used for computing the transmittance maps. We will demonstrate in detail how a change in excitation parameters and number of layers of the mesh change the transmittance emerging from the diabolo structure. Next section gives the detail about the process involved in the fabrication of the diabolo structure. Last section will cover the transmittance properties of diabolo with triangular pads of similar sizes. We will study in detail different ways to control and tune the transmittance of SP signal from one point to another in the diabolo structure taking the advantages of the complex resonances of the prismatic building blocks.

6.2 Computation of the transmission maps

The computed transmission maps like the one plotted in figure 6.1(a, b) depend on various parameters like design of the mesh, type of excitation, height of the plane of observation, excitation position, etc. In this section, we discuss the effect of all three different types of excitation namely dipole excitation, plane wave excitation with Gaussian weighted intensity profile and full Gaussian beam excitation on the transmission maps and spectra.

6.2.1 Excitation of the diabolo structure by a dipole

In chapter III, we have demonstrated in detail the numerical tool that we used for calculation of transmission maps and spectra. To calculate the local field at any given point in or above the diabolo, we first define the excitation field. A dipole is a commonly used illumination source for excitation of metallic nanoparticles as it corresponds to a realistic experimental configuration with a molecule emitting near a nanoparticle for instance [10]–[13]. Here, we have used a dipole positioned above the surface of the diabolo for excitation at the input (I) of the diabolo. We have considered a symmetrical diabolo with triangular pads of size 650nm each connected by a 500nm x 100nm channel. We first used a hexagonal mesh of cell size 10nm with a single layer. Figure 6.2 (a, b) shows the near field transmission map computed on such a system with dipole excitation. In the right insets are the corresponding intensity enhanced maps at the output (O). Next we used a 3 layers mesh of same dimensions (cell size =10nm). In figure 6.2 (c, d), we display, the near field transmission maps calculated on 3-layer mesh for excitation with two orthogonal dipole orientations as indicated by the double headed white arrows. The maps corresponding to single layer mesh suggest an intensity modulation on the other right triangular pad on changing the dipole orientation from 0° to 90° (figure 6.2a,b).A black region parallel to the edge of the right triangular pad is also noticed around 100nm from the edge for a dipole orientation of 0°. In addition, we observe a very high noise to signal ratio on the upper edge of the right triangular cavity. In case of mesh with 3 layers, we see two hot spots at the apices of the right triangular pads. Here the background noise has been significantly reduced as compared to the previous model and signal to noise ratio on the upper edge of the right triangular pad has improved. The improvement in signal to noise ration suggest that this model with 3 layers can be used to simulate diabolo with dipole excitation.

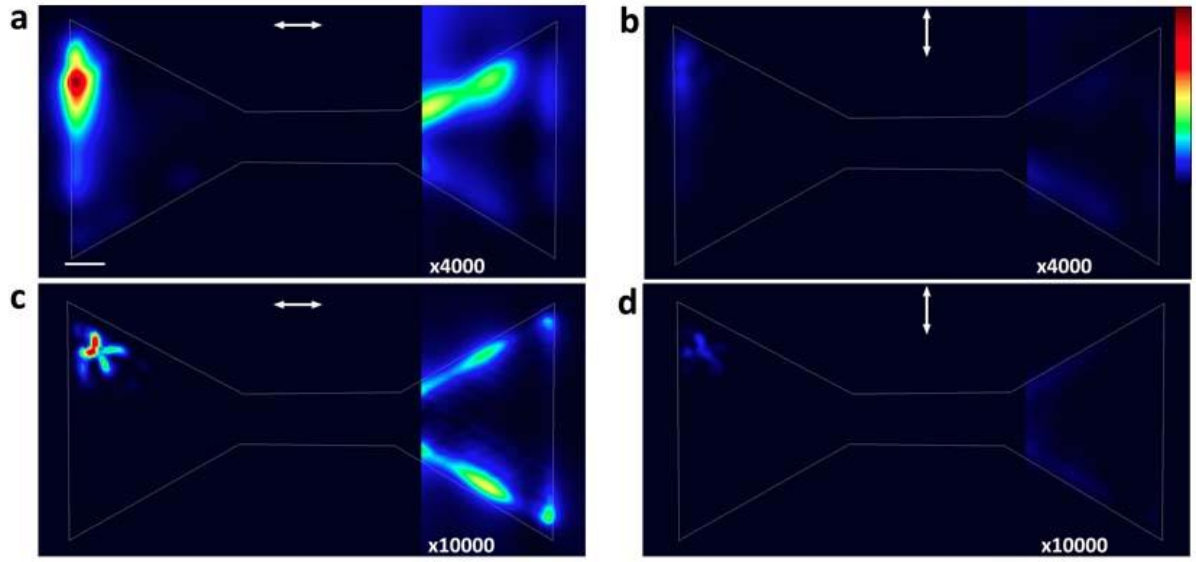


Figure 6.2(a,b) Near field transmission maps for a dipole orientation of 0° and 90° (to the x-axis) respectively computed by exciting the upper left apex of a 650nm symmetrical diabolo with a point dipole source. A single layer mesh is used for the computation, prepared with hexagonal mesh of size 10nm. The dimensions of the triangular pads of diabolo is 650nm each and the channel is 500nm long and 100nm wide. The inset on the right of both the maps are in 4000X color scale. (c, d) Corresponding transmission maps computed on 3- layer mesh of the same dimensions. The insets color scale are magnified by 10000 times. The scale bar in white in figure (a) is 100nm. The double headed arrows represent the direction of the orientation of the exciting dipole

6.2.2 Excitation of the diabolo structure by a Gaussian shaped plane wave

A plane wave convoluted into Gaussian shape is next used for excitation at the input I on the diabolo shaped metallic structure. The idea is to use a source as close as possible to the real Gaussian excitation since the experiments have been performed using a Gaussian excitation. In figure 6.3(a, b), we have used the plane wave to excite the diabolo for horizontal and vertical polarizations respectively. The size of the diabolo, the point of excitation and the height of the observation plane are same as in the case of dipole excitation. There is a noticeable difference in the transmission image obtained here (figure 6.3a). The linear signal emerging from the left triangular cavity is spread along the edges instead of being concentrated near the apex as in the case of the dipole excitation(figure 6.2a). However, the transmission of the signal from input position (I) to the apices of the right triangular pad is again limited by a region parallel to the edge of the pad with no signal, for both the incident polarization directions (figure 6.3a,b). Also, the upper edge of the right pad has background noises for both polarizations (figure 6.3a). We next use the plane wave excitation for the 3-layer mesh. The transmission maps for the horizontal and vertical polarizations are shown in figure 6.3(c, d) respectively. We can immediately notice a much improved signal to noise ratio with the 3-

layer mesh. Also, we find an emergence of signal from a confined spot on lower corner of the diabolo for horizontal polarization (figure 6.3c). For the in-plane polarization of 90°, we see a much weaker signal along both the edges of the right triangular cavities (figure 6.3d).

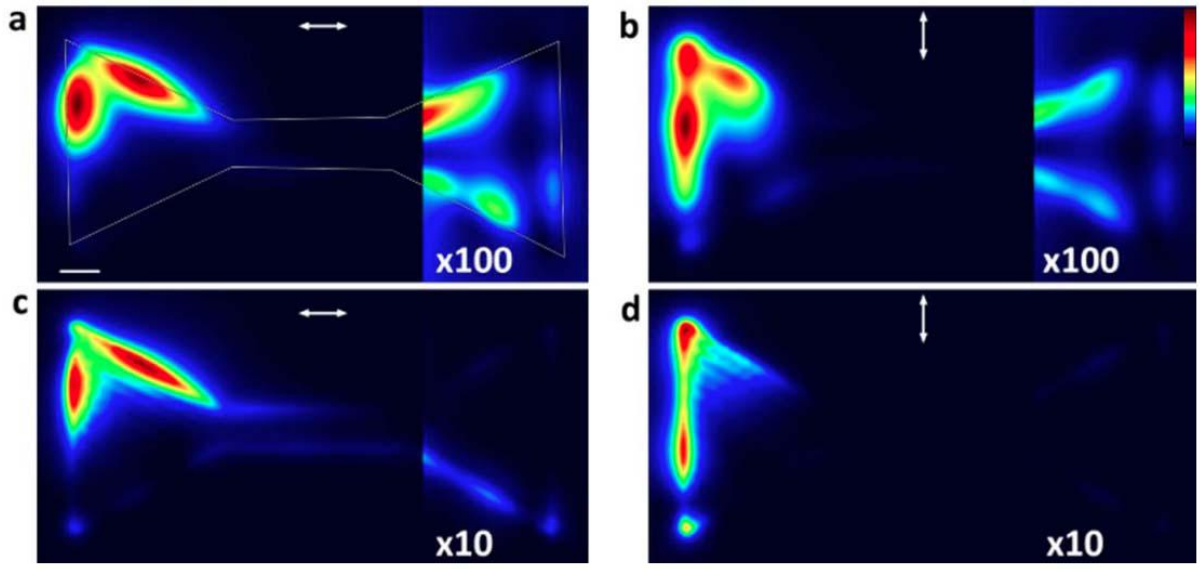


Figure 6.3 (a, b) Near-field transmission maps for horizontal and vertical polarization respectively computed by exciting the upper left apex of a 650nm symmetrical diabolo with a plane wave convoluted in the shape of a Gaussian beam. A single layer mesh is used for the computation, prepared with hexagonal mesh of size 10nm. The dimensions of the triangular pads of diabolo is 650nm each and the channel is 500nm long and 100nm wide. The inset on the right of both the maps are in 100X color scale. (c, d) Corresponding transmission maps computed on 3- layer mesh of the same dimension. The insets are magnified in the color scale by 10 times. The scale bar in white in figure (a) is 100nm. The double headed arrows represent the direction of polarization of the excitation beam.

6.2.3 Excitation of the diabolo structure by real Gaussian function

The excitation mechanism was further improved by Christian Girard by defining the real Gaussian illumination source [14]. The source has been defined in materials and methods chapter. The shape of the beam has also been presented in chapter III followed by its application on a 1500nm nanorod. Here, we will use the same source for excitation of 650nm symmetrical diabolo structure. Figure 6.4 shows the two transmission maps for (a) horizontal polarization and (b) vertical polarization computed on 1-layer mesh with Gaussian excitation. Well defined and confined hot spots appear, irrespective of the polarization on both the triangular cavities. Interestingly, we have very less noise in the upper right part of the diabolo in this case as compared to the dipole and plane wave excitation for horizontal polarization (figure 6.4a). The muted region parallel to the edge of the triangular pad has also disappeared with the Gaussian excitation. Thus, the computational limitations that appeared with the previous two excitation

sources on single layer mesh have been successfully suppressed with the use of Gaussian beam. Well-defined hot spots are observed along both the edges of the right triangular cavity with slightly more signal on the lower edge.

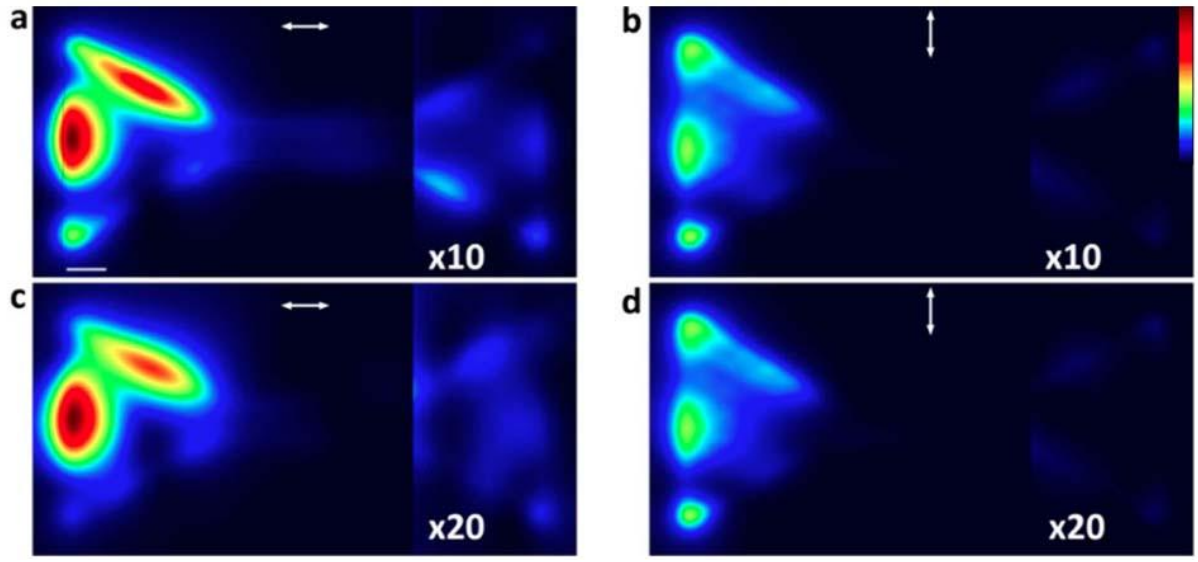


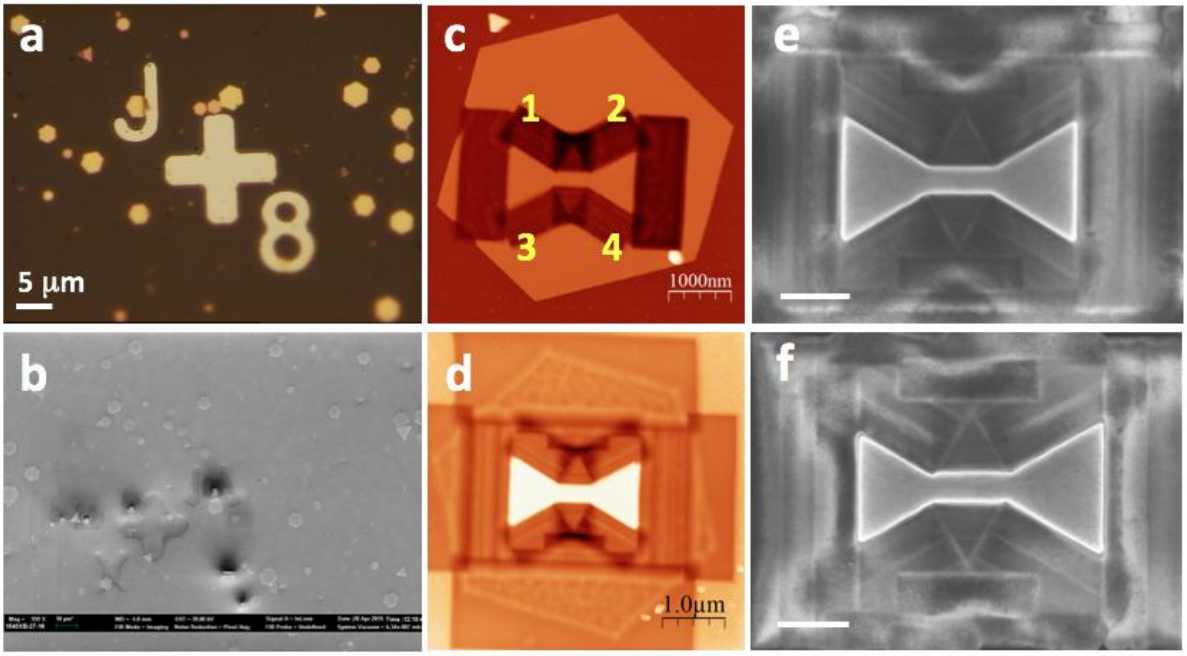
Figure 6.4 (a, b) Near field transmission maps for horizontal and vertical polarization respectively computed by exciting the upper left apex of a 650nm symmetrical diabolo with a real Gaussian beam. A single layer mesh is used for the computation, prepared with hexagonal cells of size 10nm. The dimensions of the triangular pads of diabolo is 650nm each and the channel is 500nm long and 100nm wide. The inset on the right of both the maps are in 10X color scale. (c, d) Corresponding transmission maps computed on 3- layer mesh of the same dimension. The insets are magnified in the color scale by 20 times. The scale bar in white in figure (a) is 100nm. The double headed arrows represent the direction of polarization of the excitation beam.

For the in-plane polarization of 90°, a much weaker hotspots are observed on both the edges of the right cavity (figure 6.4b). The simulation is repeated with 3 layer mesh and the corresponding transmission maps are shown in figure 6.4(c,d) for the two orthogonal in-plane polarizations. The transmission in the diabolo structure is similar to what we observed for the single layer mesh for both the polarizations other than a muted hot spot on the lower apex of the left cavity for horizontal polarization (figure 6.4c). A decrease in the transmitted intensity to the right cavity is also observed irrespective of the polarization direction of the excitation beam.

6.3 Designing of diabolo

The structure proposed in figure 6.1(a) As is difficult to synthesize by colloidal chemistry. Thus, we used a mixture of top down and bottom up approach to fabricate such structures. The diabolo shaped devices were produced by milling out crystalline gold micro

platelets deposited on ITO coated glass coverslip. The hexagonal platelets of adequate size can be easily selected due to polydispersity of the colloidal suspension. These platelets can be easily located in optical microscope and electron microscope with labelled cross-marks as shown in figure 6.5 (a,b) respectively. The hexagonal platelets with diameter of 3-5 μm were milled by using a FIB system integrated in a Zeiss 1540 XB dual beam microscope (See Materials and methods).



Figures 6.5 (a, b) Optical and SEM images of hexagonal gold microplatelets along with cross marks respectively. (c) AFM image recorded after the first FIB milling step and showing the diabolo structure defined inside a 5-mm diameter hexagonal platelet. (d) AFM image of the same sample after the second step dedicated to the removal of the peripheral Au platelet areas. (e-f) SEM images of two diabolo structures with different triangular pad sizes and channel dimensions. Scale bars are 500 nm milled with Gallium ion beam.

The milling protocol consists of two steps. In the first step the diabolo pattern is milled out of the hexagonal gold platelets. The second step of milling takes care of the peripheral area of the starting hexagon which results in a well separated diabolo shaped structure on the substrate. Figure 6.1 (c, d) display the AFM image of the milled structure after step 1 and step 2 respectively. The milling of diabolo pattern is performed by designing a pattern comprising several milling boxes. A set of three boxes at angles of 120° is used to mill the upper left region (region 1 in figure 6.1c) on the microplatelet. Similar boxes are used to mill out region 2,3 and 4. This is followed by use of three horizontal boxes in between region 1 and 2 to mill out gold from the region. Similarly, the area between region 3 and 4 is also cleaned. The two big vertical boxes are then used to mill the left and the right sides of the platelet. The overlap in the position

of the milling boxes results in uneven milling around the diabolo. This is evident from the AFM images (figure 6.5c, d) and the SEM images of the two diabolos in figure 6.5 (e, f). To avoid the uneven milling of the diabolo, the milling protocol was improved by interfacing our dual beam microscope with a Raith Elphy Multibeam pattern generator. We can design trapezium of desired dimension in the pattern generator and avoid the overlaps. A much even and improved milling of diabolo is obtained from this protocol. The SEM images of diabolo prepared from this protocol is shown in figure 6.6 (a-c). A typical ion current of 1pA and a dose of 8000μC/cm^2 were used to ensure a thorough milling of the gold substrate while avoid milling too much into the ITO substrate. The lateral size of the triangular pads of the diabolo designed ranges from 600 to 1000 nm, which is in same range as of chemically synthesized triangular cavities. The typical length and width of the channel is 500nm and 200nm respectively.

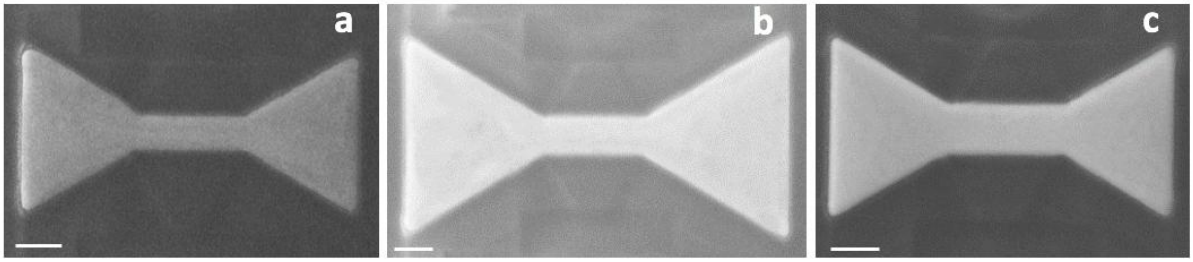


Figure 6.6 SEM images of diabolo milled with Raith Elphy multibeam pattern generator. The scale bars are 200nm.

6.4 Transmittance of plasmonic signal in a 2D diabolo cavity

The diabolo has been experimentally investigated by TPL in two mapping modes, namely confocal and image plane microscopy. Confocal TPL maps provide maps proportional to the squared in-plane SP-LDOS and reveal the sharp modal structure of the 2D confined plasmons as explained in the material and method section. The image plane maps are recorded from the entire structure by leakage radiation microscopy with a fixed excitation spot and will be commented in the next section. We first consider the simulation of the projected in-plane SPLDOS (figure 6.7a-d) and TPL maps (figure 6.7e-f) with a beam waist of 300nm for different polarizations of the incident beam. The modal structure of the diabolo is evident from the projected SPLDOS maps. The SPLDOS map in figure 6.7(a) indicates that when the SPLDOS is projected along the horizontal linear polarization, a finite SPLDOS exists along the channel, thus potentially allowing transfer of the plasmonic signal. However, on turning the polarization to vertical direction, a sharp dip in the projected SPLDOS in the channel is observed (figure

6.7b). On further rotating the polarization direction of the incident beam to 120° and 150° in figure (6.7c,d) respectively a break in symmetry of the SPLDOS pattern is observed. The four TPL hotspots at the extremities of the diabolo in the figure 6.7(e) are strongly reminiscent of the ones observed in the crystalline triangular gold prism [15] .

-

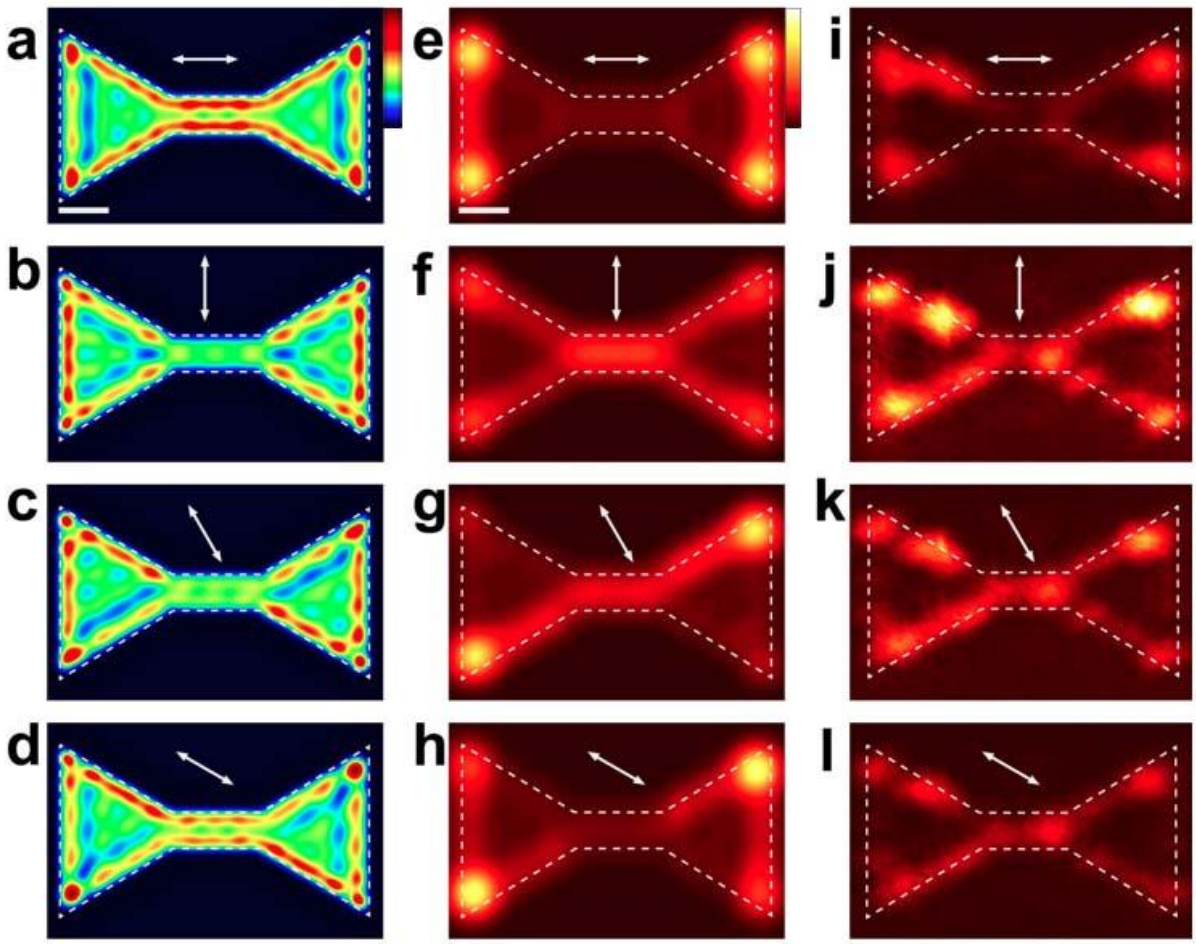


Figure 6.7 (a-d) Partial SPLDOS maps at 810 nm, obtained for projection along the (a) 0°, (b) 90°, (c) 120°,(d) 150° polarization directions. (e-h) Simulated confocal TPL maps for an excitation at 810 nm, with a realistic beam waist of the incident Gaussian beam of 250 nm diameter. (i-l) Experimental confocal maps recorded for the same corresponding polarization directions. The sample is described in Fig. 6.2. The SPLDOS maps, the experimental and simulated maps are separately normalized.

The presence of these hot spots on the apices of the diabolo structure suggests that the modal features of the structure is preserved even after the introducing a channel in between. These hotspots at the extremities are thus good candidates as efficient input and output location in the diabolo structure for the transmission of plasmonic signal. The intensity of the hotspots at the extremities in figure 6.7(f) decreases as the linear polarization is flipped along the vertical

direction. Thus when the position at hotspot is excited with a vertical linear polarization, it does not result in bright TPL indicating a less effective incoulping (Figure 6.7(b)). Interestingly this coincides with a minimal SPLDOS intensity in the channel. Both aspects would be detrimental to proper transmission. As in the earlier studies of crystalline prisms, we have performed experimental mapping of the TPL in diabolo. Figure 6.7 (i-l) display experimental TPL confocal maps corresponding to simulated maps in figure 6.7 (e-h). A nice match between the experimental and simulated maps is observed. In figure 6.7(e) and (i), for horizontal polarization, the hotspots generated by the TPL emission are localized at the extremities of the diabolo structure, while for vertical polarization excitation in figure 6.7(f) and (j), the TPL emission can be observed from the channel and the extremities like wise. Similarly, for the figure 6.7(g) and (k) where the linear polarization is 120° and for the figure 6.7(h) and (l) where the linear polarization is 150°, we have TPL emission along the diagonally opposite corner, edges and the channel. One should notice that in all the four experimental maps, a constant hot spot is visible in the upper left edge of the triangular cavity, which was due to some defect on the diabolo structure.

6.4.1 Tuning of transmittance with incident polarization and excitation position

In this section we focus on the plasmonic information transmittance in the diabolo structures from one apex of the first triangular cavity to the opposite triangular cavity. The SEM image of the diabolo under observation is shown in figure 6.8(a). The side of the triangular cavities are 937 and 913nm while the channel is 500nm long and 200nm wide and corresponds to the structure examined in the confocal configuration before. The input and output positions have been highlighted by red and blue circles respectively. Figure 6.8 (b) shows the near-field simulated transmittance spectra where the spectral distribution of the delocalized plasmon modes have been computed at output (O) for excitation with the horizontal or vertical polarization at input (I). The transmittance spectra has been calculated in the spectral window ranging from 660nm to 900nm with 20 points of computation and a step size of 12.5nm to get a smooth spectra. For a horizontally polarized excitation of the diabolo (black curve), the spectra show a broad peak between 750 and 850 nm. When the polarization is flipped by 90°(red curve), the spectrum is completely flatten. This contrast in transmittance intensity at the output for the two orthogonal polarizations leads us to choose 810nm among the available excitation wavelength for the experiments.

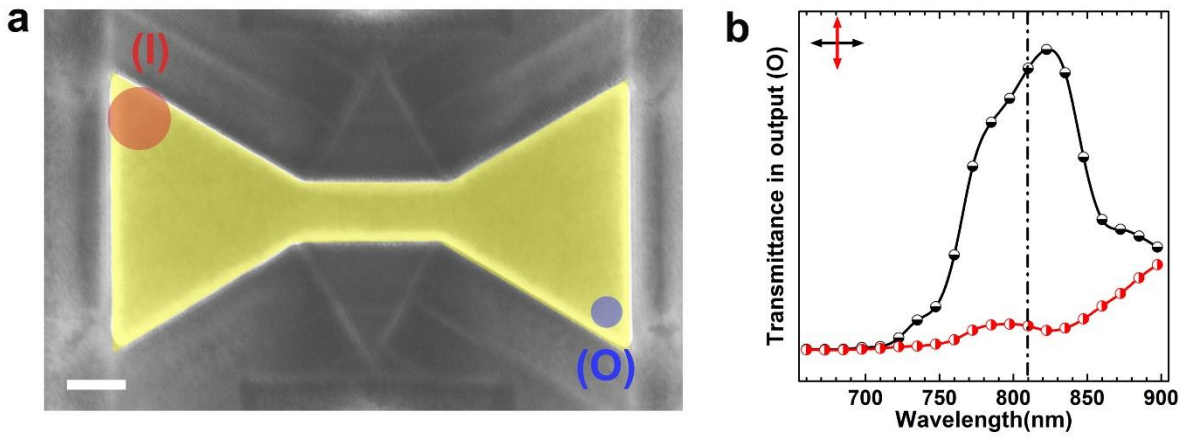


Figure 6.8 SEM image of the diabolo considered for the experimentation with triangular pads of size 937nm(left) and 913nm(right) connected by 500nm x 200nm channel. The red dot on the left - top corner denotes the input position (I) and the blue dot in the right corner denotes the point of collection (O). (b) Near-field transmittance spectra calculated at readout (O) for an excitation in (I) for the 0° and 90° polarization of the excitation beam (black and red curve respectively). Scale bar in black in (a) is 200nm.

On flipping the polarization of the excitation beam by 90°, there is no more emergence of localized TPL signal from the right triangular cavity of the diabolo as shown in the figure 6.9(b). This switching of TPL signal at the output (O) of the diabolo on changing the polarization of the incident beam becomes more evident in the 10X magnified color scale insets on the right display in figure 6.9 (a, b). This effective modulation of transmitted signal for two orthogonal polarizations can also be seen in the TPL intensity versus position plot obtained from the cross-cut on the diabolo (figure 6.9(c)). The cross-cut starts from the excitation spot (I) and goes through the channel to end at the output (O) as displayed by black dashed line in figure 6.9(a). These results are very faithfully reproduced in the simulated near-field transmission maps shown in figure 6.9(c, d) which correspond to image plane transmission maps in figure 6.9(a, b). The Gaussian beam excitation has been used to compute the transmission maps with a single layer mesh. Out of the three excitation sources discussed in the section 6.2, the plane wave excitation and dipole excitation result in significant noise in upper part of the right triangular cavity for single layer mesh (figure 6.2a and 6.3a). The 3-layer mesh cannot be used for a diabolo with cavity size as large as 925nm as number of points on the mesh far exceeds the permissible computation limit on our supercomputer. This leads to the selection of real Gaussian beam for the excitation of the diabolo with single layer mesh. Also, the Gaussian beam excitation gives similar result for both single layer and 3-layer mesh (figure 6.4a-d). It also accounts for most of the features observed in the experimental

transmission maps irrespective of the incident polarization. Here, it is important to mention that the transmittance maps are computed in the near-field and are linear in nature while the experimental transmission maps are recorded in the far-field and are nonlinear TPL signal. A transmission of 2.05% is observed on the diagonally opposite apex of the right triangular cavity, 'O' for a horizontal linear polarization (figure 6.9c). So, the introduction of the channel between the triangular pads has certainly increased the transmission.

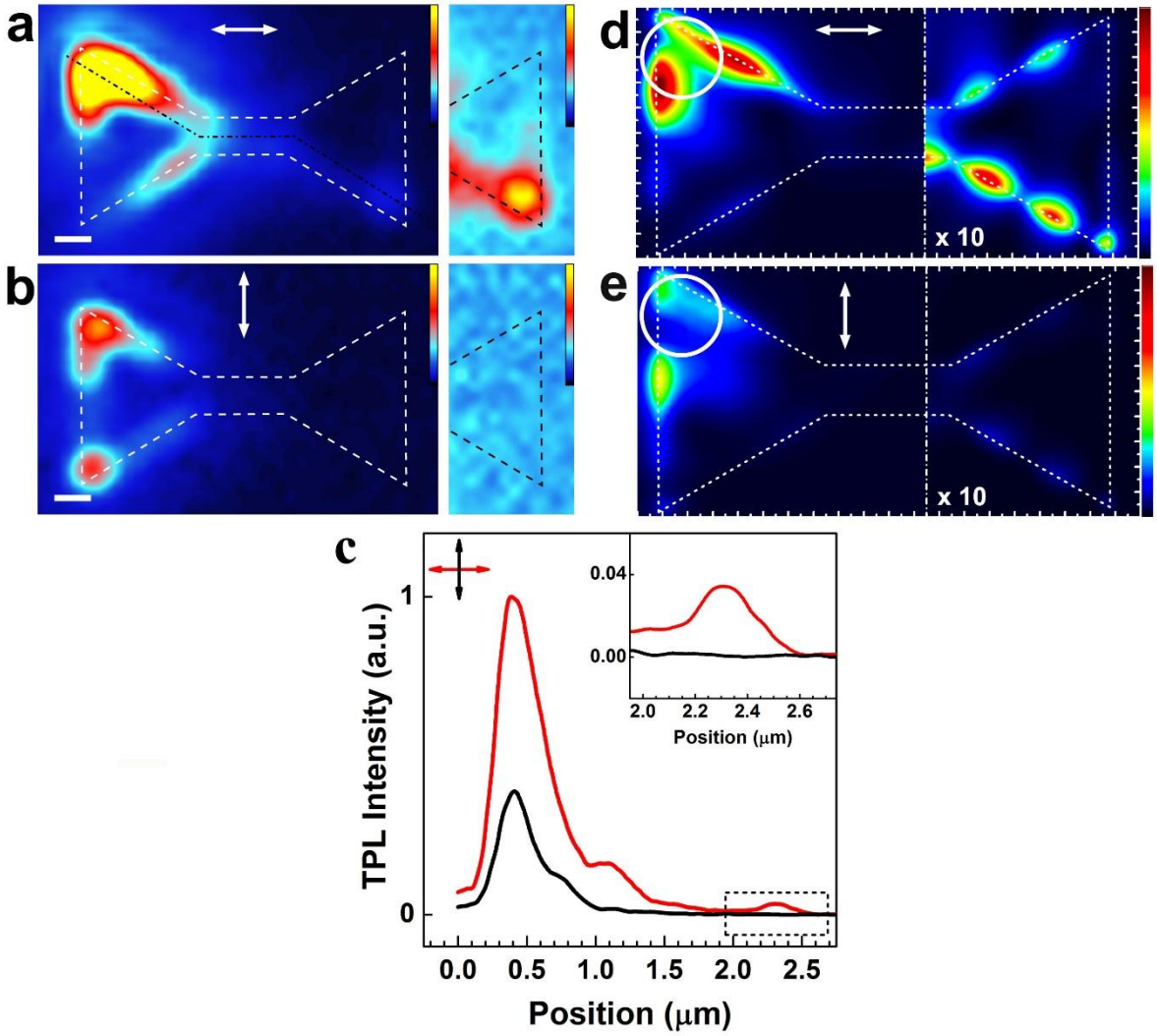


Figure 6.9 (a, b) Image plane non-linear luminescence maps of the diabolo structure shown in figure 6.2(a) when the 810-nm excitation is placed in (I) for an incident beam polarized at (a) 0°and (b) 90°. The insets on the right display the signal from the right triangular area with a 10x magnified color scale. (c) Non-linear luminescence profiles extracted from (a) and (b) along the path indicated by the dash-dotted line in (a). Inset: Magnified plot of the output (O) region corresponding to the dotted box in the main graph. (d,e) Simulated near field transmittance maps corresponding to experimental image plane maps in 9a,b) respectively. Scale bars are 200 nm.

In order to examine the sensitivity of the fabrication procedure, several diabolo were produced and studied. Confocal TPL maps were then recorded on a similar diabolo structure with slightly different pad sizes to check the reproducibility of the transmission modulation in the diabolo structure. The new diabolo structure has triangular cavities of lateral size 1018nm and 967nm with channel of length 498nm and width 190nm (figure 6.6(b)). This diabolo structure will be referred now onwards as "990nm symmetrical diabolo" and the previous one as "925nm symmetrical diabolo" for avoiding the confusion. Figure 6.10(a-d) display the projected SPLDOS maps computed for projection along 0°, 90°, 120° and 150° to the horizontal respectively. If we compare the projected SPLDOS maps presented here with the ones for the 925nm diabolo, we can see that overall SPLDOS distribution pattern is similar. However, the bigger diabolo sustain more antinodes on its edges in comparison to the previous diabolo structure.

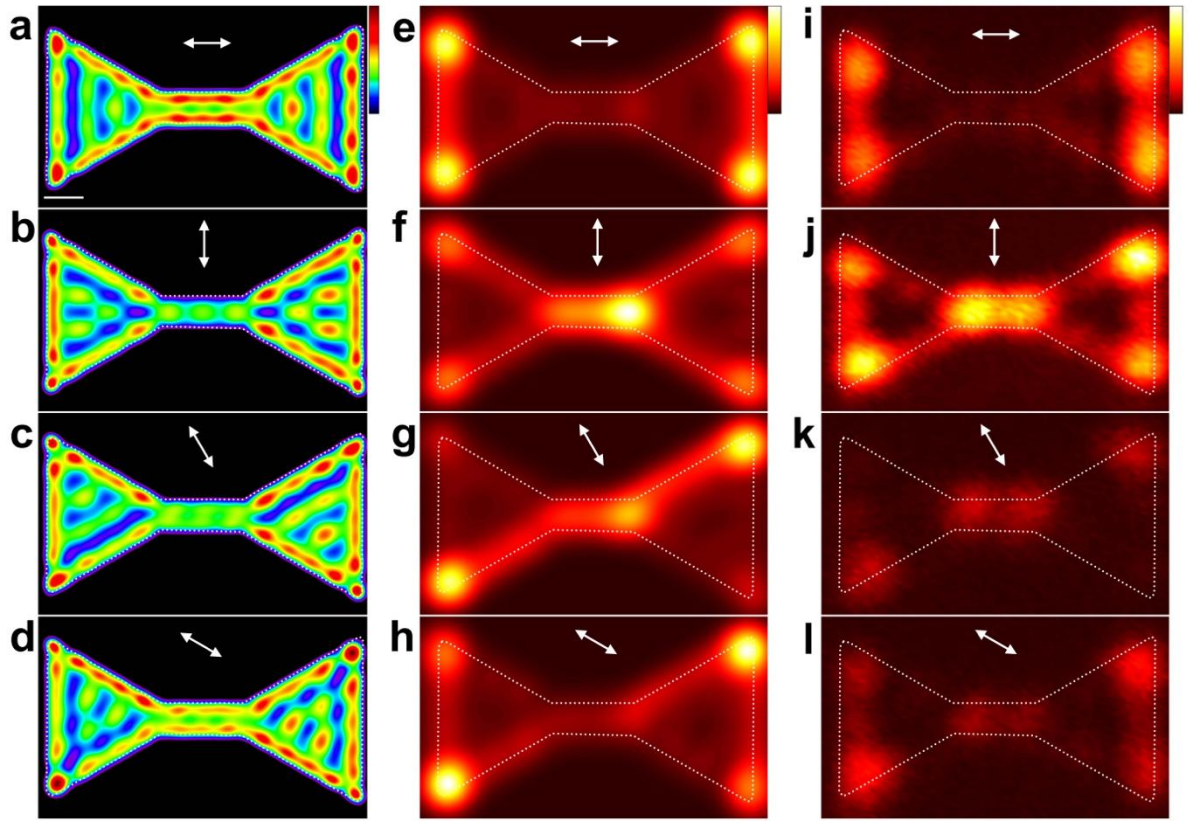


Figure 6.10 (a-d) Partial SPLDOS maps of symmetrical diabolo with 990nm symmetrical diabolo at 810 nm, obtained for projection along the (a) 0°, (b) 90°, (c) 120°,(d) 150° polarization directions for 990nm symmetric diabolo (e-h) Simulated confocal TPL maps for an excitation at 810 nm, with a realistic incident Gaussian beam waist of 250 nm. (i-l) Experimental confocal maps recorded for the same corresponding polarization directions. The SPLDOS maps, the experimental and simulated maps are separately normalized.

The simulated TPL maps shown in figure 6.5(e-h) also show similar pattern as shown by the TPL maps for 925nm diabolo. Only notable difference observed here is the presence of the higher intensity spot on the right end of the channel for the excitations with 90° and 120° polarizations. This hotspot in the channel is probably due to the larger cavity on the right side as compared to the left side which results in a dominant hotspot at the right end of the channel. The corresponding experimental TPL maps for the 990nm symmetric diabolo is displayed in figure 6.10(i-l). A cleaner and defect free diabolo structure ensure an even better match of the experimental and simulated pattern as compared to the 925nm diabolo.

Figure 6.11 shows simulated near-field transmittance spectra of the two diabolo for the two orthogonal polarizations (horizontal in black and vertical in red) computed at output (O). At 810nm we can see a similar transmittance intensity for both the diabolo for both the polarizations. These suggests that the 990nm diabolo should have similar transmittance behavior as the 925nm diabolo. This repeat in transmittance modulation features over micrometer distance in two different diabolo structures suggest reproducibility and robustness of the fabrication technique. Figures 6.7, 6.9 and 6.10 strongly suggest that the transmittance is obtained by a specific spatial and spectral excitation of SP modes of the diabolo, yet direct propagation could occur in the thin patterned film.

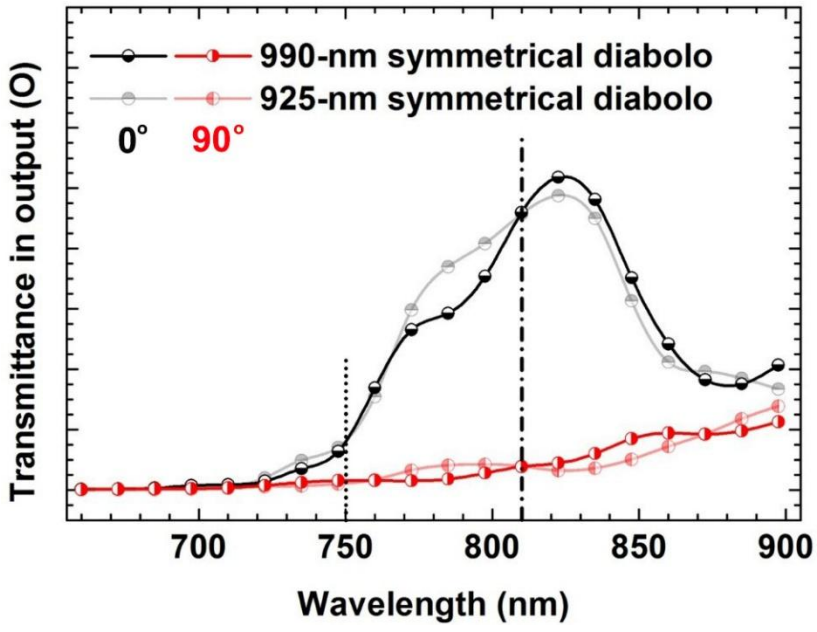


Figure 6.11 Near-field transmittance spectra calculated at readout (O) for an excitation in (I) for the 990 nm symmetrical diabolo with that of 925nm symmetric diabolo shown in figure 6.8(e).

If condition for transmission is related to adequate excitation of an eigenstate, it should be depending in a non-trivial way on the excitation location. We thus considered exciting the

structure in other locations while monitoring the output non-linear emission. In figure 6.12, we show the nonlinear luminescence maps when the 925nm symmetric diabolo is excited at the left entrance of the channel (Channel input point C_i, figure 6.8(a)). The insets on the right show corresponding 10x magnified intensity maps of the output regions. All the other excitation parameters are kept same as in the figure 6.9. In this case, a horizontally polarized excitation generated a weak TPL signal from the apex of the right triangular cavity (figure 6.12(a)) while for the vertical polarized excitation a high intensity spot can be seen at output (O) (figure 6.12(b)) in addition to the confocal emission at C_i. Stronger confocal emission in 6.12(b) compared to 6.12(a) is consistent with the relative intensities at C_i in figure 6.7(f) versus figure 6.7(e) and figure 6.7(j) and figure 6.7(i). The simulated near-field SP transmittance maps are shown in figure 6.12(c) and (d) for horizontally and vertically polarized excitation at C_i respectively with 10X color scale in the inset. Both the relative intensity distributions and the spatial emission patterns observed in the TPL image plane maps are faithfully accounted for in the transmittance maps both in the channel and output triangle regions. The transmission pattern on both side of the channel match quite well with the transmittance map. The asymmetry at the output in the experimental transmission images might be due to asymmetry in the experimental TPL pattern on the upper edge of the left pad (figure 6.7i). The transmittance modulation can be clearly seen in the experimental intensity I-C_i-O profiles plotted in Figure 6.12(e). The 90° polarization flip produces a 9.0-fold increase of the confocal emission at C_i in contrast to an ON/OFF ratio of 3.2 at the output (O). It is important to note here that the distance between the channel entry point (C_i) and the output (O) is around 1.1 μm which is almost half of the distance between in input at the apex (I) and the output (O) (~ 1.9 μm). This suggests that the transmission does not occur only by simple propagation of a SPP in the patterned film as the emission would be higher upon excitation in C_i versus I. We attribute this lack of transmittance efficiency to the low density of state at point (C_i) observed in Fig. 6.4(e), which makes the energy in-coupling less effective. The optimal transmittance for excitation at C_i for the vertical polarization is consistent with the confocal map variation and suggests that in spite of its shape, the channel cannot be considered as a rod which do not transmit for the vertical polarization [18], [19]. This counter-intuitive behavior also indicates that the diabolo is just not a juxtaposition of two triangular shaped cavities and a rod shaped channel sub-structures and the SP transmission through the diabolo structure is different from that through individual triangular cavities or rectangular channel of same dimensions. The diabolo sustains specific resonances, the spatial distribution of which specifically carry the

plasmon signal from a high SP-LDOS area to another through the finite SPLDOS present in the channel. This is more accurately demonstrated by calculating the near-field plasmon transmittance in which the SP-LDOS is now calculated in a chosen output point as a function of the excitation in a different input point.

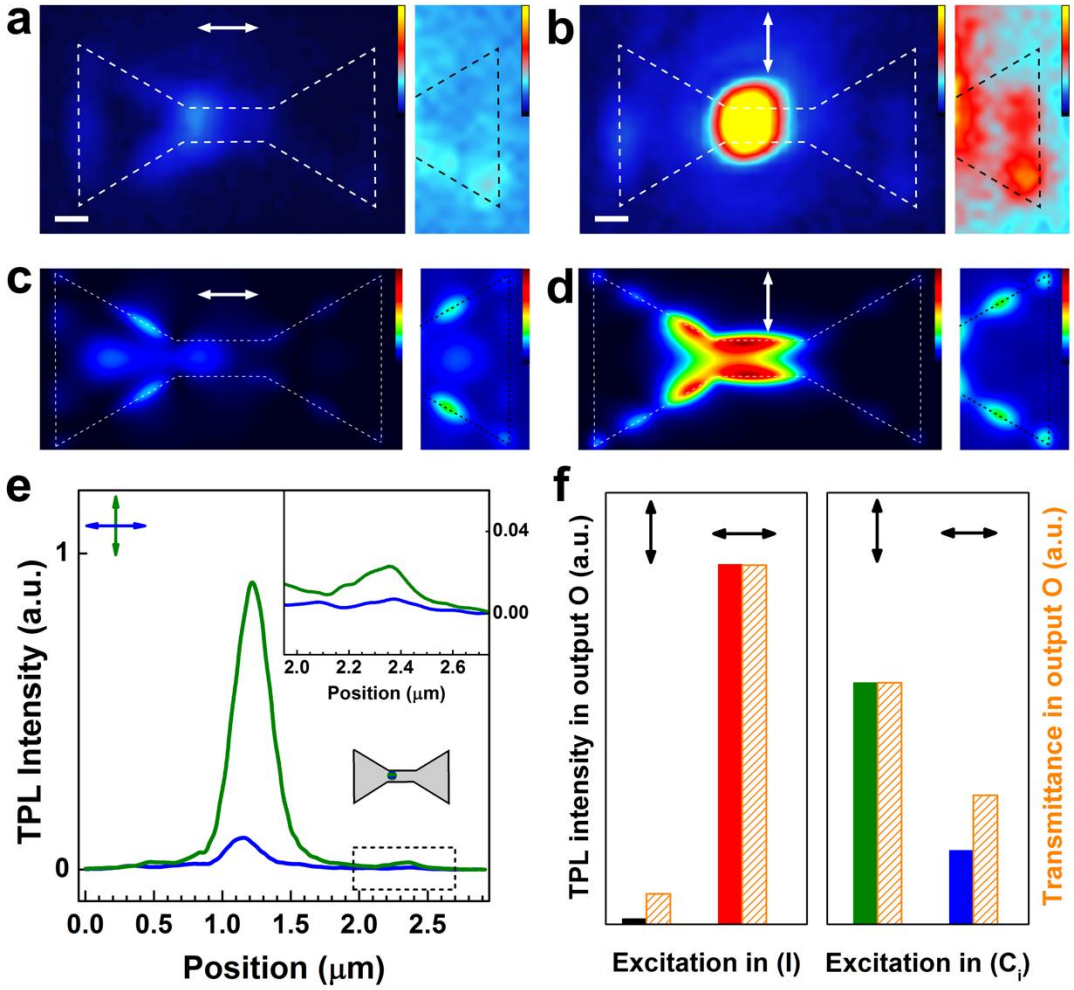


Figure 6.12(a, b) Non-linear transmittance maps of the diabolo structure shown in Fig. 6.2a when the excitation is placed at the channel input (Ci) for an incident beam polarized at (a) 0°and (b) 90°. The insets on the right display the signal from the right triangular area with a 10x magnified color scale. Scale bars are 200 nm. (c) and (d) Simulated near-field linear SP transmittance maps corresponding to (a) and (b) respectively. Realistic discretized 2D model of the sample and Gaussian beam (250-nm diameter, λexc = 810 nm) are used. (e) Non-linear luminescence profiles extracted from (a) and (b) along the path indicated by the dash-dotted line in Fig. 6.2(a). Inset: Magnified plot of the output (O) region corresponding to the dotted box in the main graph. (f) Histograms comparing the experimental non-linear luminescence intensity at the output O (full colored bars) with the near-field SP transmittance (striped orange bars) when the excitation beam is placed in either input I (left panel) or channel input Ci (right panel), for both 0° and 90° incident polarizations. The display of the SP transmittance is adjusted in each panel to match the largest experimental output of a given excitation location.

Figure 6.7f shows the transmittance intensity calculated at output (O) for excitation at

the inputs (I) or (C_i). This result has been compared to the experimental TPL intensity measured in image plane maps for the two polarization configurations. For comparison, the output intensity has been maximized for the horizontal polarization when excited at input (I) and for vertical polarization when excited at the entrance of the channel (C_i). The relative simulated transmittance intensity faithfully follow the relative intensity obtained from the experimental confocal TPL maps. This indicates that the eigensates used for transmittance, which are present in I, C_i and O contribute significantly to the SPLDOS in these locations. This comparison also suggests that the variations of both the in-coupling and emission efficiency play a major role in the modulation of the transmittance. For excitation at (I), a higher TPL intensity is observed at the output for horizontal polarization as compared to the vertical polarization where this trend flips for the excitation at (C_i). It is worth noting here that the transmittance maps are recorded in near field and are linear in nature while the image plane TPL are the non-linear far field maps. So, the linear signal travels and produces the nonlinear signal locally at the distant apex. The quantitative difference between the simulated transmittance and the experimental transmittance thus can be attributed to the fact that the simulated transmittance has been computed in the near-field and does not account for the information corresponding to far field propagation.

6.4.2 Tuning of transmittance with incident wavelength

The transmittance through symmetrical diabolo structures sustain broad resonance peak in the spectral window ranging from 650nm to 900nm centered at around 820nm as shown in figure 6.11. Thus, another way to modulate the transmittance in the diabolo structure is to tune the excitation wavelength. Experimentally, the image plane TPL maps recorded on the 990nm symmetric diabolo show significant transmittance on the right triangular cavity when the excitation is polarized along the horizontal direction (figure 6.13(a)) with an excitation wavelength of 810nm. When the polarization is flipped along the vertical direction (figure 6.13(b)), there is no signal on the right triangular cavity. This result is consistent with the TPL image plane results on the 925nm diabolo (figure 6.3(a-e)). The transmittance spectra in figure 6.11 indicates that the transmittance can be spectrally suppressed for both the polarizations when the diabolo structure is excited at wavelengths which are out of resonance. Here we have considered using the wavelength of 750 nm for excitation. At 750nm, the spectral intensity is the same and low for both diabolo structures and low for both polarizations (figure 6.11). In figure 6.13(c,d), simulated near-field transmittance maps are displayed for 0° and 90° excitation polarization respectively for 750nm excitation wavelength. For excitation at the

input (I), there is very small transmittance in the output (O) for 0° polarization as compared to what we observed for excitation at 810nm. Also there is no transmission in the structure for 90° polarization.

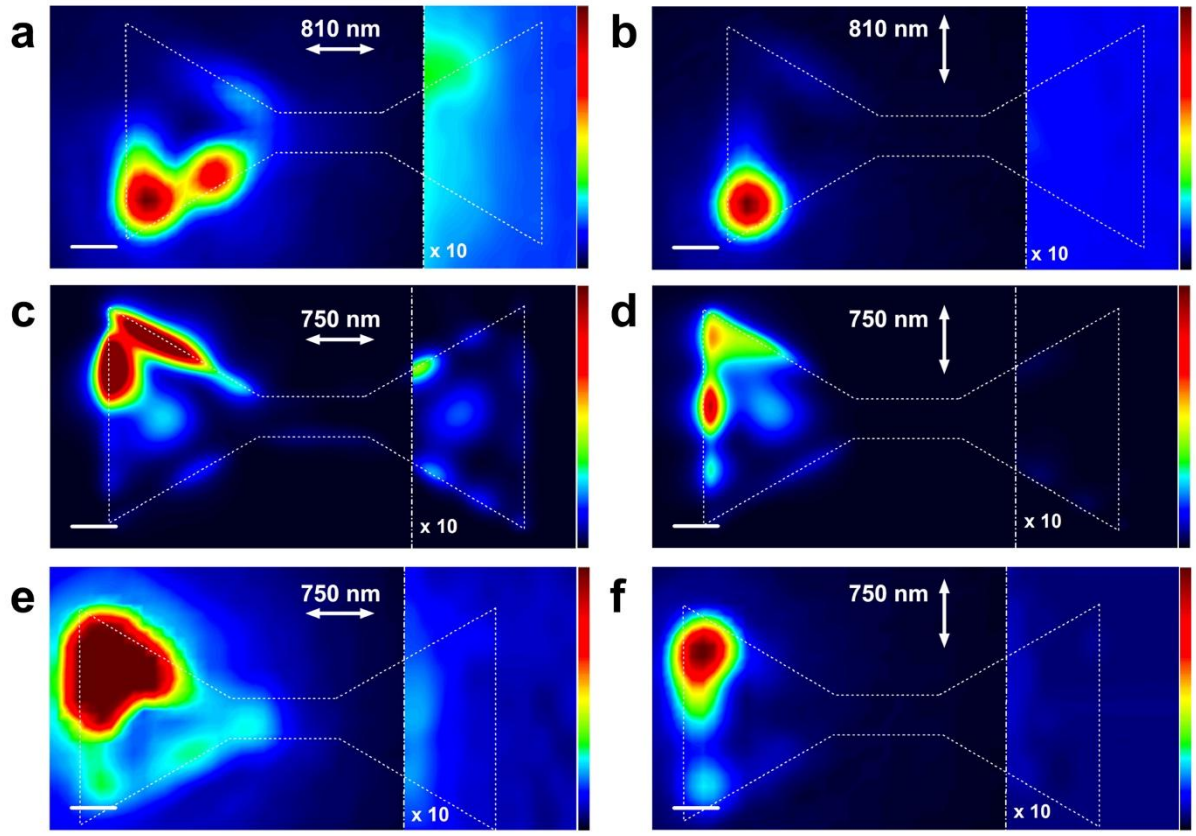


Figure 6.13 (a, b) Image plane TPL maps for the diabolo shown in figure 6.1(a) obtained upon excitation in the lower left corner at 810 nm. (c, d) Transmittance maps for the diabolo upon non-resonance excitation in (I) at 750 nm. (e, f) Image plane TPL maps for the diabolo upon excitation in (I) at 750 nm. Scale bars are 200 nm. In maps in panels (a) to (f), the portion on the right of the dotted lines is plotted with a 10x magnified intensity using the same rainbow color scale.

We also performed image plane TPL mapping experiments at 750nm excitation. The results are displayed in figure 6.8(e,f) for 0° and 90° polarizations respectively. The patterns in the excitation pad match closely the simulated near-field maps for both polarizations. The 10X color scale insets on the right show that there is no transmittance in the right triangular cavity of the structure for either of the polarizations. This set of experimental and simulated results further confirms the delocalized mode-mediated transmittance in the resonant diabolo structures.

6.4.3 Spectral detuning in asymmetrical diabolo

In the previous section, we have studied two diabolo structures with similar input and output triangular structures leading to similar transmittance behavior. For the 925nm diabolo, there was a difference of around 25nm between the lateral size of the two triangular cavities while for the 990nm the difference was around 50nm. However, the transmittance spectra of both shows similar characteristics at 810nm. This suggests that a difference of 50nm is not enough to introduce a spectral mismatch between the two triangular pads of the diabolo. The selection of the size of the triangular pads were done based on the dispersion curve we have obtained by plotting the resonance peak position and triangular prism size in chapter IV. The dispersion plot has been redisplayed in figure 6.14. We can see from the dispersion curve that the triangle of size roughly 650nm has four SP modes (denoted by 1,2,3 and 4). If we increase the size of the triangle approximately by 50nm at 700nm, we see the same set of modes. Thus for 990 nm diabolo, in spite of having a gap of 50nm, which induces a slight red shift of the resonances we could transmit through the structure because of presence of same set of resonances which are shifted in energy.

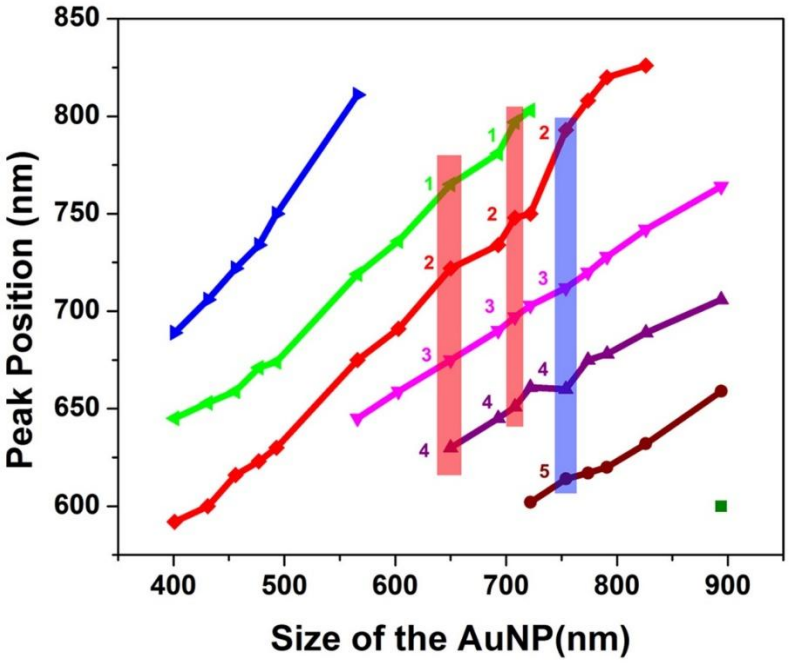


Figure 6.14 Dispersion curve – Size of the gold cavities versus resonance peak position. Horizontally (respectively vertically) split symbols correspond to the 0° (resp. 90°) polarization direction.

Next when we further increase the size of the triangular prism by 50nm to around 750nm now we have a different set of resonances (denoted by 2,3,4,5). This mismatch in the set of resonances in the two pads is potentially a deciding factor for suppression of the

transmission from one pad to another. So, in order to further test the potential of modal engineering of the transmittance features in diabolo structures, we considered a non-symmetrical diabolo with a 90nm difference in the size of the two triangular pads. The dimensions of the channel were kept similar to the one used previously.

Figure 6.15(a) shows the SEM image of the non-symmetrical diabolo with 640-nm left side triangular pad and 730-nm right side triangular pad. For excitation at input (I) with 810nm linearly polarized beam along horizontal direction we have no output observed in output (O) (figure 6.15(b)). Starting from the smaller triangular pad, the TPL signal appears to transmit upto the channel but could not go pass the channel. Similarly, for the linearly polarized beam along vertical direction, we have no output at (O) and the TPL signal transmits inside the first triangular cavity. The series of profiles along the I-C_i-O path in the figure 6.15(d) even demonstrates that this transmission blockage stays for all polarization directions of the excitation beam. This implies that by changing the lengths of the two pads by 90nm we have suppressed the transmission of TPL signal from one apex of the diabolo to the diagonally opposite apex of the diabolo even though the overall size of the diabolo is much smaller. We assume that this broken symmetry of the diabolo design keeps the system off-resonance due to the spectral mismatch between the two modal resonators and does not allow for a delocalized transmission. This spectral mismatch has been shown in figure 6.15(b) where the total in-plane SPLDOS plotted at 810 nm evidences the non-symmetrical modal structure with a predominant m=3 mode on the left side and a predominant m=5 mode on the right side. In figure 6.15 (e, f) shows the near-field SP transmittance maps for horizontally and vertically polarized excitation respectively at (I). The simulated maps match nicely with our experimental results and confirm the suppression of the transmittance. In the left pad, the confined hotspot with the extension along the edges observed in the figure 6.15(b) can also be seen in the simulated maps in the figure 6.15(f). The simulated map for the horizontal polarization also shows the continuation of the signal upto the channel as in the experimental maps. There is also a very good match of the spatial distribution of the very weak transmittance signal on the right triangular pad as shown in the 10x color scale image on the right inset of the figure 6.15(b, f) for the experimental and the simulated maps respectively. Similarly, for the vertical polarization, we have an excellently well matching TPL signal merging from the left triangular pads and absolutely no signal from the 10x enhanced inset on the right of the diabolo (figure 6.15(c, g)). The spatially modulated long-range transmittance monitored in the TPL image plane maps results from the spectral match or mismatch between the modes of the two triangular cavities of the diabolo structure but give no information about the spectral distribution of the modes.

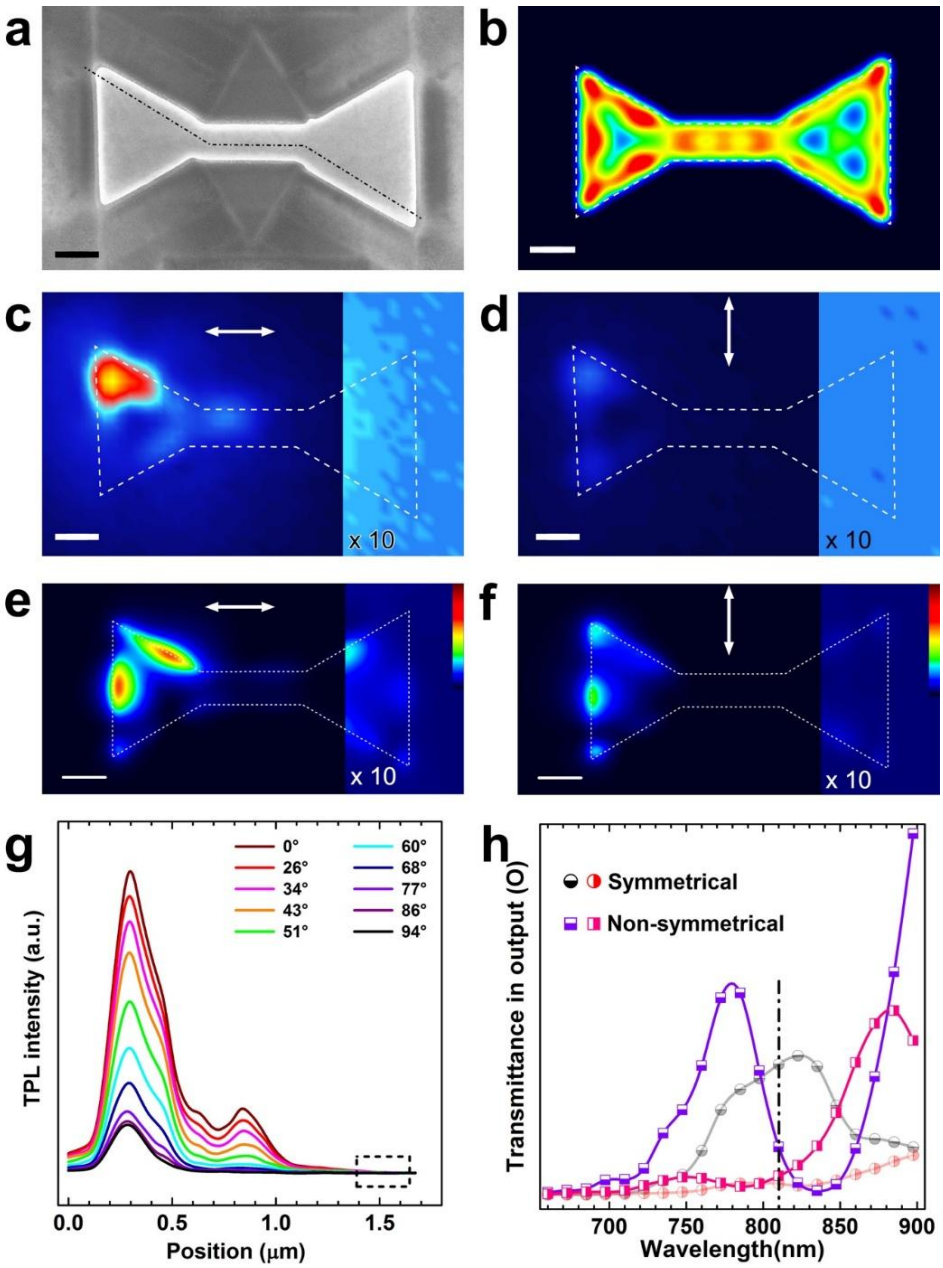


Figure 6.15 Transmission blockade by spatial and spectral mismatch in non-symmetrical diabolo. (a) SEM image of a non-symmetrical diabolo structure composed of a small (630 nm side) and a large (730 nm side) triangles on the left (respectively right) of the 498 x 160 nm channel. (b, c) Image plane non-linear luminescence maps of the non-symmetrical diabolo structure shown in (a) when the excitation is placed in (I) for an incident beam polarized at (b) 0°and (c) 90°. (d) Non-linear luminescence profiles along the path indicated by the dash-dotted line in (a) for a series of polarization directions of the incident beam between 0° and 94°. The dashed box indicates the output O region. (e) Full in-plane SP-LDOS map of the non-symmetrical diabolo shown in (a). (f, g) Simulated near-field SP transmittance maps corresponding to (b), (c) respectively. Realistic discretized 2D model of the sample and Gaussian beam (250-nm diameter, □exc = 810 nm) are used. (h) Near-field transmittance spectra calculated at readout (O) for an excitation in (I) for the symmetrical (black and red) and non-symmetrical (purple and pink) diabolos.

We next use the near-field transmittance simulation to compute the spectral distribution of the delocalized plasmon modes present in the diabolo structure. In figure 6.15h, we show two transmission spectra computed at the output (O) for asymmetrical diabolo excited with linear polarization along horizontal and vertical directions at input (I). As a comparison the previously discussed spectra for the 925nm symmetrical diabolo structure are overlaid. The transmission curve for the asymmetrical diabolo shows a comparatively sharper peak (700-800nm) centered around 775nm for horizontal polarization excitation (in purple). The spectrum is comparatively lower in the intensity at 810nm. Also for the vertical polarization excitation (in pink), the intensity is lower below 830nm. Thus, both the excitation configurations show a low transmittance intensity at 810 nm, which confirms the off-resonance response observed in the transmission map. The spectral differences between the two diabolo are related to the size difference, the non-symmetrical one comprising smaller triangular cavities naturally shows blue-shifted peaks compared to the symmetrical one.

6.5 Conclusion

In conclusion, we have successfully designed and investigated a 2D mesoscale crystalline diabolo structure comprised of two triangular cavities connected by a rectangular channel from a large hexagonal crystalline gold platelet. These diabolo structures sustain SP modes that can be modulated spatially and also delocalized to micrometers length. The complex higher order modes present in the system were probed by confocal TPL microscopy and match excellently with the simulated maps. An image plane mapping of the TPL signal was performed using leakage radiation microscopy. We achieved a confined TPL signal emerging from an apex of the triangular pad upon excitation at the diagonally opposite apex (I) of the other pad. In addition, with the change in position of excitation from the apex to the entrance of the channel, we could successfully tune the transmission. Interestingly, we found that the signal recorded at the output is less for excitation at the channel which is at shorter distance from the output as compared to input (I). The transmission in the diabolo structure was found to depending on the in-coupling efficiency along with SPLDOS distribution along the transmission path. Thus the exact point of excitation was decided by measuring the SPLDOS distribution near the apex so that maximum coupling efficiency can be achieved. The performances of the transmission modulation upon polarization flipping at 810 nm show a large ON/OFF ratio of 130 for the spectrally-matched symmetrical diabolo and an overall transmission efficiency of 3.5% at 2 μm distance. We could thus achieve a successful

implementation of an efficient transmission device by using suitable excitation wavelengths and polarizations at specific input locations in the modal engineered diabolo structure. An even better understanding and control of the system can be achieved by investigating the phase of the transmitted SP signal which could be helpful in explaining the tuning of the transmission in the diabolo structure. This modal design approach for modulation of SP transmission in complex 2D plasmonic cavity contribute to the recent strategies to design active information processing devices. The diabolo structures examined here form the basis of the more complex input/output device for the optical logic gate operations to be discussed in the next chapter.

References

[1] H. S. Chen, J. Y. Wang, S. S. Yeh, C. D. Chen, and H. Y. Lin, "Modulation of surface plasmon wave by photo-induced refractive index changes of CdSe quantum dots," *Appl. Phys. Lett.*, vol. 100, no. 011102, 2012.

[2] D. Pacifici, H. J. Lezec, and H. a. Atwater, "All-optical modulation by plasmonic excitation of CdSe quantum dots," *Nat. Photonics*, vol. 1, no. 7, pp. 402–406, 2007.

[3] J. A. Dionne, K. Diest, L. A. Sweatlock, and H. A. Atwater, "PlasMOStor: A metal-oxide-si field effect plasmonic modulator," *Nano Lett.*, vol. 9, no. 2, pp. 897–902, 2009.

[4] M. J. Dicken, L. a. Sweatlock, D. Pacifici, H. J. Lezec, K. Bhattacharya, and H. A. Atwater, "Electrooptic modulation in thin film barium titanate plasmonic interferometers," *Nano Lett.*, vol. 8, no. 11, pp. 4048–4052, 2008.

[5] R. A. Pala, K. T. Shimizu, N. A. Melosh, and M. L. Brongersma, "A nonvolatile plasmonic switch employing photochromic molecules," *Nano Lett.*, vol. 8, no. 5, pp. 1506–1510, 2008.

[6] M. Rudé, R. E. Simpson, R. Quidant, V. Pruneri, and J. Renger, "Active Control of Surface Plasmon Waveguides with a Phase Change Material," *ACS Photonics*, vol. 2, no. 6, pp. 669–674, 2015.

[7] W. Li, B. Chen, C. Meng, W. Fang, Y. Xiao, X. Li, Z. Hu, Y. Xu, L. Tong, H. Wang, W. Liu, J. Bao, and Y. R. Shen "Ultrafast all-optical graphene modulator," *Nano Lett.*, vol. 14, no. 2, pp. 955–959, 2014.

[8] M. Liu, X. Yin, E. Ulin-Avila, B. Geng, T.Zentgraf, L. Ju, F. Wang, and X. Zhang "A graphene-based broadband optical modulator," *Nature*, vol. 474, no. 7349, pp. 64–67, 2011.

[9] S. Viarbitskaya, A. Teulle, R. Marty, J. Sharma, C. Girard, A.Arbouet and E. Dujardin, "Tailoring and imaging the plasmonic local density of states in crystalline nanoprisms," *Nat. Mater.*, vol. 12, no. 5, pp. 426–432, 2013.

[10] P. Ginzburg, N. Berkovitch, A. Nevet, I. Shor, and M. Orenstein, "Resonances on-demand for plasmonic nano-particles," *Nano Lett.*, vol. 11, no. 6, pp. 2329–2333, 2011.

[11] S. Y. Liu, L. Huang, J. F. Li, C. Wang, Q. Li, H. Xu, H. Guo, Z. Meng, Z. Shi, and Z. Li, "Simultaneous excitation and emission enhancement of fluorescence assisted by double plasmon modes of gold nanorods," *J. Phys. Chem. C*, vol. 117, no. 20, pp. 10636–10642, 2013.

[12] A. M. Kern and O. J. F. Martin, "Excitation and reemission of molecules near realistic plasmonic nanostructures," *Nano Lett.*, vol. 11, no. 2, pp. 482–487, 2011.

[13] A. E. Krasnok, A. E. Miroshnichenko, P. A. Belov, and Y. S. Kivshar, "All-Dielectric Optical Nanoantennas," vol. 20, no. 18, pp. 837–842, 2012.

[14] P. Török, P. Varga, Z. Laczik, and G. R. Booker, "Electromagnetic diffraction of light focused through a planar interface between materials of mismatched refractive indices: an integral representation," *J. Opt. Soc. Am. A*, vol. 12, no. 2, p. 325, 1995.

[15] S. Viarbitskaya, A. Teulle, A. Cuche, J. Sharma, C. Girard, E. Dujardin, and A. Arbouet, "Morphology-induced redistribution of surface plasmon modes in two-dimensional crystalline gold platelets," *Appl. Phys. Lett.*, vol. 103, p. 131112, 2013.

[16] M. Song, J. Dellinger, O. Demichel, M. Buret, G. Colas des Francs, D. Zhang, E. Dujardin, and A. Bouhelier, "Selective excitation of surface plasmon modes propagating in Ag nanowires," *Opt. Express*, vol. 25, no. 8, p. 9138, 2017.

[17] S. Viarbitskaya, O. Demichel, B. Cluzel, and A. Bouhelier, “Delocalization of Nonlinear Optical Responses in Plasmonic Nanoantennas,” 2015.

[18] M. Song, A. Bouhelier, P. Bramant, J. Sharma, E. Dujardin, D. Zhang, and G. Colas-des-Francs, “Imaging symmetry-selected corner plasmon modes in penta-twinned crystalline Ag nanowires,” in *ACS Nano*, 2011, vol. 5, no. 7, pp. 5874–5880.

[19] Z. Li, K. Bao, Y. Fang, Y. Huang, P. Nordlander, and H. Xu, “Correlation between incident and emission polarization in nanowire surface plasmon waveguides,” *Nano Lett.*, vol. 10, no. 5, pp. 1831–1835, 2010.

Chapter VII

Reconfigurable modal plasmonic logic gates

7.1 Introduction

Computation procedures of an arbitrary complexity can be broken down to a very limited number of operations based on certain logic. The choice of the function defines the corresponding logic paradigm. For example, in Boolean algebra, the fundamental logic gates are AND, OR and NOT which can be used to realise more complex logic gate operations such as NAND, NOR, XOR, X-NOR, etc. We will come back to the detail functioning of all the logic gate operations after a brief discussion on technological advancement of the Boolean logic gates. Boolean algebra dates back to 1847 when G. Boole published 'The Mathematical Analysis of Logic' in which for the first time logical statements were expressed in mathematical form. It made a little impact at that time and his work remained obscure for long time. In 1919, W. H. Eccles and F. W. Jordan invented a bi-stable switching circuit based on vacuum tubes [1]. C. E. Shannon was first to realise the similarity between electric switching circuits and Boolean logic. In his master thesis in 1940, he used these principles as a basis for information processing by using electromechanical relays to build logic circuits [2]. Two decades later, in 1959, R. Noyce realized first electronic gates based on transistors. At present, the dominant technology is based on implementation of fundamental logic gates based on field-effect transistors (FET) and complementary metal-oxides semiconductor (CMOS) [3]–[5]. In CMOS logical operations, both n-type and p-type transistors are used to design logic functions. The same signal which turns ON a transistor of one type is used to turn OFF a transistor of the other type. This characteristic allows the design of logic devices using only simple switches. Other models for logic gate operations are based on molecules [6], [7] and DNA [8]. In optics, the logic gate implementation has been theoretically proposed mainly by cascading individual structures [9] or by interferential techniques [10]. Experimentally, the basic logic gate operations have been recently realized by group of H. Xu group in a simple silver nanowire interconnects [11]. The logic gate implemented in this work are based on the principle of interference of plasmons in a nanowire with those introduced by another adjacent nanowire. Similarly, Fu et. al. has reported realizations of nanoscale integrated OR, NOT, XOR and X-NOR, all optical logic gates based on linear interference between SPP modes present in

plasmonic slot waveguides [12]. XOR and NAND gates have also been proposed based on non periodic gold disk-shaped nanoparticles [13]. All these logic gate operations have been obtained by using phase dependent constructive and destructive interferences between plasmon beams in the systems. The working of these kind of interferential devices depends upon the positioning of the one nanoparticle or building block with respect to other. Also, building an integrated circuit based on interferential logic gates will require concatenation of various logic gate structures. For example, in a work reported by H. Xu group, a NOR gate has been implemented by cascading a NOT gate and an OR gate [14]. This will result in very low intensity at the output of the system due to consecutive losses due to concatenation. In this work, we have used here an alternative technique in which various logic gate operations can be realized in a single 2D metallic cavity based on the gedanken experiment (described in [15]). Before going into the details in gedanken experiments, it is worth explaining the functioning of different kinds of logic gates.

All these gates mentioned above have their respective truth tables which defines the value of the output as a function of the input values (figure 7.1). The simplest logic gate operation is NOT gate which is basically a one input – one output gate and performs a negation operation. It means that the NOT gate converts a 1 to 0 and vice versa [figure 7.1(a)]. The NOT gate is also called inverter and NOT A is represented by $\bar{A}$. Next is AND gate which has a minimum of two inputs. For two inputs 'A' and 'B', the output will be '1' only when both A and B are 1. In all other cases, the AND gates return '0' as the output. AND gate works as an electronic circuit with two switches 'A' and 'B' connected in series. Only when both the switches are ON, we have current at the output. The truth table and the graphical symbol of the AND gate has been shown in figure 7.1(b). The figure also shows the NAND gate which is made of an AND gate and a NOT gate and thus just inverse the output of the AND gate. Another basic gate is OR gate (figure 7.1c) which is again a logic operation with a minimum of two inputs. The OR gate works as an electronic circuit with two inputs 'A' and 'B' as two switches connected in parallel. When either of the two switches is ON, we have current flowing through the circuit. The negation of OR gate is called NOR gate and is concatenation of an OR gate and a NOT gate. The other important gate for building an integrated circuitry is exclusive OR gate or XOR gate. These are also a minimum two input gates which gives output as '1' when only one input is '1'. Similarly, for X-NOR gate, when both the inputs are same, the output is '0'. The truth table and the graphical diagram of both XOR and X-NOR gates have been shown in the figure 7.1(d). Other possible logic gate configurations are Copy, Contradiction and

Tautology. As the name suggest, in a Copy operation, a copy of the input is produced at the output (figure 7.1e). In Contradiction logical operation (figure 7.1f), irrespective of the state of the inputs, the output is always zero while in the case of Tautology, irrespective of the input state, the output is always ON.

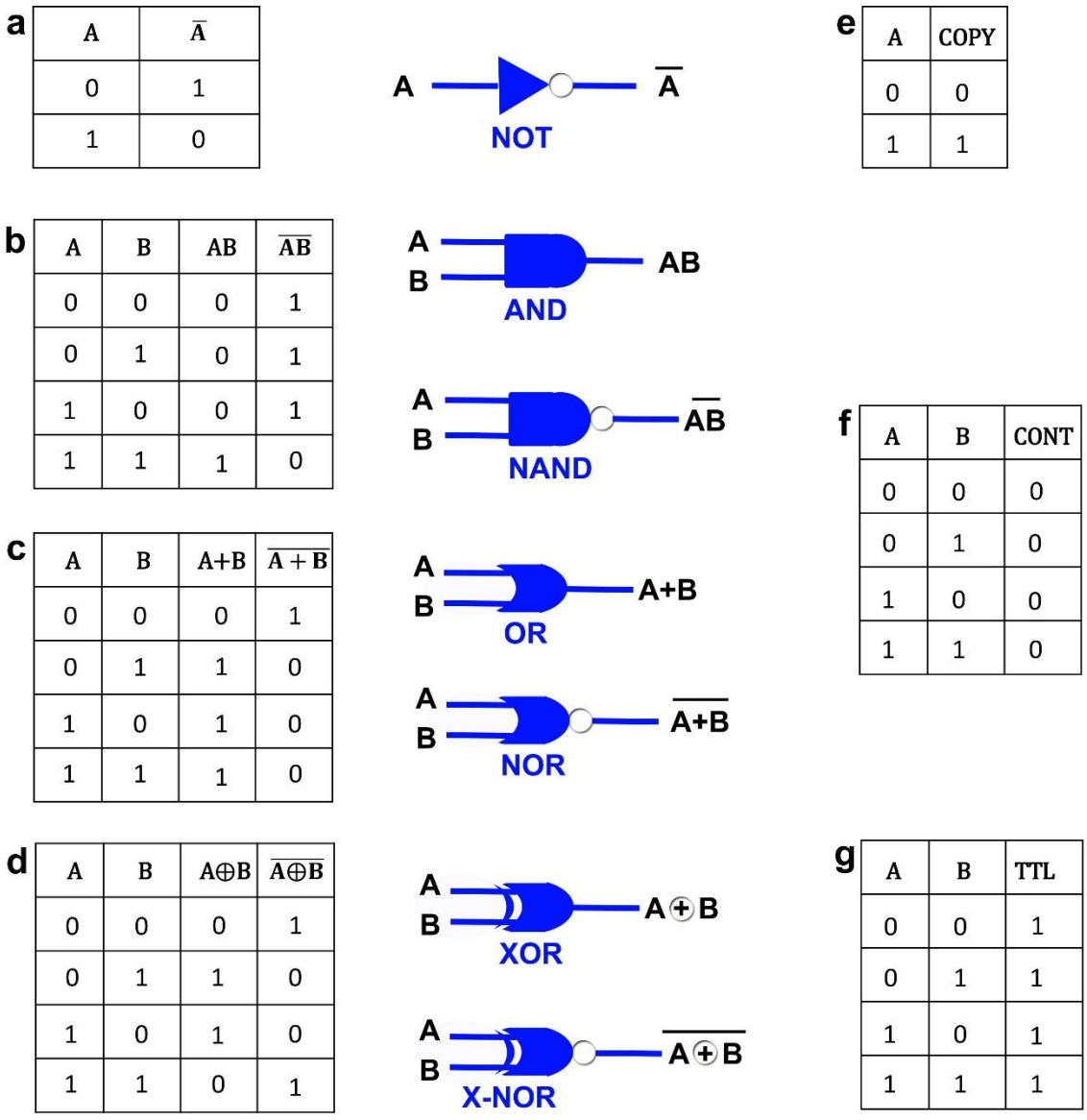
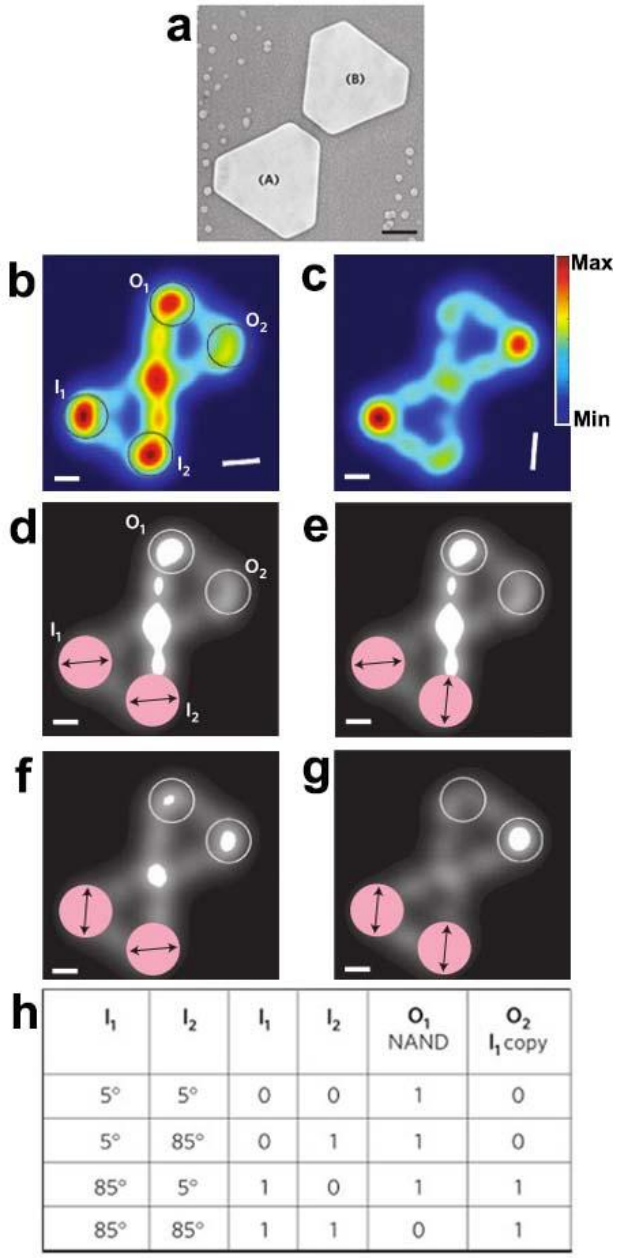


Figure 7.1 Truth table and symbols of (a) NOT gate, (b) AND and NAND gates (c) OR and NOR gates (d) XOR and X-NOR gates. Truth table of (e) Copy , (f) Contradiction and (g) Tautology respectively.

7.2 Gedanken Experiments

A gedanken experiment consists of using two tightly focused laser spots of identical wavelength and power but different linear polarizations for excitation of two input positions and reading the TPL intensity in distant output positions.



h

I_1	I_2	I_1	I_2	O_1 NAND	O_2 I_1 copy
5°	5°	0	0	1	0
5°	85°	0	1	1	0
85°	5°	1	0	1	1
85°	85°	1	1	0	1

Figure 7.2 Plasmonic modal logic gates in coupled nanoprisms. (a)SEM image of a bowtie antenna comprising two truncated triangular prisms. Simulated maps of the TPL signal for the coupled prisms for a series of incident linear polarization directions: 5° (b), and 85° for λ_0 = 800nm and beam waist=270nm. Time-lapsed illumination of I_1 and I_2 with a polarization orientation of 5◦ or 85◦ is correlated to the time-integrated TPL signal in O_1 and O_2. Map (d) corresponds to inputs polarized at 5◦ on I_1 and I_2, and results from the sum of b weighted by its maximal values in I1 and I2. Maps e , f and g are obtained by the same method for 5°(I_1) - 85°(I_2), 85°(I_1) - 5°(I_2) and 85°(I_1) - 85°(I_2) incident polarization directions respectively, (h) Table summarizing the four illumination and detection configurations. Polarization of 5◦ (85◦) in I_1 or I_2 is ascribed a 0 (1) binary code. Intensity in O_1 and O_2 is ascribed a 0 (1) digital value if it is below (above) the common threshold. O_1 accomplishes a NAND gate while O_2 duplicates the I1 input. The direction of the in-plane polarization is indicated by the white line in the lower right corners. Scale bars, 200nm.

The realization of logic gates based on this technique was first proposed by Viarbitskaya et. al. [15] where effect of coupling of two individual prisms placed in close proximity of each other on the overall TPL of the combined system has been studied. The SEM maps of two prisms separated by a distance of 50nm is displayed in figure 7.2(a). Figure 7.2(b-c) shows simulated TPL maps for incident polarizations of 5° and 85° respectively. It can be seen that the intensity in the positions O_1 and O_2 varies significantly when the excitation polarization changes from 5° to 85°. Here, the authors used the correlation of the TPL intensity at positions (I_1, I_2) and (O_1, O_2) for two different polarizations, to construct the output maps shown in figure 7.2(d-g). For example, to construct the output map in figure 7.2(e), a three steps procedure is followed. First step consists of multiplying the TPL intensity at I_1 for linear polarization of 5°. with the overall TPL map (in figure 7.2b). In the next step TPL intensity at I_2 for the linear polarization of 85° is multiplied with the TPL map (in figure 7.2c). This is followed by integration of the two weighted TPL maps to construct the output map corresponding to "0-1" input states. The same procedures are followed to construct other output maps for "0-0", "1-0" and "1-1" input configurations. We have a higher intensity spot at output O_1 for input state "0-0". When we changed the linear polarization corresponding to the second input is changed to 85° (which corresponds to a "0-1" input state), the higher intensity spot at O_1 still present (figure 7.2e). On flipping the incident polarizations at the two inputs (i.e. 85° at I_1 and 5° at I_2), we see a comparatively weaker spot at output O_1 (figure 7.2f) . However, when polarization at both the inputs are rotated to 85°, the hotspot at O_1 completely diminishes. (figure 7.2g). A truth table is then constructed by setting a threshold just below the output intensity obtained at output O_1 for "1-0" input state. This result in a NAND gate at output O_1 as shown in the table 7.2h. Similarly, a copy of I_1 is obtained at output position O_2 by setting the threshold just below the output intensity obtained at O_2 for the input state "1-0" (in figure 7.2f).

At the time of proposition of the gedanken experiments for realization of logical operations, there were many issues that needed to be addressed before we could realize it experimentally. Firstly, it was not confirmed if we could generate a TPL signal at distant location. This issue has been addressed during course of this thesis when we generated TPL signal at the distant apex in the diabolo. Another challenge was to strategize a way to excite two input locations experimentally. Here we have proposed two excitation mechanism to address this problem. The first possible excitation mechanism involves excitation at two input locations alternatively with identical beams of same wavelength and power. This technique is depicted in figure 7.3(a) where input positions A and B are excited alternatively with a time

delay to avoid any interference between the two signals. The excitation mechanism can be better understood by square wave diagram shown in figure 7.3(c). The first diagram shows the states of input 'I_2'(red) and 'I_3'(blue) respectively. The trigger at the output (the second square wave diagram) is ON throughout the two excitations to integrated the output signal. The output signals as collected for the two excitations are shown in the third square wave diagram. These individual outputs are then integrated to obtain the final output shown in the fourth square wave diagram.

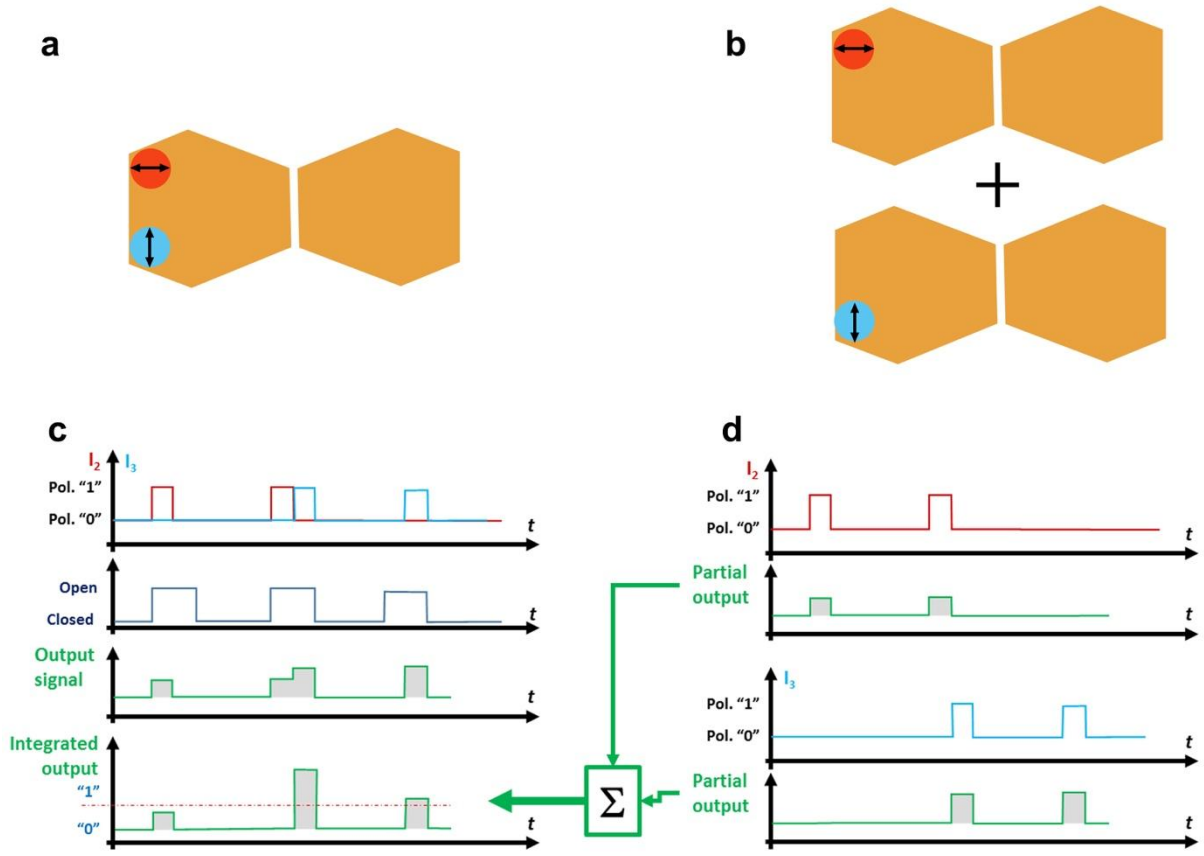


Figure 7.3 Schemes depicting two different possible excitation mechanisms for realization of logic gates based on gedenken experiments. (a) Model representing simultaneous excitation of the bowtie at two inputs shown in red and blue circle. (b) model representing excitation of bowtie structure at two inputs separately. The two transmission images are then combined to get different input states. The direction of black arrows inside the circle show the direction of the incident polarization. (c) The square function diagram representing the principle of simultaneous excitation at two inputs. (d) The square function diagram displaying the summing up of the intensities at the output for two individual excitations at two inputs to obtain the final output.

The second way to realize gate experimentally is to excite the inputs separately and add the output maps (figure 7.3(b)). The square wave diagram explaining this technique has been displayed in figure 7.3(d) where input 'I_2' (1st diagram) and 'I_3' (2nd diagram) are excited

separately. Corresponding output intensities are displayed in 2nd and 4th diagram of the figure 7.3(d). These separate outputs are then integrated to obtain the final output. A threshold is then applied to the integrated output diagram (dashed orange line). The output below the threshold is considered as '0' while the one above the threshold is considered as '1'. The image plane mapping described in chapter VI allow us to implement the second technique for realization of logic gate operations in this work. It is important to mention here that while the first technique can be implemented in an operational device, the second one works only as a proof of principle.

7.3 Choice of the structure for the modal logic gates device

There is no existing set of rules or blueprint to implement logic gate operations based on designing of eigen states in a 2D plasmonic cavity. However, one important principle that can be useful while designing such a device is the need to the break the symmetry of the excitation scheme or the geometry of the device. The introduction of the asymmetry in the system can potentially result in a non-trivial output behaviour. For example, in the case of nanowire, a cylindrical rod modelled with a circular cross-section results in a highly degenerated SP modes which only partially explain the propagation in the crystalline nanowire. However, a break in symmetry introduced by considering a pentagonal cross-section for modelling the cylinder results in a lift of degeneracy with SP modes distributed in similar way to the molecular orbitals of cyclopentadienyl [16] (figure 7.4a,b). This analogy of SP modes distribution with molecular orbital led us to consider molecular logic gates realized on a flat conjugated molecule. For example, in the case of anthracene, a simultaneous implementation a 2-input, 2-output AND and a XOR gate has been achieved [6]. In this model, the "0" and "1" input are encoded as the 0° or 90°dihedral angle between the molecular plane and the NO_2 substituent (See figure 7.4c), while the output is the current measured between the drive atom and the output atom.

In the absence of any guiding principle, we started designing of the logic gate architecture based on the modest dimer geometry proposed by Viarbitskaya et. al. for implementation of gedanken experiment. Taking a clue from the transmission eigen state designed in the previous chapter, we decided to fuse two dimers to achieve a better delocalization of signal from one dimer to another. Here, we propose three fused structures also keeping in mind the break in symmetry principle which was also used in the gedenken experiment where 5° and 85° linear polarization were used instead of 0° and 90° to induce asymmetry.

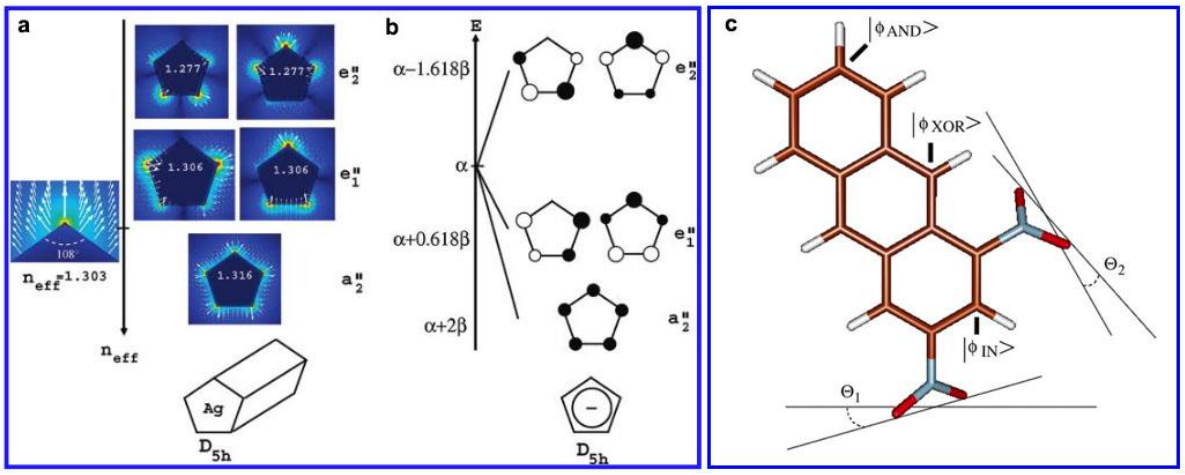


Figure 7.4 (a) Intensity profile of an isolated silver corner. When combined to form a pentagonal section, the interaction between the five corners creates mode symmetries in analogy with the molecular orbitals. The wire diameter is 1.25 μm embedded in a medium of optical index n = 1.25. (b) Schematic of the orbital configuration of the molecule displaying a D_{5h} symmetry. The weight and relative signs of the atomic orbital are depicted by the circle area and color (white = positive, black = negative); R is the energy of an isolated atomic π orbital, and β (<0) refers to the coupling strength between orbitals of two adjacent carbons. (c) The dinitro[1,3]anthracene half adder molecule. $|\phi_{IN}>$is the driving input state of the adder. ϕ_1 and ϕ_2 are the angles between the respective planes of NO_2 groups and the plane of the anthracene skeleton. Each $\{\phi_1, \phi_2\}$ are supposed to take only the discrete values 0 and π/2. [Reprinted with permission from [6], [16]].

The first proposed structure is a fused structure made up of a rectangle with C2 symmetry and a hexagon with C6 symmetry (figure 7.6a). Corresponding projected SPLDOS maps for polarization along 0°, 30°, 60° and 90° has been displayed in figure 7.5 (b-e) respectively. The SPLDOS maps show a large variation in the SPLDOS intensity in the rectangular geometry specially at positions R_1, R_2 and R_3 on changing the linear polarization from 0° to 90°. However, contrast in the SPLDOS distribution at the apices ($H_1 – H_4$) and centre of the edges ($C_1 – C_5$) of the hexagon for a similar change in linear polarization is very less which make it less probable to obtain different outputs for different in-plane polarizations.

The second proposed structure is a combination of two rhombus combined together to form an open book like structure (figure 7.5f). The corresponding projected SPLDOS maps obtained from simulation for different polarizations have been shown in figure 7.5 (g-j). The open book structure comes with asymmetry at the fused edge of the two rhombus. This result in sharp contrast in the SPLDOS intensity distribution at lower left apex(B_6) of the structure when incident polarization is changed from 0°(figure 7.5g) to 30° (figure 7.5h). However,

again there is very low contrast in the intensity on the left part of the fused structure (B_1, B_2 and B_3) which makes the structure not so interesting for implementation of logical operations.

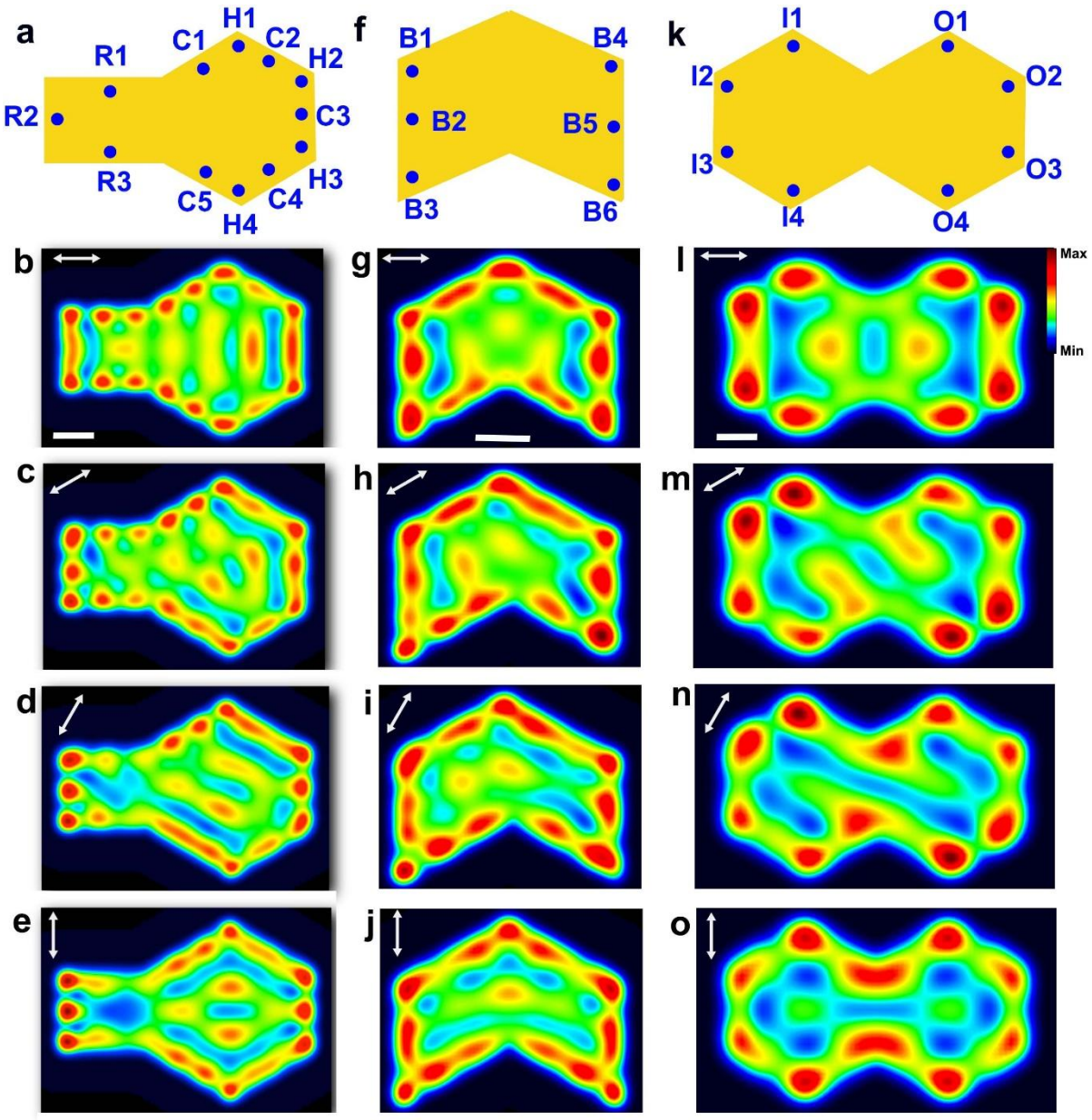


Figure 7.5 (a) Model of arrow shaped structure, (b-e) projected SPLDOS maps for in-plane polarization of 0°, 30°, 60° and 90° respectively, (f) model representing an open book structure, (g-j) corresponding SPLDOS for different incident polarizations (0°, 30°, 60° and 90° respectively), (k) model showing double hexagon structure , (l-o) show SPLDOS maps simulated on double hexagon for polarization along 0°, 30°, 60° and 90° respectively. The doubled headed arrow in the SPLDOS maps represents the direction of in-plane polarization. The scale bars in (b) and (g) are 200nm. Scale bar for l is 100nm.

The last proposed structure is made of two identical hexagons fused together as shown in the model in figure 7.5 (k). The projected SPLDOS maps for the double hexagon structure

shown in figure 7.5 (l-o) The maps suggests a significant intensity variation in corners of both left and right hexagon with the polarization of the incident beam. For example, the SPLDOS intensity at O_2 apex decreases sharply, while that at O_4 increases on changing the polarization. This sharp variation of intensity at apices on both the hexagons makes them ideal candidates to be used as input and output locations.

7.4 Realization of modal logic gates on double hexagon structures

7.4.1 Numerical proof of the principle

To realize modal plasmonic logic gate on the double hexagon structure, a more realistic size of double hexagon is considered with edge length of around 700nm each. The transmission maps were calculated for excitation at different apices of the left hexagon for 0° and 90° incident polarizations. A set of transmission maps for excitation at position I_2 corresponding to the two orthogonal linear polarizations are shown in figure 7.6 (a,b). On excitation at I_2 with incident polarization of 0°, hotspots along the edges of right hexagon is observed. On switching the polarization to 90°, comparatively lesser signal is transmitted to the right hexagon. Here, we have used one set of these simulated transmission maps with excitation at two different positions and with two different incident polarizations for theoretical implementation of logic gates on double hexagon structure. The input positions chosen here are I_1 and I_3 (figure 7.6c). The in-plane polarizations of 0° and 90° have been considered as '0' and '1' input states respectively. Figure 7.6(d) shows the cumulated transmission map for input state 0-1. This has been constructed by cumulating the transmission map for excitation at input I_1 with incident polarization of 0° with the transmission map corresponding to excitation at I_3 with in cident polarization 90°. Similarly, cumulated transmission maps for the input states 0-0 (figure 7.6b), 1-0 (figure 7.6e) and 1-1 (figure 7.6f) are constructed. All the four cumulated transmission maps are plotted on the same colour scale. The colour scale on the right hexagon has been rescaled by a factor 4x in all four maps to increase the visibility of the maps.

A cross-cut was then performed along the edges of the right hexagon (shown by white broken line in figure 7.6c). The intensity profiles on the cross-cut for different input states have been plotted in figure 7.6(g). Now, if we choose a threshold (as shown by the green dashed line) we obtain atleast three different logic gates at three different output positions. For example, at x = 0.75μm, all the outputs are '1' except the one corresponding to 0-0 input states (shown in black).

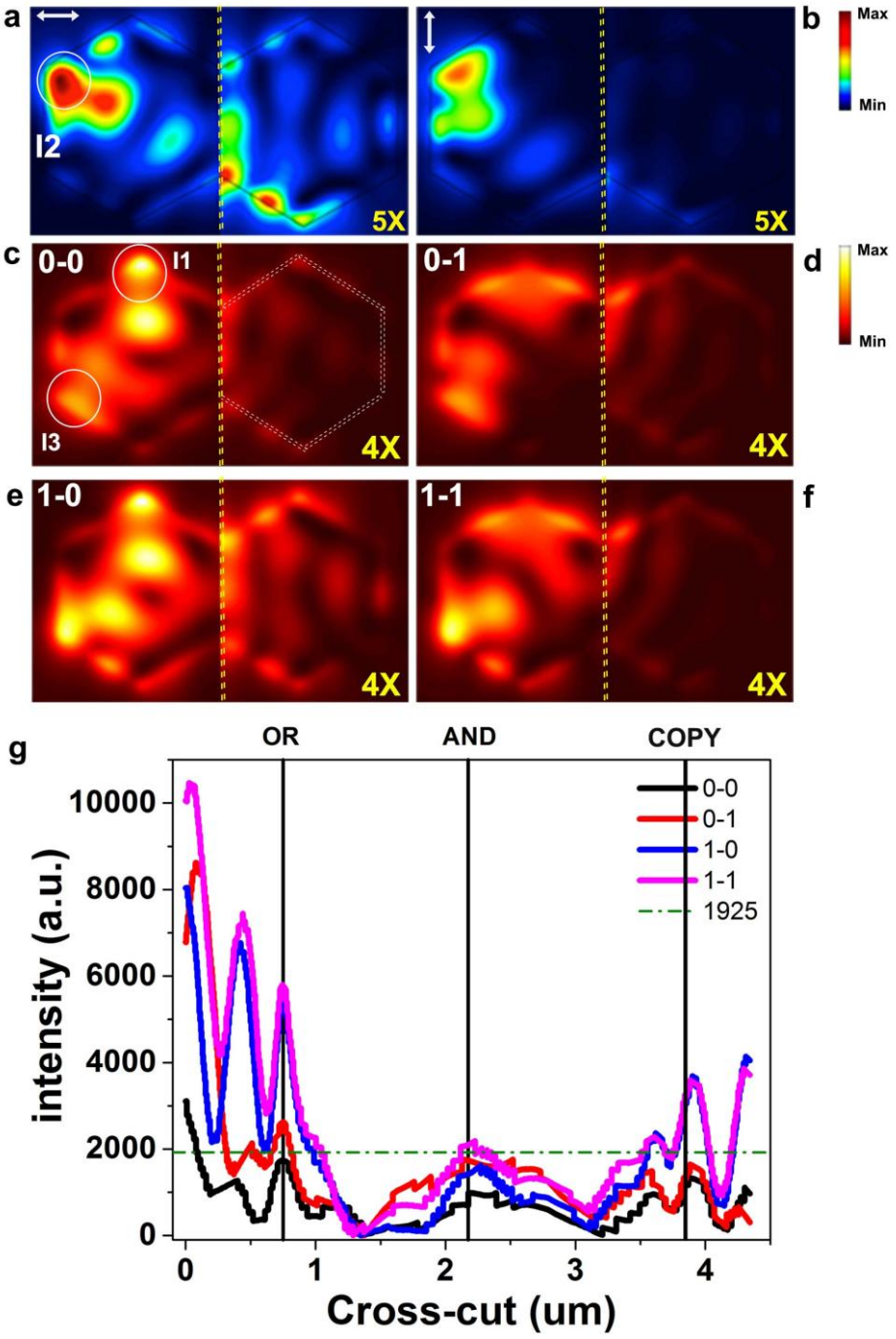


Figure 7.6 (a,b) Simulated transmission map for excitation at position I_2 (shown by white circle) at λ = 810nm with in-plane polarization of 0° and 90° respectively. Both the imaged are at the same colour scale. The colour scale of the right part of the images separated by the yellow dashed line have been enhanced le by a factor of 5X. (c-f) Cumulated transmission images with excitation at apices I_1 and I_3 (shown by black circles) for input states 0-0, 0-1, 1-0 and 1-1 input states. The input '0' and '1' correspond to in-plane polarizations of 0° and 90° respectively. The colour scale for the right part of the images have been enhanced by a factor of 4x. (g) Intensity profile plotted by performing a cross-cut along the edges of the right hexagon in figure 9 (a-d). The input profile for 0-0, 0-1, 1-0 and 1-1 input states have been shown in black, red, blue and magenta colours respectively. The green horizontal dashed line denotes the threshold position which has been kept at 1925 a.u. The white dashed line in (c) display the cross-cut position.

This results in an OR gate which gives '1' as output if atleast one of the input is '1'. Similarly, for, x = 2.2μm, we have all the outputs low except the one corresponding to 1-1 input states (in magenta) which gives an AND gate. Also, at x = 3.9μm, we have a copy of the first input.

7.4.2 Experimental implementation

The double hexagon structures were patterned out from the larger hexagonal micro platelets by following a similar FIB milling protocol as developed for the diabolo structures. SEM image of double hexagon with edge length of 715nm is shown in figure 7.7 (a).

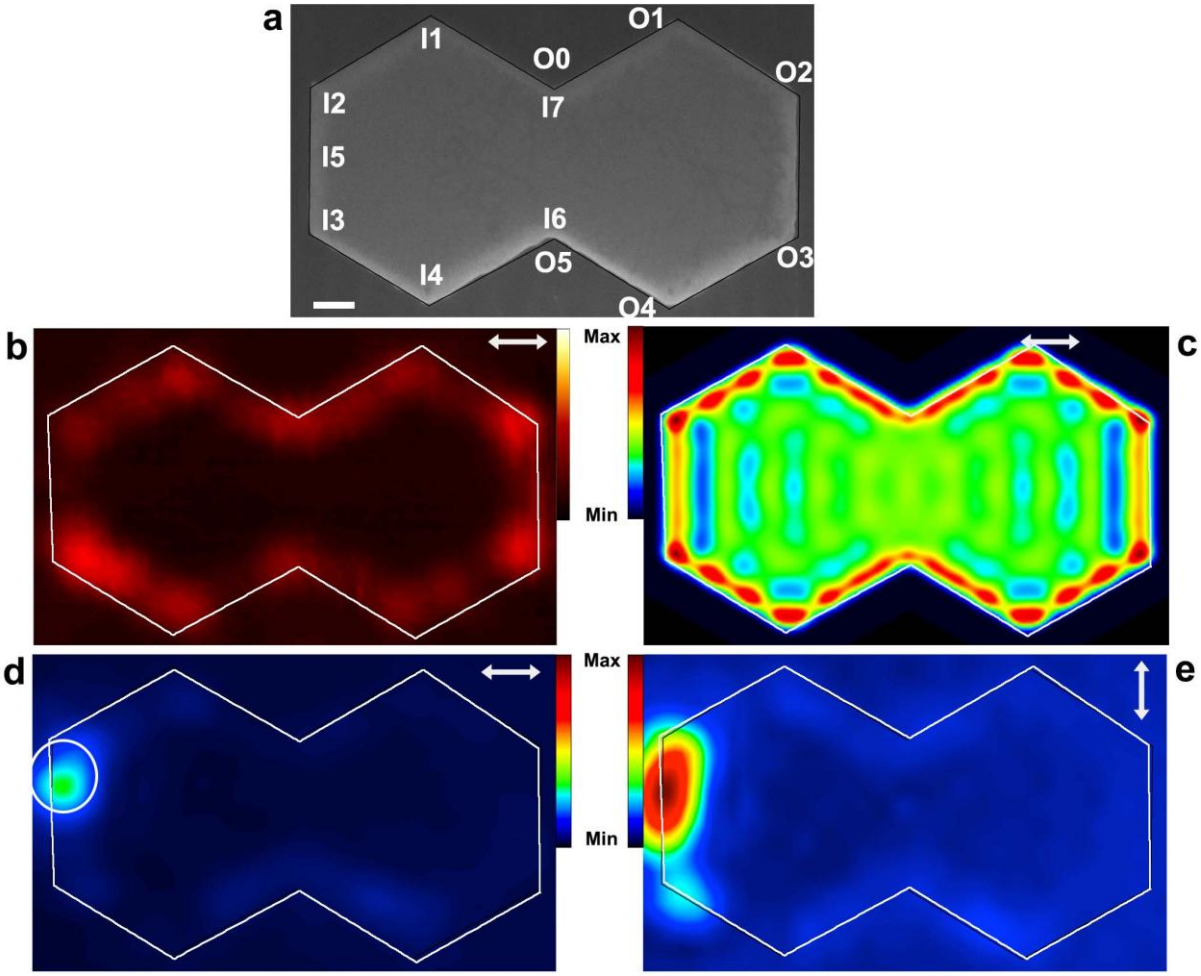
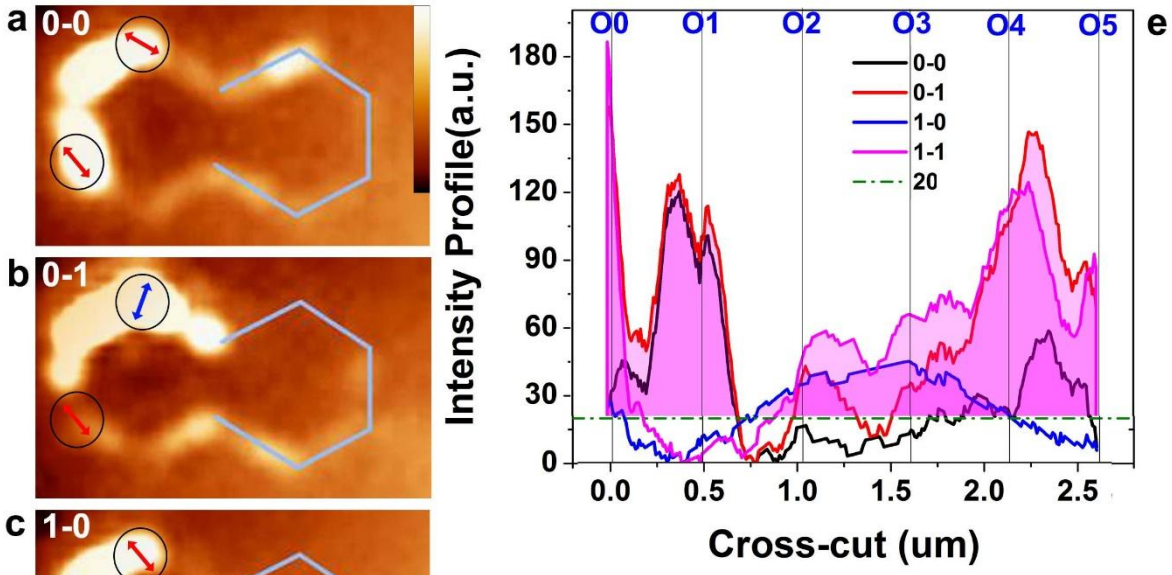


Figure 7.7 (a) SEM image of double hexagon with size length 714nm. The scale bar in white is 200nm. (b, c) experimental transmission images for 0° and 90° polarizations respectively. The double headed arrow represents the direction of in-plane polarization. The black overlay is used to align the images with SEM image. The excitation wavelength used for experimentation and simulation is 810nm. The white circle in figure (b) indicates the point of excitation. The scale bar in (a) is 200nm.

The FIB milling assisted by RAITH software ensure smooth milling of the double hexagon structure with very sharp edges. Figure 7.7(b) shows the confocal TPL map recorded

at an excitation wavelength of λ = 810nm for an in-plane polarization of 0°. High intensity TPL spots on all the apices of the double hexagon structure is observed. There are high intensity TPL hotspots also on the upper and lower edges of the hexagon. The two vertical edges in the centre comparatively less bright. Similar pattern is observed in the projected SPLDOS map computed for an in-plane polarization of 0° where upper and lower edges contain bright nodes and anti-nodes while the signal along the vertical edges is comparatively weaker. We chose to probe the behaviour of the structure by exciting it in one of the apex of the left hexagon. For example, the experimental transmission images for excitation of the double hexagon at apex I_2 with horizontal and vertical in-plane polarizations have been shown in figure 7.7 (c) and (d) respectively. Both the images have been normalized by square of the corresponding input power and the colour scale for both the images are same. From the transmission images, we infer that plasmonic signal can be transferred from one hexagon to the other hexagon (like in the case of diabolo structures). On comparing the two transmission images, we observe a large variation in the signal transmitted to the right hexagon for two orthogonal incident polarizations.

Using these transmission maps, the first experimental implementation of the logic gate on the double hexagon structure has been shown in figure 7.8. Here positions I_1 and I_3 are chosen as two input locations and 0 and 1 inputs are encoded with 130° and 70° in-plane polarization of the incident beam. Six apices on the right hexagon O_0, O_1, O_2, O_3, O_4 and O_5 are chosen as the output. The first transmission image in the figure 7.8 (a) has been obtained by adding the transmission images corresponding to excitation at inputs I_3 and I_1 with in-plane polarization of 130°. The combination of the two transmission images with 130° incident polarization results in the output map corresponding to the 0-0 configuration. Similarly, figure 7.8 (b) was obtained by adding up transmission images corresponding to excitation at inputs I_3 and I_1 with 130° and 70° in-plane polarizations. This gives us output map corresponding to 0-1 input state. The output maps corresponding to other two input configurations (1-0 and 1-1) were similarly obtained in figure 7.8 (c) and figure (d) respectively. A cross-cut is then performed along the edges of the right side hexagon for all four superposed transmission images (figures 7.8 a-d). The profiles obtained from the cross-cuts for four different sets of input configurations are plotted in figure 7.8 (e). The profiles corresponding to different output states are crossing each other several times over a distance of around 2.5μm. This is very crucial for obtaining different logic gate configurations as different output readouts. The threshold on the intensity axis is set at 20 a.u. as shown by dashed green line.



f

TRUTH - TABLE

I_3	I_1	O_0	O_1	O_2	O_3	O_4	O_5
0	0	1	1	0	0	1	0
0	1	1	1	1	1	1	1
1	0	1	0	1	1	1	0
1	1	1	0	1	1	1	1
		TTL	NOT I_3	OR	OR	TTL	COPY I_1

Figure 7.8 (a-d) Superposed experimental transmission images for 0-0, 0-1, 1-0 and 1-1 inputs respectively. The double hexagon was excited at inputs I_1 and I_3. (e) Intensity profile obtained from cross-cut performed on images in figures (a-d). The threshold in the intensity profile plot is kept at 20nm. (f) Truth table has been drawn from outputs at position O_0, O_1, O_2, O_3, O_4 and O_5 respectively. The region above the threshold is shaded in light magenta. The shaded region denotes output state '1' while the unshaded region denotes output state '0'. Tautology (TTL) NOT gate, OR gate, and Copy have been realized as shown in the table. The black circles show the positions of excitation while red and blue circles denote incident polarization direction which is 130° and 70° respectively.

The six outputs are denoted by black vertical lines on the x-axis. The area above the threshold has been shaded in light magenta colour to differentiate the '1' outputs (above threshold) from the '0' outputs (below threshold). Based on the signal intensity at the different apices of the right hexagon, we can construct truth table as shown in table 7.8 (f). At the output O_0, all four intensity profile curves are above the threshold. That is irrespective of the input configurations, the output is always '1'. This logic function is a tautology gate denoted by TTL in the truth table. At the output position O_1, only "0-0"(black) and "0-1"(red) curves are above the

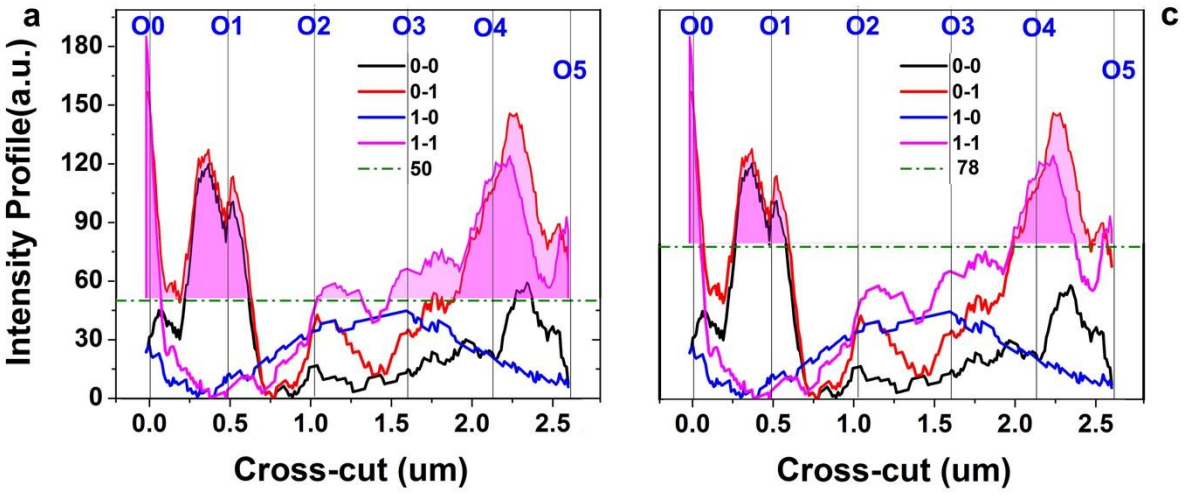
threshold while the intensity curves for "1-0" (blue) and "1-1"(magenta) are below the threshold. This corresponds to a NOT gate of the first input I_3, i.e. when I_3 is '0', the O_1 is '1' and when I_3 is '1', the O_1 is '0'. Next, at the output position O_2 , the intensity curves for "0-1", "1-0" and "1-1" fall in the shaded region while the one corresponding to "0-0" falls in the unshaded region. An OR gate is thus obtained at position O_2 which is '1' when at least one of the input is '1'. Similarly, at O_3 output position, we can construct another OR gate as shown in the table. The output O_4 is another tautology. And lastly, at the output O_5, the intensity profile curves corresponding to input states 0-1 and 1-1 are above the threshold line while ones corresponding to 0-0 and 1-0 fall below the threshold. The output at O_5 is '0' when the input I_1 is '0' and is '1' when the input I_1 is '1'. This means that we have obtained a Copy of input I_1 at the output position O_5. Thus, we have seen that for a fixed threshold, one obtain simultaneously four different logic gate configurations depending on the readout positions. In this specific case, we have been able to construct two OR gate, an NOT gate, two Tautology and one Copy. Our device is even more resourceful as we can reconfigure it by different means and obtain more logic gates as described in the next section.

7.5 Reconfiguration of the modal plasmonic logic gates

7.5.1 Reconfiguration of logic gates with different threshold

The output of the plasmonic logic gate constructed in previous section varies with several implementation parameters like polarization of the excitation beam, the selection of the input positions, the selection of the threshold, the wavelength of the excitation beam and the readout positions. In last section, we have already seen that we can construct different logic gates with simultaneous processing of the inputs at different readout positions. In this section, we show how by varying one of the above stated parameters and keeping the rest identical we can reconfigure the plasmonic logic gates, i.e. change the logic transfer function for fixed input configurations. In the first case, let us keep all the parameters same as in intensity profile curve shown in figure 7.8 but just change the readout threshold value to 50a.u. The intensity profile curve with the new threshold can be seen in figure 7.9 (a). If we carefully examine all readouts, we see that at readout position O_0 , only "0-1" and "1-1" curves are above threshold which means that we have a copy of input I_1 . So, just by changing the threshold the output at the readout O_0 has been changed from Tautology to a Copy (Truth table 7.9b). Similarly, at the next readout position O_1, we observe a NOT gate of input I_3 which means, in this case, the output stays the same on changing the threshold from 20 a.u. to 50 a.u. The next read out

position O_2 has all the four profile curves below the threshold. This means that irrespective of the different input configurations, the output is always '0'. This set of outputs is termed as Contradiction as in denoted by term 'CONT' in the truth table. At readout O_3, only curve corresponding to 1-1 input state is above the threshold.



b

TRUTH - TABLE

I_3	I_1	O_0	O_1	O_2	O_3	O_4	O_5
0	0	0	0	0	0	0	0
0	1	1	0	0	0	1	1
1	0	0	0	0	0	0	0
1	1	1	0	0	1	1	1
		COPY I_1	NOT I_3	CONT	AND	COPY I_1	COPY I_1

d

TRUTH - TABLE

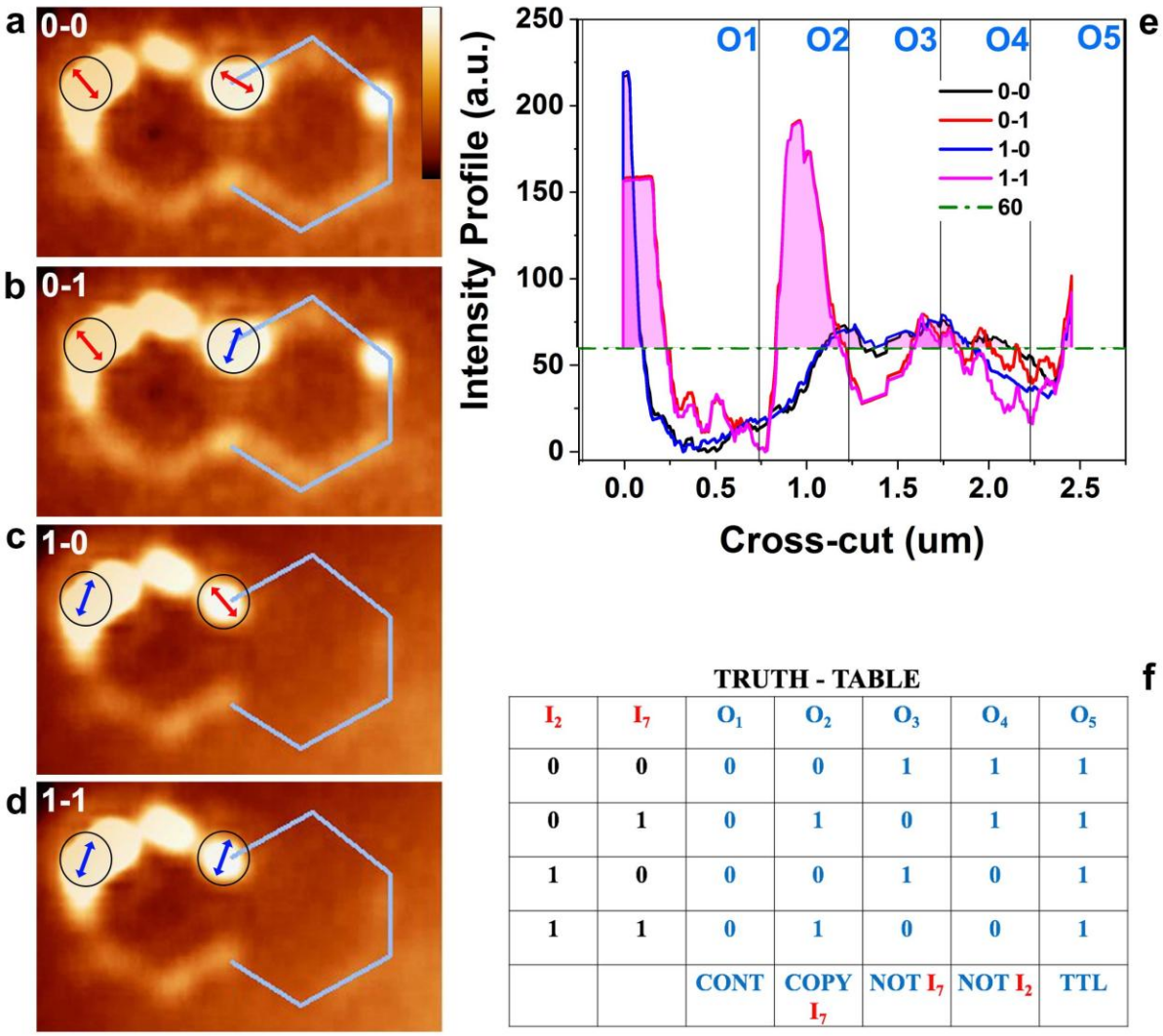
I_3	I_1	O_0	O_1	O_2	O_3	O_4	O_5
0	0	0	0	0	0	0	0
0	1	1	0	1	1	1	0
1	0	0	0	1	1	0	0
1	1	1	0	1	1	1	1
		COPY I_1	NOT I_3	CONT	CONT	COPY I_1	AND

Figure 7.9 (a, c) Intensity profiles plotted from the cross-cut in figure 7.8(a-d) with threshold at 50a.u. and 78a.u. respectively. The area above the threshold is shaded with light magenta colour. The dashed green line indicates the threshold position. (b,d) Truth table constructed from the two new thresholds in figure (a) and (c) respectively. 3 Copies, one NOT gate, one Contradiction (CONT) and one gate has been obtained in Truth Table (b) while 2 copies, while Truth table (d) gives one NOT gate, two Contradiction and an AND gate.

This means that output is '1' only when both the outputs are '1' which gives us an AND gate at O_3. So, the readout O_2 and O_3 where we had two OR gates in previous case, now have a Contradiction and an AND gate. At last two output positions, we have a Copy of the second input I_1. While we could already obtain a Copy of 'I_1' , a NOT of 'I_3' and a CONT in the figure 7.8, a new AND gate has been realized by changing the threshold. Similarly, if we further increase the threshold to 78a.u. (figure 7.9c), we can construct two Copies of I_1, a NOT of I_3, two Contradictions and an AND gate. However, in this case, the AND gate has been obtained

at another read out position. For each of the two threshold, we have simultaneously obtained 4 different logic gates configurations.

7.5.2 Reconfiguration based on different set of input locations



TRUTH - TABLE

I_2	I_7	O_1	O_2	O_3	O_4	O_5
0	0	0	0	1	1	1
0	1	0	1	0	1	1
1	0	0	0	1	0	1
1	1	0	1	0	0	1
		CONT	COPY I_7	NOT I_7	NOT I_2	TTL

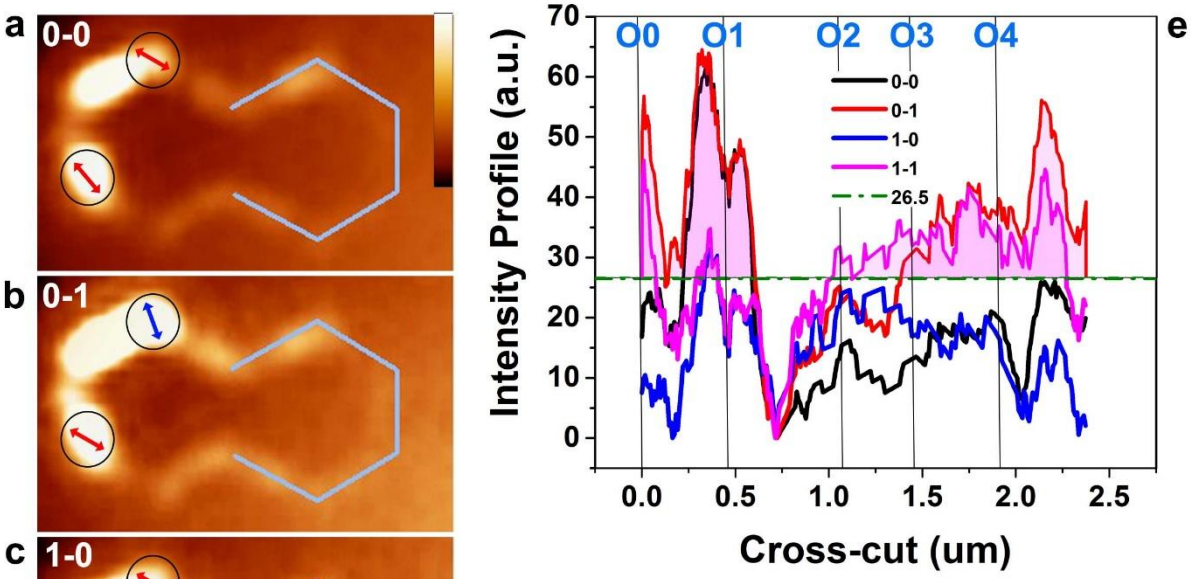
Figure 7.10 (a-d) Summed up experimental transmission images for 0-0, 0-1, 1-0 and 1-1 inputs respectively. '0' and '1' inputs correspond to 130° and 70° incident polarizations respectively. The double hexagon was excited at inputs I_2 and I_7. (e) Intensity profile obtained from cross-cut performed on images in figures (a-d). The threshold in the intensity profile plot is kept at 60nm. (f) Truth table has been drawn from outputs at position O_0, O_1, O_2, O_3, O_4 and O_5 respectively. The region above the threshold is shaded in light magenta. The shaded region denotes output state '1' while the unshaded region denotes output state '0'. Tautology (TTL), NOT gate, Contradiction, and Copy have been realized as shown in the table. The black circles show the positions of excitation while red and blue circles denote incident polarization direction which is 130° and 70° respectively.

Another possibility to reconfigure the output of the logic gate is by choosing different sets of inputs. In the next example we have chosen I_2 and I_7 as the two inputs instead of I_1 and I_3 as in earlier case. The two incident polarizations of 130° and 70° have been kept the same as earlier. We have repeated the process explained before to construct transmission images corresponding to 0-0, 0-1, 1-0 and 1-1 (figure 7.10 a-d respectively). A simultaneous cross-cut has been performed on the all the four transmission images as indicated by lines on the right hexagon. The intensity profiles extracted from the cross-cut have been plotted in figure 7.10(e) for all the four input configurations. In this case, since the one of the input position coincides with O_0, so we will only read the outputs at the rest five apices. If we set the threshold at 60 a.u., we obtain a Contradiction at the output O_1 (Table f) since all the curves at that position are below the shaded region. The output position O_2 yields a Copy of second input I_7. At the output O_3, only profile curves corresponding 0-0 and 1-0 are above the threshold which results in a NOT gate of the input I_7. Another NOT gate can be constructed from the output at O_4 but this time of the first input I_2. The last readout position O_5 gives us a Tautology as all the outputs are in the shaded region. Thus, a change of set of input positions give us different set of logic gates which includes a Contradiction, a tautology, a Copy and a NOT gate each for the two inputs. Here, it is worth noting that by choosing different set of inputs, we have obtained five different logic gate operations on five different outputs which include NOT gates corresponding to both the inputs at O_3 and O_4.

7.5.3 Reconfiguration based on different set of polarizations

The polarization of the incident beam gives us another degree of freedom to reconfigure the logic gates in the current geometry. Here, we consider the same set of inputs (I_1 and I_3) as in the figure 7.8. The incident polarization directions, however, have been changed 150° and 110° corresponding to input ‘0’ and ‘1’ respectively. The transmission images corresponding to four possible input configurations are shown in figure 7.11 (a-d). The intensity profile corresponding to the cross-cuts on the transmission images are plotted in figure 7.11e. For a threshold of 26.5 a.u., this set of polarizations give 3 Copies of input I_1, a NOT gate of input I_3 and an AND gate at 5 different positions as shown in the truth table 7.11(f). The output O_2 in this case is not exactly at the apex but around 150nm away as indicated in the intensity profile curves. The set of logic gate configurations obtained in this case is similar to what we obtained in figure 7.9(a) for polarizations of 130° and 70° for the threshold of 50nm. The intensity

profile, however, in this case is much more compressed and therefore the gap between the different intensity profiles at any particular point in much lesser.



f

TRUTH - TABLE

I_3	I_1	O_0	O_1	O_2	O_3	O_4
0	0	0	1	0	0	0
0	1	1	1	0	1	1
1	0	0	0	0	0	0
1	1	1	0	1	1	1
		COPY I_1	NOT I_3	AND	COPY I_1	COPY I_1

Figure 7.11 (a-d) Experimental transmission images obtained for 0-0, 0-1, 1-0 and 1-1 inputs respectively. '0' and '1' inputs correspond to 110° and 150° incident polarizations respectively. The double hexagon was excited at inputs I_3 and I_1. (e) Intensity profile obtained from cross-cut performed on images in figures (a-d). The threshold in the intensity profile plot is kept at 60nm. (f) Truth table has been drawn from outputs at position O_0, O_1, O_2, O_3, O_4 and O_5 respectively. The region above the threshold is shaded in light magenta. The shaded region denotes output state '1' while the unshaded region denotes output state '0'. Tautology (TTL), NOT gate, Contradiction, and Copy have been realized as shown in the table. The black circles show the positions of excitation while red and blue circles denote incident polarization direction which is 150° and 110° respectively.

Nevertheless, this result suggests that, the logic gate realization on the double hexagon structure is robust and same set of logic gates can be reproduced with different encoding of '0' and '1' in form of incident polarization. It is also worth noting here that we achieved a successful

switching between five different logical operations – OR (table 7.8f), AND (table 7.9b), Contradiction (table 7.9d), NOT (table 7.10f) and Copy (table 7.11f) at the output O_3 by the three reconfiguration mechanisms. In addition, the present configuration (in figure 7.11) also offers possibility of realization of NOR gate by inverting encoding of 150° and 110° polarizations to '1' and '0' respectively. The inversion of the input coding results in an output at O_2 which is '1' only for "0-0" input state. This corresponds to a NOR gate. Similarly, an inversion of the input coding in figure 7.8 will result in two NAND gates at positions O_2 and O_3.

7.6 Conclusion

To conclude, we have successfully realized modal plasmonic logic gates based on gedenken experiments. The experiment was performed on a double hexagon structure with multiple input and outputs positions. We have implemented a total of 10 out of 12 possible logic gate configurations like NOT of both the inputs, Copy of both the inputs, AND, OR, NAND, NOR, Tautology and Contradiction. For same set of implementation parameters, we obtained 5 different logic gates configurations at five readouts. The plasmonic logic gates were reconfigured by changing the threshold, set of inputs and set of incident polarizations at the inputs. This resulted in five different logic gate operations at the same readout position. The two logic gates which could not be constructed based on current excitation mechanism are XOR and NXOR. In order to realize XOR gates, we need a '1' at the output when the two inputs have complimentary values (0-1 and 1-0) and '0' otherwise (0-0 and 1-1). This criterion cannot be matched by superposing two transmission images corresponding to two different input conditions because a simple addition means when 0-1 and 1-0 are above the threshold either 0-0 or 1-1 must be above the threshold too. Similarly, for XNOR, when 0-1 and 1-0 input states give us '0' at the output, either of 0-0 or 1-1 must also be less than the threshold if we superpose two transmission images. So, this absence of XOR and XNOR gates is just due to our implementation assumptions. One way to realize XOR and NXOR is by concatenation of basic logic gates. Two AND gates, two NOT gates and an OR gate can be used to build XOR gate as shown in the figure 7.12(a) while an extra NOT gate is required to construct a NXOR gate (figure 7.12b). Although XOR and NXOR could not be realize by currently employed technique, the realization of rest 10 logic gate configurations on a single double hexagon structure is surely a major step forward in realization of more complicated operation likes half adder and full adder.

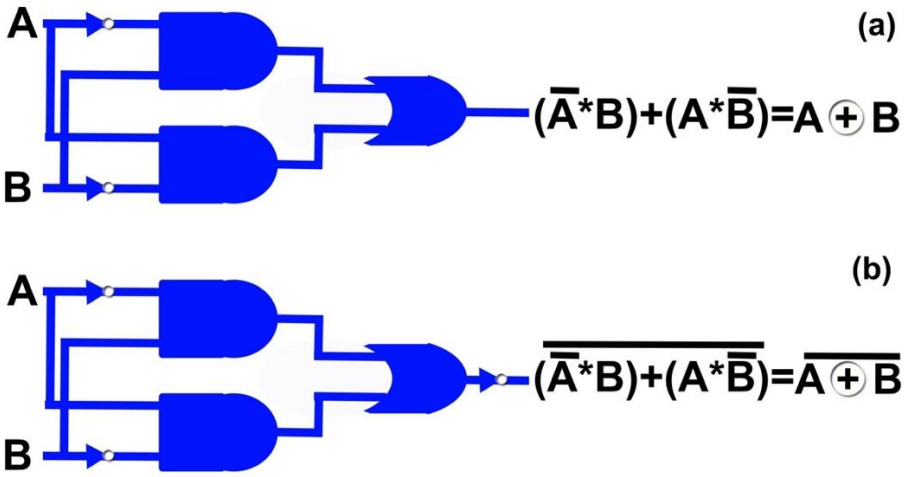


Figure 7.12 Implementation of (a) XOR and (b) NXOR by concatenation of fundamental logic gates – AND, OR and NOT

References

[1] W. H. Eccles and F. W. Jordan, "A trigger relay utilizing three-electrode thermionic vacuum tubes," *Electr.*, vol. 83, no. 298, 1919.

[2] C. E. Shannon, "Symbolic Analysis Of Relay And Switches," 1940.

[3] A. F. González, M. Bhattacharya, S. Kulkarni, and P. Mazumder, "CMOS implementation of a multiple-valued logic signed-digit full adder based on negative-differential-resistance devices," *IEEE J. Solid-State Circuits*, vol. 36, no. 6, pp. 924–932, 2001.

[4] K. W. Current, "Current-Mode CMOS Multiple-Valued Logic Circuits," *IEEE J. Solid-State Circuits*, vol. 29, no. 2, pp. 95–107, 1994.

[5] A. Beg, "Designing array-based CMOS logic gates by using a feedback control system," in *2014 IEEE International Conference on Systems, Man, and Cybernetics (SMC)*, 2014, pp. 935–939.

[6] I. Duchemin and C. Joachim, "A quantum digital half adder inside a single molecule," *Chem. Phys. Lett.*, vol. 406, no. 1–3, pp. 167–172, 2005.

[7] S. Ami, M. Hliwa, and C. Joachim, "Molecular 'OR' and 'AND' logic gates integrated in a single molecule," *Chem. Phys. Lett.*, vol. 367, no. 5–6, pp. 662–668, 2003.

[8] W. Li, Y. Yang, H. Yan, and Y. Liu, "Three-input majority logic gate and multiple input logic circuit based on DNA strand displacement," *Nano Lett.*, vol. 13, no. 6, pp. 2980–2988, 2013.

[9] A. Dolatabady and N. Granpayeh, "All optical logic gates based on two dimensional plasmonic waveguides with nanodisk resonators," *J. Opt. Soc. Korea*, vol. 16, no. 4, pp. 432–442, 2012.

[10] Z. Chen *et al.*, "Simulation of nanoscale multifunctional interferometric logic gates based on coupled metal gap waveguides," *IEEE Photonics Technol. Lett.*, vol. 24, no. 16, pp. 1366–1368, 2012.

[11] H. Wei *et al.*, "Quantum dot-based local field imaging reveals plasmon-based interferometric logic in silver nanowire networks," *Nano Lett.*, vol. 11, no. 2, pp. 471–475, 2011.

[12] Y. Fu, X. Hu, C. Lu, S. Yue, H. Yang, and Q. Gong, "All-optical logic gates based on nanoscale plasmonic slot waveguides," *Nano Lett.*, vol. 12, no. 11, pp. 5784–5790, 2012.

[13] N. Nozhat, H. Alikomak, and M. Khodadadi, "All-optical XOR and NAND logic gates based on plasmonic nanoparticles," *Opt. Commun.*, vol. 392, no. August 2016, pp. 208–213, 2017.

[14] H. Wei, Z. Wang, X. Tian, M. Käll, and H. Xu, "Cascaded logic gates in nanophotonic plasmon networks," *Nat. Commun.*, vol. 2, p. 387, 2011.

[15] S. Viarbitskaya *et al.*, "Tailoring and imaging the plasmonic local density of states in crystalline nanoprisms," *Nat. Mater.*, vol. 12, no. 5, pp. 426–432, 2013.

[16] M. Song *et al.*, "Imaging symmetry-selected corner plasmon modes in penta-twinned crystalline Ag nanowires," in *ACS Nano*, 2011, vol. 5, no. 7, pp. 5874–5880.

Chapter VIII

Conclusions and future perspectives

The main aim of this PhD work was to design, fabricate and characterize individual; plasmonic devices able to implement far-field to near-field conversion, transfer and reconfigurable logic processing by harnessing the properties of highly crystalline 2D gold and silver cavities of micrometric size. Each of these information processing function has been examined in dedicated systems.

We have studied the spectral behaviour of triangular gold nanoprisms with lateral sizes comprised between 400 and 1000 nm by means of dark field spectroscopy supported with SPLDOS spectra computed by GDM based numerical tool. These plasmonic cavities were found to bear multiple resonance peaks in a spectral window ranging from 450nm to 850nm. The comparison with calculated SPLDOS spectra revealed that each planar mode obtained from simulation can be associated to one Lorentzian peak obtained from the fitting of the experimental spectra. These SP resonance peaks red shift as the size of the cavity increases. When the size of the cavity was increased by ~90nm, a new SP resonance peak can be accommodated. In order to explore the possible tuning of these resonances, the nanoplates were placed in the direct vicinity of a metallic thin film. In a Metal-Insulator-Metal (MIM) configuration on a 30-nm thick gold film, the red shift of the individual SP resonance peak with size was also observed. Furthermore, by changing the nature of the metal of the thin film, we could trigger a global red or blue shift of the dark field response of the nanoprisms. As a complementary method to tune the spectral response of the prismatic cavities, we also exposed the possibility of by introducing a sub-wavelength hole defect.

The first functional component studied in this thesis is a far-field/near-field conversion antenna constructed by bringing close to each other two such multimodal plasmonics cavities in a bowtie configuration. These mesoscale bowties antennas were found to exhibit a nanoscale confinement and field enhancement at the gap location with a polarization dependency orthogonal to standard small dipolar bowtie antennas. The mesoscopic dimensions of our bowtie antennas confer them the extra feature to delocalize plasmonic hotspots in the remote regions of the triangular arms suggesting the possibility to use them as planar channels to extract information away from the gap region. The performances and spatial SP patterns of

these bowtie antennas were found to be dictated by the spectral matching conditions between the two arms while the antenna effect was set by the local geometrical configuration of the gap, in particular by the relative orientation of the crystalline facets defining the gap.

Next we addressed the question of information transfer by exploiting the modal behaviour observed in individual prisms. We thus designed the eigenstates of a diabolo shaped structure which consist of two triangular cavities connected by a rectangular channel. The confocal TPL maps confirmed that our device essentially preserved the modal features of the individual cavities with a small but essential alteration due to the presence of the conductive channel. Next, we used one TPL hotspot position in one of the cavity as an input port and monitored the transmission of plasmonic signal to the distant apex of the second cavity. We demonstrated a transmission over a distance of 2 microns with an efficiency of 3.5% and a modulation with On/Off ratio of 130 by simply rotating the incident polarization direction. Interestingly, a thorough probing of the excitation scheme suggested that the transmission is operated by activating the SP modes of the structure and that the device efficiency was directly set by the in-coupling efficiency at the excitation location and by the SPLDOS distribution along the transmission path. A complete shutdown of the transmission when the two cavities showed a size difference exceeding 90nm further supported the modal mechanism of the transmission. Further investigations of the phase of the transmitted SP signal could reinforce the understanding of the transmission mechanism in such multimodal diabolo structures. Nevertheless, our results demonstrate the successful realization of an efficient transmission device in which transmission modulation could be achieved.

At last, we convene all the knowledge acquired on the previsous systems to design and realize plasmonic logic gates based on a gedanken experiment proposed earlier in the group but never experimentally tested so far. The double hexagon devices were used as plasmonic logic gates by remotely exciting the non-linear luminescence from two linearly polarized incident beams and by setting a read-out threshold. By choosing the input and output ports of the gate, the polarization of the excitation beam and the threshold, we could implement a total of 10 out of the 12 possible 2-input, 1-output Boolean logic gates: NOT of either inputs, COPY of either inputs, AND, OR, NAND, NOR, TAUTOLOGY and CONTRADICTION were thus successfully realized. The potential for complex logic functions was illustrated by the simultaneous operation of up to five different logic gates on single double hexagon device. These logic gates operation could be easily reconfigured by changing any of the

aforementioned parameters. The two logic gates which could not be obtained are XOR and NXOR. However, these two gates cannot be implemented by the chosen excitation scheme which consists in superposing two the response of the device to two different input conditions and their implementation will require a different operation method. In the future, our reconfigurable plasmonic logic gates concept could be improved by incorporating an active control. One approach is to use a metallic layer supporting SP mode as a contact electrode which can work as an electrically pumped SP source. Integration of such contact electrode with the current double hexagon geometry can provide us with highly desirable active control of the plasmonic logic gate device.

Active control of plasmonic components has also been demonstrated based on interaction between single emitters and the plasmonic cavity [1], [2] . In particular, nitrogen vacancies (NV) centre nanodiamonds (ND) have been used as an active probe because of its remarkable photo stability and broadband fluorescence spectrum in the visible for excitation at 532nm [3], [4].

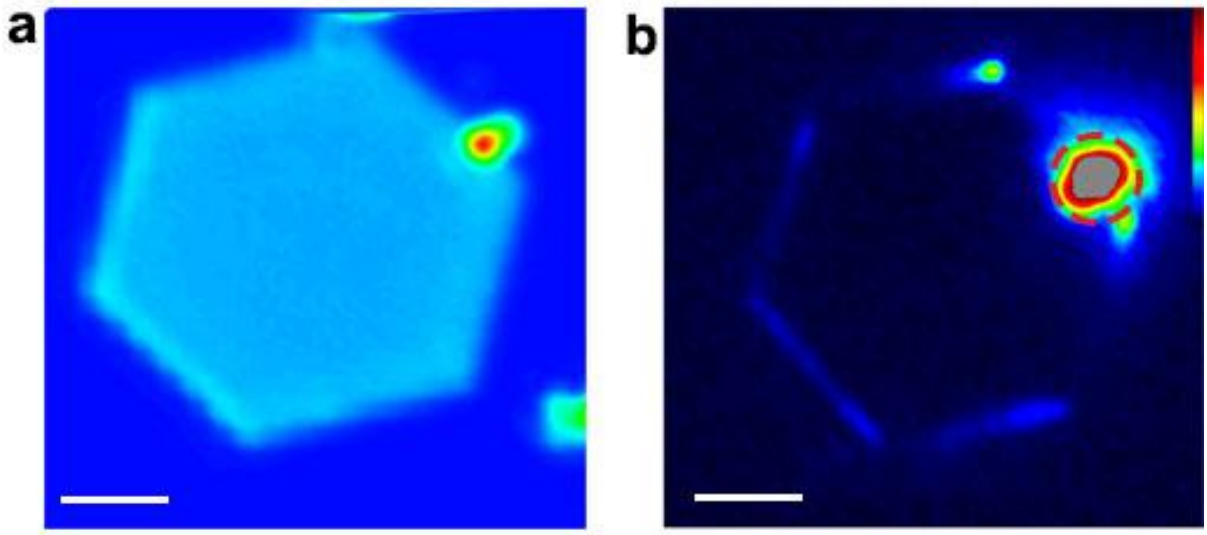


Figure 8.1 (a) Confocal map of NV centre nanodiamonds coupled with multimodal gold cavity excited at λ = 532nm, (b) Leakage radiation map of the coupled system for excitation at the position of nanodimaonds (shown by red circle). The scale bar is 2 microns.

Recently, a quantum probing of multimodal plasmonic resonators based on NV centre NDs at the apex of an optical tip was reported by Cuche et. al. [5]. In this work, photonic LDOS maps for different wavelengths were recorded in the immediate vicinity of the plasmonic resonators by selective filtering of the broad emission spectra. Alternatively, we can also spread the emitters close to the plasmonic cavity. The SPLDOS probing can be imagined by recording the

luminescence of the emitter as a function of its position with respect to the plasmonic cavity. As a first step in this direction, we have started investigation of NV centre NDs placed in the vicinity of a multimodal plasmonic cavity. The confocal map of the coupled system is shown in figure 8.1(a) for excitation at λ =532nm. In the second step, we parked the beam on the NDs (shown by red broken circle). The leakage radiation image of the coupled system is shown in figure 8.1(b). Although, these are only preliminary results, but it certainly paves the way for more detailed study focussing on exploitation of NV centre NDs for launching and addressing single SPPs locally near the plasmonic cavities. Alternatively, multimodal plasmonic cavities can also be used to control the emission features of the single quantum emitters.

References

[1] M. Frimmer, Y. Chen, and A. F. Koenderink, "Scanning emitter lifetime imaging microscopy for spontaneous emission control," *Phys. Rev. Lett.*, vol. 107, no. 12, pp. 1–5, 2011.

[2] D. Cao *et al.*, "Mapping the radiative and the apparent nonradiative local density of states in the near field of a metallic nanoantenna," *ACS Photonics*, vol. 2, no. 2, pp. 189–193, 2015.

[3] A. Cuche *et al.*, "Near-field optical microscopy with a nanodiamond-based single-photon tip.," *Opt. Express*, vol. 17, no. 22, pp. 19969–80, 2009.

[4] A. Drezet, A. Cuche, and S. Huant, "Near-field microscopy with a single-photon point-like emitter: Resolution versus the aperture tip?," *Opt. Commun.*, vol. 284, no. 5, pp. 1444–1450, 2011.

[5] A. Cuche *et al.*, "Near-field hyperspectral quantum probing of multimodal plasmonic resonators," *Phys. Rev. B*, vol. 95, no. 12, 2017.

Résumé en français de la thèse

Chapitre I

Motivations

Les résonances plasmon peuvent être classées en deux catégories. Les plasmons polaritons de surface (SPP) qui sont des ondes électromagnétiques de surface se propageant à l'interface entre un métal et un diélectrique et qui se caractérisent par une oscillation collective et longitudinale des électrons du métal. Les plasmons de surface localisés (LSP) qui sont des oscillations confinées d'électrons de surface dans une nanoparticule métallique. Jusqu'`a présent, la recherche sur les plasmons a essentiellement porté sur les propriétés des structures métalliques macroscopiques qui facilitent la propagation, le guidage et l'acheminement des SPPs, ou celles des particules métalliques nanométriques, qui produisent des résonances intenses et un fort confinement du champ. Étonnamment, une attention moindre a été accordée au régime intermédiaire des structures de taille micrométrique dans lequel coexistent des résonances localisées et des excitations délocalisées. Ce travail de doctorat est consacré à une étude approfondie des structures métalliques individuelles dans ce régime de taille intermédiaire et explore de nouvelles applications dans le traitement de l'information à base de plasmon.

Jusqu'à présent, les dispositifs et les interconnexions plasmoniques les plus avancés ont été produits avec une approche standard de microfabrication "top-down" qui est limitée par la dissipation de l'énergie liée à la diffusion due à la nature amorphe ou polycristalline du film utilisé comme matériau de départ. Il y a plus d'une décennie, il a été démontré qu'un nanofil cristallin produit chimiquement subirait relativement moins de dissipation d'énergie par diffusion. Le fonctionnement général d'un dispositif de traitement d'information requiert la mise en œuvre du codage de l'information d'entrée (par exemple sous la forme de polarisation ou de longueur d'onde du (des) faisceau(s) incident(s)), de la fonction de transfert du dispositif (par exemple une porte logique booléenne) et du codage de l'information de sortie (par exemple, une intensité localisée au point de lecture). Des fonctions de porte logique complexes ont été construites à l'aide de portes logiques élémentaires en cascade, par exemple par Wei et coll. [20]. Les performances de tels dispositifs interférentiels sont limitées par la précision du positionnement relatif des blocs élémentaires actifs l'un par rapport à l'autre et de l'emplacement du point d'excitation.

Dans cette thèse, nous proposons d'aborder ce sujet avec un autre paradigme, c'est-à-dire de concevoir des dispositifs plasmoniques à deux dimensions et dans un régime de taille

qui leur confère des modes confinés caractéristiques indépendamment de la configuration d'excitation. Le chapitre II de cette thèse fournit une brève introduction au domaine de la plasmonique. Nous y détaillons le concept de densité locale des états plasmoniques qui décrit commodément les propriétés des objets portant un nombre important mais fini de modes. Le chapitre se termine par une description des nanoparticules plasmoniques cristallines spécifiques utilisées dans ce travail. Le troisième chapitre recueille les détails techniques concernant toutes les procédures expérimentales de fabrication et les techniques de caractérisation utilisées tout au long de la thèse. Une section détaillée est consacrée à la description des outils de simulation basés sur la méthode de la fonction de Green Dyadique développée par Christian Girard (CEMES). Toutes les simulations présentées dans ce travail ont été effectuées à l'aide de ces codes.

Dans le chapitre IV, nous commençerons par une étude systématique des propriétés spectrales des nanoprismes d'or triangulaires et pointus pour des longueur de côté allant de 400 nm à 900 nm. Ces objets contiennent un ensemble de résonances dont les caractéristiques sont examinées expérimentalement et comparées aux simulations. Ensuite, nous nous sommes demandé si la réponse spectrale des nanoprismes d'or déposés sur un substrat verre pouvait être modifiée par la présence d'un film métallique mince voisin ou par l'introduction d'un défaut résonant, sous forme d'un trou, dans le nanoprisme d'or. Le chapitre V est consacré à une première fonction de traitement de l'information : des antennes de conversion du champ lointain vers le champ proche. Une configuration d'antenne en forme de noeud de papillon (*bowtie*) sera construite par couplage de deux de ces prismes cristallins. Nous examinerons si la polarisation incidente et la position relative d'une cavité par rapport à une seconde cavité ont un effet sur le comportement de l'antenne. Dans le chapitre VI, nous nous concentrerons sur les moyens de transmettre l'information d'un point d'incident à un autre point d'émission en excitant des modes délocalisés mais possédant une répartition spatiale bien définie. Pour cela, nous envisagerons d'introduire un canal rectangulaire reliant les deux cavités triangulaires individuelles dans une géométrie de type « diabolo ». Une étude expérimentale et numérique exhaustive de la transmission du plasmon sera effectuée en examinant les effets de la position d'excitation, de la direction de sa polarisation, de la taille relative des deux prismes ou de la longueur d'onde d'excitation. Le chapitre VII présente la proposition la plus avancée de ce travail en décrivant la conception et la mise en œuvre d'une architecture modale plasmonique réalisant les fonctions des portes logiques booléennes. Les expériences par la pensée proposées dans notre groupe en 2013 seront mises en œuvre expérimentalement pour la première fois. En particulier, nous démontrerons comment créer des portes logiques à 2 entrées et 1 sortie en fonction des

caractéristiques modales des structures métalliques 2D. Dans la partie finale de ce chapitre, nous étudierons le concept de portes logiques reconfigurables.

Chapitre II

Introduction

2.1 Introduction à la Plasmonique

Les plasmon polaritons de surface (SPP) sont des ondes électromagnétiques bidimensionnelles se déplaçant le long d'une interface entre des matériaux avec des constantes diélectriques de signe opposé (c'est-à-dire un conducteur et un diélectrique) et sont évanescentes dans la direction perpendiculaire à l'interface. Ainsi, les modes SPP n'existent qu'avec une polarisation TM, où le champ électrique E est parallèle au plan d'incidence, nous avons donc une composante du champ électrique suivant les directions x et z. La courbe de dispersion des SPPs est illustrée sur la figure 2.2 qui montre que celle-ci est toujours placée à droite de la courbe de dispersion des photons se propageant à l'air libre. Avec une projection des vecteurs d'onde des photons arrivant sur l'interface avec un angle 'θ' par rapport à la normale de la surface, $k_x=k_o\sin\theta$ sera toujours inférieure à β. Toutefois, les vecteurs d'onde de la lumière et des SPPs peuvent être adaptés en utilisant différentes configurations de couplage à base de prismes (configurations Kretschamn et Otto) [13], [14], de réseaux [16] - [18], d'une pointe de champ proche optique [19] ou un objectif à grande ouverture numérique [20] afin de permettre l'excitation des SPP par les photons incidents.

Les plasmons de surface localisés (LSP) sont une autre excitation plasmonique fondamentale qui résulte du confinement de gaz d'électrons dans une nanoparticule de taille comparable ou inférieure à la longueur d'onde de la lumière utilisée pour exciter le plasmon. Ces oscillations des électrons de conduction par rapport au réseau d'ions positif dépendent de la densité de charge, de la masse effective de l'électron, ainsi que de la taille et de la forme des nanoparticules.

Les structures métalliques macroscopiques supportent la propagation [24], [25] et le guidage d'onde et [26] du signal SPP, tandis que les structures métalliques à échelle nanométrique soutiennent les résonances LSP qui produisent un champ évanescent, et un fort confinement [27]. Dans cette thèse, nous avons utilisé des nanostructures métalliques de taille micrométrique intermédiaire entre les systèmes à échelle nanométrique et les systèmes d'échelle macroscopique et sont donc appelés de taille mésoscopique. Les systèmes de taille mésoscopique combinent les caractéristiques de SPP et de LSP et se sont avérés être des un candidats pertinents pour la conception de dispositifs optiques plasmoniques.

2.2 La densité locale d'états plasmoniques

La probabilité de trouver l'intensité du champ électrique associé aux photons d'énergie dans un petit volume infinitésimal 'dr' à un point donné 'r' est ρ(r,ω). Le terme ρ(r,ω) est la densité local d'états (LDOS) photoniques. Il est lié à la susceptibilité du champ électrique, S(r,r',ω), par –

$$\rho(\boldsymbol{r},\omega) = \frac{1}{4\pi k_0^2}\, Im[Tr\{\boldsymbol{S}(\boldsymbol{r},\boldsymbol{r}',\omega)\}] \tag{2.22}$$

Pour comprendre le concept de densité d'états locale de plasmon de surface, considérons par exemple un nanoprisme d'or triangulaire. La figure 2.7 (a) montre les cartes de LDOS photonique calculées sur un plan parallèle au nanoprisme d'or à Z = 100nm. La LDOS photonique se compose d'un motif d'intensité complexe, principalement situé en dehors du périmètre du nanoprisme d'or. A Z = 0 nm, la LDOS du système est liée aux modes plasmoniques qui ne sont présent qu'à l'intérieur de la nanostructure métallique. À ce stade, nous souhaitons introduire un concept équivalent mais distinct appelé densité d'états locale des plasmons de surface ou SPLDOS qui est la densité d'états locale associée aux oscillations électroniques collectives à l'intérieur d'une nanostructure métallique. La SPLDOS peut être étudiée par des techniques expérimentales telles que la spectroscopie des pertes d'énergie électronique (EELS) et la cathodoluminescence [37]. Dans ce travail, nous avons utilisé une autre technique expérimentale appelée microscopie de photoluminescence non linéaire (NPL), dont il a été montré dans le groupe qu'elle permettait aussi d'étudier la SPLDOS à l'intérieur d'une nanostructure métallique. Dans notre cas, la non-linéarité est surtout proche du second ordre [39]. Donc, nous allons maintenant utiliser dans ce travail, le terme luminescence à deux photons (TPL). L'intensité TPL issue d'une cellule élémentaire de volume 'v' au point 'r' est liée à la SPLDOS au même point par l'équation

$$I_{TPL}(\boldsymbol{r_0},\boldsymbol{r},\omega) = \eta^2(\omega_0)\pi^4{\omega_0}^4 A^{-2} \int_V |\boldsymbol{E_0}(\boldsymbol{r_0},\boldsymbol{r},\omega)|^4 . {\rho^2}_{||}(\boldsymbol{r},\omega_0) d\boldsymbol{r} \tag{2.37}$$

Ce qui nous indique que l'intensité TPL résulte de la convolution de la SPLDOS au carré avec le profil du faisceau gaussien à un point donné 'r'. Lorsque la taille du faisceau tend vers zéro, les cartes TPL convergent vers les cartes SPLDOS au carré.

2.3 Les systèmes colloïdaux cristallins pour des dispositifs plasmoniques reconfigurables

La performance des dispositifs plasmoniques actuels et des prototypes est en partie limitée par les pertes dues aux défauts du réseau et aux limites granulaires du système [51].

Ces limitations peuvent être surmontées en utilisant des stratégies “bottom-up” et avec la fabrication de nanostructures hautement cristallines. Dans ce travail, nous avons utilisé deux nanostructures d'or différentes pour nos études. La première avec les nanoprismes triangulaires et hexagonaux, de taille variant de 300 nm à 2 µm et d'une épaisseur de 20 nm. Un autre type de nanostructures en or utilisé dans ce travail a été produit par une méthode en une étape (discuté le chapitre suivant). Ces nanoparticules d'or sont comparativement plus grandes que les cavités d'or vues précédemment avec une taille allant de 1 à 20 microns et une épaisseur de 30 nm.

Chapitre III

Matériaux et méthodes

3.1 Fabrication et techniques de caractérisation

Deux échantillons différents produits par chimie colloïdale ont été utilisés au cours de ce travail. Du point de vue de ce travail, ils diffèrent exclusivement par leurs dimensions latérales qui sont de 0,3 à 2 µm pour la première et de 1 à 30 µm pour la seconde. Les nanoprismes d'or cristallins utilisés dans ce travail ont été synthétisé par une nouvelle méthode en une étape développée par J. Sharma [1]. Les autres microplaquettes d'or sont le résultat d'une réduction d'une solution aqueuse d'acide chloroaurique par des fibrilles de protéines amyloïdes β-lactoglobulines (figure 3.1) et sont produites par R. Mezzenga (ETH Zurich) [2].

Un microscope à faisceau d'ions focalisés (FIB) est utilisé pour découper des structures spécifiques à partir des microplaquettes. Le principe de fonctionnement du FIB est semblable à celui des microscopes électroniques à balayage (SEM) à l'exception du fait que le FIB utilise un faisceau d'ions finement focalisé. Lorsqu'il fonctionne avec des courants de faisceau faibles, il permet d'effectuer de l'imagerie. Avec des courants de faisceau élevés, cette technique est utilisée pour de la pulvérisation locale ou du découpage spécifique.

La spectroscopie de diffusion en champ sombre est utilisée pour caractériser les nanoprismes d'or dans ce travail. La lumière incidente de la lampe n'éclaire pas directement l'échantillon. Le condenseur de champ sombre produit un anneau de lumière à un angle extrêmement oblique par rapport à la surface de l'échantillon, qui est focalisé sur celui-ci. Il diverge alors tellement que seule la lumière diffusée par l'échantillon entre dans l'objectif de collection.

L'outil de caractérisation suivant utilisé dans cette étude est la microscopie de photoluminescence non linéaire. Le principe de l'excitation multi-photons est basé sur l'idée que deux ou plusieurs photons, avec une énergie des photons comparativement inférieure à celles nécessaires pour une excitation linéaire, peuvent également exciter une molécule. Par exemple, dans le cas du microscope de luminescence à deux photons (TPL), chaque photon contient environ la moitié de l'énergie nécessaire à la transition. Une excitation entraîne l'émission subséquente d'un photon, typiquement à une énergie supérieure à l'un ou l'autre des deux photons d'excitation. Un premier photon de longueur d'onde proche IR favorise une transition intrabande à l'intérieur de la bande de conduction sp. Le second photon excite une

transition intrabande entre les bandes d et sp. Après l'absorption par des transitions interbandes, les paires d'électrons-trous générées se recombinent et émettent un photon.

Le développement de dispositifs SPP 2D nécessite des techniques de recherche expérimentales capables d'imager la propagation des SPPs dans les systèmes 2D. La nature évanescente des SPPs et leur fuite dans le substrat diélectrique à travers un film métallique mince permet leur découplage en ondes lumineuses propagatives avec une conservation du vecteur d'onde. Ceci a conduit au développement d'une technique simple mais puissante appelée microscopie de rayonnement de fuite. Cet outil mis en place par A. Bouhelier dans son groupe de ICB à Dijon sur lequel j'ai effectué des campagnes de mesures. Il a été utilisé ici pour l'étude de la transmission dans les dispositifs plasmoniques 2D.

3.2 Techniques de simulation

Les progrès récents dans les techniques de fabrication et de caractérisation ont nécessité des efforts simultanés sur le front théorique pour comprendre les propriétés optiques des systèmes d'échelle mésoscopique et nanométrique. Dans ce travail, la méthode de la fonction de Green Dyadique développée par C. Girard est utilisée pour simuler les propriétés de structures réalistes. La réponse totale à un champ d'incident donné, à l'intérieur d'une nanostructure de forme arbitraire, peut être dérivée d'un propagateur de champ généralisé unique, K (r,r',ω) et est donnée par

$$\boldsymbol{E}(\boldsymbol{r},\omega) = \int d\boldsymbol{r}'\boldsymbol{K}(\boldsymbol{r},\boldsymbol{r}',\omega)\boldsymbol{E_0}(\boldsymbol{r}',\omega) \tag{3.23}$$

où

$$\boldsymbol{K}(\boldsymbol{r},\boldsymbol{r}',\omega) = \delta(\boldsymbol{r}-\boldsymbol{r}')\boldsymbol{I} + \chi_0(\boldsymbol{r}',\omega)\boldsymbol{S}(\boldsymbol{r},\boldsymbol{r}',\omega) \tag{3.24}$$

I est le tenseur identité. Le propagateur généralisé dépend uniquement de la géométrie de la nanostructure et non du champ lumineux incident E_0(r',ω). Le tenseur de susceptibilité du champ, S(r,r',ω) dans l'équation ci-dessus, peut être calculé par un calcul itératif suivant l'algorithme de séquence de Dyson proposé par Olivier J.F. Martin et al. [39] -

$$\boldsymbol{S}(\boldsymbol{r_i},\boldsymbol{r_i},\omega) = \boldsymbol{S_0}(\boldsymbol{r_i},\boldsymbol{r_i},\omega) + \sum_{k=1}^{N}\boldsymbol{\chi_k}(\boldsymbol{R_k},\omega)\,\boldsymbol{S}(\boldsymbol{r_i},\boldsymbol{R_k},\omega)\boldsymbol{S}(\boldsymbol{R_k},\boldsymbol{r_i},\omega) \tag{3.27}$$

Afin de calculer le champ local en un point donné, nous devons d'abord définir le champ d'illumination. Nous avons modélisé un éclairage par faisceau Gaussien pour effectuer toutes les simulations de cette thèse qui peuvent être décrites en utilisant le modèle développé par Török et al [40]. L'intensité TPL à un point 'r' est liée à la SPLDOS au même point par la formule –

$$I_{TPL}(\boldsymbol{r}, \boldsymbol{r_0}, \omega) = \eta^2(\omega_0)\pi^4{\omega_0}^2 A^{-2} \int_V |\boldsymbol{E}_0(\boldsymbol{r}, \boldsymbol{r_0}, \omega)|^4 . {\rho^2}_{||}(\boldsymbol{r}, \omega_0) \quad (3{,}35)$$

Cette équation montre que l'intensité TPL résulte de la convolution du carré des SPLDOS dans le plan avec le profil Gaussien du faisceau en un point donné «r». Fait intéressant, lorsque la taille du faisceau gaussien tend vers zéro, les cartes TPL convergent vers des cartes SPLDOS au carré.

Ensuite, nous avons cherché à calculer le champ électrique local, à un point donné 'r' dû à l'excitation par un éclairage focalisé à la fréquence angulaire ω, et positionné en r_0. Le propagateur généralisé de l'équation (3.26) qui ne contient pas le terme de distribution de Dirac. Grâce à cette équation, on ne calcule que le transfert de signal dû aux plasmons dans les structures métalliques et non la contribution directe de la lumière incidente en sortie du système «r».

Chapitre IV

Ingénierie spectrale des nanoprismes plasmoniques bidimensionnels

Les nanoparticules plasmoniques bidimensionnelles (2D) de taille micrométrique offrent un grand potentiel pour des applications de réalisation de dispositifs plasmoniques et traitement de l'information. Ces cavités monocristallines possèdent des modes plasmoniques longitudinaux d'ordre supérieur et un mode transversal dans la région du visible et proche infrarouge. La conception d'un dispositif basé sur ces cavités plasmoniques multimodales en tant que blocs de construction élémentaires nécessite une étude préalable pour comprendre, contrôler puis manipuler les caractéristiques spatiales et spectrales des modes SP. Dans ce chapitre, nous étudierons les caractéristiques spectrales des nanoprismes d'or sur des substrats de verre/ITO au moyen de la spectroscopie en champ sombre. Nous examinerons l'effet de la présence à proximité de substrats métalliques sur la réponse spectrale de la cavité d'or. La dernière section traite de la démonstration de l'altération de la réponse spectrale des nanoprismes d'or percé d'un trou de taille nanométrique.

4.1 Nanoprismes d'or sur des substrats verre-ITO

Nous avons effectué une étude approfondie des spectres de diffusion en champ sombre de nanoprismes d'or (Au NP) individuels, cristallins, de forme triangulaire et de tailles allant de 400nm à 900nm sur des substrats de silice revêtus de 10 nm d'ITO. Le spectre en champ sombre révèle la présence de plus d'un pic (figure 4.3). Une décomposition en série de courbes lorentziennes est utilisée pour ajuster les spectres expérimentaux avec plusieurs pics associés à des résonances plasmon d'ordre supérieur de la cavité d'or. Une faible contribution du mode transversal est également observée dans les spectres expérimentaux. L'ensemble des spectres expérimentaux a pu être comparée aux des spectres de champ proche simulés au sommet et milieu du côté des triangles. La comparaison qualitative suggère que plusieurs résonances planaires SP contribuent à la lumière diffusée par ces cavités d'or. Les cartes SPLDOS simulées correspondant à chaque pic des spectres SPLDOS simulés révèlent l'ordre de chaque résonance. Un décalage dans le rouge des pics de résonance SP avec une augmentation de la taille de la cavité pour 16 cavités est observé (figure 4.4). Ceci est en accord avec la courbe de dispersion basée sur les spectres SPLDOS simulés (figure 4.4).

4.2 Réponse spectrale des nanoprismes d'or en présence d'un film métallique

Les nanoprismes d'or sont déposés sur un film d'or de 30 nm d'épaisseur dans une configuration métal-isolant-métal (MIM). La figure 4.6 compare les spectres en champ sombre enregistrés pour des cavités d'or de trois tailles différentes 455nm, 650nm et 720nm déposés sur des substrats verre-ITO ou sur un film mince d'or. La variation de l'intensité de diffusion en fonction de la taille de la cavité est similaire pour des cavités sur l'or à celles sur le substrat verre-ITO. Le spectre total d'une cavité de taille donnée subit un décalage global vers les longueurs d'onde bleues d'environ 50 - 75 nm dans les trois cas. Nous pensons que ce décalage vers le bleu provient d'un couplage électromagnétique entre le film et la cavité. Dans notre cas, il y a en effet un couplage, mais dont l'interaction n'est probablement pas très forte.

La figure 4.8 montre le potentiel de la configuration MIM pour décaler les résonances d'ordre supérieur portées par ces cavités d'or. Nous avons placé les résonateurs à proximité de films mince de métaux différents, de 30 nm d'aluminium ou 30 nm de platine. La figure 4.8 montre la comparaison entre les spectres de diffusion des cavités d'or de trois dimensions latérales différentes 460nm, 600nm et 725nm respectivement pour trois substrats différents: Al (bleu), Au (noir) et Pt (rouge). Les courbes montrent du platine à l'or puis à l'aluminium, on observe un décalage monotone vers le bleu de la réponse de diffusion globale du système MIM pour les cavités d'or. La partie réelle de la fonction diélectrique de l'or se situe entre celle des deux métaux donnés ($i.e.$ (ε_{Al})> (ε_{Au})> $Re(\varepsilon_{Pt})$) dans la gamme d'énergie de 1,5 eV à 3 eV). Par conséquent, le spectre de diffusion total, qui résulte du couplage film-particule, suit la même tendance que la partie réelle des fonctions diélectriques (aluminium - or - platine) du film métallique. Ce phénomène permet un ajustement spectral à la demande des résonances d'ordre élevé dans ces cavités.

4.3 Réponse spectrale des nanoprismes d'or en présence de trous

La réponse spectrale des nanoprismes d'or peut également être modulée en introduisant un défaut résonant sous la forme d'un trou. Cela a été démontré expérimentalement en découpant un trou au bord de la cavité triangulaire. La figure 4.10 montre la comparaison des spectres de diffusion expérimentale enregistrés sur une cavité d'or d'origine d'une taille latérale de 600 nm avec celle d'une cavité d'or de même taille le long d'une des arêtes. Nous observons une forte modification de la réponse spectrale. Le spectre de diffusion qui était auparavant centré autour de 700nm (pour le prisme d'origine) est maintenant à 660nm avec une réponse totale beaucoup plus étroite. L'intensité des spectres de diffusion a également diminué de

manière significative. Le spectre SPLDOS correspondant est montré dans la figure 4.10 (d) et (e) pour les cavités d'origines et découpées respectivement. Le point de calcul des spectres est montré dans l'encart de la figure 4.10 (a). Les spectres SPLDOS calculés suggèrent également une diminution du nombre de modes SP dans la fenêtre spectrale donnée pour le prisme perçé.

4.4 Conclusion

En conclusion, le spectre des cavités d'or cristallines de tailles allant de 400 à 900 nm a été étudié par spectroscopie de diffusion en champ sombre. Les pics de résonance SP pour chaque mode planaire dans ces cavités complexes se déplacent vers les longueurs d'onde rouges lorsque la taille des cavités augmente. Les spectres SPLDOS obtenus à partir de simulations ainsi que les résultats expérimentaux ont révélé que chaque mode planaire obtenu à partir de la simulation peut être associé à un pic de la décomposition Lorentzienne des spectres expérimentaux. Ce résultat s'est également avéré exact pour le substrat d'or, définissant le paysage plasmonique complet pour les résonances planaires de ce système dans le domaine du visible. En outre, la position des pics de résonance SP ajustés par une Lorentzienne est très dépendante de la fonction diélectrique du substrat. Ainsi, en changeant la nature du film métallique dans une géométrie MIM, nous avons démontré qu'un décalage vers le rouge ou bleu de la résonance globale peut être obtenu. Une autre stratégie pour régler la réponse spectrale du système avec de l'introduction d'un défaut local sous la forme d'un trou de longueur d'onde secondaire a été étudiée. Cette étude montre en détail des techniques pour l'ingénierie de la réponse spectrale des cavités d'or 2D qui ouvrent la voie à la réalisation de composants intégrés complexes.

Chapitre V

Antennes papillon multimodales

5.1 Introduction

Les prismes mésoscopiques d'or possèdent, dans le visible, des modes SP d'ordre supérieur d'un fondamental situé dans le proche infrarouge. Ils peuvent donc être des candidats appropriés pour réaliser le concept d'antennes plasmoniques intégrées à des dispositifs plasmoniques pour le traitement d'information optique. Dans ce chapitre, nous montrons que les antennes en forme de nœud papillon (dites "*bowtie"*) comprenant deux cavités plasmoniques de taille micrométrique fournissent une réponse optique plus riche que les antennes dipolaires sub-longueur d'onde classiques. Ces antennes en forme de nœud papillon sont sondées par microscopie TPL pour étudier la répartition spatiale des modes d'ordre supérieur portés par les cavités plasmoniques. Les cartes TPL expérimentales sont comparées à des cartes correspondantes simulées avec le formalisme GDM. Une étude numérique détaillée du taux de désexcitation normalisé d'un système moléculaire au voisinage de l'espace entre les cavités en fonction de la longueur d'onde est également réalisée. Ce travail souligne également l'utilité des antennes papillon multimodales pour la réalisation d'une porte d'entrée-sortie pour des volumes optiques nanométriques.

5.2 Réponse TPL des antennes papillon multimodales

La figure 5.1 montre la carte SPLDOS de deux antennes multimodales symétriques de taille 450nm. Une légère modification est visible dans la carte SPLDOS. La proximité des deux structures a légèrement affecté les deux modes de distribution m = 3. Les cartes TPL expérimentales correspondantes suggèrent une interaction entre les deux cavités qui changerait la réponse TPL des deux prismes par rapport à la réponse TPL des cavités isolées. La réponse TPL de la cavité triangulaire individuelle a été discutée par Viarbitskaya et al. qui montre l'apparition séquentielle de points chauds aux sommets de la cavité triangulaire lorsque la polarisation linéaire du champ incident est variée. La superposition des cartes TPL de deux polarisations orthogonales aboutit à trois points chauds à chacun des trois sommets de la cavité correspondant à la symétrie de la cavité triangulaire. Une forte réponse TPL de l'antenne papillon est observée dans le gap central pour une polarisation de 90 ° tandis que deux zones symétriques de TPL intenses sont observées à la périphérie de l'antenne pour une polarisation de 0 °. Il est intéressant de constater ici que le comportement des antennes papillon

multimodales contraste singulièrement avec celui des antennes sub-longueur d'onde standards, où la forte exaltation centrale est observée pour une polarisation incidente de 0 ° alors qu'une polarisation de 90 ° entraine une extinction du signal TPL. Les cartes TPL de l'antenne papillon multimodale ont été reproduites à l'aide d'un outil de simulation basé sur GDM, qui montre une excellente correspondance entre les résultats expérimentaux. Contrairement aux antennes papillon dipolaires, l'ordre de résonance qui se produit dans chaque bras des antennes multimodales peut être réglé en changeant la taille des cavités (figure 5.2). L'évolution de l'amplitude de la SPLDOS lorsque nous changeons la polarisation incidente suggère qu'un réglage précis de la réponse des antennes peut être obtenu par le choix de la taille du bras et par conséquent de l'ordre du mode SP actif.

En comparaison avec les antennes nœud *bowtie* dipolaires dont la réponse consiste uniquement en un basculement "on" / "off" de la réponse optique centrale, les antennes multimodales présentent une modulation différenciée du champ exalté dans le gap et à la périphérie de l'antenne, en fonction de la polarisation incidente. L'accord spectral des modes SP est régi par la taille et la forme de la cavité, mais leur accord spatial est défini par le positionnement relatif d'une cavité par rapport à l'autre. Le rapprochement des prismes ne modifie pas les modes SP natifs des cavités, mais modifie de façon spectaculaire la réponse TPL globale du dimère. Il a un impact énorme sur l'exaltation local du champ au centre de l'antenne (figure 5.4). Les antennes papillon multimodales offrent ainsi plus de degrés de liberté pour régler la réponse TPL du système par rapport aux antennes dipolaires. Ces paramètres complémentaires fournissent un moyen de contrôler la réponse plasmonique localisée (dans le gap) et délocalisée (à la périphérie des prismes) de ces antennes. Ceci procure un nouveau régime pour le développement de composants entrée-sortie pour les dispositifs de traitement de l'information plasmonique 2D. La région du gap peut être utilisée pour améliorer l'absorption ou l'émission d'émetteurs uniques tandis que les deux cavités peuvent être utilisées comme structures de propagation initiales ou terminales.

5.3 Renforcement local du champ et nature multi-échelles des antennes

La dynamique et le taux d'émission d'un dipôle placé au centre d'une telle antenne peuvent être quantifiés sous la forme d'un taux de désexcitation total normalisé de l'émetteur. La figure 5.6 montre que ces antennes papillon multimodales présentent une exaltation du taux d'émission normalisé du dipôle dans le proche infrarouge. La figure suggère qu'un comportement contre-intuitif du dipôle au voisinage de la structure. L'augmentation du taux d'émission total et l'amélioration du champ électrique local affiché dans les cartes TPL sont

directement corrélées. Le même comportement du taux de désexcitation normalisé est observé à la fois pour les deux configurations d'antenne et pour toutes les longueurs d'onde. Nous montrons que la dynamique d'émission est régie par l'environnement local autour du dipôle et par son orientation par rapport aux surfaces métalliques du gap. Cela est démontré dans la figure 5.7 où l'orientation du dipôle est choisie selon un axe préférentiel orienté respectivement parallèlement et perpendiculairement flanc du gap au centre de l'antenne. Le taux de désexcitation total est maintenant augmenté jusqu'à 8 fois pour un dipôle perpendiculaire aux bords du gap tandis que l'orientation du dipôle parallèlement aux bords du gap conduit à une augmentation de 3 fois. Ces résultats sont compatibles avec l'exaltation du champ observée en TPL. L'étude souligne donc l'importance de la géométrie locale du gap entre les deux prismes de l'antenne.

5.4 Conclusions

Pour conclure, nous avons démontré que deux cavités prismatiques plasmoniques et multimodales associées à une configuration symétrique et asymétrique en forme de nœud papillon résultent en un renforcement du champ dépendant de la polarisation et un confinement du champ à l'échelle nanométrique à des emplacements spécifiques. L'ordre du mode SP dans cette nouvelle classe d'antenne papillon dicte la condition d'accord spectral tandis que l'accord spatial est déterminée par le positionnement relatif des cavités l'une par rapport à l'autre. La rotation de la polarisation incidente permet un contrôle efficace de la réponse du gap tandis que les dimensions mésoscopiques des antennes leur confèrent un caractère multimodal qui permette le transfert d'information optiques à travers un canal plasmonique au-delà de la longueur d'onde efficace SP, ce qui n'est pas possible avec les antennes papillon dipolaire standards (ceci sera discuté plus en détail dans le chapitre suivant). Cette nouvelle famille d'antennes plasmoniques offre une excellente possibilité de concevoir des composants entrée-sortie plasmoniques visant à intégrer des architectures plasmoniques coplanaires.

Chapitre VI

Ingénierie des états propres plasmoniques dans un dispositif plasmonique 2D pour le contrôle de la transmission

6.1 Introduction

On assiste à un effort émergeant pour concevoir des composants plasmoniques afin de les intégrer dans des circuits plasmoniques opérationnels. Cependant, il existe plusieurs problèmes qui doivent être résolus avant qu'un circuit entièrement basé sur la plasmonique ne devienne réalité. L'un de ces principaux défis est de moduler et de contrôler la propagation SPP. Dans ce travail, nous proposons une nouvelle façon de contrôler la propagation de SPP en façonnant spécifiquement des états propres de transmission dans une géométrie multimodale 2D. Les caractéristiques des modes plasmoniques supportés par des cavités individuelles et couplées d'or, qui ont été discutées aux chapitres IV et V, sont la clé de la conception de ces états propres de transmission. Le comportement optique de deux cavités couplées est modifié par l'interaction électromagnétique entre elles. Une faible transmission dans la structure couplée en forme de papillon nous amène à concevoir une structure légèrement modifiée appelée diabolo, composée de deux nanoantennes papillon reliés par un canal métallique rectangulaire afin de faciliter le couplage entre les deux prismes triangulaires multimodaux (figure 6.1).

6.2 Calcul des cartes de transmission

Les cartes de transmission calculées dépendent de divers paramètres comme la forme du réseau, le type d'excitation, la hauteur du plan d'observation, la position d'excitation, etc. Pour calculer le champ local à n'importe quel point donné du diabolo ou au-delà, nous définissons d'abord l'excitation du champ. Dans cette section, nous discutons de l'effet des trois différents types d'excitation, à savoir l'excitation par un dipôle, l'excitation par une onde plane avec un profil d'intensité Gaussien et l'excitation par un faisceau Gaussien complet sur les cartes et les spectres de transmission. Pour l'excitation par dipôle et onde plane, dans le cas d'un réseau à 3 couches, le bruit de fond est nettement inférieur à celui d'un réseau d'une seule couche (figure 6.2 et 6.3). Pour l'excitation par faisceau Gaussien, des points chauds bien définis apparaissent avec une polarisation dans le plan de 0° sur les cavités triangulaires (figure

6.4) pour des réseaux à 1 et 3 couches. Pour la polarisation dans le plan à 90 °, des points chauds beaucoup plus faibles sont observés sur les deux bords de la cavité droite.

6.3 Conception du diabolo

La structure proposée dans la figure 6.1 (a) ne peut pas être synthétisée par chimie colloïdale. Ainsi, nous avons utilisé un mélange d'approche top-down et bottom-up pour fabriquer de telles structures. Les dispositifs en forme de diabolo ont été produits en découpant des micro plaquettes d'or cristallines déposées sur une lamelle de verre revêtue par 10 nm d'ITO. Des plaquettes hexagonales d'un diamètre de 3 à 5 µm ont donc été découpées en utilisant un système FIB intégré dans un microscope à double faisceau Zeiss 1540 XB (voir Matériaux et méthodes). Le protocole de gravure se compose de deux étapes. Dans la première étape, le motif du diabolo est découpé dans des plaquettes hexagonales d'or. La deuxième étape conssite à éliminer l'or de la zone périphérique de la microplaquette de départ, créant une structure en forme de diabolo bien isolée sur le substrat. Le chevauchement des zones de gravure entraîne une découpe inégale du substrat et du pourtour du diabolo. Pour éviter ces imperfections, le protocole a été amélioré en connectant à notre microscope à un générateur de motifs Raith Elphy Multibeam qui donne un bien meilleur résultat (figure 6.6).

6.4 Transmittance du signal plasmonique dans une cavité 2D en forme de diabolo

Le diabolo a été étudié expérimentalement par TPL dans deux modes de cartographie, à savoir la microscopie confocale et dans le plan image. La structure modale du diabolo obtenue par microscopie TPL confocale est comparée aux cartes SPLDOS projetées. La carte SPLDOS de la figure 6.7 (a) indique que lorsque le SPLDOS est projetée le long de la polarisation linéaire horizontale, une densité d'états plasmonique finie existe le long du canal, ce qui permet potentiellement le transfert du signal plasmonique. Cependant, en tournant la polarisation dans la direction verticale, on observe une forte diminution de la SPLDOS partielle le long du canal (figure 6.7b). La présence des points chauds sur les sommets de la structure diabolo suggère par ailleurs que les caractéristiques modales des triangles sont conservées même après l'introduction d'un canal entre les deux. Ces points chauds aux extrémités sont donc de bons candidats comme entrées et sorties opérationnelles de la structure diabolo pour la transmission du signal plasmonique. Une bonne correspondance entre les cartes expérimentales et simulées est observée. Ensuite, nous nous concentrons sur la transmission de l'information plasmonique dans les structures diabolo d'un sommet de la première cavité triangulaire à la cavité triangulaire opposée. Le contraste de l'intensité de transmittance à la sortie pour les deux

polarisations orthogonales nous permet de choisir 810nm comme longueur d'onde d'excitation expérimentale.

La figure 6.9 suggère que nous pouvons régler le signal TPL localisé émergeant de la cavité triangulaire droite du diabolo en basculant la polarisation du faisceau d'excitation de 0° à 90°. Ces résultats sont précisément reproduits dans les cartes de transmission simulées de champ proche. L'excitation par faisceau Gaussien a été utilisée pour calculer les cartes de transmission avec un réseau à une seule couche. Elle reproduit fidèlement la plupart des caractéristiques observées dans les cartes de transmission expérimentales.

Pour l'excitation à l'entrée du canal Ci, un changement de polarisation de 90° produit une augmentation de 9,0 fois de l'émission confocale en Ci mais seulement un rapport ON / OFF de 3,2 à la sortie (O) (figure 6.12). Il est important de noter ici que la distance entre le point d'entrée du canal (Ci) et la sortie (O) est d'environ 1,1 µm, soit près de la moitié de la distance entre l'entrée au sommet (I) et la sortie (O) (~ 1,9 µm). Cela suggère que la transmission ne se produit pas par simple propagation d'un SPP dans le film structuré, mais que la structure modale sous-jacente ainsi que les variations spatiales de l'efficacité d'excitation des modes décrite par les cartes de SPLDOS jouent également un rôle déterminant dans la modulation de la transmittance.

Une autre façon de moduler la transmittance dans la structure diabolo est de choisir la longueur d'onde d'excitation. À 750 nm, la transmittance calculée est faible pour les deux polarisations (figure 6.11). Ceci est vérifié expérimentalement. Les motifs dans le bloc d'excitation correspondent étroitement aux cartes simulées de champ proche pour les deux polarisations.

En outre, si nous augmentons la taille d'un prisme triangulaire d'environ 100nm par rapport à l'autre, de 650nm à 750nm, nous observons un ensemble différent de résonances (figure 6.14). Ce désaccord de résonances dans les deux blocs est potentiellement un facteur décisif pour la suppression de la transmission d'un bloc à l'autre. Nous avons considéré un diabolo non symétrique avec des tailles de prismes différant de 90nm. Pour l'excitation à l'entrée (I) avec un faisceau linéairement polarisé à 810nm le long de la direction horizontale, nous n'observons pas de signal de sortie observée en sortie (O) (figure 6.15) pour la polarisation du plan 0° et 90°. Nous supposons que la rupture de symétrie lors de la conception du diabolo maintient le système hors résonance en raison de l'incompatibilité spectrale entre les deux résonateurs modaux et ne permet pas une transmission délocalisée. Les cartes et spectres simulés correspondent bien à nos résultats expérimentaux et confirment la suppression de la transmittance.

6.5 Conclusion

En conclusion, nous avons conçu, fabriqué et étudier une structure cristalline mésoscopique en forme de diabolo 2D composée de deux cavités triangulaires reliées par un canal rectangulaire à partir d'une grande plaquette hexagonale en or cristallin. Nous avons obtenu un signal TPL confiné émergeant d'un sommet du bloc triangulaire lors de l'excitation au sommet diagonalement opposé (I) de l'autre bloc. En outre, avec le changement de position de l'excitation, du sommet à l'entrée de la chaîne, nous pouvons régler avec succès la transmission. Les performances de la modulation de transmission lors du changement de polarisation à 810 nm montrent un large rapport ON / OFF de 130 pour le diabolo symétrique et un rendement de transmission globale de 3,5% à 2 m de distance. Nous réalisons ainsi un dispositif de transmission opérationnel en utilisant des longueurs d'onde d'excitation appropriées et des polarisations à des emplacements d'entrée spécifiques dans la structure du diabolo. Cette approche par conception modale pour la modulation de la transmission SP dans la cavité plasmique 2D complexe contribue aux stratégies actuelles pour concevoir des dispositifs actifs de traitement de l'information.

Chapitre VII

Portes logiques plasmoniques modales reconfigurables

7.1 Introduction

Tout calcul de complexité arbitraire peut être ramené à une série d'opérations simples réalisées par des portes logiques Booléennes. Dans l'algèbre booléen, les portes logiques fondamentales sont AND, OR et NOT, elles peuvent être utilisées pour réaliser des opérations de porte logique plus complexes telles que NAND, NOR, XOR, X-NOR, etc. Actuellement, la technologie dominante est basée sur la mise en œuvre de portes logiques fondamentales reposant sur des transistors à effet de champ (FET) et la technologie des semi-conducteurs métal-oxydes complémentaires (CMOS) [3] - [5]. En optique, la réalisation d'une porte logique a été théoriquement proposée principalement par des structures individuelles en cascade [9] ou par des techniques interférentielles. Jusqu'à présent, la plupart des portes logiques optiques exploitent des interférences constructives et destructives dépendant de la phase entre les faisceaux de plasmons dans les systèmes. Le fonctionnement de ce type de dispositifs interférentiels dépend directement du positionnement d'une nanoparticule ou d'un bloc de construction par rapport à d'autres. En outre, la construction d'un circuit intégré basé sur des portes logiques interférentielles nécessitera une concaténation de diverses structures de portes logiques et une reconstruction du dispositif pour chaque nouvelle fonction logique souhaitée. Dans ce chapitre, nous montrons que plusieurs opérations de porte logique peuvent être réalisées dans une seule et même cavité métallique 2D selon l'idée proposée dans [15]. Toutes les portes logiques à deux entrées et une sortie possibles hormis XOR/NXOR ont été réalisées (leurs tables de vérité respectives sont présentées à la figure 7.1).

7.2 Une expérience par la pensée

Une expérience de principe consiste à utiliser deux spots laser étroitement focalisés de longueur d'onde et de puissance identiques, mais de polarisations linéaires différentes pour exciter deux positions d'entrée et lire l'intensité TPL à des positions de sortie éloignées [15]. Les entrées sont excitées alternativement avec une temporisation pour éviter toute interférence entre les deux signaux. La sortie ON-OFF est choisie en définissant une intensité de seuil à la sortie. Si l'intensité TPL est supérieure au seuil, la sortie est '1', ou dans le cas contraire '0'. De cette façon, la table de la vérité est construite en fonction de toutes les configurations d'entrée et des intensités TPL de sortie correspondantes.

7.3 Le choix de la structure pour le dispositif de portes logiques modales

Un principe important qui peut être utile lors de la conception d'une porte logique est la nécessité de briser la symétrie d'excitation ou celle du dispositif lui-même. L'introduction de l'asymétrie dans le système peut entraîner un comportement de sortie non trivial. Nous avons décidé de fusionner deux dimères pour obtenir une meilleure délocalisation du signal d'un dimère à l'autre. Ici, nous proposons trois structures fusionnées. La première structure proposée est une structure fusionnée constituée d'un rectangle à symétrie C2 et d'un hexagone à symétrie C6 (figure 7.6a). La deuxième est une combinaison de deux rhomboïdes combinés pour former une structure ressemblant à un livre ouvert (figure 7.5f). La dernière structure proposée est constituée de deux hexagones identiques fusionnés comme indiqué dans le modèle de la figure 7.5 (k). Les cartes SPLDOS projetées pour la double structure hexagonale suggèrent une variation d'intensité significative dans les coins de l'hexagone gauche et droit avec la polarisation du faisceau incident. Cela en fait un bon candidat pour être utilisé comme emplacement d'entrée et de sortie.

7.4 Réalisation de portes logiques modales sur des structures à double hexagone

Les structures à double hexagones ont été usinées à partir de micro plaquettes hexagonales cristallines. Les cartes de transmission ont été enregistrées pour une excitation sur les positions d'entrée I1, I2, I3, I4, I5, I6 et I7 (Figure 7.7). À l'aide de ces cartes de transmission, la première implémentation expérimentale de la porte logique sur la structure double hexagone est montrée en figure 7.8. Ici, les positions I1 et I3 sont choisies comme deux emplacements d'entrée et les entrées “0” et “1” sont encodées avec une polarisation du rayon incident de 130° et 70°. Six sommets de l'hexagone droit O0, O1, O2, O3, O4 et O5 sont choisis comme sorties. Une coupe transversale est ensuite effectuée le long des bords du côté droit de l'hexagone pour les quatre images de transmission superposées (figures 7.8 a-d). Les profils obtenus à partir des coupes transversales avec quatre ensembles différents de configurations d'entrée sont tracés à la figure 7.8 (e). Une intensité de seuil de 20 a.u. aboutit à deux portes OR, une porte NOT, deux Tautologie et une Copie (Tableau 7.8f).

7.5 Reconfiguration des portes logiques plasmoniques modales

Les valeurs de sortie de la porte logique plasmonique construite dans la section précédente varie avec plusieurs paramètres de mise en oeuvre comme la polarisation du faisceau d'excitation, la sélection des positions d'entrée, la sélection du seuil, la longueur d'onde

du faisceau d'excitation et les positions de lecture des sorties. Une variation de seuil de 20 a.u. à 50 a.u. nous donne trois COPY, une porte NOT, une porte AND et une Contradiction (figure 7.9). Dans l'exemple suivant, nous avons choisi un ensemble d'entrées I2 et I7 différent (figure 7.10). Cet ensemble d'entrées crée une contradiction, une tautologie, une copie et une porte NOT pour chacune des deux entrées. Ensuite, nous considérons le même ensemble d'entrées (I1 et I3) comme dans la figure 7.8 mais en modifiant les polarisations incidentes à 150° et 110°, ce qui a abouti à 3 COPIES, une porte AND et une porte NOT. La configuration actuelle (figure 7.11) offre également la possibilité de réaliser la porte NOR en inversant les valeurs des polarisations de 150° et 110° à '1' et '0' respectivement.

7.6 Conclusion

Pour conclure, nous avons réussi à réaliser des portes logiques plasmoniques modales à partir du principe énoncé en 2013. L'expérience a été réalisée sur une double structure hexagonale avec plusieurs positions d'entrée et de sortie. Nous avons réalisé un total de 10 configurations de portes logiques sur 12 possibles, telles que NOT aux deux entrées, Copie au deux entrées, AND, OR, NAND, NOR, Tautologie et Contradiction. Les portes logiques plasmoniques ont été reconfigurées en modifiant le seuil, l'ensemble des entrées et l'ensemble des polarisations incidentes aux entrées.

Chapitre VIII

Conclusions et perspectives

L'objectif principal du travail de ce doctorat était de concevoir, fabriquer et caractériser des composants plasmoniques composé de cavités métalliques 2D hautement cristallines conduisant à des applications en modulation du signal plasmonique et à la réalisation d'un dispositif de porte logique reconfigurable. Pour acquérir une meilleure compréhension du sujet, nous avons étudié le comportement spectral de ces cavités d'or multimodales à l'aide de mesures spectroscopiques en champ sombre appuyées par le calcul des spectres SPLDOS obtenus avec un outil numérique basé sur GDM. On a constaté que ces cavités plasmoniques présentaient de multiples pics de résonance dans une fenêtre spectrale allant de 450 nm à 850 nm. Les spectres SPLDOS ont révélé que chaque mode planaire issu de la simulation peut être associé à un pic ajusté par une Lorentzienne dans les spectres expérimentaux. Ces pics de résonance SP se déplacent au fur et à mesure que nous augmentons la taille de la cavité. Un nouveau pic de résonance SP a émergé lorsque la taille de la cavité a été augmentée de ~ 90nm. Un décalage vers le rouge des longueurs d'onde du pic de résonance SP avec la taille a également été observé pour les cavités d'or déposées sur un film mince en or de 30 nm dans la configuration MIM. De plus, en changeant la constante diélectrique du film mince métallique dans la géométrie MIM, nous pourrions obtenir un décalage vers le rouge ou le bleu de la réponse globale du spectre de diffusion. Nous avons également discuté de la possibilité de régler la réponse spectrale des cavités prismatiques en introduisant un défaut de taille inférieur à la longueur d'onde sous forme de trou.

Les cavités plasmoniques multimodales ont ensuite été rapprochées l'une de l'autre pour former une antenne multimodale en forme de nœud papillon (*bowtie*). On a constaté que ces antennes présentaient un confinement à l'échelle nanométrique une exaltation du champ dans des endroits spécifiques et dépendant de la polarisation. La condition d'accord spectral dans ces antennes *papillon* a été déterminée par l'ordre du mode SP. La position relative des cavités l'une par rapport à l'autre régit l'accord spatial. La dimension mésoscopique de ces antennes permet d'envisager une utilisation dans la conception d'un composant plasmonique d'entrée-sortie avec la possibilité de canaliser des informations plasmoniques sur une distance beaucoup plus longue que la longueur d'onde effective des SPPs.

Nous avons façonné des états propres de transmission plasmonique dans une structure en forme de diabolo qui se compose de cavités triangulaires reliées par un canal rectangulaire.

Les cartes confocales TPL expérimentales conservent les caractéristiques modales des cavités individuelles dans cette géométrie complexe. La position du point chaud TPL dans l'une des cavités (I) est excitée pour obtenir une transmission du signal plasmonique vers un sommet éloigné de l'autre cavité (O) avec une efficacité de transmission de 3,5% sur une distance d'environ 2 microns. Nous obtenons un rapport ON / OFF de 130 en ajustant la polarisation du faisceau incident. On observe une dépendance directe de la transmission avec l'efficacité d'excitation qui suit la distribution SPLDOS le long de la voie de transmission. Un arrêt complet de la transmission d'une cavité à l'autre est obtenu en sélectionnant deux cavités avec une différence de taille supérieure à 90nm. Ainsi, une réalisation réussie d'un dispositif de transmission efficace en choisissant une taille appropriée, des longueurs d'onde d'excitation et des polarisations ainsi que des emplacements d'entrée spécifiques pourrait être réalisée.

Des portes logiques plasmoniques ont été réalisées avec succès sur une double structure hexagonale a partir des principes énoncé dans une expérience par la pensée proposée en 2013. Les portes logiques plasmoniques ont été mises en œuvre en choisissant un ensemble d'entrées et un ensemble de polarisations incidentes et un seuillage du signal de sortie. Au total, 10 configurations de portes logiques à deux entrées et une sortie sur les 12 possibles - NOT aux deux entrées, Copie au deux entrées, AND, OR, NAND, NOR, Tautologie et Contradiction - ont été réalisées avec succès. Nous avons obtenu jusqu'à cinq opérations de porte logique différentes simultanément sur un seul dispositif. Ces opérations logiques peuvent être facilement reconfigurées en modifiant les paramètres précités. Les deux portes logiques qui ne peuvent être réalisées avec le mécanisme d'excitation actuel sont XOR et NXOR. Ces deux portes ne peuvent être mises en œuvre en superposant deux images de transmission correspondant à deux conditions d'entrée différentes et nécessitent une approche différente. À l'avenir, nous souhaitons appliquer cette approche pour réaliser une porte logique plasmonique reconfigurable avec un contrôle actif. Une approche consiste à ajouter une électrode de contact qui peut fonctionner comme une source SP pompée électriquement. L'intégration d'une telle électrode de contact avec la double géométrie hexagonale actuelle peut nous fournir une commande active hautement désirable pour un dispositif à porte logique plasmonique.

L’intégration des composants plasmoniques a également été démontrée en couplant des émetteurs de photons uniques à des cavités plasmoniques [1], [2]. Récemment, Cuche et al. ont démontré qu’il était possible d’étudier des résonateurs plasmoniques multimodaux dans le régime quantique, et cela grâce à quelques centres NV contenus dans un nanodiamant (ND) accroché à l’extrémité d'une pointe optique [5]. Dans ce travail, les cartes de LDOS

photoniques ont été enregistrées à différentes longueurs d'ondes à proximité immédiate des résonateurs plasmoniques par filtrage sélectif en énergie des spectres d'émission. Alternativement, nous pouvons également disperser des émetteurs auprès de cavités plasmoniques. L'effet de la SPLDOS sur la dynamique d'émission de ces nanoparticules fluorescentes peut aussi être étudié en enregistrant la luminescence de l'émetteur en fonction de sa position par rapport à la cavité plasmonique. Dans un premier pas vers cette direction, nous avons commencé à étudier le couplage de centres NV dans des NDs positionnés à proximité d'une cavité plasmonique multimodale. La carte confocale du système couplé est illustrée à la figure 8.1 (a) pour une excitation à λ= 532nm. Dans un second temps, nous avons positionné le faisceau d'excitation sur un ND (montré par le cercle rouge en pointillé). L'image du rayonnement de fuite du système couplé est illustrée à la figure 8.1 (b). Bien que ce ne soient que des résultats préliminaires, cela ouvre la voie à une étude plus approfondie axée sur l'exploitation des centres NV pour la génération locale de SPPs individuels dans ces cavités plasmoniques, et leur utilisation pour la réalisation de dispositifs plasmoniques dans le régime quantique.

Conception et réalisation de dispositifs et portes logiques plasmoniques par ingénierie modale de cavités métalliques cristallines bidimensionnelles

L'objectif principal de cette thèse est de concevoir, fabriquer et caractériser les dispositifs plasmoniques basés sur les cavités métalliques bidimensionnelles monocristallines pour le transfert d'information et la réalisation d'opérations logiques. Les fonctionnalités ciblées émergent de l'ingénierie spatiale et spectrale des résonances plasmon d'ordre supérieur supportées par ces cavités prismatiques. Les nouveaux éléments étudiés dans cette thèse ouvrent la voie à de nouvelles stratégies de transfert et de traitement de l'information en optique intégrée et miniaturisée. Dans un premier temps, nous caractérisons la réponse optique des nanoplaquettes d'or ultra-fines et de taille submicronique (400 à 900 nm) par spectroscopie en champ sombre. La dispersion des résonances plasmoniques d'ordre supérieur de ces cavités est mesurée et comparée avec un bon accord aux simulations obtenues par la méthode des dyades de Green (GDM). En outre, nous présentons une analyse par décomposition lorentzienne des réponses spectrales de ces nanoprismes déposés sur des minces substrats métalliques. Nous avons, par ailleurs systématiquement étudié les effets qui pourraient modifier les résonances plasmoniques par microscopie de luminescence non-linéaire, qui s'est avérée un outil efficace pour observer la densité d'états locale des plasmons de surface (SPLDOS). En particulier, nous montrons que les caractéristiques spectrale et spatiale des résonances plasmoniques d'ordre supérieur peuvent être modulées par la modification du substrat (diélectrique ou métallique), par l'insertion contrôlée d'un défaut dans la cavité ou par le couplage électromagnétique, même faible, entre les deux cavités. L'ingénierie rationnelle de la répartition spatiale des résonances confinées 2D a été appliquée à la conception de dispositifs à transmittance accordable entre deux cavités connectées. Les géométries particulières sont produites par gravure au faisceau d'ions focalisé sur des plaquettes cristallines d'or. Les dispositifs sont caractérisés par cartographie de luminescence non-linéaire en microscopie confocale et en microscopie de fuites. Cette dernière méthode offre un moyen unique d'observer la propagation du signal plasmon dans la cavité. Nous démontrons la dépendance en polarisation de la transmission plasmonique dans les composants à symétrie et géométrie adéquates. Les résultats sont fidèlement reproduits par notre outil de simulation GDM adapté à la configuration de transmission. Enfin, notre approche est appliquée à la conception et à la fabrication d'une porte logique reconfigurable avec plusieurs entrées et sorties. Nous démontrons que dix des douze portes logiques possibles à 2 entrées et 1 sortie sont activable sur une même structure en choisissant les trois points d'entrée et de sortie et en ajustant le seuil de luminescence non-linéaire pour le signal de sortie.

Plasmon logic gates designed by modal engineering of 2D crystalline metal cavities

The main objective of this PhD work is to design, fabricate and characterize plasmonic devices based on highly crystalline metallic cavities for the two-dimensional information transfer and logic gate operations. First, we thoroughly characterize the optical response of ultra-thin gold colloidal cavities of sub-micronic size (400 to 900 nm) by dark-field spectroscopy (Fig. 1a). The dispersion of the high order plasmonic resonances of the cavities is measured and compared with a good agreement to simulations obtained with a numerical based on the Green Dyadic Method (GDM). We further extend our experiments to systematically tune the spectral responses of these colloidal nanoprisms in vicinity of metallic thin film substrates. A comprehensive study of these sub-micronic size cavity in bowtie antenna configuration is performed. We show a polarization-dependent field enhancement and a nanoscale field confinement at specific locations in these bowtie antennas. We systematically study the effects that could potentially affect the plasmonic resonances by non-linear photon luminescence microscopy, which has proved to be an efficient tool to observe the surface plasmon local density of states (SPLDOS). In particular, we show that an effective spatially and spectrally tuning of the high order plasmonic resonances can be achieved by the modification of the substrate (dielectric or metallic), by the controlled insertion of a defect inside a cavity or by the weak electromagnetic coupling between two adjacent cavities. The rational tailoring of the spatial distribution of the 2D confined resonances was applied to the design of devices with tunable plasmon transmittance between two connected cavities. The specific geometries are produced by focused ion milling crystalline gold platelets. The devices are characterized by non-linear luminescence mapping in confocal and leakage radiation microscopy techniques. The latter offers a unique way to observe propagating SPP signal over a 2D plasmonic cavity. We demonstrate the polarization-dependent mode-mediated transmittance for devices with adequate symmetry. The results are faithfully reproduced with our simulation tool based on Green dyadic method. Finally, we extend our approach to the design and fabrication of a reconfigurable logic gate device with multiple inputs and outputs. We demonstrate that 10 out of the possible 12 2-input 1-output logic gates can be implemented on the same structure by choosing the two input and the one output points. We also demonstrate reconfiguration of the device by changing polarization of the incident beam, set of input locations and threshold of the non-linear luminescence readout signal.